Chemistry of the Nanomaterial Interface: Controlling Nanoparticle Morphology, Self-Assembly, and Catalysis

By

Grayson Johnson

B.S. University of Virginia 2016

A Dissertation in Partial Fulfillment of the Requirements for the Degree of Doctor of Philosophy in the Department of Chemistry at the University of Virginia, 2021

Charlottesville, Virginia

Doctoral Committee:

Professor Sergei Egorov, Chair

Professor Ian Harrison

Assistant Professor Charles Machan

Professor Josh Choi

Assistant Professor Sen Zhang, Advisor

Abstract

Nanomaterials present a suite of properties that are advantageous for broad applications in the catalytic processes that will solve our energy requirements in the next century and beyond. They have a large surface area to volume ratio, maximizing the use of materials, and often have unique reactivities relative to their bulk counterparts. Moreover, colloidal chemistry approaches in recent decades have advanced to a stage where many unique and robust approaches to precisely control parameters such as size, shape, and composition exist. This tunability provides excellent model systems for studying heterogeneous catalysis in real conditions to optimize catalytic output by generating relationships between the well-defined nanomaterial structure and the activity.

The ability of nanomaterials to form these precisely controlled structures and to perform desired catalytic reactions are dictated by their surface chemistries. The binding of molecules to stabilize the surface directly impacts the final structure of the nanomaterial. Interactions of reaction intermediates with the surface dictate how successfully the material will catalyze a given reaction. The goal of this dissertation is to explore the surface chemistries of various nanomaterials through experimental and theoretical means to understand how these interactions influence nanoparticle morphology and improve catalytic activity.

For nanomaterial synthesis, the importance of surfactants and other chemical additives in producing anisotropic nanoparticles is explored in brookite TiO_2 and late

transition metal systems by application of Density Functional Theory (DFT). Furthermore, atomically precise rare earth oxides superlattices are generated by a self-assembly method driven by high-temperature surface ligand switching. Molecular dynamics simulations show the favorability of this switch and point to the interactions that generate the assembly.

For exploring nanomaterial catalysis, surface chemistry of catalytic intermediates is probed through DFT methods for CO_2 reduction over AgPd alloy nanoparticles and hydrogen evolution reaction over Ir-Co_2P nanoparticles. Surface enhanced infrared absorption spectroscopy (SEIRAS) is shown as an experimental probe for direct observation of reaction intermediates in the ethanol oxidation reaction. Each of these works derives information about how the surface strain, ligand, and ensemble effects influence catalysis over nanomaterials.

Acknowledgements

By the grace of God, I have lived a blessed life so far. I grew up in the beautiful county of Middlesex, VA on the Rappahannock river and developed a great appreciation for the natural world. I am grateful to my parents who invested so heavily in me and my academic development. Bringing me to the football games, basketball games, and summer camps at UVA gave me a deep appreciation for this place and inspired me to work to come here for undergrad.

I want to express my gratitude for all of the teachers who I had along the way to this point. Particularly, I want to thank to teachers at the Chesapeake Bay Governor's School for Marine and Environmental Science, Mr. Jim Beam, Mrs. Sarah Beam, Mrs. Sherry Pettyjohn, Mr. Stephen Mutisya, Mr. Phillip Sanderson, Mr. Robert Todd, and Mr. Robert Wright who gave me my first experience in research.

I would like to thank the chemistry and physics departments at UVA who helped me build my fundamental understandings of science both in undergraduate and in graduate schools. I have always found the professors here willing to discuss science whenever I would drop by. I especially want to thank Dr. Ian Harrison under whom I worked for 4 years developing my researching skills. I will always value the conversations that we had when I dropped by your office as some of the most intellectually stimulating discussions that I have had.

It has been a privilege to work with Dr. Sen Zhang as one of his first graduate students. Many might find such a proposition as a gamble, but the recruitment

committees that the chemistry department has put together since my time began at UVA have pulled (and continue to pull) great people to join the department, inspiring my confidence in him. In his recruitment talk, he displayed a great enthusiasm in his work and the possibilities that it has to improve the future. He has brought me many great opportunities to work with collaborators. I am honored to have been included on these projects, and that my opinions have been valued. When I finish the graduation process, I look forward to receiving the recipe for the duck that he promised at the first group Thanksgiving.

I have had many collaborators through my work here who I am grateful to have worked with. I want to thank Dr. Xu Zhang from the California State University at Northridge hosted me for several months while I learned density functional theory. It was a fantastic experience getting to experience living outside of Virginia for the first time. I thank the scientists who helped me with all of my X-ray needs, Dr. Diane Dickie and Dr. Cathy Dukes. I also want to thank Dr. Sheng Dai for collaborating with me in my award of the Department of Energy Office of Science Graduate Student Research Award.

I am grateful that organizations were willing to provide funding to me and my research. I acknowledge the Department of Energy Office of Science and the women of the Achievement Rewards for Collegiate Scientists Foundation for their financial support.

The members of the Zhang lab past and present, Dr. Zhiyong (Jerry) Zhang, Dr. Zhouyang Yin, Chang Liu, Perrin Godbold, Meiyang Cui, J.T. Brosnahan, Shen-Wei Yu, Xiao Wang, Bingkai Wang, Xiangru Wei, and Liyue Zhang, have been valuable friends and

coworkers. The discussions that I have had with them keep me sharp and inspire my research. Jerry was especially helpful in learning the new techniques for nanomaterials research. I am honored to have published papers with Jerry, Chang, Meiyang, and Perrin. I wish them all the best in their futures and I hope to continue to collaborate with those who continue to research.

Finally, I want to thank Chantel Bailey, my love, who has been patient with me while I finished this work. She gives me something to look forward to every day even when research is not working as I would hope.

Table of Contents

List of Figures and Tables

Chapter 1
Introduction: Morphological Control of Nanomaterials for Heterogeneous Catalytic Applications

1.1 Atomic Scale Structure, Nanoparticles, and Catalysis

Fundamental to chemistry is that atomic scale geometry is as critical to chemical reactivity and physical characteristics as properties like oxidation state or the elemental composition of the system. All life is only possible due to the specificity of proteins, the chemical kings of geometric complexity, and their binding pockets famously described by the lock and key model. Subtle structural changes of the molecule thalidomide, going from R to S chirality, converts a morning sickness sedative to a teratogen historically responsible for over 10,000 severe birth defects.[1] Elemental Au is ordinarily inert on the bulk scale[2], but when in the form of nanoparticles, Au may catalyze interconversion between CO and CO_2 with remarkable efficiency.[3-5]

A key challenge in chemistry, is to manipulate geometry at the atomic scale to achieve targeted chemical and physical properties. Much success has been achieved in the realm of homogeneous, molecular catalysts due to the maturity in their chemical syntheses and purification techniques at the laboratory scale. Tens of thousands of ligands may be designed and combined to generate unique active sites that can be well characterized and understood. Yet, from an industrial standpoint, homogenous catalysts have a major disadvantage. Because they exist in the same phase as the chemicals on which they are acting, expensive and energy intensive separation processes to purify the products and recycle the catalysts are required.[6] Heterogeneous catalysts, typically solids, that exist in a phase separate from the reactants and products, solve this issue with ease, but the active sites of most examples are ill-defined at the atomic level. Moreover, many of the catalyst atoms are buried in the bulk away from the reaction interface and unable

to participate in catalysis. This is particularly an issue when expensive precious metals are used as catalysts.

Nanomaterials provide a reasonable means to take advantage of the benefits of heterogeneous catalysis while addressing the weaknesses of these systems. Nanomaterials, broadly, encompass materials that have at least one dimension below ~100 nm (100 billionths of a meter). This class of materials includes nanoparticles (NP's 0-dimensional or point-like), nanowires (1-dimensional), and nanosheets (2-dimensional).[7, 8] The extremely small nature of these particles imparts several benefits beyond bulk materials (**Figure 1.1**).[9] By having the finely divided material, exceptional surface areas and enhanced atomic efficiency (the number of catalyst atoms able to participate in catalysis) may be achieved. Furthermore, as the size of a material is reduced to the nanoscale, its properties become more molecular like, and quantum size effects are able to manifest.[10] These effects can generate enhanced optical activities and exciting photocatalytic capabilities.[11-15] The small size allows scientists to more finely and uniformly tune the structure of the particles to generate geometries that are most favorable for the desired application. In the most uniform, i.e. monodispersed, samples nanoparticles may even behave as pseudo-atoms comprising self-assembled superlattices[16] generating unique, catalytic enhancements in several systems such as the oxygen reduction reaction (ORR)[17], oxygen evolution reaction (OER)[18], and CO_2 reduction[19] along with electronic couplings that have applications as electronic or optical components in devices.[20-23]

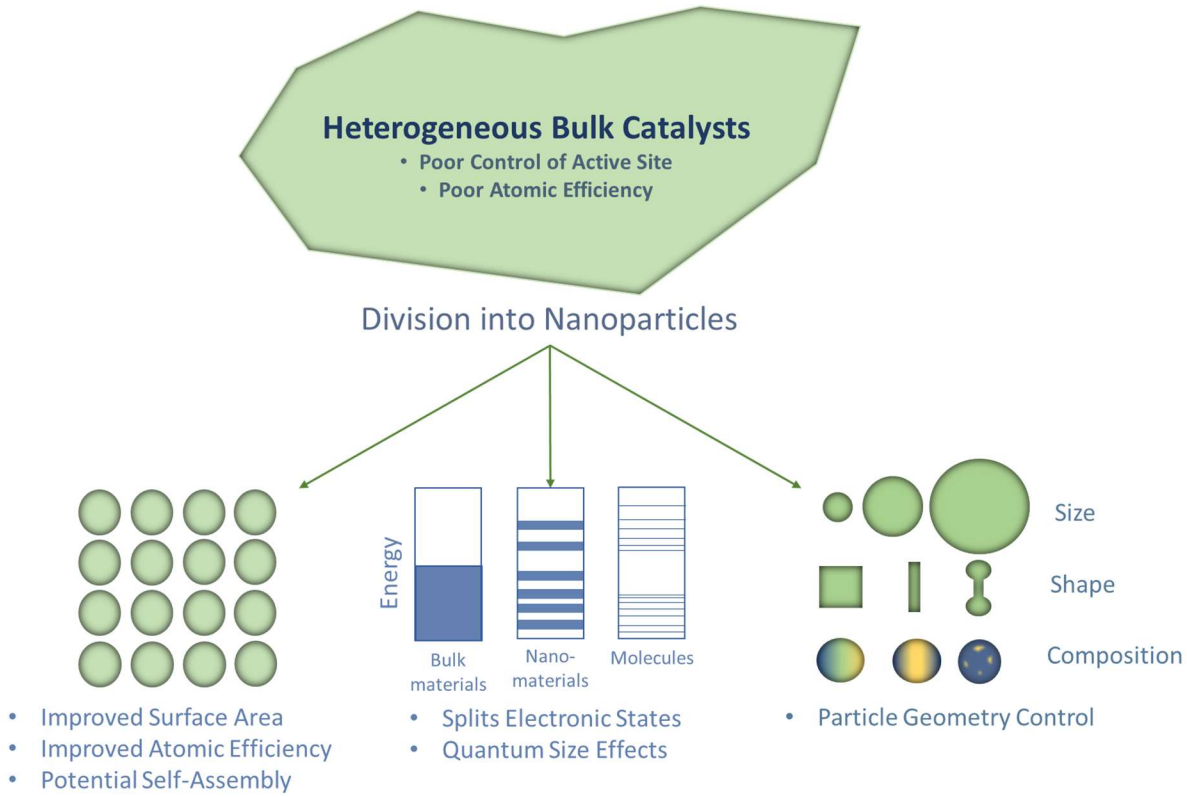

Figure 1.1 The adoption of nanomaterials rather than bulk heterogeneous catalysts generates several benefits due to the increased control of the atomic geometry over that in typical bulk catalysts.

The ability to finely tune nanoparticle geometry, including size[24-28], shape[29-35], and elemental distributions[36-40] as well as nanoparticle assembly[41-43] has developed significantly and allows researchers to study heterogeneous systems with rigor. Combining the ability of researchers to generate monodisperse nanoparticles with advanced materials characterization techniques such as transmission electron microscopy (TEM), X-ray diffraction (XRD), electron energy loss spectroscopy (EELS), X-ray absorption spectroscopy (XAS), X-ray photoelectron spectroscopy (XPS), and others, highly accurate information about structure can be derived. This information can better inform density functional theory (DFT) models to be highly relevant to the systems under study, and we can generate more reliable structure-activity relationships. Finally, we can recycle this procedure, having DFT guide the next synthetic targets until an optimal material performance is delivered (**Figure 1.2**).

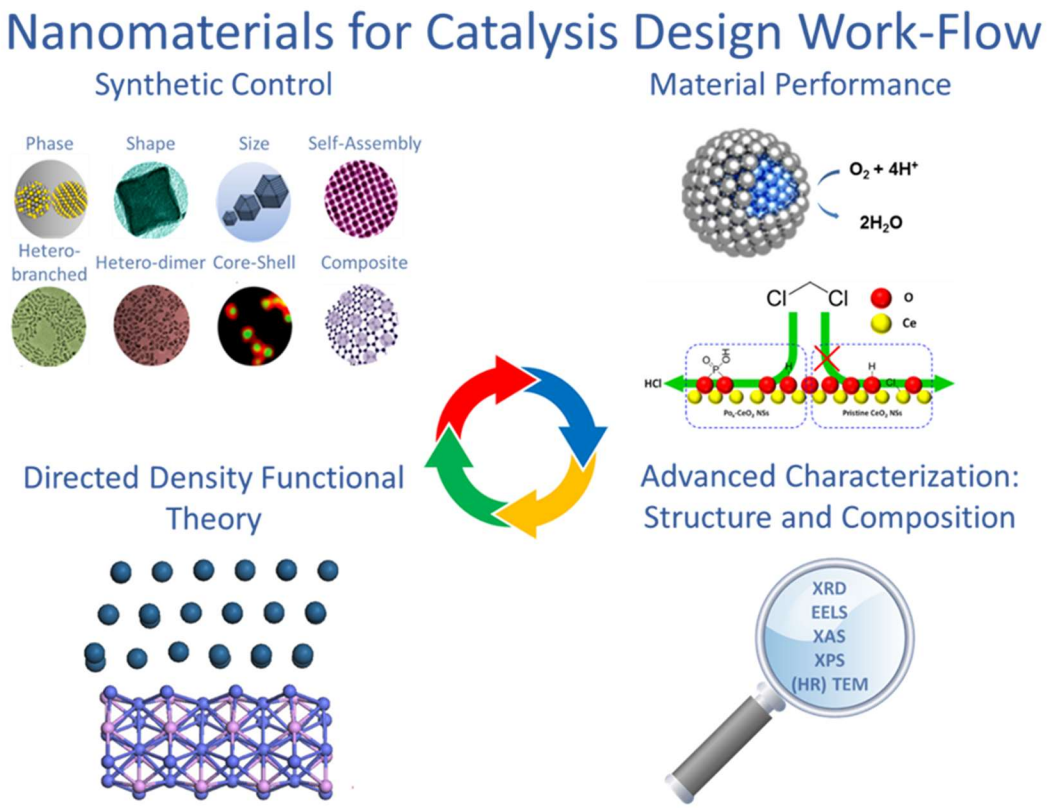

Figure 1.2 Work-flow describing the benefits of working with well-defined nanoparticles. Developing and employing refined synthetic methods to form nanoparticles, properties like phase, shape, size, and monodispersity may be controlled. These materials can be applied to different reactions such as ORR or hydrodechlorination[44] to find suitable catalysts. The optimal catalysts may be further interrogated through advanced characterization techniques. From the information derived there, DFT models (such as this core shell Pt-Co_2P structure) are used to explain the structure-activity. The cycle is repeated to find more optimal catalysts.

Being able to synthesize nanostructures to a desired morphology is the cornerstone of this rational method for nanomaterial catalyst development. While it is true that much work has been done to develop methods for generating these materials, often the work is phenomenological trial and error. Generally, more work is needed to generate theory that pinpoints the determining factors of nanoparticle structure. To achieve this, a marriage of experimental evidence with calculations, like that which is used to derive structure-activity relationships, is required.

My PhD studies aim to combine experiment and theory across several levels of nanoparticle catalyst development to better understand how nanoparticle structure is related synthetic conditions and chemical behavior. I experimentally demonstrate a new, colloidal method of generating self-assembled superlattices and rationalize their assembly based on *in-situ* and *ex-situ* characterization and molecular dynamics simulations. I use DFT to explore the thermodynamic driving factors of anisotropic nanoparticle generation with TiO_2 nanorods, Pt nanoparticles, and Cu_3M (M = Cu, Pd, Pt) nanoparticles. Furthermore, I explore the interactions of small molecule adsorbates with different models of experimentally demonstrated catalysts for the hydrogen evolution reaction (HER) and CO_2 reduction reaction (CO2RR).

1.2 Synthetic Control of Nanoparticle Geometry

The morphology of nanoparticles can take a wide array of forms, and with each of these forms, unique reactivities can be derived. This is a consequence in part from the differing arrangements of surface atoms for each nanoparticle geometry. Excluding

atomic clusters, which are small enough to be like molecules, nanoparticles will have a bulk crystal phase associated with them. The surfaces of these nanoparticles are defined in terms of Miller indices, values (HKL), that specify how the surface is cut from the bulk material. For facet (HKL), it is defined as the plane that intersects the unit vectors $\hat{\mathbf{x}}$, $\hat{\mathbf{y}}$, and $\hat{\mathbf{z}}$ at (1/H), (1/K), and (1/L) respectively as demonstrated in **Figure 1.3**. Low index facets (H,K,L) ≤ 1 are typically flat and stable while high index facets have steps, kinks, and corners that contribute to instability. For isotropic crystals like fcc, body-centered cubic (bcc), and simple cubic (sc) monoelemental crystals, there will be equivalence between families of crystals. The (100), (010), and (001) facets of Pt, for example, are all equivalent. More complicated crystal structures such as Co_2P, on the other hand, will have inequivalences between these facets, increasing the diversity of available surfaces. Furthermore, when incorporating different elements, different surface terminations for the same Miller Index may be possible due to the arbitrary nature of the unit cell origin.

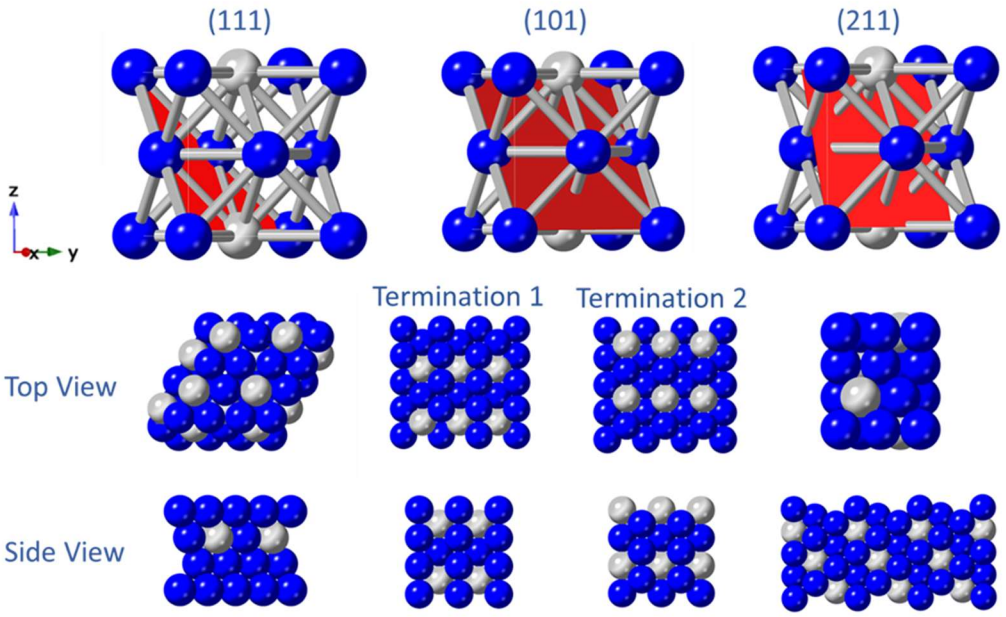

Figure 1.3 Surface models for a*n fcc* Cu_3Pt intermetallic phase crystal are presented. *Cu atoms are represented in blue while Pt is represented as grey.* The lattice planes (red) for the (111), (101), and (211) facets are shown intercepting the unit cell at (1,1,1), (1,∞,1), and (½, 1, 1) respectively. Top views and side views are shown for the surfaces represented by these Miller indices. Two terminations are shown for the (101) corresponding to two choices of origin. A clear step pattern is observed on the (211) surface while the other low index facets are relatively flat.

Often for synthesized materials, these facets are ill-defined and random. Ideal nanospheres will contain surface facets sampling all configurations. Other geometric shapes of nanoparticles like nanocubes[45, 46] or icosahedra[34] more selectively express the (100) and (111) facets for fcc metals. By controlling these nanoparticle shapes, different facets can be experimentally controlled in a way that allows researchers to draw correlations between a particular surface facet and a desired activity. Furthermore, by tuning the size of these anisotropic nanoparticles, researchers can further probe the importance of the edges and corners that join these facets since the ratio of open face to edges changes with size.

Due to the importance of tuning nanoparticle morphology, Chapters 3 and 8 of this work directly explore the surface chemistry responsible for particle anisotropy in brookite TiO_2 nanorods and in doped Cu_3M nanocrystals. Chapter 9 explores NHC as a potential structure directing agent to inform future experimental directions.

1.2.1 Size Control

The first major theory of colloidal nanoparticle formation comes from the work of LaMer discussing the formation of S nanoparticles (**Figure 1.4**).[47] At the most basic level, colloidal nanoparticle synthesis is preceded by the generation of component atoms from a precursor until a critical concentration above solution saturation is reached. At the critical concentration, nucleation of nanoparticles occurs, depleting the concentration of atoms below where nucleation occurs and where growth of the formed nanoparticles occurs. Growth of the nanoparticles is favored when organic ligands stabilize the surface against dissolution or agglomeration. This theory points to a direct means of controlling

nanoparticle size by reducing the nucleation time to as short of a period as possible. This is known as burst nucleation, and the idea is that if there is one time at which all nuclei form, they will all grow at the same rate to generate monodispersed nanoparticles. Strategies to improve burst nucleation typically involve increasing the rate at which the component atoms are produced from the precursor with fast temperature ramps[26, 28, 38, 48-52], injections of precursor at high temperature[53-61], or the rapid injection of chemical reductants[3, 62-64].

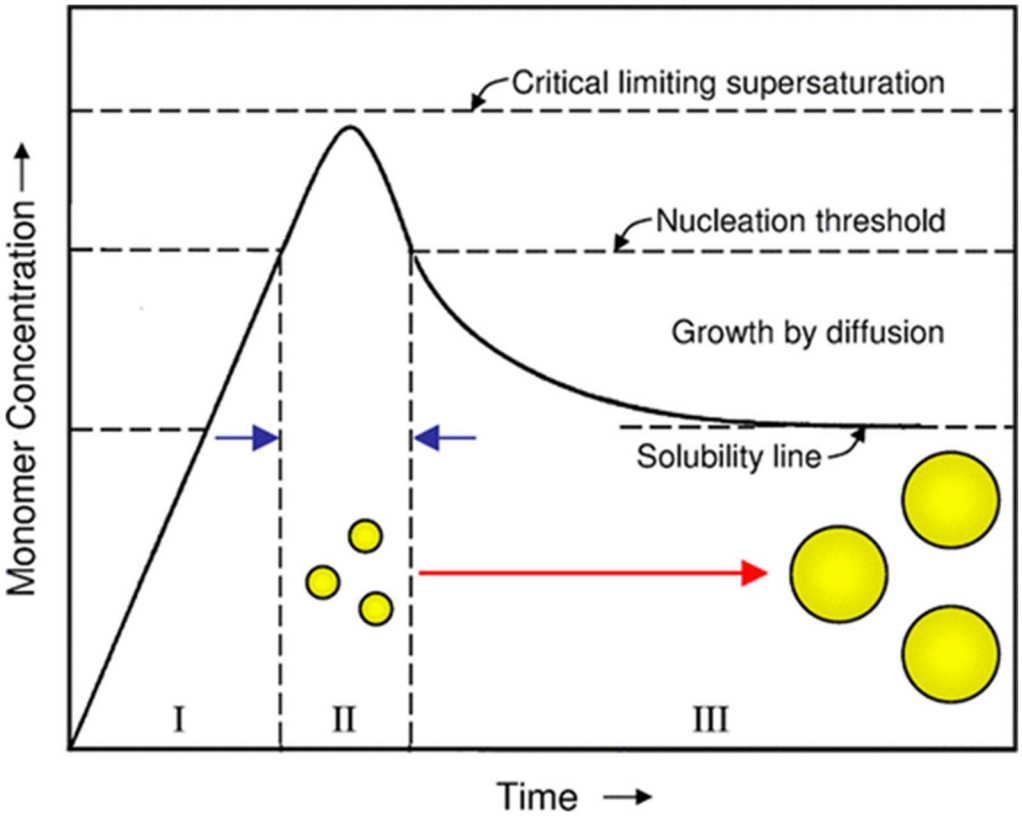

Figure 1.4 Figure describing classical LaMer theory of nanoparticle generation.[65] Monomers are generated rapidly above the nucleation threshold, at which point nanoparticles form and deplete the monomer concentration. Nanoparticles grow by diffusion past this point.

Generally, this is a good strategy, but deviations from classical nucleation theory also occur to complicate the synthesis. Some systems may go through a two stage nucleation process in which disordered clusters may first form and interact before crystalizing.[66] Aggregative nucleation of nanoparticles may result from the buildup of primary nanoclusters to a critical level at which secondary nucleation begins.[65, 67] This mechanism can manifest as a bimodal or multimodal size distributions, as often observed in the growth of Ag nanoparticles.[68] The growth process and beyond may also be complicated by additional processes. Ostwald ripening[69], in which material from smaller particles may dissolve and redeposit on larger particles, can occur when enough monomer is consumed. Alternatively, digestive ripening, when larger particles are consumed to reform monomer and deposit on smaller particles, may act as a size narrowing phenomenon as observed in PbS[70], Cd(S,Se)[71], and Au nanoparticles[72].

1.2.2 Shape and Composition Control

The growth phase of nanomaterials is often where nanoparticle anisotropy and composition are determined. A complex mix of growth kinetics and surface energy thermodynamics must be considered when explaining these phenomena. Surfaces are considered high energy structures due to the unsaturated bonds that make up the interface between the bulk and the external environment. This energy is facet dependent due to the different geometry, and thus bond saturation, that is possible in each case. In the simplest cases, the most thermodynamically stable facet(s) will be preferentially expressed on the nanoparticle, and the system will tend to minimize surface area. This extends to surface composition with elemental or alloy preferences also minimizing the

surface free energy. Formally, the Wulff construction model balances surface free energy and surface area to predict ideal equilibrium particle geometries.[73] For FCC metals, the closed-packed (111) facet tends to have the lowest surface free energy, followed by the (100), and the (110) surfaces. While an octahedron or tetrahedron would preferentially express the (111) facet, a cube has lower surface area per volume.[74] Combining these effects truncated octahedron, which are commonly observed for FCC metals, minimizes the total surface free energy.[75]

Surface free energy is generally reduced by chemically bonding to other moieties. This is why surfactants are crucial to nanoparticle syntheses; they stabilize the surface of the nanoparticles against agglomeration. Small molecules, however, do not bind to all facets equally. Therefore, they are an important tool for the nanomaterial scientist to vary the surface free energies of a material and influence the shape of the nanoparticle. Likewise, small ion adsorbates, polymers, and solvents all influence the interface to tune surface free energies and particle shape.[76] Anatase TiO_2, for instance, can be driven to form (101) nanobipyramids with Cl^- and or (001) nanosheets with F^- and 1-octadecanol.[29] Switching the surfactant from the alcohol to oleylamine generates mixed (100) and (101) structures with F^- and changes phase to form brookite with Cl^-.[77] Varying $SnBr_4$ concentrations can change $Cu_{2-x}S$ nanoparticles from bipyramids to nanoplates as well.[78] Decreasing the oleic acid – oleate ratio by increasing the pH in the synthesis of $NaYF_4$ nanoparticles will grow the length of the (100) facet over the (001) facet.[33] Overall, a wide array of shapes can be generated, although these methods are often derived through much trial and error.

More advanced strategies may also be employed to direct shape and control elemental distributions in multicomponent nanoparticles. Dynamic conditions on the Cu(111) facet resulting from Cl^- inhibiting surfactant adsorption is thought to drive Cu nanowire growth along this axis, but not on the (100) axis.[79] Core-shell methods in which a shape controlled particle has an unlike material grown on its surface can impose structure for an element that might not otherwise take it. For example, transition metals may be grown over Co_2P nanorods to form core/shell nanorods that are catalytically active for oxygen evolution and oxygen reduction chemistry.[40] In other cases entirely new geometries can be derived as the new material only deposits on particular facets of the nanoparticle. In this way, Au-Pd nano "dogbones"[14], nanoparticle dimers[80, 81], and other heterostructures[82] may be formed.

Nanoparticle morphology may also be tuned with post-synthetic modifications. Thermal annealing of nanoparticles can be a simple route. Annealing core-shell Co_2P/transition metal nanorods will result in diffusion of the shell into the core to generate transition metal doped Co_2P nanorods.[40] Annealing of intermetallic AuCu nanoparticles in air has been used to drive selective migration of Cu to the shell generating either AuCu/Cu or Au/Cu core shell nanoparticles from the face-centered tetragonal (fct) or face-centered cubic (fcc) phases respectively.[83] Hollow Cu_2O nanoparticles may be generated by the annealing of Cu nanoparticles in air due to the Kirkendall effect[84] in which Cu^+ ions diffuse to the surface faster than O^{2-} diffuses into the particle.[49] Nanoparticles comprised of ions can undergo cation or anion exchange to modify the composition with minimal disturbance of the crystal structure.[85-87] Partial

exchange can result in unique heterogeneous structures such as $Cu_{1.81}S$ capped at its poles by ZnS[88] or more complicated amalgamations of elements with repeated treatments.[89] From the heterogeneous structures, etching of the nanoparticles by dissolution in acid or other solvents has been used to selectively remove elements to generate core-shell nanoparticles,[64] hollow shell nanoparticles,[90] or more exotic hourglass like structures.[88]

1.2.3 Nanoparticle Self-Assembly

A more recent development in nanomaterials is the advent of self-assembled nanoparticle superlattices, and currently, there are few good methods for generating them at a large scale. Generally, self-assembly relies on highly monodisperse nanoparticles. Without monodisperse nanoparticles, defects would be introduced to the lattice, disrupting the order. While this is already a challenging experimental barrier, research into synthesizing more monodisperse nanoparticles has contributed to expansions of these materials significantly.

One set of methods to generate superlattice structures includes lithography or substrate templating that select nanoparticles and guide them into an assembled structure.[91] In another method, nanoparticles self-assemble at the interface of two phases, either liquid-air[92, 93] or liquid-liquid.[94] Commonly, a sample of freely dispersed, i.e. solvated, monodisperse nanoparticles is dropped onto an immiscible liquid. The solvating liquid is allowed to slowly evaporate while the nanoparticles concentrate and self-assemble to form a layer on the underlying liquid. Commonly, hexane or toluene dispersed nanoparticles set over polar diethylene glycol is used.[77, 95] Impressively, even

multicomponent assemblies can be achieved in this method.[17, 96-98] Alternatively, oil-water emulsions can trap high concentrations of nanoparticles such as the case of cobalt iron oxide nanoparticles that go on to assemble into icosahedron superparticles.[99]

Bottom-up, solution phase syntheses encompass the other class of nanoparticle assembly methods. In these methods, nanoparticle superlattices are generated in solution building up from the base components in solution. These methods are more desirable for scaling up for ease of study and eventual application. Often, this is accomplished by introducing interactive domains on the nanoparticles that force association and assembly into superlattices.[100] DNA functionalization of nanoparticles has been one procedure that accomplishes this with impressive selectivity.[42, 101, 102] Interactions between π systems of ligands from the synthesis of rare earth oxide[103, 104] and transition metal oxide[41, 105] nanoparticles has also been suggested. Solvent depletion interactions, often between lamellar, i.e. plate-like, particles is an entropy driven process that may also drive bottom up assembly.[106] Superlattice assemblies may also be formed by the generation of surfactant micelles that constrict nanoparticle formation into an ordered array.[43] In these cases, even gram scale quantities of materials have been generated.

In Chapter 5 of this work, the bottom-up self-assembly of atomically precise rare earth oxide nanoclusters is explored with in-situ and computational methods to provide important insights into this field.

1.3 References

1. Vargesson, N., Thalidomide-induced teratogenesis: history and mechanisms. *Birth Defects Res C Embryo Today* **2015,** *105* (2), 140-56.

2. Hammer, B.; Norskov, J. K., Why Gold Is the Noblest of All the Metals. *Nature* **1995,** *376* (6537), 238-240.

3. Zhu, W.; Michalsky, R.; Metin, O.; Lv, H.; Guo, S.; Wright, C. J.; Sun, X.; Peterson, A. A.; Sun, S., Monodisperse Au nanoparticles for selective electrocatalytic reduction of CO_2 to CO. *J. Am. Chem. Soc.* **2013,** *135* (45), 16833-6.

4. Kleis, J.; Greeley, J.; Romero, N. A.; Morozov, V. A.; Falsig, H.; Larsen, A. H.; Lu, J.; Mortensen, J. J.; Dulak, M.; Thygesen, K. S.; Norskov, J. K.; Jacobsen, K. W., Finite Size Effects in Chemical Bonding: From Small Clusters to Solids. *Catal. Lett.* **2011,** *141* (8), 1067-1071.

5. Mistry, H.; Reske, R.; Zeng, Z.; Zhao, Z. J.; Greeley, J.; Strasser, P.; Cuenya, B. R., Exceptional size-dependent activity enhancement in the electroreduction of CO_2 over Au nanoparticles. *J. Am. Chem. Soc.* **2014,** *136* (47), 16473-6.

6. Kazemi, M.; Ghobadi, M.; Mirzaie, A., Cobalt ferrite nanoparticles ($CoFe_2O_4$ MNPs) as catalyst and support: magnetically recoverable nanocatalysts in organic synthesis. *Nanotechnology Reviews* **2018,** *7* (1), 43-68.

7. Gogotsi, Y., *Nanomaterials Handbook*. CRC Press: 2006.

8. Ozin, G. A.; Arsenault, A., *Nanochemistry: a chemical approach to nanomaterials*. Royal Society of Chemistry: 2015.

9. Roduner, E., Size matters: why nanomaterials are different. *Chem Soc Rev* **2006,** *35* (7), 583-92.

10. Balaya, P., Size effects and nanostructured materials for energy applications. *Energy & Environmental Science* **2008,** *1* (6), 645-654.

11. Du, L. C.; Shi, X. P.; Zhang, G. R.; Furube, A., Plasmon induced charge transfer mechanism in gold-TiO_2 nanoparticle systems: The size effect of gold nanoparticle. *J. Appl. Phys.* **2020,** *128* (21), 213104.

12. Kim, Y.; Wilson, A. J.; Jain, P. K., The Nature of Plasmonically Assisted Hot -Electron Transfer in a Donor-Bridge-Acceptor Complex. *ACS Catal.* **2017,** *7* (7), 4360-4365.

13. Yu, S.; Jain, P. K., Plasmonic photosynthesis of C1-C3 hydrocarbons from carbon dioxide assisted by an ionic liquid. *Nat Commun* **2019,** *10* (1), 2022.

14. Yin, Y. Y.; Yang, Y.; Zhang, L. Z.; Li, Y. S.; Li, Z. Y.; Lei, W. W.; Ma, Y. F.; Huang, Z. R., Facile synthesis of Au/Pd nano-dogbones and their plasmon-enhanced visible-to-NIR light photocatalytic performance. *RSC Adv.* **2017,** *7* (59), 36923-36928.

15. Waiskopf, N.; Ben-Shahar, Y.; Banin, U., Photocatalytic Hybrid Semiconductor-Metal Nanoparticles; from Synergistic Properties to Emerging Applications. *Adv. Mater.* **2018,** *30* (41), e1706697.

16. Yu, C.; Guo, X.; Muzzio, M.; Seto, C. T.; Sun, S., Self-Assembly of Nanoparticles into Two-Dimensional Arrays for Catalytic Applications. *Chemphyschem* **2019,** *20* (1), 23-30.

17. Kang, Y.; Ye, X.; Chen, J.; Cai, Y.; Diaz, R. E.; Adzic, R. R.; Stach, E. A.; Murray, C. B., Design of Pt-Pd binary superlattices exploiting shape effects and synergistic effects for oxygen reduction reactions. *J. Am. Chem. Soc.* **2013,** *135* (1), 42-5.

18. Wu, L.; Li, Q.; Wu, C. H.; Zhu, H.; Mendoza-Garcia, A.; Shen, B.; Guo, J.; Sun, S., Stable Cobalt Nanoparticles and Their Monolayer Array as an Efficient Electrocatalyst for Oxygen Evolution Reaction. *J. Am. Chem. Soc.* **2015,** *137* (22), 7071-4.

19. Kim, D.; Resasco, J.; Yu, Y.; Asiri, A. M.; Yang, P., Synergistic geometric and electronic effects for electrochemical reduction of carbon dioxide using gold-copper bimetallic nanoparticles. *Nat Commun* **2014,** *5*, 4948.

20. Urban, J. J.; Talapin, D. V.; Shevchenko, E. V.; Kagan, C. R.; Murray, C. B., Synergism in binary nanocrystal superlattices leads to enhanced p-type conductivity in self-assembled PbTe/Ag_2Te thin films. *Nat. Mater.* **2007,** *6* (2), 115-21.

21. Ross, M. B.; Ku, J. C.; Vaccarezza, V. M.; Schatz, G. C.; Mirkin, C. A., Nanoscale form dictates mesoscale function in plasmonic DNA-nanoparticle superlattices. *Nat. Nanotechnol.* **2015,** *10* (5), 453-8.

22. Dong, A.; Chen, J.; Vora, P. M.; Kikkawa, J. M.; Murray, C. B., Binary nanocrystal superlattice membranes self-assembled at the liquid-air interface. *Nature* **2010,** *466* (7305), 474-477.

23. Zhou, J.; Wei, Y.; Pan, Y.; Wang, Y.; Yuan, Z.; Zhang, F.; Song, H.; Yue, J.; Su, H.; Xie, X.; Huang, L., A luminescent view of the clickable assembly of LnF_3 nanoclusters. *Nat Commun* **2021,** *12* (1), 2948.

24. Peng, S.; McMahon, J. M.; Schatz, G. C.; Gray, S. K.; Sun, Y., Reversing the size-dependence of surface plasmon resonances. *Proc Natl Acad Sci U S A* **2010,** *107* (33), 14530-4.

25. Reske, R.; Mistry, H.; Behafarid, F.; Roldan Cuenya, B.; Strasser, P., Particle size effects in the catalytic electroreduction of CO_2 on Cu nanoparticles. *J. Am. Chem. Soc.* **2014,** *136* (19), 6978-86.

26. Willis, J. J.; Goodman, E. D.; Wu, L.; Riscoe, A. R.; Martins, P.; Tassone, C. J.; Cargnello, M., Systematic Identification of Promoters for Methane Oxidation Catalysts Using Size- and Composition-Controlled Pd-Based Bimetallic Nanocrystals. *J. Am. Chem. Soc.* **2017,** *139* (34), 11989-11997.

27. Rekha, M. Y.; Akash, R.; Srivastava, C., Effect of Solvent on Average Size and Size Distribution of Platinum Nanoparticles. *Natl Acad Sci Lett* **2018,** *41* (3), 169-172.

28. Yang, Y.; Dai, C. Q.; Wu, D. F.; Liu, Z. P.; Cheng, D. J., The Size Effect of PdCu Bimetallic Nanoparticles on Oxygen Reduction Reaction Activity. *Chemelectrochem* **2018,** *5* (18), 2571-2576.

29. Gordon, T. R.; Cargnello, M.; Paik, T.; Mangolini, F.; Weber, R. T.; Fornasiero, P.; Murray, C. B., Nonaqueous synthesis of TiO_2 nanocrystals using TiF_4 to engineer morphology, oxygen vacancy concentration, and photocatalytic activity. *J. Am. Chem. Soc.* **2012,** *134* (15), 6751-61.

30. Kang, Y.; Pyo, J. B.; Ye, X.; Gordon, T. R.; Murray, C. B., Synthesis, shape control, and methanol electro-oxidation properties of Pt-Zn alloy and Pt_3Zn intermetallic nanocrystals. *ACS Nano* **2012,** *6* (6), 5642-7.

31. Zeng, H.; Rice, P. M.; Wang, S. X.; Sun, S., Shape-controlled synthesis and shape-induced texture of $MnFe_2O_4$ nanoparticles. *J. Am. Chem. Soc.* **2004,** *126* (37), 11458-9.

32. Qiao, L.; Fu, Z.; Li, J.; Ghosen, J.; Zeng, M.; Stebbins, J.; Prasad, P. N.; Swihart, M. T., Standardizing Size- and Shape-Controlled Synthesis of Monodisperse Magnetite (Fe_3O_4) Nanocrystals by Identifying and Exploiting Effects of Organic Impurities. *ACS Nano* **2017,** *11* (6), 6370-6381.

33. Liu, D.; Xu, X.; Du, Y.; Qin, X.; Zhang, Y.; Ma, C.; Wen, S.; Ren, W.; Goldys, E. M.; Piper, J. A.; Dou, S.; Liu, X.; Jin, D., Three-dimensional controlled growth of monodisperse sub-50 nm heterogeneous nanocrystals. *Nat Commun* **2016,** *7*, 10254.

34. Wu, J. B.; Qi, L.; You, H. J.; Gross, A.; Li, J.; Yang, H., Icosahedral Platinum Alloy Nanocrystals with Enhanced Electrocatalytic Activities. *J. Am. Chem. Soc.* **2012,** *134* (29), 11880-11883.

35. Yuan, X.; Zhang, L.; Li, L.; Dong, H.; Chen, S.; Zhu, W.; Hu, C.; Deng, W.; Zhao, Z. J.; Gong, J., Ultrathin Pd-Au Shells with Controllable Alloying Degree on Pd Nanocubes toward Carbon Dioxide Reduction. *J. Am. Chem. Soc.* **2019,** *141* (12), 4791-4794.

36. Hodges, J. M.; Kletetschka, K.; Fenton, J. L.; Read, C. G.; Schaak, R. E., Sequential Anion and Cation Exchange Reactions for Complete Material Transformations of Nanoparticles with Morphological Retention. *Angew Chem Int Ed Engl* **2015,** *54* (30), 8669-72.

37. Kuzuya, T.; Kuwada, T.; Hamanaka, Y.; Hirai, S., Synthesis of Ag/$CuInS_2$ Core-Shell Nanoparticles. *Mater. Trans.* **2017,** *58* (1), 65-70.

38. Dai, C.; Yang, Y.; Zhao, Z.; Fisher, A.; Liu, Z.; Cheng, D., From mixed to three-layer core/shell PtCu nanoparticles: ligand-induced surface segregation to enhance electrocatalytic activity. *Nanoscale* **2017,** *9* (26), 8945-8951.

39. Wang, P.; Yang, H.; Xu, Y.; Huang, X.; Wang, J.; Zhong, M.; Cheng, T.; Shao, Q., Synergized Cu/Pb Core/Shell Electrocatalyst for High-Efficiency CO_2 Reduction to C_{2+} Liquids. *ACS Nano* **2021,** *15* (1), 1039-1047.

40. Zhang, Y.; Li, N.; Zhang, Z.; Li, S.; Cui, M.; Ma, L.; Zhou, H.; Su, D.; Zhang, S., Programmable Synthesis of Multimetallic Phosphide Nanorods Mediated by Core/Shell Structure Formation and Conversion. *J. Am. Chem. Soc.* **2020,** *142* (18), 8490-8497.

41. Antonietti, M.; Niederberger, M.; Smarsly, B., Self-assembly in inorganic and hybrid systems: beyond the molecular scale. *Dalton Trans.* **2008,** (1), 18-24.

42. Nykypanchuk, D.; Maye, M. M.; van der Lelie, D.; Gang, O., DNA-guided crystallization of colloidal nanoparticles. *Nature* **2008,** *451* (7178), 549-52.

43. Nevers, D. R.; Williamson, C. B.; Savitzky, B. H.; Hadar, I.; Banin, U.; Kourkoutis, L. F.; Hanrath, T.; Robinson, R. D., Mesophase Formation Stabilizes High-Purity Magic-Sized Clusters. *J. Am. Chem. Soc.* **2018,** *140* (10), 3652-3662.

44. Dai, Q.; Zhang, Z.; Yan, J.; Wu, J.; Johnson, G.; Sun, W.; Wang, X.; Zhang, S.; Zhan, W., Phosphate-Functionalized CeO_2 Nanosheets for Efficient Catalytic Oxidation of Dichloromethane. *Environ. Sci. Technol.* **2018,** *52* (22), 13430-13437.

45. Peng, S.; Sun, Y. G., Synthesis of Silver Nanocubes in a Hydrophobic Binary Organic Solvent. *Chem. Mater.* **2010,** *22* (23), 6272-6279.

46. Guo, H.; Chen, Y.; Ping, H.; Jin, J.; Peng, D. L., Facile synthesis of Cu and Cu@Cu-Ni nanocubes and nanowires in hydrophobic solution in the presence of nickel and chloride ions. *Nanoscale* **2013,** *5* (6), 2394-402.

47. Lamer, V. K.; Dinegar, R. H., Theory, Production and Mechanism of Formation of Monodispersed Hydrosols. *J. Am. Chem. Soc.* **1950,** *72* (11), 4847-4854.

48. Han, W.; Yi, L.; Zhao, N.; Tang, A.; Gao, M.; Tang, Z., Synthesis and shape-tailoring of copper sulfide/indium sulfide-based nanocrystals. *J. Am. Chem. Soc.* **2008,** *130* (39), 13152-61.

49. Hung, L. I.; Tsung, C. K.; Huang, W.; Yang, P., Room-temperature formation of hollow Cu_2O nanoparticles. *Adv. Mater.* **2010,** *22* (17), 1910-4.

50. Wu, L.; Willis, J. J.; McKay, I. S.; Diroll, B. T.; Qin, J.; Cargnello, M.; Tassone, C. J., High-temperature crystallization of nanocrystals into three-dimensional superlattices. *Nature* **2017,** *548* (7666), 197-201.

51. Osowiecki, W. T.; Ye, X.; Satish, P.; Bustillo, K. C.; Clark, E. L.; Alivisatos, A. P., Tailoring Morphology of Cu-Ag Nanocrescents and Core-Shell Nanocrystals Guided by a Thermodynamic Model. *J. Am. Chem. Soc.* **2018,** *140* (27), 8569-8577.

52. Xie, H.; Chen, S.; Ma, F.; Liang, J.; Miao, Z.; Wang, T.; Wang, H. L.; Huang, Y.; Li, Q., Boosting Tunable Syngas Formation via Electrochemical CO_2 Reduction on Cu/In_2O_3 Core/Shell Nanoparticles. *ACS Appl. Mater. Interfaces.* **2018,** *10* (43), 36996-37004.

53. Kuzuya, T.; Itoh, K.; Ichidate, M.; Wakamatsu, T.; Fukunaka, Y.; Sumiyama, K., Facile synthesis of nearly monodispersed copper sulfide nanocrystals. *Electrochimica Acta* **2007,** *53* (1), 213-217.

54. Hongtao, L.; Yan, L.; Zan, W.; Ping, H., Facile synthesis of monodisperse, size-tunable SnS nanoparticles potentially for solar cell energy conversion. *Nanotechnology* **2010,** *21* (10), 105707.

55. Liu, S.; Chen, G. Y.; Prasad, P. N.; Swihart, M. T., Synthesis of Monodisperse Au, Ag, and Au-Ag Alloy Nanoparticles with Tunable Size and Surface Plasmon Resonance Frequency. *Chem. Mater.* **2011,** *23* (18), 4098-4101.

56. Sahu, A.; Qi, L.; Kang, M. S.; Deng, D.; Norris, D. J., Facile synthesis of silver chalcogenide (Ag_2E; E=Se, S, Te) semiconductor nanocrystals. *J. Am. Chem. Soc.* **2011,** *133* (17), 6509-12.

57. Jiang, C.; Lee, J. S.; Talapin, D. V., Soluble precursors for $CuInSe_2$, $CuIn_{(1-x)}Ga_{(x)}Se_2$, and $Cu_2ZnSn(S,Se)_4$ based on colloidal nanocrystals and molecular metal chalcogenide surface ligands. *J. Am. Chem. Soc.* **2012,** *134* (11), 5010-3.

58. Liu, Y.; Liu, M.; Swihart, M. T., Shape Evolution of Biconcave Djurleite $Cu_{1.94}S$ Nanoplatelets Produced from $CuInS_2$ Nanoplatelets by Cation Exchange. *J. Am. Chem. Soc.* **2017,** *139* (51), 18598-18606.

59. Sun, Y.; Zuo, X.; Sankaranarayanan, S.; Peng, S.; Narayanan, B.; Kamath, G., Quantitative 3D evolution of colloidal nanoparticle oxidation in solution. *Science* **2017,** *356* (6335), 303-307.

60. Lin, L.; Chen, M.; Qin, H.; Peng, X., Ag Nanocrystals with Nearly Ideal Optical Quality: Synthesis, Growth Mechanism, and Characterizations. *J. Am. Chem. Soc.* **2018,** *140* (50), 17734-17742.

61. Cademartiri, L.; Bertolotti, J.; Sapienza, R.; Wiersma, D. S.; von Freymann, G.; Ozin, G. A., Multigram scale, solventless, and diffusion-controlled route to highly monodisperse PbS nanocrystals. *J Phys Chem B* **2006,** *110* (2), 671-3.

62. Tang, Y.; Ouyang, M., Tailoring properties and functionalities of metal nanoparticles through crystallinity engineering. *Nat. Mater.* **2007,** *6* (10), 754-9.

63. Sigman, M. B., Jr.; Saunders, A. E.; Korgel, B. A., Metal nanocrystal superlattice nucleation and growth. *Langmuir* **2004,** *20* (3), 978-83.

64. Jiang, G.; Zhu, H.; Zhang, X.; Shen, B.; Wu, L.; Zhang, S.; Lu, G.; Wu, Z.; Sun, S., Core/Shell Face-Centered Tetragonal FePd/Pd Nanoparticles as an Efficient Non-Pt Catalyst for the Oxygen Reduction Reaction. *ACS Nano* **2015,** *9* (11), 11014-22.

65. Wang, F. D.; Richards, V. N.; Shields, S. P.; Buhro, W. E., Kinetics and Mechanisms of Aggregative Nanocrystal Growth. *Chem. Mater.* **2014,** *26* (1), 5-21.

66. Erdemir, D.; Lee, A. Y.; Myerson, A. S., Nucleation of crystals from solution: classical and two-step models. *Acc Chem Res* **2009,** *42* (5), 621-9.

67. Leffler, V.; Ehlert, S.; Forster, B.; Dulle, M.; Forster, S., Nanoparticle Heat-Up Synthesis: In Situ X-ray Diffraction and Extension from Classical to Nonclassical Nucleation and Growth Theory. *ACS Nano* **2021,** *15* (1), 840-856.

68. Richards, V. N.; Rath, N. P.; Buhro, W. E., Pathway from a Molecular Precursor to Silver Nanoparticles: The Prominent Role of Aggregative Growth. *Chem. Mater.* **2010,** *22* (11), 3556-3567.

69. Ostwald, W., Lehrbuch der Allgemeinen Chemie. Bd. 2. *Stöchiometrie* **1896,** *2*, 705-742.

70. Hines, M. A.; Scholes, G. D., Colloidal PbS nanocrystals with size-tunable near-infrared emission: Observation of post-synthesis self-narrowing of the particle size distribution. *Adv. Mater.* **2003,** *15* (21), 1844-1849.

71. Razgoniaeva, N.; Yang, M. R.; Garrett, P.; Kholmicheva, N.; Moroz, P.; Eckard, H.; Romero, L. R.; Porotnikov, D.; Khon, D.; Zamkov, M., Just Add Ligands: Self-Sustained Size Focusing of Colloidal Semiconductor Nanocrystals. *Chem. Mater.* **2018,** *30* (4), 1391-1398.

72. Lin, X. M.; Sorensen, C. M.; Klabunde, K. J., Digestive ripening, nanophase segregation and superlattice formation in gold nanocrystal colloids. *Journal of Nanoparticle Research* **2000,** *2* (2), 157-164.

73. Ringe, E.; Van Duyne, R. P.; Marks, L. D., Wulff construction for alloy nanoparticles. *Nano Lett.* **2011,** *11* (8), 3399-403.

74. An, K.; Somorjai, G. A., Size and Shape Control of Metal Nanoparticles for Reaction Selectivity in Catalysis. *ChemCatChem* **2012,** *4* (10), 1512-1524.

75. Pimpinelli, A.; Villain, J., Chapter 6. In *Physics of Crystal Growth*, Cambridge University Press Cambridge, UK: 1998.

76. Wu, Z.; Yang, S.; Wu, W., Shape control of inorganic nanoparticles from solution. *Nanoscale* **2016,** *8* (3), 1237-59.

77. Zhang, Z.; Wu, Q.; Johnson, G.; Ye, Y.; Li, X.; Li, N.; Cui, M.; Lee, J. D.; Liu, C.; Zhao, S.; Li, S.; Orlov, A.; Murray, C. B.; Zhang, X.; Gunnoe, T. B.; Su, D.; Zhang, S., Generalized Synthetic Strategy for Transition-Metal-Doped Brookite-Phase TiO_2 Nanorods. *J. Am. Chem. Soc.* **2019,** *141* (42), 16548-16552.

78. van der Stam, W.; Gradmann, S.; Altantzis, T.; Ke, X.; Baldus, M.; Bals, S.; de Mello Donega, C., Shape Control of Colloidal $Cu_{2-x}S$ Polyhedral Nanocrystals by Tuning the Nucleation Rates. *Chem Mater* **2016,** *28* (18), 6705-6715.

79. Kim, M. J.; Alvarez, S.; Chen, Z.; Fichthorn, K. A.; Wiley, B. J., Single-Crystal Electrochemistry Reveals Why Metal Nanowires Grow. *J. Am. Chem. Soc.* **2018,** *140* (44), 14740-14746.

80. Li, X. F.; Schaak, R. E., Reactive AgAuS and Ag_3AuS_2 Synthons Enable the Sequential Transformation of Spherical Nanocrystals into Asymmetric Multicomponent Hybrid Nanoparticles. *Chem. Mater.* **2017,** *29* (9), 4153-4160.

81. Huang, J.; Mensi, M.; Oveisi, E.; Mantella, V.; Buonsanti, R., Structural Sensitivities in Bimetallic Catalysts for Electrochemical CO_2 Reduction Revealed by Ag-Cu Nanodimers. *J. Am. Chem. Soc.* **2019,** *141* (6), 2490-2499.

82. Fantechi, E.; Roca, A. G.; Sepulveda, B.; Torruella, P.; Estrade, S.; Peiro, F.; Coy, E.; Jurga, S.; Bastus, N. G.; Nogues, J.; Puntes, V., Seeded Growth Synthesis of Au-Fe_3O_4 Heterostructured Nanocrystals: Rational Design and Mechanistic Insights. *Chem. Mater.* **2017,** *29* (9), 4022-4035.

83. Zhan, W.; Wang, J.; Wang, H.; Zhang, J.; Liu, X.; Zhang, P.; Chi, M.; Guo, Y.; Guo, Y.; Lu, G.; Sun, S.; Dai, S.; Zhu, H., Crystal Structural Effect of AuCu Alloy Nanoparticles on Catalytic CO Oxidation. *J. Am. Chem. Soc.* **2017,** *139* (26), 8846-8854.

84. Smigelskas, A. D.; Kirkendall, E. O., Zinc Diffusion in Alpha-Brass. *Trans. AIME* **1947,** *171*, 130-142.

85. Son, D. H.; Hughes, S. M.; Yin, Y.; Paul Alivisatos, A., Cation exchange reactions in ionic nanocrystals. *Science* **2004,** *306* (5698), 1009-12.

86. Jain, P. K.; Amirav, L.; Aloni, S.; Alivisatos, A. P., Nanoheterostructure cation exchange: anionic framework conservation. *J. Am. Chem. Soc.* **2010,** *132* (29), 9997-9.

87. Han, H.; Yao, Y.; Robinson, R. D., Interplay between Chemical Transformations and Atomic Structure in Nanocrystals and Nanoclusters. *Acc Chem Res* **2021,** *54* (3), 509-519.

88. Ha, D. H.; Caldwell, A. H.; Ward, M. J.; Honrao, S.; Mathew, K.; Hovden, R.; Koker, M. K.; Muller, D. A.; Hennig, R. G.; Robinson, R. D., Solid-solid phase transformations induced through cation exchange and strain in 2D heterostructured copper sulfide nanocrystals. *Nano Lett.* **2014,** *14* (12), 7090-9.

89. Steimle, B. C.; Fenton, J. L.; Schaak, R. E., Rational construction of a scalable heterostructured nanorod megalibrary. *Science* **2020,** *367* (6476), 418-424.

90. Yang, X. A.; Gilroy, K. D.; Vara, M.; Zhao, M.; Zhou, S.; Xia, Y. N., Gold icosahedral nanocages: Facile synthesis, optical properties, and fragmentation under ultrasonication. *Chemical Physics Letters* **2017,** *683*, 613-618.

91. Wang, D. Y.; Mohwald, H., Template-directed colloidal self-assembly - the route to 'top-down' nanochemical engineering. *J. Mater. Chem.* **2004,** *14* (4), 459-468.

92. Geuchies, J. J.; van Overbeek, C.; Evers, W. H.; Goris, B.; de Backer, A.; Gantapara, A. P.; Rabouw, F. T.; Hilhorst, J.; Peters, J. L.; Konovalov, O.; Petukhov, A. V.; Dijkstra, M.; Siebbeles, L. D. A.; van Aert, S.; Bals, S.; Vanmaekelbergh, D., In situ

study of the formation mechanism of two-dimensional superlattices from PbSe nanocrystals. *Nat. Mater.* **2016,** *15* (12), 1248-1254.

93. Weidman, M. C.; Smilgies, D. M.; Tisdale, W. A., Kinetics of the self-assembly of nanocrystal superlattices measured by real-time in situ X-ray scattering. *Nat. Mater.* **2016,** *15* (7), 775-81.

94. Kutuzov, S.; He, J.; Tangirala, R.; Emrick, T.; Russell, T. P.; Boker, A., On the kinetics of nanoparticle self-assembly at liquid/liquid interfaces. *Phys. Chem. Chem. Phys.* **2007,** *9* (48), 6351-8.

95. Paik, T.; Ko, D. K.; Gordon, T. R.; Doan-Nguyen, V.; Murray, C. B., Studies of liquid crystalline self-assembly of GdF_3 nanoplates by in-plane, out-of-plane SAXS. *ACS Nano* **2011,** *5* (10), 8322-30.

96. Smith, D. K.; Goodfellow, B.; Smilgies, D. M.; Korgel, B. A., Self-assembled simple hexagonal AB(2) binary nanocrystal superlattices: SEM, GISAXS, and defects. *J. Am. Chem. Soc.* **2009,** *131* (9), 3281-90.

97. Kang, Y.; Ye, X.; Chen, J.; Qi, L.; Diaz, R. E.; Doan-Nguyen, V.; Xing, G.; Kagan, C. R.; Li, J.; Gorte, R. J.; Stach, E. A.; Murray, C. B., Engineering catalytic contacts and thermal stability: gold/iron oxide binary nanocrystal superlattices for CO oxidation. *J. Am. Chem. Soc.* **2013,** *135* (4), 1499-505.

98. Paik, T.; Diroll, B. T.; Kagan, C. R.; Murray, C. B., Binary and ternary superlattices self-assembled from colloidal nanodisks and nanorods. *J. Am. Chem. Soc.* **2015,** *137* (20), 6662-9.

99. de Nijs, B.; Dussi, S.; Smallenburg, F.; Meeldijk, J. D.; Groenendijk, D. J.; Filion, L.; Imhof, A.; van Blaaderen, A.; Dijkstra, M., Entropy-driven formation of large icosahedral colloidal clusters by spherical confinement. *Nat. Mater.* **2015,** *14* (1), 56-60.

100. Zhang, Z.; Glotzer, S. C., Self-Assembly of Patchy Particles. *Nano Lett.* **2004,** *4* (8), 1407-1413.

101. Auyeung, E.; Li, T. I.; Senesi, A. J.; Schmucker, A. L.; Pals, B. C.; de la Cruz, M. O.; Mirkin, C. A., DNA-mediated nanoparticle crystallization into Wulff polyhedra. *Nature* **2014,** *505* (7481), 73-7.

102. Wang, P.; Huh, J. H.; Park, H.; Yang, D.; Zhang, Y.; Zhang, Y.; Lee, J.; Lee, S.; Ke, Y., DNA Origami Guided Self-Assembly of Plasmonic Polymers with Robust Long-Range Plasmonic Resonance. *Nano Lett.* **2020,** *20* (12), 8926-8932.

103. Karmaoui, M.; Ferreira, R. A. S.; Mane, A. T.; Carlos, L. D.; Pinna, N., Lanthanide-based lamellar nanohybrids: Synthesis, structural characterization, and optical properties. *Chem. Mater.* **2006,** *18* (18), 4493-4499.

104. Karmaoui, M.; Mafra, L.; Ferreira, R. A. S.; Rocha, J.; Carlos, L. D.; Pinna, N., Photoluminescent rare-earth based biphenolate lamellar nanostructures. *J. Phys. Chem. C* **2007,** *111* (6), 2539-2544.

105. Pinna, N.; Garnweitner, G.; Beato, P.; Niederberger, M.; Antonietti, M., Synthesis of yttria-based crystalline and lamellar nanostructures and their formation mechanism. *Small* **2005,** *1* (1), 112-21.

106. Young, K. L.; Jones, M. R.; Zhang, J.; Macfarlane, R. J.; Esquivel-Sirvent, R.; Nap, R. J.; Wu, J.; Schatz, G. C.; Lee, B.; Mirkin, C. A., Assembly of reconfigurable one-

dimensional colloidal superlattices due to a synergy of fundamental nanoscale forces. *Proc Natl Acad Sci U S A* **2012,** *109* (7), 2240-5.

Chapter 2
Density Functional Theory Simulations of Nanomaterials

In Chapter 1, I discussed some of the synthetic controls that are being studied and that can be achieved in nanomaterials chemistry. They form an important cog in the development of catalysts by improving the relevance of computational models that are restricted mostly to regularly cut crystals. In this Chapter, I discuss Density Functional Theory (DFT) as the leading quantum chemistry method for surface chemistry and how it can be used in conjunction with experiment to guide towards better catalysts. I also discuss DFT as a tool for explaining trends in nanoparticle anisotropy by looking at how molecules in synthesis interact with surfaces.

2.1 Introduction to Density Functional Theory

To know everything that we want to know of a system, (energy, angular momenta, etc.), all we must know is the wavefunction of all particles of which the system is made. It is a simple proposition that unfortunately does not come to a simple conclusion in any case but H. We attempt to derive the wavefunction from the Schrödinger equation

$$\widehat{H}\Psi = E\Psi \qquad \text{Eq. (2. 1)}$$

where Ψ is the all-particle wavefunction, E is the energy, and $\widehat{H}$ is the Hamiltonian, but when multiple electrons are present, a major problem is presented. Based on single-particle approximation, we can break the wavefunction into orbital eigenfunctions for the i^{th} electron, each with their own operator h_i, the Hartree Hamiltonian, we can see the problem.[1]

$$h_i = -\frac{1}{2}\nabla_i^2 - \sum_{k=1}^{M}\frac{Z_k}{r_{ik}} + \sum_{j\neq i}\int\frac{\rho_j}{r_{ij}}d\boldsymbol{r} \qquad \text{Eq. (2.2)}$$

Noting that ∇_i^2 is the Laplacian operator for the kinetic energy operator for the i^{th} electron, Z is the nuclear charge, r_{ik} is the distance of the i^{th} electron to the k^{th} nucleus, r_{ij} is the distance of the i^{th} electron to the j^{th} electron, and ρ_j is the probability density associated with electron j, we see that the final term can not be properly accounted for. Electrons are delocalized, in constant motion, so properly computing this electron – electron interaction term is impossible with current methods. The most successful attempt by Hartree to solve this issue used an iterative self-consistent field method in which guessed, trial wavefunctions are used to solve the Schrödinger equations for new, more accurate set of wavefunctions.[2] While time consuming, this method could be repeated until an approximate answer is reached.

Particularly for large systems, the necessity of extracting wavefunctions for each particle in the system turns out to be costly depending on the spatial and spin coordinates of each. A breakthrough occurred when Hohenberg and Kohn showed that the non-degenerate ground state electron density corresponds to a unique Hamiltonian and, therefore, wavefunction.[3] Moreover, any function of electron density will obey the variational principle such that any density that differs from the non-degenerate ground state density will yield an energy that is greater than ground state energy. This is convenient because we can frame the electron-electron interactions to an electron in an external potential dictated by the nuclei and electron density, which is a function of only the spatial coordinates. The Hamiltonian becomes a functional, a function of a function that in this case is the electron density.

Unfortunately, the exact form of this functional is not known, and further work was required to achieve a usable method based on this insight. Kohn and Sham worked out this component of the problem by reframing the system as one containing non-interacting particles in the potential field dictated by the charge density of an interacting system.[4] The energy can be divided the following way

$$E[\rho(\boldsymbol{r})] = T_0[\rho(\boldsymbol{r})] + V_{Ne}[\rho(\boldsymbol{r})] + V_{ee,0}[\rho(\boldsymbol{r})] + \Delta T[\rho(\boldsymbol{r})] + \Delta V_{ee}[\rho(\boldsymbol{r})] + V_{NN}$$

Eq. (2.3)

T_0 is the kinetic energy of in a non-interacting system with the electron density of $\rho(\mathbf{r})$, V_{Ne} is the potential interaction between the nucleus and the electron, V_{ee} is the classical electron-electron repulsion, V_{NN} is the nuclear repulsion (constant at a given molecular geometry), ΔT is a kinetic energy correction from the electron interactions, and ΔV_{ee} incorporates non-classical interactions of the electron-electron repulsions. The last two terms are grouped into the exchange-correlation energy,

$$E_{xc}[\rho(\boldsymbol{r})] = \Delta T[\rho(\boldsymbol{r})] + \Delta V_{ee}[\rho(\boldsymbol{r})] \qquad \text{Eq. (2. 4)}$$

This term contains quantum mechanical effects such as Pauli repulsion and an exact form of the functional is unknown.

The total energy of the system can be calculated by the sum of one-electron energies from the Kohn-Sham equation using this division

$$h_i^{KS}\varphi_i = \epsilon_i\varphi_i \quad \text{Eq. (2. 5)}$$

$$h_i^{KS} = -\frac{1}{2}\nabla_i^2 - \sum_k^{Nuclei}\frac{Z_k}{|\boldsymbol{r}_i-\boldsymbol{r}_k|} + \int\frac{\rho(\boldsymbol{r}')}{|\boldsymbol{r}_i-\boldsymbol{r}'|}d\boldsymbol{r}' + V_{xc} \quad \text{Eq. (2. 6)}$$

where V_{xc} is the operator that generates the exchange correlation energy. These equations are variational such that the ground state electron density corresponds with the ground state energy, and with a self-consistent theory, they could approach an exact answer. They can not be solved as written however, since the V_{xc} operator is unknown.

To make this solvable, researchers have had to approximate the V_{xc} operator. There are several iterations of this approximation that have been developed. The first is the Local Density Approximation (LDA) that calculates the exchange correlation from a uniform electron gas defined by the electron density function.[5] The exchange and correlation components are split to an exact exchange contribution, but a fit correlation component. The next class of V_{xc} approximations accounts for more inhomogeneity in the electron density by incorporating a dependence on the gradient of the density and is known as the generalized gradient approximation (GGA).[6-9] This is the most common approximation used today in solid state and interfacial systems. Finally, there is the class of functionals that incorporate a fraction of Hartree – Fock (HF) exchange using the Kohn – Sham orbitals called hybrid functionals.[10-13] These functionals are often more accurate for electronic properties, such as the band gap, than the GGA, but the dependence on HF exchange increases computational costs substantially.

The development of these approximate V_{xc} operators has made DFT a workable tool, but it has been at the expense of the variational principle that requires an exact

operator to hold true. Therefore, care must be taken when interpreting results from DFT to understand that the results may be either above or below the true value. That being stated, DFT still uses a self-consistent calculation method with success (**Figure 2.1**). Starting with a basis set, typically either plane waves or gaussian functions, and an initial system geometry, an initial electronic density is formed. A convenient starting place is from the ground state isolated elements. An effective potential is generated from this electron density and used to solve the Kohn-Sham equations to generate the Kohn-Sham orbitals. These orbitals can construct a new electron density. From this point, the energy is compared to the previous iteration, to determine if the energies are sufficiently close (a parameter set by the computationalist) to end the calculation. For geometry relaxations, the forces on all atoms or the structural energy may be evaluated to determine if it is converged to an energy minimum or if another geometry should be calculated.

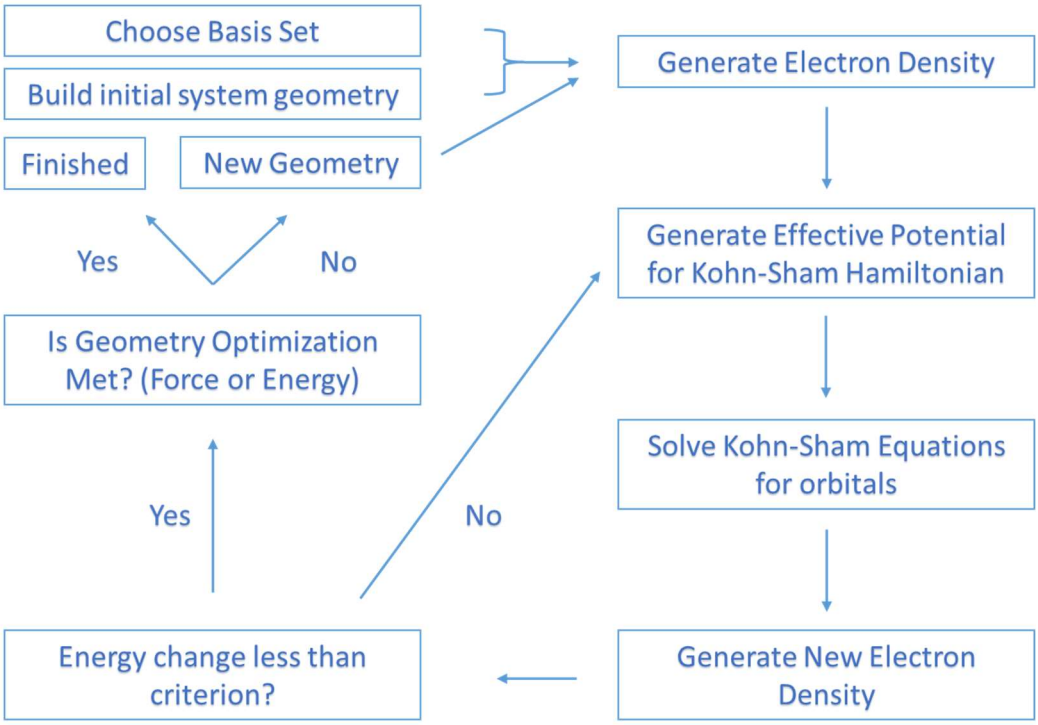

Figure 2.1 Flow chart showing the self-consistent method used in the Kohn-Sham approach of DFT.

The final point that makes DFT practical for applications with solids involves simplifying the geometry to a manageable size. Solid systems will have atoms numbering from 10^2 to 10^{23} or more, so solving for the N electron wavefunctions that exist in the system of interest ranges from computationally daunting to impossible with current computing power. The simplification here is to represent these systems as a periodic system and to calculate the energy of the unit cell that may only contain tens to hundreds of atoms. In this way, we can use Bloch plane waves,

$$\psi_{\boldsymbol{k}}(\boldsymbol{r}) = u_{\boldsymbol{k}}(\boldsymbol{r})e^{i\boldsymbol{k}\cdot\boldsymbol{r}} \qquad \text{Eq. (2. 7)}$$

with their periodicity function $u_{\mathbf{k}}(\mathbf{r})$ and wavevector **k**. For each **k** point in the first Brillouin zone, we will solve the Kohn-Sham equations. Moreover, symmetry operations can be used in the unit cell to drastically reduce the number of **k** points. Consequently, DFT is better suited to crystalline materials, but with sufficient sampling and resources, information about amorphous materials may also be derived.[14, 15] Additionally, surfaces introduce a large asymmetry into the unit cell, and sufficient care must be taken to make the unit cell large enough that spurious interactions between layers are avoided.

2.2 DFT for Nanoparticle Anisotropy

A reasonable approach towards understanding and predicting nanoparticle anisotropy is to calculate the minimum surface energy facets for a crystal structure. Wulff constructions can then be used to minimize the total surface energy by balancing surface area of each of the facets weighted by their surface energy.[16, 17] DFT is in an invaluable

tool for calculating different surface energies for a crystal structure, and has seen great use for this application predicting equilibrium crystal shapes[18-22] and surface segregation of elements.[23-26]

The surface energy of any crystalline surface can be calculated in DFT by modelling a slab of the desired crystal facet and performing a geometry optimization, allowing all atoms but the middle layer to relax (**Figure 2.2**). This middle layer provides an anchoring by serving as a bulk structured underlayer to the surface. The surface energy is calculated by the difference in energy between the slab and a crystal made up of the same number of units as the slab.

$$\gamma(clean) = \frac{E_{slab} - N * E_{Bulk}}{2A} \quad \text{Eq. (2. 8)}$$

E_{slab} is the calculated energy of the optimized slab structure, E_{bulk} is the energy per unit of the bulk crystal, N is the number of crystal units that comprise the structure, and A is the surface area. Alternatively, a series of slabs may be calculated with increasing numbers of layers and the energy may be fit according to

$$E_{slab}(N) = 2\gamma + N * E_{Bulk} \quad \text{Eq. (2. 9)}$$

with the values retaining their meanings from above (**Figure 2.2**).[27] Essentially, since the surface remains the same for all of the slabs, the only addition is to the number of bulk layers and the energy becomes a linear function of the bulk energy. This can smooth out noise to increase confidence over the single point the calculated surface energy. It is also great for surfaces that terminate at off integer ratios of the bulk unit cell.

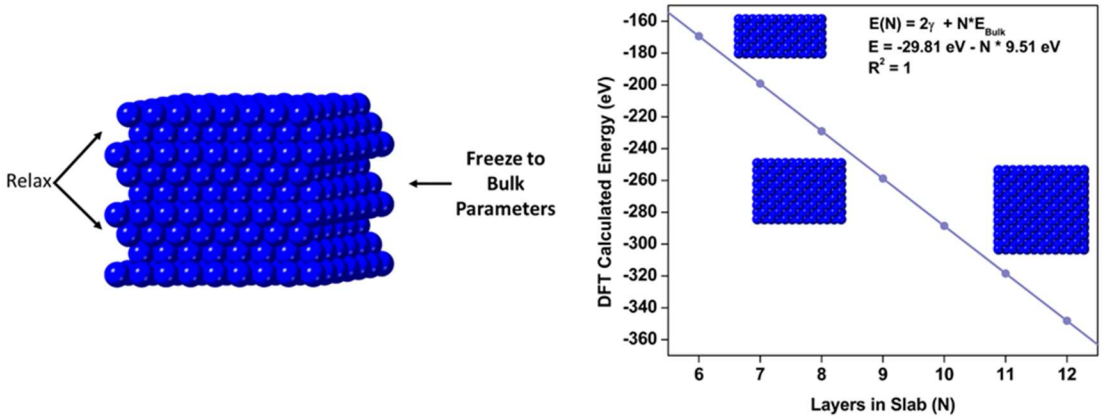

Figure 2.2 Surface energy can be calculated two ways with DFT, the first is to build a slab model in which the middle layer of atoms is not allowed to optimize. Energy is computed by subtracting from the energy of a bulk crystal containing the same number of atoms and normalizing for energy. Alternatively, multiple slabs with increasing thickness can be calculated and their energies be fit to a linear model. The surface energy is the intercept and can be normalized by the surface area of the slabs. In the case of this figure for Cu(100), the surface area is 52.7 Å and the surface energy is calculated to be 0.09 eV/Å or 1.45 J/m^2.

From only the calculation of surface energies, the equilibrium crystal shape in vacuum can be derived. However, for experimentally relevant conditions, the presence of adsorbates must also be considered since they will saturate previously undersaturated atoms and lower the surface energy. We can calculate this dependence by

$$\gamma(covered) = \gamma(clean) + \frac{\theta \Delta H(\theta)}{A^*} \quad \text{Eq. (2. 10)}$$

where θ is the fractional coverage of the adsorbed molecules, A^* is the area per surface site, and ΔH is the adsorption enthalpy.[28] By this relation, molecules stabilize the surface that they most strongly bind with, as expected.

Despite the simplicity of this relation, this approach is only rarely used in the literature due to the computational cost of calculating adsorption of floppy ligands like oleylamine, oleic acid, and tri-octylphosphine, which are most used in nanomaterial synthesis, that have many local energetic minima. These local minima "trap" calculations away from the global minimum and require researchers to try many initial configurations manually. Some success has been found by reducing the calculated interaction to the head group such as ethyl amine or acetate.[29, 30] In this way, DFT was used to show how pH can tune morphology of $NaYF_4$ to dominantly express (001) under acidic conditions or the (100) facet under basic conditions by controlling the protonation of oleic acid which reacts more strongly with the (100) facet in its deprotonated state.[30]

On the other hand, these large molecules should be expected to have large van der Waals interactions, and it has been shown that this can help promote ligand layer coverage and stability in Cu/hexadecylamine systems, so care must be taken when using

this approach.[31] In Chapters 4, 8, and 9. I use DFT as a tool for calculating ligand-nanoparticle interactions and how nanoparticle anisotropy can be rationalized. Particularly in Chapter 8, vdW interactions are shown to be critical in stabilizing overlayers of tri-octylphosphine oxide on metal surfaces.

2.3 DFT and Nanoparticle Catalysis

One of the main applications of DFT is broadly understanding materials that catalyze different reactions. By calculating important intermediates along a reaction path, we can understand how different elements and geometries can guide the reactant to our desired products. Nanomaterials offer unique opportunities to challenge the limits of DFT in heterogeneous catalysis due to their structural tunability that we explored in chapter 1. Moreover, DFT can be used to predict experimental directions to follow. Here, we will explore some of the ways that DFT is used to study catalysis in conjunction with experimental input from nanomaterials.

2.3.1 Sabatier Principle and Volcano Plots

The basis behind most DFT work for heterogeneous catalysis is the calculation of adsorbed intermediates and applying the Sabatier principle that any reaction intermediate should neither be bound too strongly nor too weakly. Intermediates that are too strongly bound have difficulty coming off a catalyst and may poison the reaction. Intermediates that are too weakly bound offer too little driving force for the reactant to proceed.

In particular, Dr. Jens Nørskov has advanced a large body of work championing the simplicity of this idea in the form of volcano plots relating catalytic activity to the binding energy of one descriptor species (**Figure 2.3**).[32-38] This approach is particularly effective for electrode catalyzed HER (Eq. 2.11 and 2.12, * represents surface site), which can be reduced to a problem of one bound intermediate, *H.[34]

$$H^+ + e^- + * \rightarrow H^* \qquad \text{Eq. (2. 11)}$$

$$H^* \rightarrow \frac{1}{2}H_2(g) + * \qquad \text{Eq. (2. 12)}$$

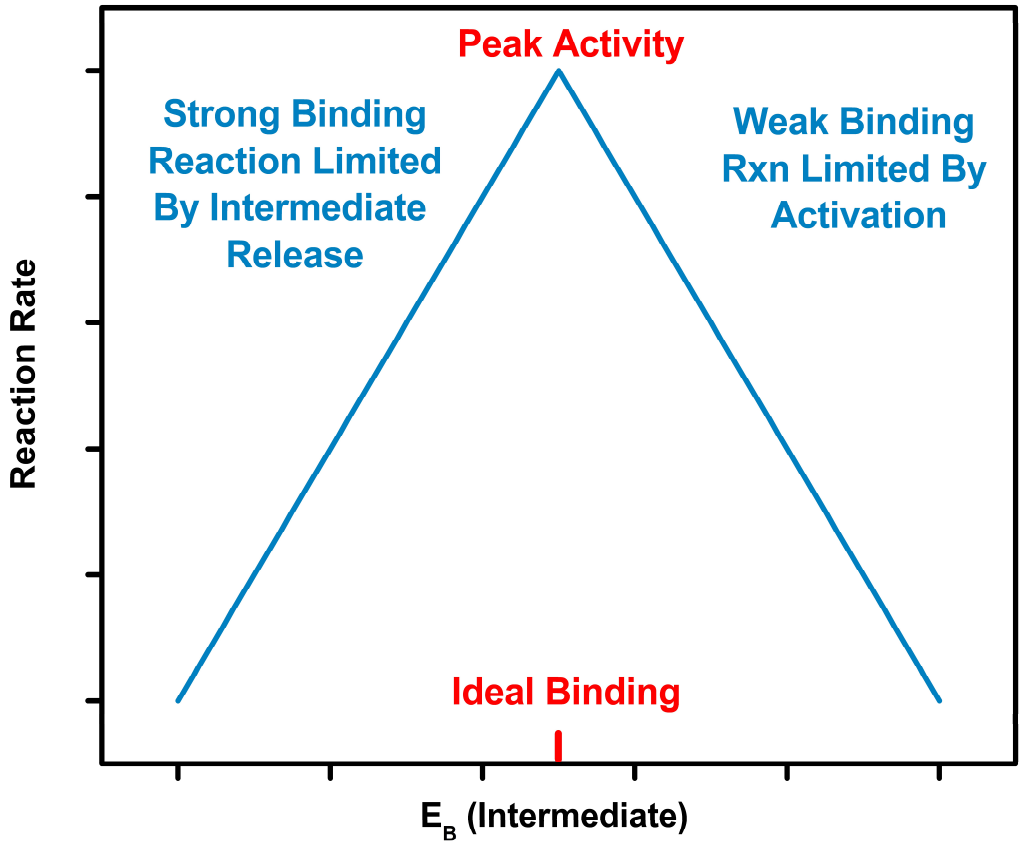

Figure 2.3 Generic volcano plot that relates the binding energy of a particular intermediate from a DFT calculated parameter to a reaction rate. Peak activity occurs when the binding is neither too strong nor too weak as predicted by the Sabatier principle.

In this case, the optimal binding free energy is 0 eV, as this is equivalent to the overall thermodynamic requirement for HER. Any additional free energy above or below this value will contribute to the thermodynamic overpotential, the extra energy input for an electrochemical reaction over the thermodynamic change of energy for the reaction, resulting in a less efficient catalyst. For oxygen electrochemistry (Eq. 2.13 – 2.16), the situation is more complex because several intermediates occur throughout the reaction, each of which should have an energy change equivalent to the overall thermodynamic change, 1.23 eV, ideally.[33, 35, 36]

$$H_2O(l) + * \rightleftharpoons HO^* + H^+ + e^- \quad \text{Eq. (2. 13)}$$

$$HO^* \rightleftharpoons O^* + H^+ + e^- \quad \text{Eq. (2. 14)}$$

$$O^* + H_2O(l) \rightleftharpoons HOO^* + H^+ + e^- \quad \text{Eq. (2. 15)}$$

$$HOO^* \rightleftharpoons +O_2(g) + H^+ + e^- \quad \text{Eq. (2. 16)}$$

The simplicity of the volcano plot can still be salvaged, however, for classes of materials that bind the intermediates in similar ways. In oxygen electrochemistry on simple metal surfaces, the *O, *OH, and *OOH intermediates have a nearly constant difference in binding energy that shifts together with the identity of the underlying layer. This difference manifests since all these intermediates are fundamentally an oxygen atom interacting with the surface, and the back end (H, OH, or nothing) modifies the interaction in a similar way across metals. Consequently, scaling relationships between the binding energies can be used to extrapolate the information from one binding energy calculation,

say *OH, to the other intermediates and the volcano plot can still be a function of one parameter.[39]

The primary utility of volcano plots is to compare classes of chemically similar materials and to computationally screen many materials for a particular reaction and to guide experimentalists to the most fruitful experiments. Especially important is the idea of scaling relations that reduces the required number of calculations for a screen to still recover useful results. Some notes should be made about its limitations, however. First, with the increased complexity of reactions, a simple two-sided volcano may no longer be appropriate. CO_2 reduction is an excellent example of this since the reaction can proceed simply to products such as CO or formate, or through a set of complex paths to form C-C coupled product and/or alcohols. For CO, formate, and even methane, volcano plots have utility since there is typically one to a few similarly bound intermediates on the way to the product.[37, 40, 41] It may even go so far as to describe that C-C coupling occurs[38], but explaining selectivity beyond this requires more deliberate calculations of diverse bonding intermediates to explore the multiple paths that can occur.

Next, it must be stated that this has all been the thermodynamic perspective of reactivity. No mention has been made of transition states and kinetics. Therefore, the predicted overpotentials are the minimum expected overpotentials for these reactions (with some leeway for DFT inaccuracies). Still, that does not invalidate the calculation results since, for a class of materials like transition metals or transition metal oxides, the kinetic barrier of a step is linearly correlated with the reaction energy as predicted by the Brønsted–Evans–Polanyi relations.[42] What this does mean is that the top several results

of a volcano curve analysis may be worthwhile for kinetic analysis through a DFT method such as the nudged elastic band method for transition states to achieve more accurate results.[43, 44] Inclusion of molecular dynamics to probe multiple reaction paths and reaction sites including explicit treatment of solvent molecules will also improve the fidelity of theoretical studies to experiment.[45, 46] These calculations take considerable effort, however, and are better applied for specific materials rather than broadly screening materials.

2.3.2 Tuning Intermediate Binding Energies for Improved Catalysis

DFT has been used to explain several design principles for nanomaterials that have been instrumental in improving catalysis. In DFT, we can consider several classes of effects relevant for nanomaterials: ligand effects, strain effects, and ensemble effects. Ligand, or electronic effects, stem from changes in chemical properties from alloying or heterostructures.[47] For transition metal alloys, a major component of the ligand effect is the modification of the d-band states. Lowering the d-band center, calculated by

$$\varepsilon_d = \frac{\int_{-\infty}^{E_F} E\rho_d(E)dE}{\int_{-\infty}^{E_F} \rho_d(E)dE} \qquad \text{Eq. (2. 17)}$$

where E_F is the Fermi level, and $\rho_d(E)$ is the density of d-states, of a transition metal will lower the adsorption energy of intermediates.[48-50] This occurs because the hybridized antibonding orbital decreases in energy with the d-band and increases its occupation. Combined with the volcano model, this simple descriptor has been fairly successful for catalyst screens.[51-54] The other component of the ligand effect is charge transfer between

elements, and this can be directly probed by calculating the charge density around each atom.[55, 56]

The strain effect is another major method to modify the binding of intermediates. It originates from either compressing or stretching the atoms of a material away from their equilibrium lattice positions. With the strain effect, compressive strain downshifts the d-band and weakens adsorption while tensile (expansive) strain upshifts the d-band and strengthens adsorption.[57] Generally, this effect is hard to distinguish from the ligand effect because the introduction of foreign elements into a system either as an alloy or as a heterostructure will introduce a strain on the active site contribute electronically to the active site.

Core-shell models in DFT offer a way to disentangle these effects. A slab can be constructed with two separate materials on top of one another and vacuum separating successive cells in the z direction. The “core” layer enforces the unit cell parameters and may be treated so that the bottom layers are frozen to bulk values. The top layer is forced into this particular unit cell, that is either larger or smaller than its equilibrium unit cell and allowed to relax. At the interface, the ligand effect is strongest, so by increasing the layers the ligand effect contribution will fall out leaving only the strain effect.[58]

Alternatively, the strain effect can be calculated without the underlayer and manually tuning the unit cell parameters. Calculating binding energies for a range of cell values, a function of strain vs. binding energy for an intermediate can be derived.[59] From this relation, any interface containing the relevant overlayer can be plotted with the

strain-binding energy relationship and compared. Points that deviate strongly from the strain function have significant electronic effects. This method has utility if several interfaces with the same metal overlayer are to be evaluated such as the case when a nanoparticle with well-defined surface facets is coated with a catalytically active metal. Combined with quantum mechanics/molecular mechanics methods, entire nanoparticles can even be evaluated computationally.[60] In Chapter 7, I explore one of these core/shell systems for Co_2P/Ir(111) as applied to the hydrogen evolution reaction.

The final effect is the ensemble effect, and is a pure geometric consideration of the system.[61] For intermediates such as *CO or *O, hollow sites comprised of multiple metal atoms are often the most stable adsorption sites on the (111) surface.[8, 62] By introducing other elements to the system, the multifold sites such as hollow sites, are disrupted leaving top sites. In this way significant reductions in binding energy can be achieved and is a useful strategy for overbinding metals. In chapter 6, this is observed as the major effect improving CO_2 reduction over AgPd nanoparticles.

2.4 References

1. Cramer, C. J., *Essentials of Computational Chemistry*. 2nd ed.; Wiley: 2004.

2. Hartree, D. R., The wave mechanics of an atom with a non-Coulomb central field Part I theory and methods. *Proceedings of the Cambridge Philosophical Society* **1928,** *24* (1), 89-110.

3. Hohenberg, P.; Kohn, W., Inhomogeneous Electron Gas. *Phys. Rev. B* **1964,** *136* (3b), B864-B871.

4. Kohn, W.; Sham, L. J., Self-Consistent Equations Including Exchange and Correlation Effects. *Phys. Rev.* **1965,** *140* (4a), 1133-&.

5. Perdew, J. P.; Wang, Y., Accurate and simple analytic representation of the electron-gas correlation energy. *Phys. Rev. B.* **1992,** *45* (23), 13244-13249.

6. Perdew, J. P.; Burke, K.; Ernzerhof, M., Generalized Gradient Approximation Made Simple. *Phys. Rev. Lett.* **1996,** *77* (18), 3865-3868.

7. Perdew, J. P.; Chevary, J. A.; Vosko, S. H.; Jackson, K. A.; Pederson, M. R.; Singh, D. J.; Fiolhais, C., Atoms, molecules, solids, and surfaces: Applications of the generalized gradient approximation for exchange and correlation. *Phys. Rev. B.* **1992,** *46* (11), 6671-6687.

8. Hammer, B.; Hansen, L. B.; Norskov, J. K., Improved adsorption energetics within density-functional theory using revised Perdew-Burke-Ernzerhof functionals. *Phys. Rev. B* **1999,** *59* (11), 7413-7421.

9. Perdew, J. P.; Burke, K.; Wang, Y., Generalized gradient approximation for the exchange-correlation hole of a many-electron system. *Phys. Rev. B.* **1996,** *54* (23), 16533-16539.

10. Perdew, J. P.; Ernzerhof, M.; Burke, K., Rationale for mixing exact exchange with density functional approximations. *J. Chem. Phys.* **1996,** *105* (22), 9982-9985.

11. Heyd, J.; Scuseria, G. E.; Ernzerhof, M., Hybrid functionals based on a screened Coulomb potential. *J. Chem. Phys.* **2003,** *118* (18), 8207-8215.

12. Heyd, J.; Scuseria, G. E., Efficient hybrid density functional calculations in solids: assessment of the Heyd-Scuseria-Ernzerhof screened Coulomb hybrid functional. *J. Chem. Phys.* **2004,** *121* (3), 1187-92.

13. Krukau, A. V.; Vydrov, O. A.; Izmaylov, A. F.; Scuseria, G. E., Influence of the exchange screening parameter on the performance of screened hybrid functionals. *J. Chem. Phys.* **2006,** *125* (22), 224106.

14. Tielens, F.; Gierada, M.; Handzlik, J.; Calatayud, M., Characterization of amorphous silica based catalysts using DFT computational methods. *Catal. Today* **2020,** *354*, 3-18.

15. Liu, C.; Hedstrom, S.; Stenlid, J. H.; Pettersson, L. G. M., Amorphous, Periodic Model of a Copper Electrocatalyst with Subsurface Oxygen for Enhanced CO Coverage and Dimerization. *J. Phys. Chem. C* **2019,** *123* (8), 4961-4968.

16. Wulff, G., XXV. Zur Frage der Geschwindigkeit des Wachsthums und der Auflösung der Krystallflächen. *Zeitschrift für Kristallographie - Crystalline Materials* **1901,** *34* (1-6), 449-530.

17. Ringe, E.; Van Duyne, R. P.; Marks, L. D., Wulff construction for alloy nanoparticles. *Nano Lett.* **2011,** *11* (8), 3399-403.

18. Gong, X.-Q.; Selloni, A., First-Principles Study of the Structures and Energetics of Stoichiometric Brookite TiO_2 Surfaces. *Phys. Rev. B* **2007,** *76* (23), 235307.

19. Zhou, C. Y.; Wang, D.; Gong, X. Q., A DFT+U revisit of reconstructed CeO_2(100) surfaces: structures, thermostabilities and reactivities. *Phys. Chem. Chem. Phys.* **2019,** *21* (36), 19987-19994.

20. Zhang, M. H.; Wang, W. Y.; Chen, Y. F., Insight of DFT and ab initio atomistic thermodynamics on the surface stability and morphology of In_2O_3. *Applied Surface Science* **2018,** *434*, 1344-1352.

21. Zhang, W. B.; Chen, C.; Zhang, S. Y., Equilibrium Crystal Shape of Ni from First Principles. *J. Phys. Chem. C* **2013,** *117* (41), 21274-21280.

22. Karim, A.; Fosse, S.; Persson, K. A., Surface structure and equilibrium particle shape of the $LiMn_2O_4$ spinel from first-principles calculations. *Phys. Rev. B* **2013,** *87* (7).

23. Ropo, M.; Kokko, K.; Vitos, L.; Kollar, J.; Johansson, B., The chemical potential in surface segregation calculations: AgPd alloys. *Surf. Sci.* **2006,** *600* (4), 904-913.

24. Schurmans, M.; Luyten, J.; Creemers, C.; Declerck, R.; Waroquier, M., Surface segregation in CuPt alloys by means of an improved modified embedded atom method. *Phys. Rev. B* **2007,** *76* (17).

25. Zhu, B.; Thrimurthulu, G.; Delannoy, L.; Louis, C.; Mottet, C.; Creuze, J.; Legrand, B.; Guesmi, H., Evidence of Pd segregation and stabilization at edges of AuPd nano-clusters in the presence of CO: A combined DFT and DRIFTS study. *J. Catal.* **2013,** *308*, 272-281.

26. Wang, Q.; Tichit, D.; Meunier, F.; Guesmi, H., Combined DRIFTS and DFT Study of CO Adsorption and Segregation Modes in Pt-Sn Nanoalloys. *J. Phys. Chem. C* **2020,** *124* (18), 9979-9989.

27. Fiorentini, V.; Methfessel, M., Extracting convergent surface energies from slab calculations. *J. Phys.: Condens. Mat.* **1996,** *8* (36), 6525-6529.

28. Barmparis, G. D.; Remediakis, I. N., Dependence on CO adsorption of the shapes of multifaceted gold nanoparticles: A density functional theory. *Phys. Rev. B* **2012,** *86* (8).

29. Duong, H. T. T.; Chen, Y. H.; Tawfik, S. A.; Wen, S. H.; Parviz, M.; Shimoni, O.; Jin, D. Y., Systematic investigation of functional ligands for colloidal stable upconversion nanoparticles. *RSC Adv.* **2018,** *8* (9), 4842-4849.

30. Liu, D.; Xu, X.; Du, Y.; Qin, X.; Zhang, Y.; Ma, C.; Wen, S.; Ren, W.; Goldys, E. M.; Piper, J. A.; Dou, S.; Liu, X.; Jin, D., Three-dimensional controlled growth of monodisperse sub-50 nm heterogeneous nanocrystals. *Nat Commun* **2016,** *7*, 10254.

31. Kim, M. J.; Alvarez, S.; Chen, Z.; Fichthorn, K. A.; Wiley, B. J., Single-Crystal Electrochemistry Reveals Why Metal Nanowires Grow. *J. Am. Chem. Soc.* **2018,** *140* (44), 14740-14746.

32. Nørskov, J. K.; Bligaard, T.; Logadottir, A.; Bahn, S.; Hansen, L. B.; Bollinger, M.; Bengaard, H.; Hammer, B.; Sljivancanin, Z.; Mavrikakis, M.; Xu, Y.; Dahl, S.; Jacobsen, C. J. H., Universality in Heterogeneous Catalysis. *J. Catal.* **2002,** *209* (2), 275-278.

33. Nørskov, J. K.; Rossmeisl, J.; Logadottir, A.; Lindqvist, L.; Kitchin, J. R.; Bligaard, T.; Jónsson, H., Origin of the Overpotential for Oxygen Reduction at a Fuel-Cell Cathode. *J. Phys. Chem. B* **2004,** *108* (46), 17886-17892.

34. Nørskov, J. K.; Bligaard, T.; Logadottir, A.; Kitchin, J. R.; Chen, J. G.; Pandelov, S.; Stimming, U., Trends in the Exchange Current for Hydrogen Evolution. *J. Electrochem. Soc.* **2005,** *152* (3), J23-J26.

35. Man, I. C.; Su, H. Y.; Calle-Vallejo, F.; Hansen, H. A.; Martinez, J. I.; Inoglu, N. G.; Kitchin, J.; Jaramillo, T. F.; Norskov, J. K.; Rossmeisl, J., Universality in Oxygen Evolution Electrocatalysis on Oxide Surfaces. *ChemCatChem* **2011,** *3* (7), 1159-1165.

36. Viswanathan, V.; Hansen, H. A.; Rossmeisl, J.; Norskov, J. K., Universality in Oxygen Reduction Electrocatalysis on Metal Surfaces. *ACS Catal.* **2012,** *2* (8), 1654-1660.

37. Peterson, A. A.; Norskov, J. K., Activity Descriptors for CO_2 Electroreduction to Methane on Transition-Metal Catalysts. *J. Phys. Chem. Lett.* **2012,** *3* (2), 251-258.

38. Montoya, J. H.; Peterson, A. A.; Nørskov, J. K., Insights into C-C Coupling in CO_2 Electroreduction on Copper Electrodes. *ChemCatChem* **2013,** *5* (3), 737-742.

39. Abild-Pedersen, F.; Greeley, J.; Studt, F.; Rossmeisl, J.; Munter, T. R.; Moses, P. G.; Skulason, E.; Bligaard, T.; Norskov, J. K., Scaling properties of adsorption energies for hydrogen-containing molecules on transition-metal surfaces. *Phys. Rev. Lett.* **2007,** *99* (1), 016105.

40. Tayyebi, E.; Hussain, J.; Abghoui, Y.; Skulason, E., Trends of Electrochemical CO_2 Reduction Reaction on Transition Metal Oxide Catalysts. *J. Phys. Chem. C* **2018,** *122* (18), 10078-10087.

41. Gong, L. L.; Zhang, D. T.; Lin, C. Y.; Zhu, Y. H.; Shen, Y.; Zhang, J.; Han, X.; Zhang, L. P.; Xia, Z. H., Catalytic Mechanisms and Design Principles for Single-Atom Catalysts in Highly Efficient CO_2 Conversion. *Adv. Energy Mater.* **2019,** *9* (44), 1902625.

42. Bligaard, T.; Norskov, J. K.; Dahl, S.; Matthiesen, J.; Christensen, C. H.; Sehested, J., The Bronsted-Evans-Polanyi relation and the volcano curve in heterogeneous catalysis. *J. Catal.* **2004,** *224* (1), 206-217.

43. Henkelman, G.; Uberuaga, B. P.; Jonsson, H., A climbing image nudged elastic band method for finding saddle points and minimum energy paths. *J. Chem. Phys.* **2000,** *113* (22), 9901-9904.

44. Henkelman, G.; Jonsson, H., Improved tangent estimate in the nudged elastic band method for finding minimum energy paths and saddle points. *J. Chem. Phys.* **2000,** *113* (22), 9978-9985.

45. Cheng, T.; Xiao, H.; Goddard, W. A., 3rd, Full atomistic reaction mechanism with kinetics for CO reduction on Cu(100) from ab initio molecular dynamics free-energy calculations at 298 K. *Proc Natl Acad Sci U S A* **2017,** *114* (8), 1795-1800.

46. Cheng, T.; Fortunelli, A.; Goddard, W. A., 3rd, Reaction intermediates during operando electrocatalysis identified from full solvent quantum mechanics molecular dynamics. *Proc Natl Acad Sci U S A* **2019,** *116* (16), 7718-7722.

47. Schneider, U.; Busse, H.; Linke, R.; Castro, G. R.; Wandelt, K., Interaction Properties of Molecules with Binary Alloy Surfaces. *J. Vac. Sci. Technol. A-Vac. Surf. Films* **1994,** *12* (4), 2069-2073.

48. Norskov, J. K.; Abild-Pedersen, F.; Studt, F.; Bligaard, T., Density functional theory in surface chemistry and catalysis. *Proc Natl Acad Sci U S A* **2011,** *108* (3), 937-43.

49. Pettersson, L.; Nilsson, A., A Molecular Perspective on the d-Band Model: Synergy Between Experiment and Theory. *Topics in Catalysis* **2014,** *57* (1-4), 2-13.

50. Hammer, B.; Norskov, J. K., Why Gold Is the Noblest of All the Metals. *Nature* **1995,** *376* (6537), 238-240.

51. Zhou, Y.; Zhou, Z. Z.; Shen, R. X.; Ma, R. G.; Liu, Q.; Cao, G. Z.; Wang, J. C., Correlating electrocatalytic oxygen reduction activity with d-band centers of metallic nanoparticles. *Energy Storage Materials* **2018,** *13*, 189-198.

52. Ou, L.; Long, W.; Huang, J.; Chen, Y.; Jin, J., Theoretical insight into effect of doping of transition metal M (M= Ni, Pd and Pt) on CO_2 reduction pathways on Cu (111) and understanding of origin of electrocatalytic activity. *RSC Adv.* **2017,** *7* (20), 11938-11950.

53. García-Mota, M.; Vojvodic, A.; Abild-Pedersen, F.; Nørskov, J. K., Electronic Origin of the Surface Reactivity of Transition-Metal-Doped TiO_2(110). *J. Phys. Chem. C* **2012,** *117* (1), 460-465.

54. Exner, K. S.; Anton, J.; Jacob, T.; Over, H., Ligand Effects and Their Impact on Electrocatalytic Processes Exemplified with the Oxygen Evolution Reaction (OER) on RuO_2(110). *Chemelectrochem* **2015,** *2* (5), 707-713.

55. Bader, R. F. W., Atoms in Molecules. *Acc. Chem. Res.* **1985,** *18* (1), 9-15.

56. Henkelman, G.; Arnaldsson, A.; Jonsson, H., A fast and robust algorithm for Bader decomposition of charge density. *Comput. Mater. Sci.* **2006,** *36* (3), 354-360.

57. Mavrikakis, M.; Hammer, B.; Norskov, J. K., Effect of strain on the reactivity of metal surfaces. *Phys. Rev. Lett.* **1998,** *81* (13), 2819-2822.

58. Back, S.; Jung, Y., Importance of Ligand Effects Breaking the Scaling Relation for Core-Shell Oxygen Reduction Catalysts. *ChemCatChem* **2017,** *9* (16), 3173-3179.

59. Liu, C.; Ma, Z.; Cui, M.; Zhang, Z.; Zhang, X.; Su, D.; Murray, C. B.; Wang, J. X.; Zhang, S., Favorable Core/Shell Interface within Co_2P/Pt Nanorods for Oxygen Reduction Electrocatalysis. *Nano Lett.* **2018,** *18* (12), 7870-7875.

60. Zhang, X.; Lu, G., Computational Design of Core/Shell Nanoparticles for Oxygen Reduction Reactions. *J Phys Chem Lett* **2014,** *5* (2), 292-7.

61. Liu, P.; Norskov, J. K., Ligand and ensemble effects in adsorption on alloy surfaces. *Phys. Chem. Chem. Phys.* **2001,** *3* (17), 3814-3818.

62. Hammer, B.; Morikawa, Y.; Norskov, J. K., CO chemisorption at metal surfaces and overlayers. *Phys Rev Lett* **1996,** *76* (12), 2141-2144.

Chapter 3
Experimental Techniques in Nanomaterials Chemistry and Catalysis

In Chapter 1, the theory of nanoparticle synthesis and growth was discussed, and in Chapter 2, computation was discussed as a tool for understanding various aspects of nanomaterials. In this chapter, general experimental details critical to the following studies are discussed, including how nanoparticles are synthesized and characterized.

3.1 Nanomaterial Synthesis

The typical strategy for synthesizing nanomaterials in this study is through a colloidal synthesis in organic solutions such as 1-octadecene (ODE) or benzyl ether (BE) with organic surfactants.[1, 2] By performing the synthesis in organic solutions, burst nucleation can be achieved through the high temperature, rapid decomposition of metal salts or organometallic complexes that are either dissolved or injected. Lipid like surfactants, such as oleylamine (OAm), oleic acid (OAc), or tri-octylphosphine (TOP), bind to the nanomaterial surface to stabilize the high surface area/volume ratioed materials against agglomeration or dissolution and to ensure their dispersibility in solvents for further application. While the theory of the synthetic control of nanomaterials is evolving rapidly, it is still in the early phases of development, and experiments are key to determining which manipulations we can achieve with the different elements.[3] In this section, I will explain the experimental procedures for synthesizing nanomaterials.

3.1.1 Synthesis Setup

Nanomaterial synthesis in this work is carried out in a 4-neck flask incorporated into a standard Schlenk line with N_2 gas protection and vacuum capabilities down to 0.2 Torr (**Figure 3.1**). The syntheses are carried out under inert conditions after removing

atmospheric oxygen and trace water by flowing N_2 through the reactor or by vacuum evacuation and N_2 cycling, both at elevated temperature (~100 °C). The mechanical pump is protected from organic components by a liquid N_2 cold trap. Temperature is controlled with a JKEM Scientific Model Apollo multichannel controller hooked up to a heating tape heating mantle and monitored via a K-type thermocouple in a stainless steel or glass coating. Temperature ramps can be controlled to between 1 and 30 °C/min and temperatures near 330 °C are achievable. Rubber septa in at least one of the flask necks allows for injection of precursor or reductants at elevated temperatures. The reaction is stirred with a polytetrafluoroethylene (PTFE) coated magnetic stir bar controlled by a Thermo Scientific Cimarec Stirring Hot Plate.

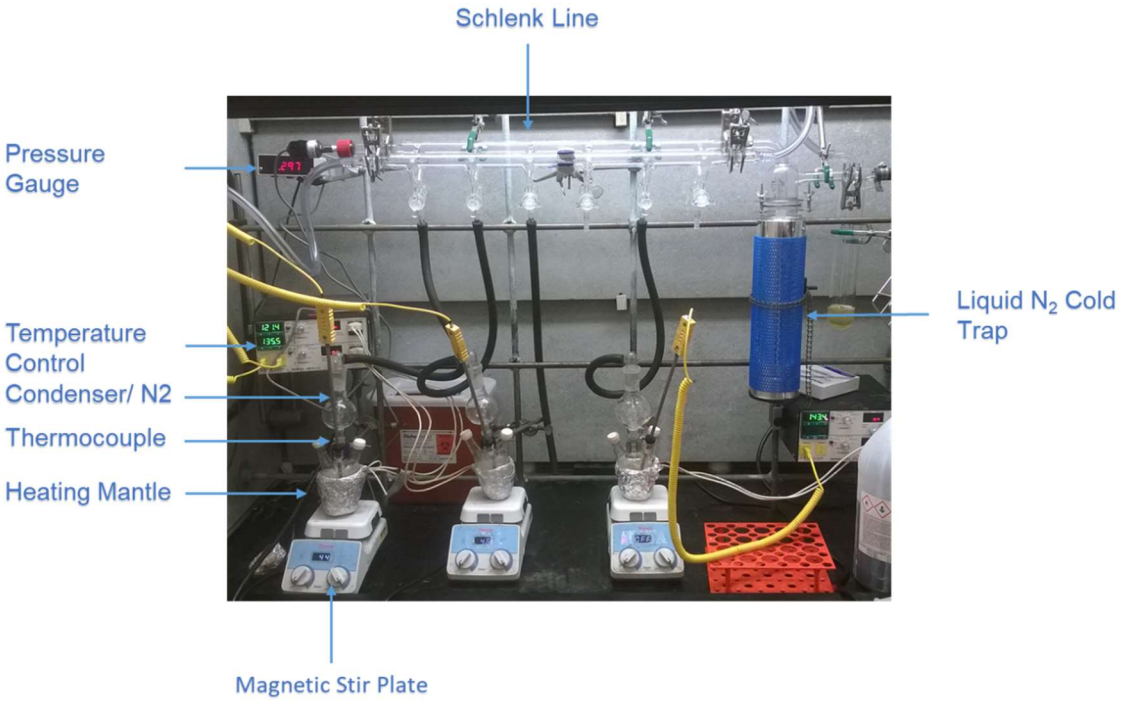

Figure 3.1 Reaction hood setup to synthesize nanomaterials in the Zhang group.

3.1.2 Nanoparticle Purification

Synthesized nanoparticles are dispersible in nonpolar solvents such as hexane, toluene, or chloroform due to the nonpolar tails of the stabilizing surfactant ligands. Excessive polar solvent (ethanol, acetone, isopropanol) addition crashes the nanoparticles out of solution and allows them to be easily crashed out. Centrifugation (between 2,000 and 10,000 rpm) separates these particles so that unreacted precursor, solvent, and other impurities may be washed away. The particles can then be redispersed in the nonpolar solvent of choice by shaking or sonication. This process is repeated several times before storing the nanoparticles in the non-polar solvent for future use. Air sensitive nanoparticles are stored in inert conditions of a glovebox. For use in catalysis, particles may be deposited on a metal oxide or carbon supporting material to prevent agglomeration. Ligands can then be removed from the surface through various methods including high temperature oxidation or ligand exchange with easy to remove molecules like acetic acid or hydrazine.

3.2 Nanoparticle Characterization

3.2.1 Transmission Electron Microscopy

Transmission electron microscopy (TEM) is a basic tool in the nanomaterial chemist's toolbox that yields information about the overall structure of the synthesized particles by passing electrons through a sample and detecting where they come through on a sample.[4] Because electrons have wavelengths much smaller than that of light, sub-angstrom at the operating voltages of the instruments, this technique is useful for observations on the nm scale. The invention of aberration correctors and high efficiency

electron detectors on high resolution TEM (HRTEM) even bring down resolution to the ~40 pm range so that individual atoms may be observed.[5]

TEM can be performed in scanning mode and scattered electrons detected at high angles in scanning transmission electron microscopy – high angle annular dark field (STEM – HAADF).[6, 7] This can be coupled with energy dispersive x-ray spectroscopy (EDS) simultaneously to gather elemental distribution information about a sample.[8]

Samples for TEM are prepared on a Formvar/carbon coated copper grid (Ted Pella Inc., 01754 – F) by depositing a diluted drop of the NP dispersion in its solvent and air drying. TEM measurements were performed on a Tecnai Spirit operated at 120 kV. STEM – HAADF images along with EDS mapping were taken with a JEOL Grand ARM 300CF operated at 300 kV at NC State University.

3.2.3 Small Angle X-ray Scattering

Small angle x-ray scattering (SAXS) is a powerful tool for the study of nanomaterial superstructures.[9] Information about particle size, shape, and concentration can be derived from these measurements. Self-assemblies of nanoparticles will generate diffraction peaks based on their lattice parameters in an analogous way to X-ray diffraction (XRD), which is used for smaller unit cells. SAXS measurements can be taken *in-situ* by using a specialized reaction flask that has a small sampling region through which X-rays can pass (**Figure 3.2**).[10] *In-situ* SAXS measurements were taken at beamline 12-ID-B of the Advanced Photon Source at Argonne National Laboratory with a wavelength of

1.033 Å. Scattered X-rays were measured with a Pilatus 2M detector (DECTRIS Ltd). The distance from the sample to the detector is 2 m.

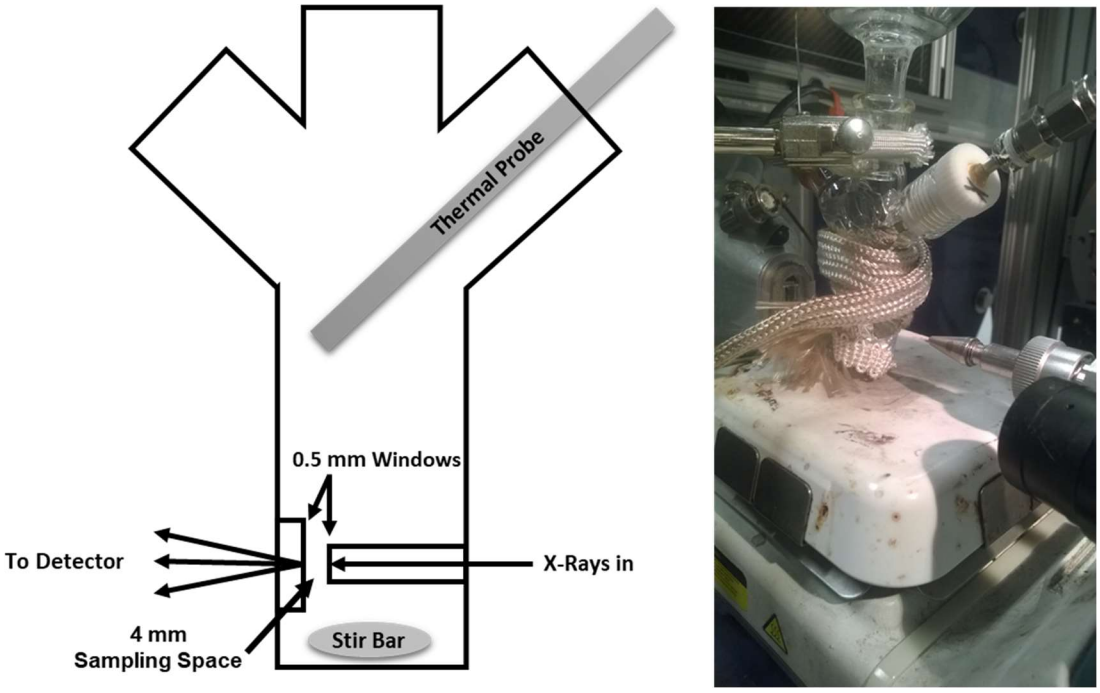

Figure 3.2 Schematic of in-situ SAXS reactor. Reactor holds 10 mL of solvent. A K-type thermocouple is used as the sampling probe. The reactor is wrapped in heating tape and hooked up to a condenser for N_2 purging. An image of the reactor in use is provided.

3.2.4 X-ray Diffraction

XRD provides bulk information about a sample, describing its crystal structure by the way that x-rays diffract through it. Nanomaterials are often poor samples for this method since small crystallite sizes contribute to significant broadening of diffraction peaks, increasing noise.[11] For sufficiently uniform samples of nanoparticles, however, it has been shown that they can form single crystals of assembled particles suitable for this technique. In these samples, precise atomic coordinates can be calculated for the particle and their surrounding ligands.[12-14] These crystals were picked out and coated in paratone oil and mounted on a MiTeGen Microloop. X-ray intensity data is measured on a Bruker Kappa APEXII Duo system. The x-ray source was an Incoatec Microfocus IμS (Cu K_α, λ = 1.54178 Å) with a multi-layer mirror monochromator.

3.2.5 X-Ray Photoelectron Spectroscopy

X-ray photoelectron spectroscopy is used to derive chemical state information such as oxidation state of surface and near surface atoms by measuring the kinetic energy of electrons ejected from an irradiated sample. These measurements were carried out using PHI VersaProbe III that is equipped with monochromatic Al K_α X-rays (1486.6 eV) and spherical capacitor energy analyzer at the nanomaterials characterization facility of UVA.

3.2.6 Electrochemical Measurements

A 3-electrode system consisting of a 5 mm diameter glassy carbon working electrode, a reference electrode (either Ag/AgCl – CO_2 reduction or Hg/HgO - HER}, and a Pt counter electrode (**Figure 3.3**). Potentials were controlled via a Biologic (Model VMP3)

potential station. CO_2 reduction was performed in an H-cell with the cathode and anode compartments separated by a Nafion™ 212 membrane and with stirred, CO_2 saturated 0.1 M $KHCO_3$ electrolyte. Gas products were measured by flushing the gas phase headspace into a Shimadzu gas chromatograph (GC2014) equipped with a methanizer equipped flame ionization detector (FID) and a thermal conductivity detector (TCD). Liquid products were measured by ^1H nuclear magnetic resonance (NMR) spectroscopy on a Bruker AV800 Spectrometer. HER was carried out in a one compartment cell containing 1 M KOH.

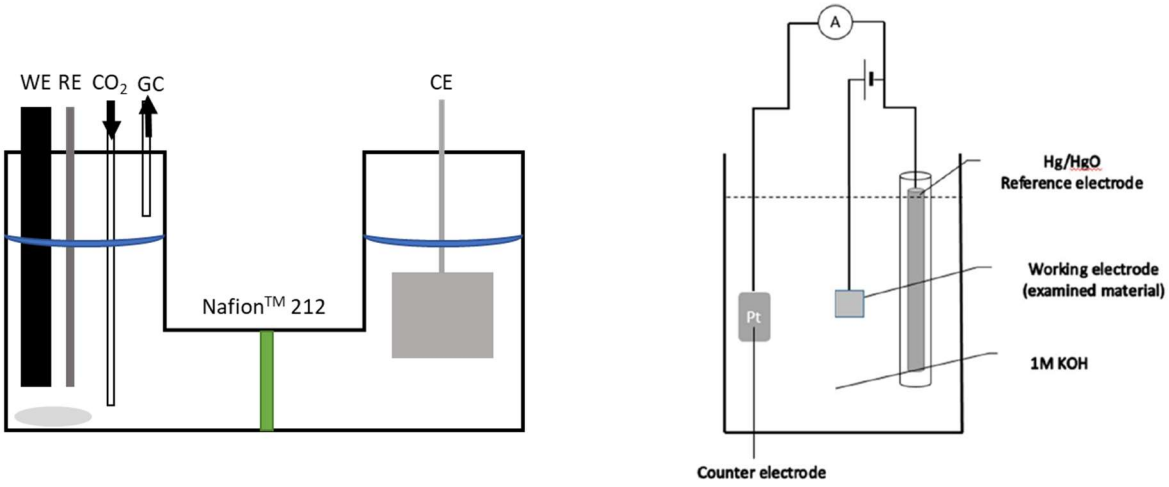

Figure 3.3 Electrochemical cells used in this work for CO_2 reduction (left) and HER (right). In left figure, the WE, RE, and CE are glassy carbon containing the catalyst, Ag/AgCl, and Pt respectively.

3.2.7 Solid-State NMR Spectroscopy

Solid-state NMR (SSNMR) has shown some recent progress in providing ligand information for synthesized nanomaterials.[15, 16] Nanoparticle samples were prepared by drying them to a powder out and packing them into an NMR tube. SSNMR experiments were performed using an Agilent DD2 400 MHz NMR spectrometer equipped with a Samoson 1.7 mm fast-MAS probe (^{1}H NMR) or a Chemagnetics 3.2 mm MAS probe (^{13}C NMR).

3.2.8 Surface Enhanced Infrared Absorption Spectroscopy

In-situ measurements of catalytic systems are critically important to improving our understanding because they mitigate the risk in *ex-situ* measurements that the catalyst's state is different from when it is under reaction conditions. Surface enhanced infrared absorption spectroscopy (SEIRAS) is an *in-situ* infrared measurement for electrocatalytic systems that takes advantage of a metal, such as Au or Cu, with surface plasmons, that enhance the electric field near the surface in attenuated total reflection (ATR) infrared measurements for surface sensitive measurements of vibrating species.[17-21] SEIRAS has been used to study reaction intermediates on nanomaterial catalysts in the following way. A Au film was chemically deposited on a Si ATR crystal cut to a 60° of incidence and cycled through oxidative and reductive potentials several times.[22] This gives the Au nanostructure necessary to generate the surface plasmons necessary for the measurement. Then the nanomaterials with deposited on C and deposited over the Au in a thin layer. The SEIRAS cell was constructed as shown in **Figure 3.4** consisting of a Ag/AgCl reference electrode and a graphite counter electrode. Care was taken not to use a

transition metal counter electrode that may contaminate the working electrode.[21] Gas was purged into the cell to remove O_2 and force stirring. This cell was set in a VEEMAX III ATR accessory, and the potential was controlled by a Metrohm Autolab potentiostat. Infrared measurements were performed in a Thermo Nicolet iS50 FTIR equipped with a nitrogen cooled mercury cadmium telluride (MCT) detector. This setup allows infrared measurements to be taken at the same time as applying a potential so that chemical intermediates may be observed.

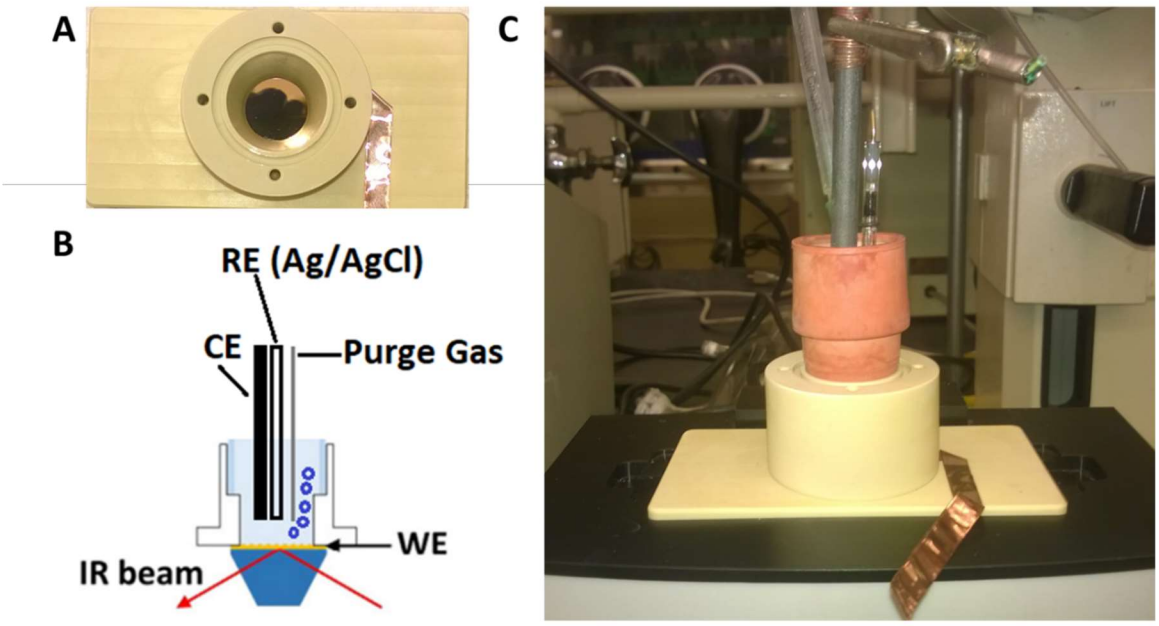

Figure 3.4 A) Top view of SEIRAS Cell showing the Au plated Si crystal. The Cu is in electrical contact with this layer, separated from the electrolyte by an o-ring, so that it may be attached to the potentiostat with undergoing any electrochemical changes. B) Schematic of the SEIRAS cell. **C**) Image of the assembled cell sitting on the VEEMAX III.

3.3 References

1. Murray, C. B.; Kagan, C. R.; Bawendi, M. G., Synthesis and characterization of monodisperse nanocrystals and close-packed nanocrystal assemblies. *Annu. Rev. Mater. Sci.* **2000,** *30* (1), 545-610.

2. Nikam, A. V.; Prasad, B. L. V.; Kulkarni, A. A., Wet chemical synthesis of metal oxide nanoparticles: a review. *Crystengcomm* **2018,** *20* (35), 5091-5107.

3. Xia, Y.; Xiong, Y.; Lim, B.; Skrabalak, S. E., Shape-controlled synthesis of metal nanocrystals: simple chemistry meets complex physics? *Angew Chem Int Ed Engl* **2009,** *48* (1), 60-103.

4. Wang, Z. L., New developments in transmission electron microscopy for nanotechnology. *Adv. Mater.* **2003,** *15* (18), 1497-1514.

5. Li, J.; Johnson, G.; Zhang, S.; Su, D., In Situ Transmission Electron Microscopy for Energy Applications. *Joule* **2019,** *3* (1), 4-8.

6. Otten, M. T., High-angle annular dark-field imaging on a TEM/STEM system. *J Electron Microsc Tech* **1991,** *17* (2), 221-30.

7. Kubel, C.; Voigt, A.; Schoenmakers, R.; Otten, M.; Su, D.; Lee, T. C.; Carlsson, A.; Bradley, J., Recent advances in electron tomography: TEM and HAADF-STEM tomography for materials science and semiconductor applications. *Microsc Microanal* **2005,** *11* (5), 378-400.

8. von Harrach, H. S.; Klenov, D.; Freitag, B.; Schlossmacher, P.; Collins, P. C.; Fraser, H. L., Comparison of the Detection Limits of EDS and EELS in S/TEM. *Microsc. Microanal.* **2010,** *16* (S2), 1312-1313.

9. Li, T.; Senesi, A. J.; Lee, B., Small Angle X-ray Scattering for Nanoparticle Research. *Chem Rev* **2016,** *116* (18), 11128-80.

10. Wu, L.; Willis, J. J.; McKay, I. S.; Diroll, B. T.; Qin, J.; Cargnello, M.; Tassone, C. J., High-temperature crystallization of nanocrystals into three-dimensional superlattices. *Nature* **2017,** *548* (7666), 197-201.

11. Scherrer, P., Nachr Ges wiss goettingen. *Math. Phys.* **1918,** *2*, 98-100.

12. Zeng, C.; Chen, Y.; Kirschbaum, K.; Lambright, K. J.; Jin, R., Emergence of hierarchical structural complexities in nanoparticles and their assembly. *Science* **2016,** *354* (6319), 1580-1584.

13. Mitchell, K. J.; Abboud, K. A.; Christou, G., Atomically-precise colloidal nanoparticles of cerium dioxide. *Nat Commun* **2017,** *8* (1), 1445.

14. Mitchell, K. J.; Goodsell, J. L.; Russell-Webster, B.; Twahir, U. T.; Angerhofer, A.; Abboud, K. A.; Christou, G., Expansion of the Family of Molecular Nanoparticles of Cerium Dioxide and Their Catalytic Scavenging of Hydroxyl Radicals. *Inorg Chem* **2021,** *60* (3), 1641-1653.

15. Cano, I.; Huertos, M. A.; Chapman, A. M.; Buntkowsky, G.; Gutmann, T.; Groszewicz, P. B.; van Leeuwen, P. W., Air-Stable Gold Nanoparticles Ligated by Secondary Phosphine Oxides as Catalyst for the Chemoselective Hydrogenation of Substituted Aldehydes: a Remarkable Ligand Effect. *J. Am. Chem. Soc.* **2015,** *137* (24), 7718-27.

16. Li, Y.; Tsang, S. C. E., Unusual Catalytic Properties of High-Energetic-Facet Polar Metal Oxides. *Acc Chem Res* **2021,** *54* (2), 366-378.

17. Heyes, J.; Dunwell, M.; Xu, B., CO_2 Reduction on Cu at Low Overpotentials with Surface-Enhanced in Situ Spectroscopy. *J. Phys. Chem. C* **2016,** *120* (31), 17334-17341.

18. Dunwell, M.; Lu, Q.; Heyes, J. M.; Rosen, J.; Chen, J. G.; Yan, Y.; Jiao, F.; Xu, B., The Central Role of Bicarbonate in the Electrochemical Reduction of Carbon Dioxide on Gold. *J. Am. Chem. Soc.* **2017,** *139* (10), 3774-3783.

19. Dunwell, M.; Yan, Y. S.; Xu, B. J., In Situ Infrared Spectroscopic Investigations of Pyridine-Mediated CO_2 Reduction on Pt Electrocatalysts. *ACS Catal.* **2017,** *7* (8), 5410-5419.

20. Dunwell, M.; Yang, X.; Setzler, B. P.; Anibal, J.; Yan, Y. S.; Xu, B. J., Examination of Near-Electrode Concentration Gradients and Kinetic Impacts on the Electrochemical Reduction of CO_2 using Surface-Enhanced Infrared Spectroscopy. *ACS Catal.* **2018,** *8* (5), 3999-4008.

21. Dunwell, M.; Yang, X.; Yan, Y. S.; Xu, B. J., Potential Routes and Mitigation Strategies for Contamination in Interfacial Specific Infrared Spectroelectrochemical Studies. *J. Phys. Chem. C* **2018,** *122* (43), 24658-24664.

22. Miyake, H.; Ye, S.; Osawa, M., Electroless deposition of gold thin films on silicon for surface-enhanced infrared spectroelectrochemistry. *Electrochem. Commun.* **2002,** *4* (12), 973-977.

Chapter 4
A Generalized Synthetic Strategy for Transition Metal Doped Brookite-Phase TiO_2 Nanorods

Portions published as: Zhang, Z.[#]; Wu, Q.[#]; Johnson, G.[#]; Ye, Y.; Li, X.; Li, N.; Cui, M.; Lee, J. D.; Liu, C.; Zhao, S.; Li, S.; Orlov, A.; Murray, C. B.; Zhang, X.; Gunnoe, T. B.; Su, D.; Zhang, S., Generalized Synthetic Strategy for Transition-Metal-Doped Brookite-Phase TiO_2 Nanorods. *J. Am. Chem. Soc.* **2019,** *141* (42), 16548-16552.

In this Chapter, I discuss a wet-chemical methodology for the synthesis of monodisperse transition metal (M) doped brookite-phase TiO2 nanorods (NRs) with a wide-range tunability in dopant composition (M = V, Cr, Mn, Fe, Co, Ni, Cu, Mo etc.). These quadrangular NRs can selectively expose (210) surface facets, which is induced by their strong affinity with oleylamine as revealed by density functional theory (DFT) calculations. Such a structure is well preserved regardless of the introduction of a single dopant or multiple dopants with varied dopant concentrations, leading to a diverse library of TiO2 NRs wherein various dopants in single-atom form are homogeneously distributed in the brookite-phase solid lattice. This allows for the tuning of optical and catalytic properties that underpin new opportunities in photocatalysis and other heterogeneous catalysis applications.

4.1 Background Motivation

Central to functional nanomaterials and achieving their desirable applications is the ability to synthetically control the physical dimensions, composition, structure, and surface profiles of nanocrystals with atomic scale precision.[1-4] TiO_2 is one of the most studied metal oxide nanomaterials[4-11] due to its semiconducting properties and important applications in optoelectronics,[12] batteries,[13-15] heterogeneous catalysis[16-18] and photocatalysis.[19-21] For example, TiO_2 can provide active lattice oxygen species and strong interactions with metal nanoparticles, allowing for the modulation of kinetics for many heterogeneous catalytic reactions.[22-24] TiO_2 can also absorb photons to generate excited electrons and holes, driving redox reactions that build the basis for photocatalytic water splitting and other photo-reforming processes.[25-28] To maximize its benefit for these

important applications, an emerging aspect in the studies of TiO_2 nanostructures is to dope them with proper foreign elements, including cations (e.g. Fe, Sn)[29, 30] and/or anions (e.g. C, N, F)[31-33], which can tune lattice oxygen activity as well as improve TiO_2's electronic structure, surface acidity/basicity, and photon absorption.[34, 35]

Such a doping strategy has been extensively studied for the rutile- and anatase-phase TiO_2 nanomaterials.[29-32, 35] In contrast, brookite phase TiO_2 is rarely studied due to the challenge of synthesizing the pure, metastable brookite phase. Recently, a high-yield synthesis of brookite-phase TiO_2 nanorods (NRs) has been reported via the hydrolysis of a titanium chloride precursor.[10] These structures were found to promote electron-hole separation under solar irradiation due to their one-dimensional (1-D) structure and, therefore, delivered a record-high photocatalytic activity towards photo-reforming of ethanol/glycerol for hydrogen (H_2) production. [36] It is this success in the synthesis of brookite-phase TiO_2 NRs that leads to the present work exploring the driving forces to achieve these materials and a robust approach to doping them for further enhanced photocatalytic properties. We found that the surfactant oleylamine (OAm) interacts more strongly with the (210) facet than the (001) facet, direction growth to occur along the (001) axis more readily. Furthermore, a broad range of single, dual, or multiple transition metal (M) dopants (M = V, Cr, Mn, Fe, Co, Ni, Cu, Mo, etc., as illustrated in **Figure 4-1**) can be homogeneously doped into monodisperse single-crystalline brookite-phase TiO_2 NRs (M-TiO_2). The resultant brookite-phase M-TiO_2 NRs are uniform in physical dimensions and surface facets, providing us a new group of well-defined TiO_2 nanocrystals with tunable compositions with improved optical and catalytic properties. Using Fe-doped TiO_2

NRs as a model system, we show that the interactions that drive the anisotropic growth are maintained and that controlling the Fe-dopant level substantially enhanced the photocatalytic performance of TiO_2 brookite-phase nanomaterials.

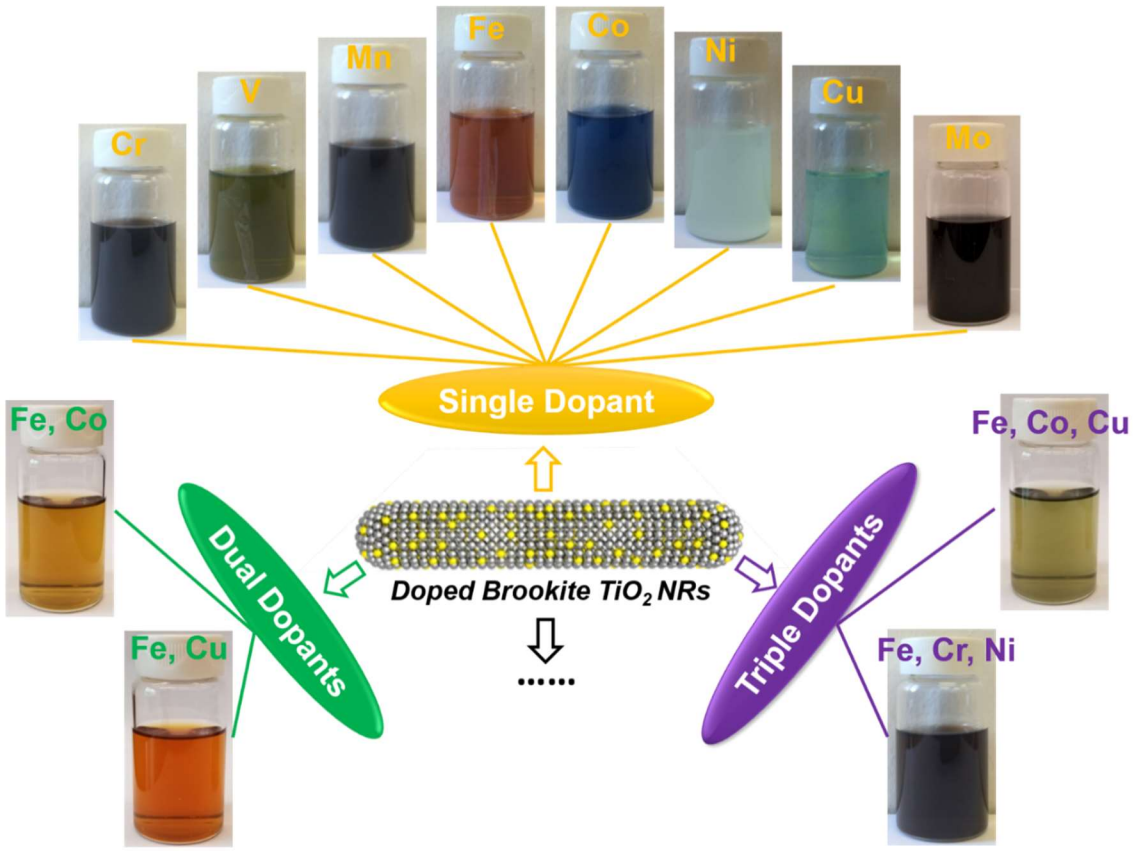

Figure 4.1 Schematic illustration of diverse, doped TiO_2 brookite-phase NRs synthesized by our generalized methodology.

4.2 Results and Discussion

4.2.1 Synthesis of M-Doped Brookite TiO_2 Nanorods

The M-TiO_2 NRs were synthesized via an organic solution colloidal hydrolysis method.[37] Typically, $TiCl_4$ precursor dissolved in oleic acid (OAc) is hydrolytically decomposed in a mixture of 1-octadecene (ODE) and oleylamine (OAm). At a high temperature (290 °C), OAm and OAc can react to generate a small amount of water, resulting in the slow hydrolysis of $TiCl_4$ to form TiO_2 and release HCl. Unlike the previous method, [17, 36] we incorporated M-oleate precursor in our synthesis by mixing it with $TiCl_4$-OAc to produce M-TiO_2. It is well-known that M-oleate complexes, such as Fe-oleate, can only be rapidly decomposed to reach metal oxide nucleation threshold at temperatures higher than 310°C.[38] Holding the reaction temperature below this at 290°C and the presence of HCl from $TiCl_4$ decomposition minimize the chance of MO_x formation. As a result, M is doped into the TiO_2 matrix, generating M-TiO_2 that can be well-dispersed in non-polar solvent and exhibit distinct colors relative to undoped TiO_2. As summarized in **Figure 4.1**, such a strategy can be generalized to cover all first-row transition metal dopants, some second-row dopants (e.g. Mo), and their binary or ternary combinations.

Transmission electron microscopy (TEM) and scanning TEM (STEM) images show that the as-synthesized mono-M-TiO_2 (**Figure 4.2 (B-H)** and **Figure 4.3 A**), bi-M-TiO_2 (**Figure 4.4 A**), tri-M-TiO_2 (**Figure 4.4 B**), and pristine TiO_2 (**Figure 4.2 A**) samples have a consistent NR morphology with an average width of 4.2 ± 0.5 nm and a length of 30-50 nm. These M-TiO_2 NRs preserve the brookite phase, as indicated by their powder X-ray diffraction (XRD) patterns (JCPDS No. 29-1360, orthorhombic) with the characteristic

brookite (121) peak at 2θ = 30.81° (**Figure 4.5**). By tuning the precursor M/Ti molar ratio, the M dopant level in the NRs can be controlled. TEM images in **Figure 4.2 H** and **4.3 A** confirm the Fe atomic concentration can be increased up to 10 % (out of all cations Fe + Ti, measured by energy-dispersive X-ray (EDS) analysis) without any obvious morphology change. Beyond this concentration, however, M-oleate precursor cannot generate M-TiO_2 NRs with higher dopant levels. Instead, M stays in the solution in this case, probably because the stability of brookite-phase TiO_2 lattice excludes the incorporation of high-concentrations of dopants.

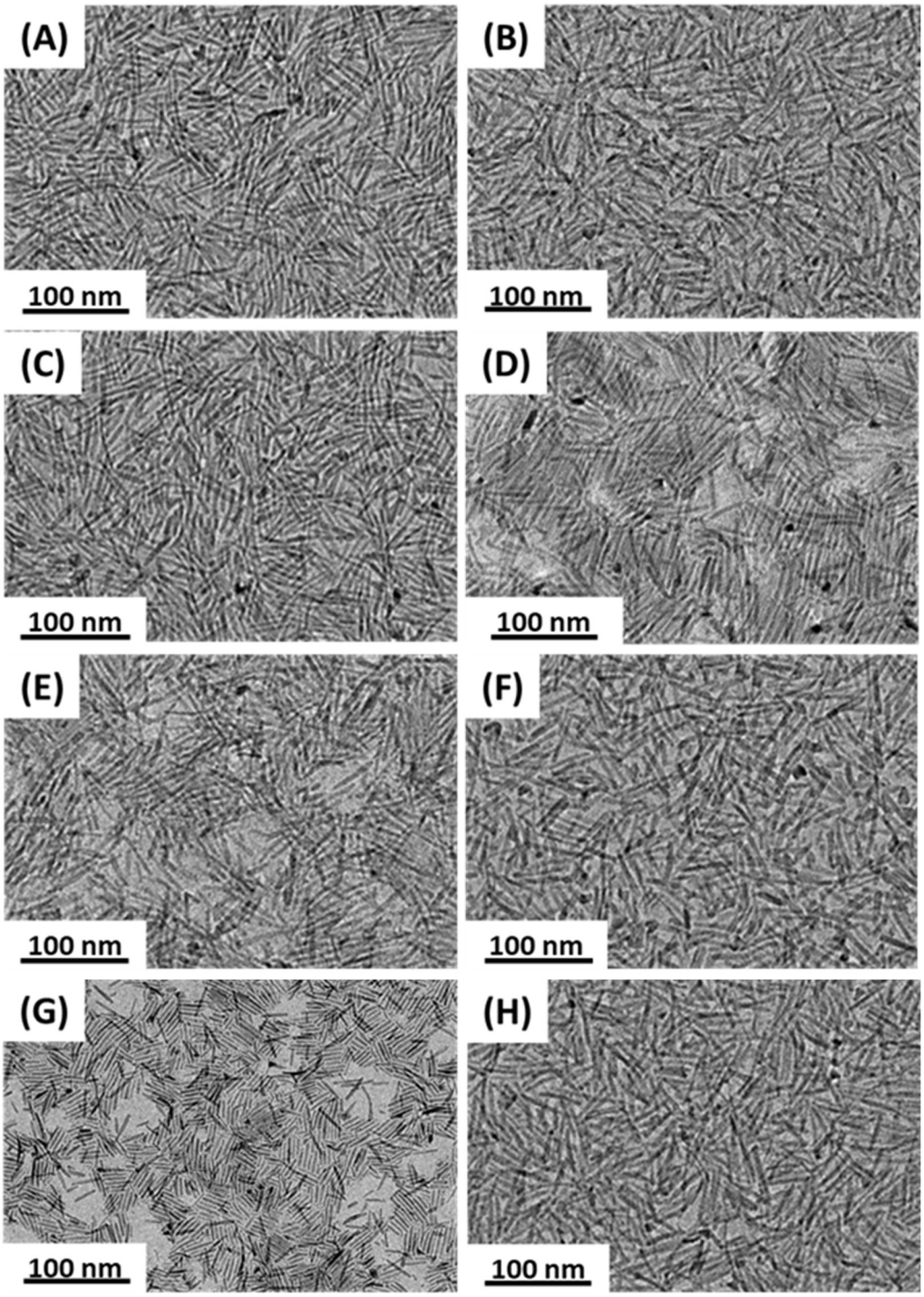

Figure 4.2 TEM images of (**A**) pristine TiO_2, (**B**) V-TiO_2, (**C**) Mn-TiO_2, (**D**) Co-TiO_2, (**E**) Ni-TiO_2, (**F**) Cu-TiO_2, (**G**) Mo-TiO_2 (all around 10% M dopant concentration), (**H**) 3.7% Fe-TiO_2 NRs

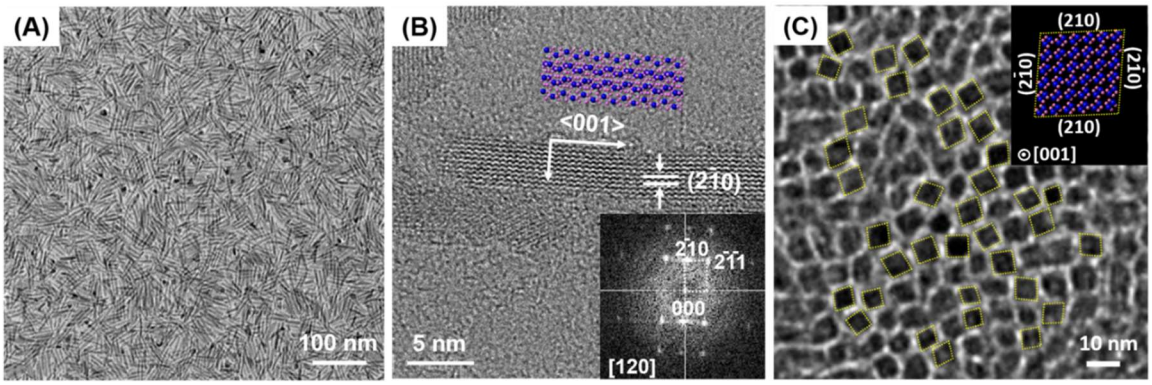

Figure 4.3 (**A**) TEM and (**B**) HRTEM images of the as-synthesized Fe-TiO_2 NRs (10% Fe); (**C**) TEM image of vertically aligned Fe-TiO_2 (10% Fe) assembly. Inset illustrates the corresponding atomic model with purple and pink atoms being Ti and O respectively.

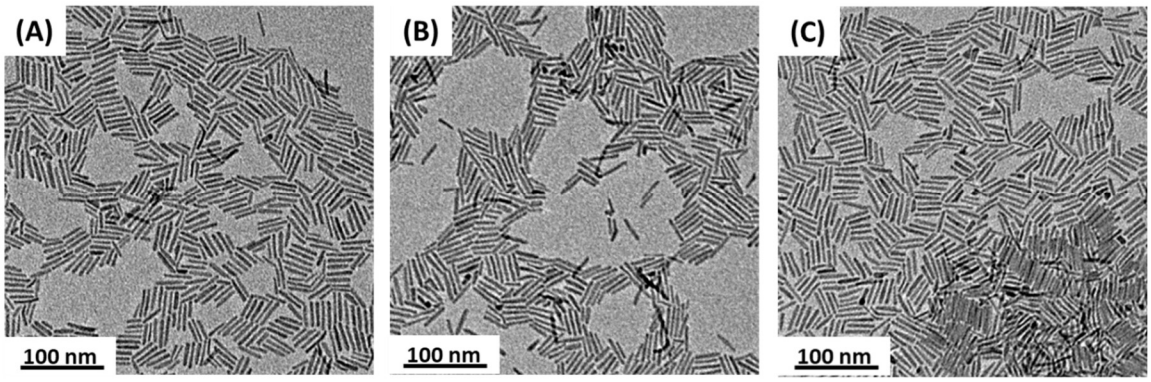

Figure 4.4 TEM images of bi-M-TiO_2 NRs: (**A**) FeCo-TiO_2, (**B**) FeCu-TiO_2 as well as tri-M-TiO_2 (**C**) FeCoCu-TiO_2

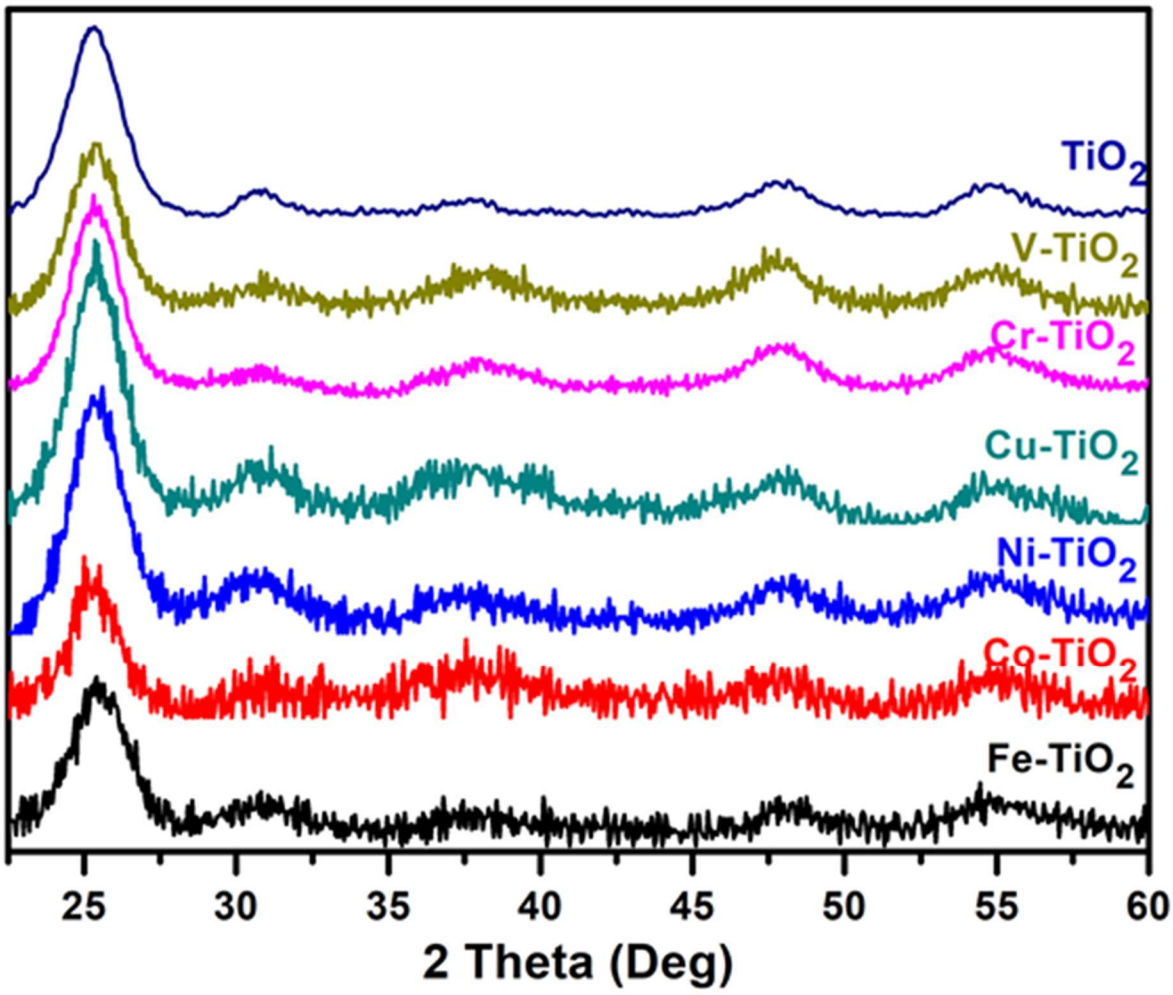

Figure 4.5 X-ray diffraction patterns of TiO_2 and M-TiO_2 NRs (10% M) demonstrate the brookite phase is maintained even upon doping with other transition metals.

High-resolution TEM (HRTEM) images of the representative Fe-TiO_2 (**Figure 4.3B**) and pristine TiO_2 NRs (**Figure 4.6A**) suggest these NRs are single crystalline and grow along the <001> direction. The Fast Fourier transform of HRTEM images indicates that the side facets are (210) planes. Thanks to their monodisperse size and morphology, the pristine TiO_2 and Fe-TiO_2 NRs can be easily aligned into ordered assemblies at the interface of air/diethylene glycol via the previously reported method (**Figure 4.6 C**). [39] The TEM images (**Figure 4.3 C** and **Figure 4.6B**) viewed along the longitudinal direction of NRs, based on their vertical assemblies, show a rhombic NR cross-section shape with an angle of ~80°/100°, confirming that the NRs expose four (210) planes as the side facets.

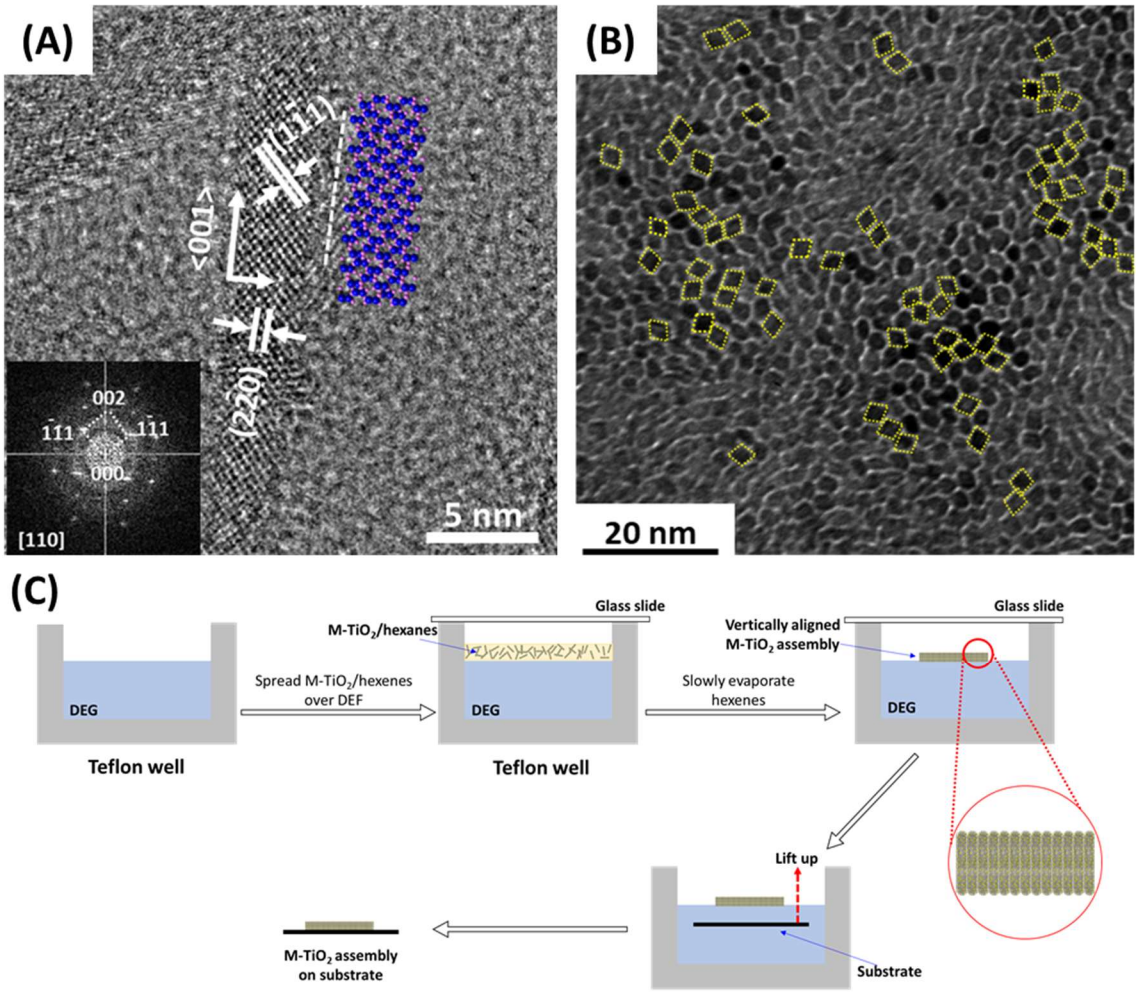

Figure 4.6 A) HRTEM image of pristine TiO_2 NRs. Inset illustrates the corresponding atomic model with purple and pink atoms being Ti and O respectively. **B**) TEM image of vertically aligned pristine TiO_2 NRs assembly. **C**) Fabrication and transferring of vertically aligned M-TiO_2 assembly over diethylene glycol by the slow evaporation of the hexane solvent.

4.2.2 Oleylamine as the Anisotropic Driving Agent

The formation of quadrangular shaped NRs can be rationalized by the interaction between a specific TiO_2 crystal plane and surfactants/ions. By using slab models for the two observed, lowest energy TiO_2 facets (**Figure 4.7**) in DFT calculations, we found, in agreement with Gong *et al.,* that the (001) plane of brookite-phase TiO_2 is not stable and undergoes a 1x1 reconstruction both under vacuum and in the presence of surfactant (OAm or OAc) or Cl^- (**Figure 4.7**).[40] This reconstruction takes a row of undersaturated, 4-coordinate Ti atoms and converts them to 5 coordinate atoms. This stabilization contributes to a relative inertness towards foreign adsorbates observed when compared to the (210) plane. The adsorption energies (E_{ad}) of OAm, OAc and Cl^- on the (210) plane are calculated to be -0.93 eV, -0.44 eV and -0.72 eV, all stronger compared to those on the (001-R) plane (-0.07 eV, -0.24 eV and -0.06 eV, respectively). It is worth noting that OAm is present in a much larger amount than OAc, which reacts with the amine to generate water and oxidize the Ti, and Cl^- in our synthesis. Therefore, OAm is expected to play the most important role in stabilizing (210) plane with the strongest E_{ad} (-0.93 eV). As a result, the (210) planes can be preferentially exhibited.

Furthermore, these calculations were repeated for brookite TiO_2 doped with 13% Fe. Reconstruction of the (001) surface is again observed, though the reconstructed (001) surface appears to be slightly more accommodating of adsorbates, particularly Cl than the pure Ti. This is also apparent from the surface reconstruction that only provided about half the stability (0.27 J/m^2 difference rather than 0.62 J/m^2 for pure TiO_2). While further concentrations of Fe were not modelled and outside the scope of this work, it could be

that the that this increased binding on the (001) could inhibit growth of the higher Fe concentration particles.

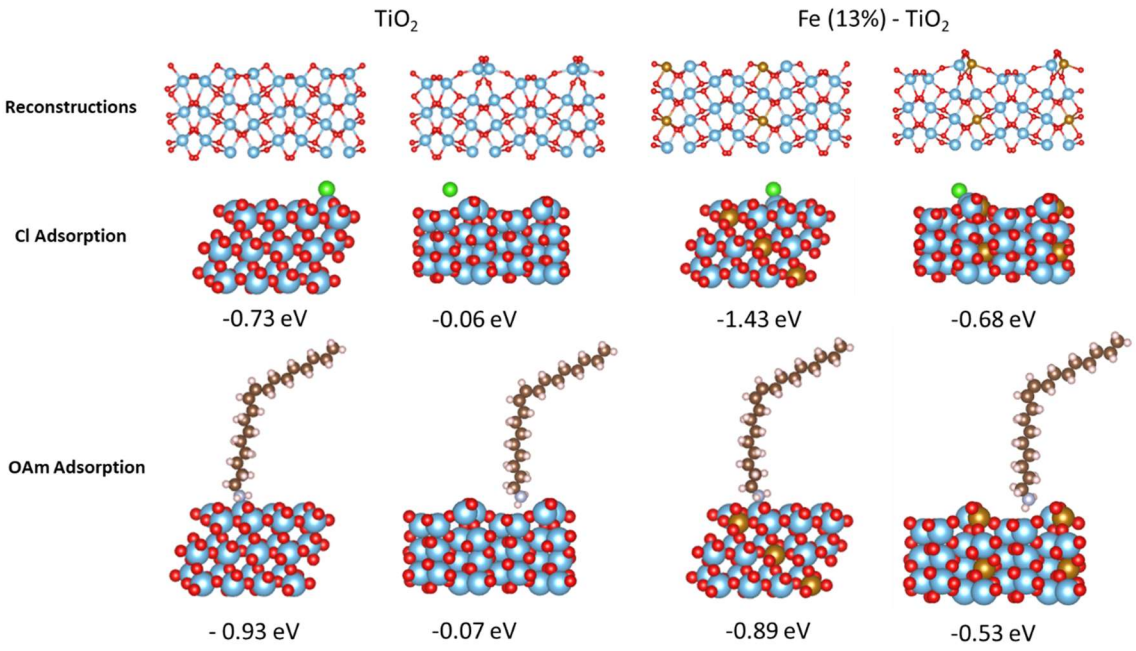

Figure 4.7 DFT Models used for adsorption energy calculations. Ti is light blue, O is red, C is black, H is white, N is blue, and Cl is green. The difference between the unreconstructed (001) surface (left) and the relaxed structure (right) is shown in the first row for both TiO_2 and Fe-TiO_2. In both the doped and undoped case, the reconstruction is the most stable surface. Adsorption energies for each case are shown below their relevant models.

4.2.3 Dopant Distribution in TiO_2 Nanorods

The distribution of dopants, such as Fe, within the NRs was first studied by STEM high-angle annular dark field (HAADF) imaging coupled with electron energy loss spectroscopy (EELS) elemental mapping (Fe doped: **Figure 4.8 A-C**, Fe-Cu-Co doped: **Figure 4.9 C-F**). It is clearly seen from the spatially overlapping signals that the doping elements are homogeneously distributed within the nanorods. To further uncover the atomic arrangement and bonding configuration of Fe dopant, we performed X-ray absorption near edge structure (XANES) and extended X-ray absorption fine structure (EXAFS) studies. **Figure 4.8 D** displays the Fe K-edge XANES spectra of Fe-TiO_2 NRs as well as reference samples, including Fe, FeO, Fe_3O_4, and Fe_2O_3. The Fe-TiO_2 spectrum is clearly distinct to those of metallic Fe, excluding the existence of the interstitial doping of Fe in the TiO_2 lattice. Meanwhile, the Fe-TiO_2 shows similar white line characteristics with those of the reference iron oxides, indicating the high valence state of Fe (+3) in the Fe-TiO_2 NRs. Additionally, the observed spectra present different profiles in the range of 7120-7160 eV, implying that the state of Fe in Fe-TiO_2 differs from that measured in the reference iron oxides. We ascribe these differences to the replacement of Fe at Ti sites in the TiO_2 lattice, which is possible due to the similarity in the ionic radii of Fe^{3+} (0.064 nm) and Ti^{4+} (0.068 nm).[41] Doping of Fe in the TiO_2 lattice alters the hybridization of Fe with O, inducing the existence of a different Fe-O bonding environment compared with that in FeO_x. Based on these discussions, it is clear that Fe is atomically doped into the TiO_2 network, without forming any FeO_x segregation.

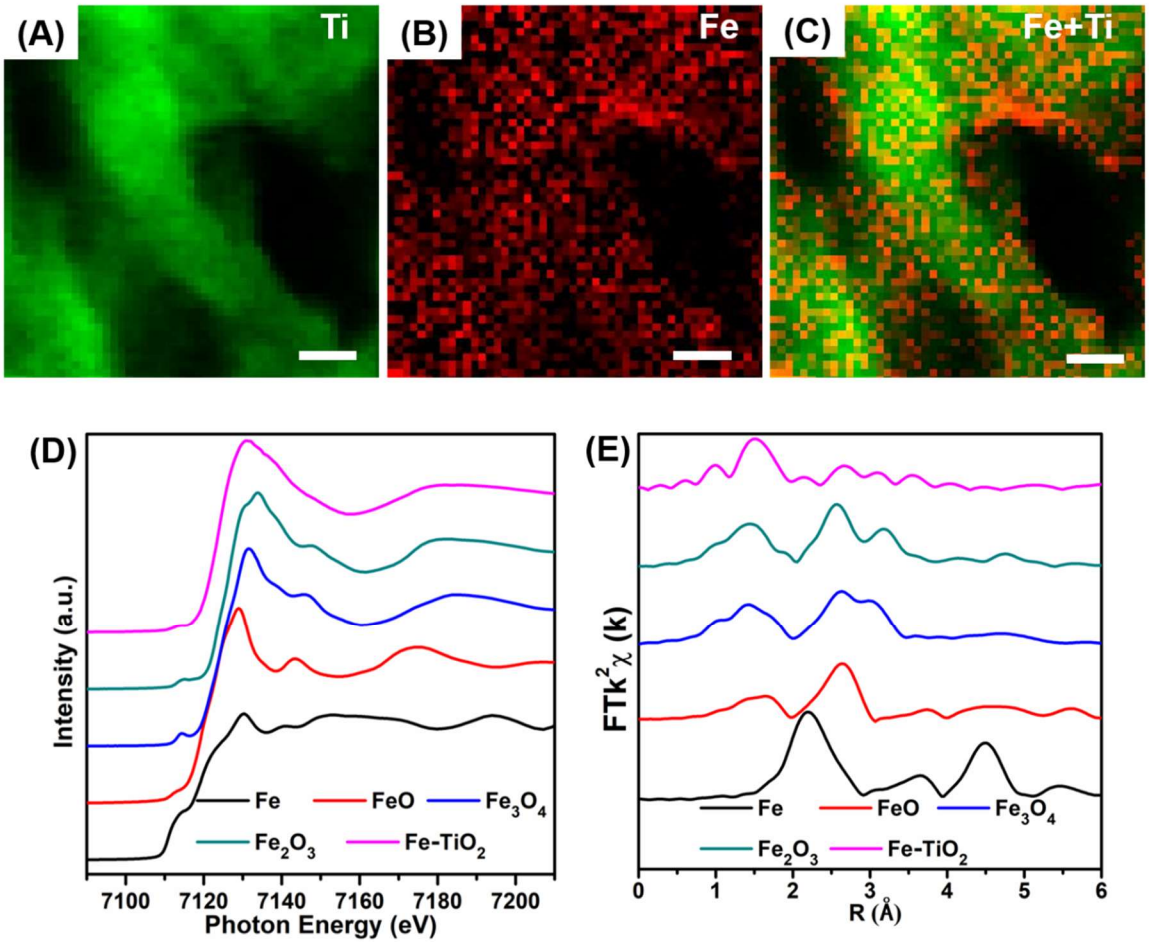

Figure 4.8 (**A-C**) HAADF-EELS elemental mappings of Fe-TiO_2 (10%) NRs (scale bar: 2 nm); (**D**) Fe K-edge XANES and (**E**) Fourier-transform EXAFS spectra of Fe-TiO_2 (10%), compared with Fe, FeO, Fe_3O_4, Fe_2O_3 standards.

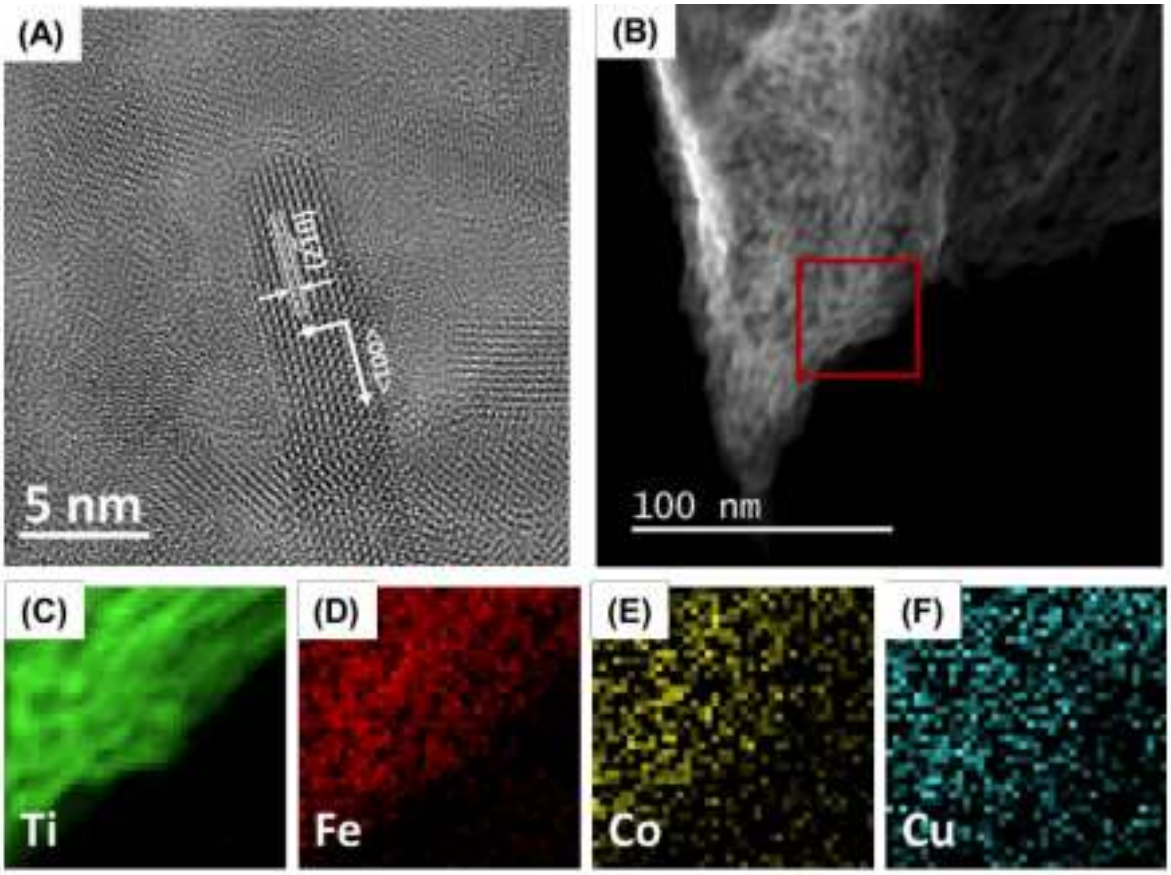

Figure 4.9 (**A**) HRTEM and (**B**) STEM -HAADF images of Fe-Cu-Co-TiO_2 nanorods. (**C-F**) Elemental components of HAADF-EELS measurements of the Fe-Cu-Co-TiO_2 nanorods.

4.2.4 M-Doped Brookite TiO_2 as a Photocatalyst

As illustrated in previous studies on rutile and anatase TiO_2, the t_{2g} state of M dopants can interact with Ti, generating an additional occupied state in the bandgap of TiO_2 and tuning the electronic structure of TiO_2. [42] As shown in **Figure 4.1 and 4.10 C**, our M-TiO_2 NRs suspensions in hexanes exhibit distinct colors from pristine TiO_2 (white), suggesting a similar electronic structure modification in brookite-phase TiO_2. The absorption edge of brookite-phase TiO_2 NRs is at ~ 400 nm in the Ultraviolet–visible (UV-Vis) diffuse reflectance spectrum (**Figure 4.10 A**) corresponding to a band gap of ~ 3.1 eV, which agrees with published results.[12] For Fe-TiO_2, it can be seen that the Fe dopant shifts the absorption edge of TiO_2 towards longer wavelength. Furthermore, the shift increases monotonically as the Fe doping concentration increases. Therefore, the present synthetic strategy offers an effective method to improve the visible-light absorption of pristine TiO_2 NRs.

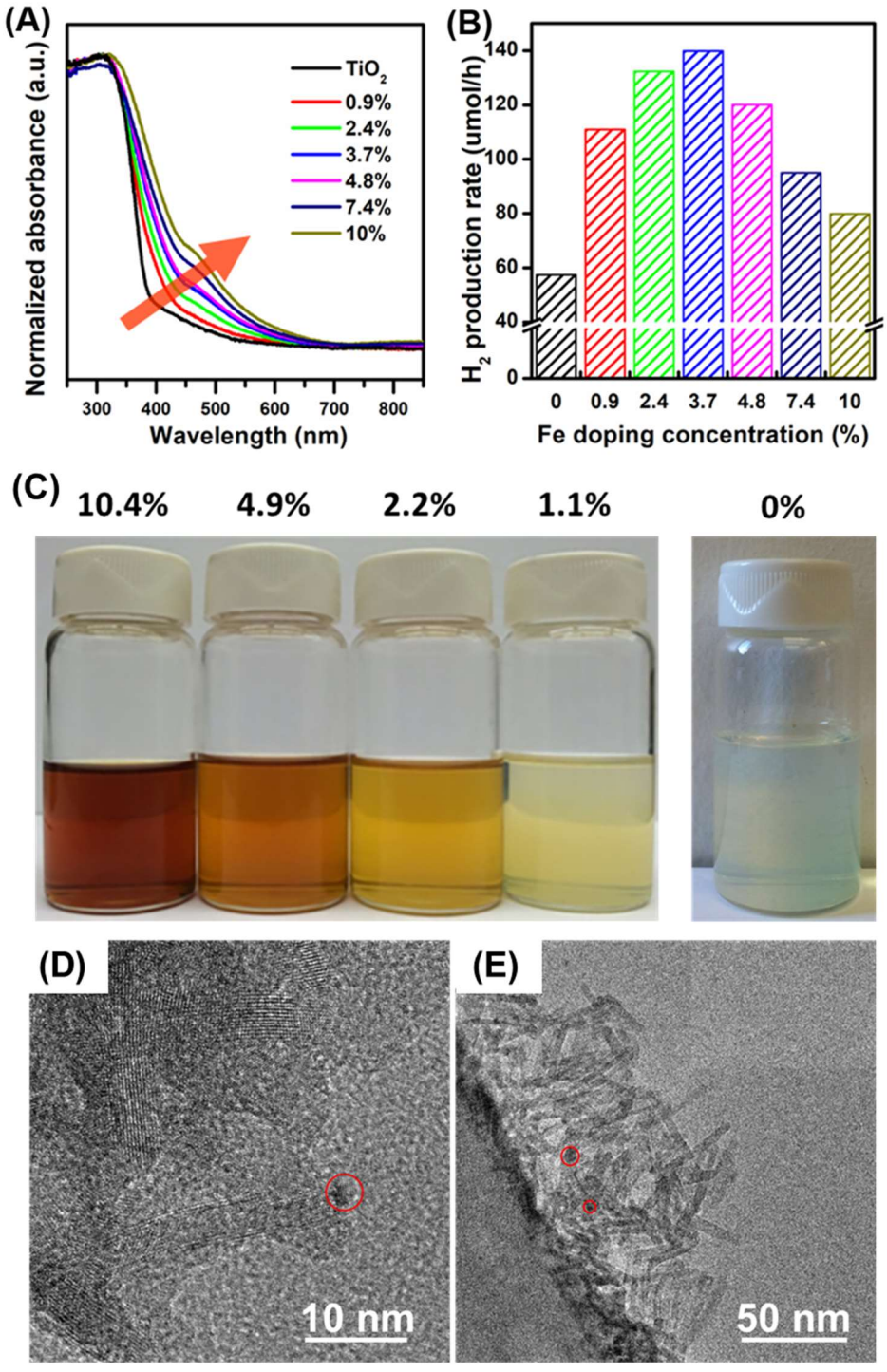

Figure 4.10 (**A**) UV-vis diffuse reflectance spectra and (**B**) photocatalytic H_2 production of TiO_2 and Fe-TiO_2 NRs with different dopant concentrations. (**C**) Typical optical images of Fe-TiO_2 with different doping ratios compared with pristine TiO_2 NRs. TEM images of (**D**) Fe-TiO_2 NRs after *in situ* Pt deposition, and (**E**) after 16-hour photocatalysis. Typical Pt NPs deposited on TiO_2 are highlighted in red circles.

To illustrate one potential impact of this general synthesis, we selected the photocatalytic H_2 production via methanol reforming as a model reaction and investigated Fe-TiO_2 NRs performance. The pristine TiO_2 brookite-phase NRs, after removing the surfactants using the reported $NOBF_4$ treatment [43] and photo-depositing 1 wt% Pt co-catalyst [17, 44], shows a hydrogen production rate of ~ 57 umol/h under 300 W Xenon lamp illumination as presented in **Figure 4.10 B**. Interestingly, all the Fe-TiO_2 NRs show higher H_2 production rates compared to the pristine TiO_2 under the same conditions. As the Fe content increases, the photocatalytic activity increases until an optimal Fe doping concentration at 3.7%. The H_2 production rate of the 3.7% Fe-TiO_2 reaches ~ 140 umol/h, corresponding to a ~ 2.5-times enhancement over that of pristine TiO_2 NRs. Such an enhancement is encouraging, given the fact that the pristine TiO_2 brookite-phase NRs has already been demonstrated as one of the most active photocatalysts in previous reports.[17, 36] Incorporating more Fe beyond 3.7% decreases activity. The enhanced activity of Fe-TiO_2 probably originates from the improved light utilization in the visible range. However, the dopant atoms can also act as charge recombination sites that compromise the charge separation efficiency.[34] Thus, an optimal doping concentration for photocatalytic hydrogen production is observed with 3.7% Fe. Meanwhile, it was observed that the H_2 production rate only decreased slightly after a 16-hour run, probably due to the decrease in methanol sacrificial reagent concentration. TEM images of the tested Fe-TiO_2 catalyst presented in **Figure 4.10 D,E** shows that the NR morphology is well-maintained after a 16-hour testing, confirming the stability of the Fe-TiO_2 NR photocatalyst.

4.3 Conclusions

This chapter highlights a generalized synthetic strategy for doped M-TiO_2 NRs with a consistent brookite phase and a monodisperse quadrangular 1-D structure as well as controllable dopant compositions and concentrations. As a result of strong binding between OAm molecules and the (210) (M)-TiO_2 plane relative to the (001) plane, the present (M)-TiO_2 NRs that grow along <001> direction can preferentially expose (210) planes as side facets. Further structural characterizations illustrate that the M dopant is uniformly distributed in TiO_2 lattice as single atoms. Photocatalytic H_2 production based on the resultant Fe-TiO_2 NRs demonstrates the Fe-doping can lead to a substantial catalytic activity enhancement due to a dopant-induced optical absorption improvement. The unique capability of our synthetic approach in preparing more improved photocatalysts opens up following studies on M-TiO_2 NRs with diverse M compositions. In addition, the present M-TiO_2 NRs may allow for additional opportunity in heterogeneous catalysis, serving as new types of either catalytic materials with highly stable single-atom M sites or catalyst supports with tunable electronic structure, oxygen activity, and surface acidity/basicity.

4.4 Experimental

Materials

Oleylamine (OAm, 70%) and oleic acid (OAc, 90%) were purchased from Sigma-Aldrich. 1-Octadecene (ODE, 90%), cobalt(II) acetylacetonate ($Co(acac)_2$, 99%), nickel(II) acetylacetonate ($Ni(acac)_2$, 96%), copper(II) acetylacetonate ($Cu(acac)_2$, 98%) and

titanium chloride ($TiCl_4$, 99.9%) were obtained from Acros Organics. Iron(III) chloride anhydrous ($FeCl_3$, 98%), vanadium(III) chloride (VCl_3, 99%), chromium(III) chloride, anhydrous ($CrCl_3$, 98%) were purchased from Alfa Aesar. Manganese(II) chloride anhydrous ($MnCl_2$, 97%), molybdenum(V) chloride anhydrous ($MoCl_5$, 99.6%) were obtained from Stream Chemical. Diethylene glycol (DEG, Reagent Grade) was purchased from Fisher Scientific.

Syntheses of TiO_2 and M-TiO_2 NRs

Brookite-phase TiO_2 and M-doped TiO_2 NRs were synthesized via a colloidal approach, based on a modification of previous publications. [10, 36] To obtain TiO_2 NRs, 10 mL of ODE, 10 ml of OAm and 0.48 ml OAc were first heated under vacuum at 90°C for one hour to remove dissolved moisture and oxygen. After that, the mixture was cooled down to 60°C under nitrogen and 1.5 mL of Ti-precursor solution containing 0.2 M $TiCl_4$ and 1.0 M OAc in ODE was injected into the solution (ODE and OAc should be pre-dried to avoid undesirable $TiCl_4$ hydrolysis). The system was then quickly heated up to 290°C and held at that temperature for 10 min. 8 mL of additional Ti precursor solution was then added dropwise into the reactor at a rate of 0.3 mL min^{-1}. Note that this solution, when heated, is corrosive due to the generation of HCl, and any unwanted metal sources like metal temperature probes should be avoided. Glass covered thermal probes were used as a suitable alternative. After being cooled down to room temperature, the TiO_2 NRs were collected and washed by the addition of isopropanol and subsequent centrifugation at 8000 rpm for 8 min. The product was further purified twice by the addition of hexane and isopropanol.

M-TiO_2 NRs were synthesized via similar approaches with Ti-M mixed solution. For example, to prepare Fe-TiO_2 NRs, a Fe-oleate precursor solution was first prepared by dissolving 0.2 M $FeCl_3$ into an ODE solution containing 1.0 M OAc, which was then mixed with the Ti-precursor solution with a desired Ti/Fe ratio. Such a Ti-M solution was then used to prepare Fe-TiO_2 NRs following the same procedure described above. The Fe doping level in TiO_2 NRs was facilely tuned by altering Ti/Fe ratio in the mixed precursor solution. For example, by tuning Ti/Fe precursor ratio from 8/1 to 8/0.75, 8/0.5, 8/0.38, 8/0.25, and 8/0.1, a Fe doping level of 10%, 7.4%, 4.8%, 3.7%, 2.4%, and 0.9% were achieved in TiO_2 NRs. Simply replacing $FeCl_3$ with other metal precursors (MCl_x or $M(acac)_x$, M = V, Cr, Mn, Co, Ni, Cu, Mo) in this procedure will yield other M-TiO_2 NRs with varied M content. Mixing two and three types of M-oleate precursor solutions with Ti precursor led to binary and ternary M-TiO_2 NRs.

Vertical alignment of M-TiO_2 NRs

A typical procedure to fabricate the vertically aligned M-TiO_2 NRs assembly is described in **Figure 4.6C**. Generally, 60 mg of the as-synthesized M-TiO_2 NRs were dispersed in 10 µl of hexanes, which was transferred on the surface of DEG in a Teflon well. The well was then covered with a glass slide to allow the hexanes to evaporate slowly for 2 hours. After all the hexanes being evaporated, a monolayer of the vertically aligned M-TiO_2 NR assembly was achieved on the surface of DEG, which can be transferred onto any substrate (including TEM grid) by placing it under the NR assembly and slowly lifting the substrate. The remaining DEG on the substrate was dried in vacuum oven overnight.

Surfactant removal of M-TiO_2 NRs

The as-synthesized M-TiO_2 NRs was stabilized with long carbon-chain surface ligands (OAm) to keep the NRs well-dispersed in the storage solution (hexanes). However, the presence of these bulky capping agents creates an inhibiting layer that blocks the active sites and mass transfer during catalysis. To remove this layer, a $NOBF_4$ ligand exchange was performed according to a previous publication. [43] Typically, 10 ml of the NR dispersion in hexanes (~ 10 mg ml^{-1}) was mixed with 10 ml of n,n dimethylformamide/$NOBF_4$ solution (0.085 M) at room temperature, and was vigorously shaken to generate a good mixing between the two phases. The NRs were then collected by centrifugation at 8000 rpm for 8 min, and was further purified twice by the addition of DMF and hexanes. After the ligand exchange, the as-obtained M-TiO_2 NRs were dried under vacuum overnight to remove the trace amount of DMF.

Characterization

The structure, morphology, and composition of the as-synthesized TiO_2 and M-TiO_2 NRs were analyzed by X-ray diffraction (XRD), transmission electron microscopy (TEM), high-resolution transmission electron microscopy (HR-TEM), scanning transmission electron microscopy (STEM), and X-ray absorption spectroscopy. XRD patterns were collected with a Rigaku Smartlab diffractometer using Cu Kα radiation (λ=1.5418Å). TEM images were obtained on a JEOL 1400 (120 kV). HR-TEM and STEM imaging was performed a Hitachi HD2700C (200kV) with a probe aberration-corrector coupled with EELS and EDS detectors, in the Center for Functional Nanomaterials at

Brookhaven National Lab. The EELS mapping and spectrum were collected using a high resolution Gatan-Enfina ER with a probe size of 1.3Å. A power law function was used for EELS background subtraction. Ultraviolet–visible (UV-Vis) diffuse reflectance spectra were collected on Thermo Scientific Evolution 300.

The X-ray absorption spectra, including the near-edge X-ray absorption near-edge structure (XANES) spectra and extended X-ray absorption fine structure (EXAFS) spectra, at the Fe K-edge were recorded at the hard X-ray XAS station (BL 10.3.2) of the Advanced Light Source, Lawrence Berkeley National Laboratory (ALS, LBL). The storage ring was operated at top-off mode (1.9 GeV, 296 buckets, 500 mA). The data collection was carried out in fluorescence mode for the Fe-TiO_2 samples in ambient conditions and transition mode for the reference samples. The beam size was limited by the horizontal and vertical slits with the area of 15 × 3 μm^2 during the measurements. The raw XAS data were processed using Athena Demeter version 0.9.24.[45] The work-up of raw XAFS data to k-space and Fourier transformed R-space was processed using a consistent methodology of background subtraction, conversion to k-space, and conversion to FT R-space. All sample data was refined using k2-weighting, a k-range of 3 -12 $Å^{-1}$, and an R-range of 0-6 Å.

Photocatalysis

Photocatalytic hydrogen production was carried out in a customized reactor equipped with a quartz window. The reactor was connected to a closed gas circulation and evacuation system. For each experiment, 50 mg of sample was dispersed in 180 mL aqueous methanol (20 vol%) solution. The system was then purged with ultra-high-purity

(UHP) grade Argon gas under stirring for 30 minutes in the dark, followed by a degassing procedure. Afterward, 0.8 bar UHP Argon gas was introduced to the system as carrier gas. The suspension was then illuminated by a 300W Xe lamp (Newport, Model 66984) which was equipped with a high pass cutoff filter to eliminate light with $\lambda < 320$ nm and a 10 cm water filter (> 800 nm) to eliminate IR irradiation. During the catalysis, 1 wt% of Pt co-catalyst was loaded by *in-situ* photo-deposition using proper amount of H_2PtCl_6. [17, 44] The gas products were quantified by using an online gas chromatography (Agilent, 7890A) which was equipped with a thermal conductivity detector (TCD) and a 5 Å molecular sieve column.

Computational Details

DFT Calculations were performed with the Vienna *ab initio* simulation package (VASP)[46] with the projector augmented-wave (PAW) pseudopotentials[47] and the revised Perdew-Burke-Ernzerhof (RPBE) exchange correlation functional.[48] An energy cutoff of 400 eV was used for the plane wave basis set. All calculations were spin polarized. The force convergence criterion was 0.02 eV $Å^{-1}$ and the energy convergence criterion was 10^{-5} eV for geometry optimizations.

The (210) surface of a brookite-phase TiO_2 was modeled by a (2×1) unit slab with 35 Å of vacuum normal to the surface to accommodate the large size of the surfactant adsorbates. The atoms in the top three layers and adsorbate were fully relaxed while the rest of the atoms were fixed in their equilibrium positions. The supercell was sampled with a 3 x 1 x 1 Monkhorst Pack k-point mesh.[49] The (001) surface was built with a (2×2)

unit slab and a 3 x 5 x 1 Monkhorst Pack k-point mesh was sampled. The binding energy between each adsorbate (oleylamine, oleic acid, and Cl) and the TiO_2 surface was calculated by

$$\mathrm{E_{Ads}} = \mathrm{E(Adsorbate + Slab)} - \mathrm{E(Slab)} - \mathrm{E(Adsorbate)} \qquad \text{Eq(4.1)}$$

Here *E*(Adsorbate+Slab) is the total energy of the TiO_2 slab with adsorbate. *E*(slab) is the total energy of the TiO_2 slab. *E*(Adsorbate) is the total energy of fully relaxed adsorbate molecules (oleylamine or oleic acid) or Cl atom. The brookite TiO_2(001) surface has a local minimum structure accessible from geometry relaxations of the as-built system. A lower energy, 1x1 reconstruction also exists and was reported by Gong *et al*.[40] The (001) system was manually rebuilt and structurally minimized to generate this reconstruction (**Figure 4.7**), and all (001) energies are reported with reference to this surface. Without including this reconstruction in the adsorption energy calculations, adsorbates initiate the reconstruction process during the course of the relaxation. In these calculations, the energy then becomes obscured between energy related to the reconstruction and the adsorption. Using the reconstruction as the reference state mitigates this issue.

4.5 References

1. Gilroy, K. D.; Ruditskiy, A.; Peng, H. C.; Qin, D.; Xia, Y., Bimetallic Nanocrystals: Syntheses, Properties, and Applications. *Chem Rev* **2016,** *116* (18), 10414-72.

2. Wu, Y.; Wang, D.; Li, Y., Nanocrystals from solutions: catalysts. *Chem Soc Rev* **2014,** *43* (7), 2112-24.

3. Zhou, Z. Y.; Tian, N.; Li, J. T.; Broadwell, I.; Sun, S. G., Nanomaterials of high surface energy with exceptional properties in catalysis and energy storage. *Chem Soc Rev* **2011,** *40* (7), 4167-85.

4. Cargnello, M.; Gordon, T. R.; Murray, C. B., Solution-phase synthesis of titanium dioxide nanoparticles and nanocrystals. *Chem Rev* **2014,** *114* (19), 9319-45.

5. Hahn, R.; Schmidt-Stein, F.; Salonen, J.; Thiemann, S.; Song, Y.; Kunze, J.; Lehto, V. P.; Schmuki, P., Semimetallic TiO_2 nanotubes. *Angew Chem Int Ed Engl* **2009,** *48* (39), 7236-9.

6. Roy, P.; Berger, S.; Schmuki, P., TiO_2 nanotubes: synthesis and applications. *Angew Chem Int Ed Engl* **2011,** *50* (13), 2904-39.

7. Bai, J.; Zhou, B., Titanium dioxide nanomaterials for sensor applications. *Chem Rev* **2014,** *114* (19), 10131-76.

8. Yang, H. G.; Sun, C. H.; Qiao, S. Z.; Zou, J.; Liu, G.; Smith, S. C.; Cheng, H. M.; Lu, G. Q., Anatase TiO_2 single crystals with a large percentage of reactive facets. *Nature* **2008,** *453* (7195), 638-41.

9. Gordon, T. R.; Cargnello, M.; Paik, T.; Mangolini, F.; Weber, R. T.; Fornasiero, P.; Murray, C. B., Nonaqueous synthesis of TiO_2 nanocrystals using TiF_4 to engineer morphology, oxygen vacancy concentration, and photocatalytic activity. *J. Am. Chem. Soc.* **2012,** *134* (15), 6751-61.

10. Buonsanti, R.; Grillo, V.; Carlino, E.; Giannini, C.; Kipp, T.; Cingolani, R.; Cozzoli, P. D., Nonhydrolytic synthesis of high-quality anisotropically shaped brookite TiO_2 nanocrystals. *J. Am. Chem. Soc.* **2008,** *130* (33), 11223-33.

11. Qin, D. D.; Bi, Y. P.; Feng, X. J.; Wang, W.; Barber, G. D.; Wang, T.; Song, Y. M.; Lu, X. Q.; Mallouk, T. E., Hydrothermal Growth and Photoelectrochemistry of Highly Oriented, Crystalline Anatase TiO_2 Nanorods on Transparent Conducting Electrodes. *Chem. Mater.* **2015,** *27* (12), 4180-4183.

12. Bai, Y.; Mora-Sero, I.; De Angelis, F.; Bisquert, J.; Wang, P., Titanium dioxide nanomaterials for photovoltaic applications. *Chem Rev* **2014,** *114* (19), 10095-130.

13. Gao, X.; Li, G.; Xu, Y.; Hong, Z.; Liang, C.; Lin, Z., TiO_2 Microboxes with Controlled Internal Porosity for High-Performance Lithium Storage. *Angew Chem Int Ed Engl* **2015,** *54* (48), 14331-5.

14. Yu, X. Y.; Wu, H. B.; Yu, L.; Ma, F. X.; Lou, X. W., Rutile TiO_2 submicroboxes with superior lithium storage properties. *Angew Chem Int Ed Engl* **2015,** *54* (13), 4001-4.

15. Singh, D. P.; George, A.; Kumar, R. V.; ten Elshof, J. E.; Wagemaker, M., Nanostructured TiO_2 Anatase Micropatterned Three-Dimensional Electrodes for High-Performance Li-Ion Batteries. *J. Phys. Chem. C* **2013,** *117* (39), 19809-19815.

16. Pepin, P. A.; Diroll, B. T.; Choi, H. J.; Murray, C. B.; Vohs, J. M., Thermal and Photochemical Reactions of Methanol, Acetaldehyde, and Acetic Acid on Brookite TiO_2 Nanorods. *J. Phys. Chem. C* **2017,** *121* (21), 11488-11498.

17. Pepin, P. A.; Lee, J. D.; Murray, C. B.; Vohs, J. M., Thermal and Photocatalytic Reactions of Methanol and Acetaldehyde on Pt-Modified Brookite TiO_2 Nanorods. *ACS Catal.* **2018,** *8* (12), 11834-11846.

18. Enache, D. I.; Edwards, J. K.; Landon, P.; Solsona-Espriu, B.; Carley, A. F.; Herzing, A. A.; Watanabe, M.; Kiely, C. J.; Knight, D. W.; Hutchings, G. J., Solvent-free oxidation

of primary alcohols to aldehydes using Au-Pd/TiO_2 catalysts. *Science* **2006,** *311* (5759), 362-5.

19. Linsebigler, A. L.; Lu, G. Q.; Yates, J. T., Photocatalysis on TiO_2 Surfaces - Principles, Mechanisms, and Selected Results. *Chem. Rev.* **1995,** *95* (3), 735-758.

20. Wang, C. J.; Thompson, R. L.; Ohodnicki, P.; Baltrus, J.; Matranga, C., Size-dependent photocatalytic reduction of CO_2 with PbS quantum dot sensitized TiO_2 heterostructured photocatalysts. *J. Mater. Chem.* **2011,** *21* (35), 13452-13457.

21. Dhakshinamoorthy, A.; Navalon, S.; Corma, A.; Garcia, H., Photocatalytic CO_2 reduction by TiO_2 and related titanium containing solids. *Energy & Environmental Science* **2012,** *5* (11), 9217-9233.

22. Ting, K. W.; Toyao, T.; Siddiki, S. M. A. H.; Shimizu, K., Low-Temperature Hydrogenation of CO_2 to Methanol over Heterogeneous TiO_2-Supported Re Catalysts. *ACS Catal.* **2019,** *9* (4), 3685-3693.

23. Widmann, D.; Behm, R. J., Active oxygen on a Au/TiO_2 catalyst: formation, stability, and CO oxidation activity. *Angew Chem Int Ed Engl* **2011,** *50* (43), 10241-5.

24. Arrii, S.; Morfin, F.; Renouprez, A. J.; Rousset, J. L., Oxidation of CO on gold supported catalysts prepared by laser vaporization: direct evidence of support contribution. *J. Am. Chem. Soc.* **2004,** *126* (4), 1199-205.

25. Fujishima, A.; Honda, K., Electrochemical Photolysis of Water at a Semiconductor Electrode. *Nature* **1972,** *238* (5358), 37-38.

26. Li, Y. F.; Selloni, A., Pathway of Photocatalytic Oxygen Evolution on Aqueous TiO_2 Anatase and Insights into the Different Activities of Anatase and Rutile. *ACS Catal.* **2016,** *6* (7), 4769-4774.

27. Lee, C. Y.; Park, H. S.; Fontecilla-Camps, J. C.; Reisner, E., Photoelectrochemical H_2 Evolution with a Hydrogenase Immobilized on a TiO_2 -Protected Silicon Electrode. *Angew Chem Int Ed Engl* **2016,** *55* (20), 5971-4.

28. Ni, M.; Leung, M. K. H.; Leung, D. Y. C.; Sumathy, K., A review and recent developments in photocatalytic water-splitting using TiO_2 for hydrogen production. *Renew. Sust. Energ. Rev.* **2007,** *11* (3), 401-425.

29. Choi, W. Y.; Termin, A.; Hoffmann, M. R., The Role of Metal-Ion Dopants in Quantum-Sized TiO_2 - Correlation between Photoreactivity and Charge-Carrier Recombination Dynamics. *J. Phys. Chem.* **1994,** *98* (51), 13669-13679.

30. Cao, Y. Q.; He, T.; Chen, Y. M.; Cao, Y. A., Fabrication of Rutile TiO_2-Sn/Anatase TiO_2-N Heterostructure and Its Application in Visible-Light Photocatalysis. *J. Phys. Chem. C* **2010,** *114* (8), 3627-3633.

31. Dong, F.; Guo, S.; Wang, H.; Li, X. F.; Wu, Z. B., Enhancement of the Visible Light Photocatalytic Activity of C-Doped TiO_2 Nanomaterials Prepared by a Green Synthetic Approach. *J. Phys. Chem. C* **2011,** *115* (27), 13285-13292.

32. Burda, C.; Lou, Y. B.; Chen, X. B.; Samia, A. C. S.; Stout, J.; Gole, J. L., Enhanced nitrogen doping in TiO_2 nanoparticles. *Nano Lett.* **2003,** *3* (8), 1049-1051.

33. Yu, J. C.; Yu, J. G.; Ho, W. K.; Jiang, Z. T.; Zhang, L. Z., Effects of F- doping on the photocatalytic activity and microstructures of nanocrystalline TiO_2 powders. *Chem. Mater.* **2002,** *14* (9), 3808-3816.

34. Schneider, J.; Matsuoka, M.; Takeuchi, M.; Zhang, J.; Horiuchi, Y.; Anpo, M.; Bahnemann, D. W., Understanding TiO_2 photocatalysis: mechanisms and materials. *Chem Rev* **2014,** *114* (19), 9919-86.

35. Liu, B.; Chen, H. M.; Liu, C.; Andrews, S. C.; Hahn, C.; Yang, P., Large-scale synthesis of transition-metal-doped TiO_2 nanowires with controllable overpotential. *J. Am. Chem. Soc.* **2013,** *135* (27), 9995-8.

36. Cargnello, M.; Montini, T.; Smolin, S. Y.; Priebe, J. B.; Delgado Jaen, J. J.; Doan-Nguyen, V. V.; McKay, I. S.; Schwalbe, J. A.; Pohl, M. M.; Gordon, T. R.; Lu, Y.; Baxter, J. B.; Bruckner, A.; Fornasiero, P.; Murray, C. B., Engineering titania nanostructure to tune and improve its photocatalytic activity. *Proc Natl Acad Sci U S A* **2016,** *113* (15), 3966-71.

37. Gordon, T. R.; Cargnello, M.; Paik, T.; Mangolini, F.; Weber, R. T.; Fornasiero, P.; Murray, C. B., Nonaqueous Synthesis of TiO2 Nanocrystals Using TiF_4 to Engineer Morphology, Oxygen Vacancy Concentration, and Photocatalytic Activity. *J. Am. Chem. Soc.* **2012,** *134* (15), 6751-61.

38. Park, J.; An, K.; Hwang, Y.; Park, J. G.; Noh, H. J.; Kim, J. Y.; Park, J. H.; Hwang, N. M.; Hyeon, T., Ultra-large-scale syntheses of monodisperse nanocrystals. *Nat. Mater.* **2004,** *3* (12), 891-5.

39. Dong, A. G.; Chen, J.; Vora, P. M.; Kikkawa, J. M.; Murray, C. B., Binary nanocrystal superlattice membranes self-assembled at the liquid-air interface. *Nature* **2010,** *466* (7305), 474-477.

40. Gong, X.-Q.; Selloni, A., First-Principles Study of the Structures and Energetics of Stoichiometric Brookite TiO_2 Surfaces. *Phys. Rev. B* **2007,** *76* (23), 235307.

41. Açıkgöz, M.; Gnutek, P.; Rudowicz, C., Modeling zero-field splitting parameters for dopant Mn2+ and Fe3+ ions in anatase TiO_2 crystal using superposition model analysis. *Chemical Physics Letters* **2012,** *524*, 49-55.

42. Park, M. S.; Kwon, S. K.; Min, B. I., Electronic structures of doped anataseTiO_2:$Ti_{1-x}M_xO_2$(M=Co,Mn, Fe, Ni). *Phys. Rev. B* **2002,** *65* (16), 161201.

43. Dong, A.; Ye, X.; Chen, J.; Kang, Y.; Gordon, T.; Kikkawa, J. M.; Murray, C. B., A generalized ligand-exchange strategy enabling sequential surface functionalization of colloidal nanocrystals. *J. Am. Chem. Soc.* **2011,** *133* (4), 998-1006.

44. Wu, Q. Y.; Xiong, S. M.; Shen, P. C.; Zhao, S.; Li, Y.; Su, D.; Orlov, A., Exceptional activity of sub-nm Pt clusters on CdS for photocatalytic hydrogen production: a combined experimental and first-principles study. *Catal. Sci. Technol.* **2015,** *5* (4), 2059-2064.

45. Ravel, B.; Newville, M., ATHENA, ARTEMIS, HEPHAESTUS: data analysis for X-ray absorption spectroscopy using IFEFFIT. *J Synchrotron Radiat* **2005,** *12* (Pt 4), 537-41.

46. Kresse, G.; Joubert, D., From ultrasoft pseudopotentials to the projector augmented-wave method. *Phys. Rev. B* **1999,** *59* (3), 1758-1775.

47. Blochl, P. E., Projector augmented-wave method. *Phys. Rev. B.* **1994,** *50* (24), 17953-17979.

48. Hammer, B.; Hansen, L. B.; Norskov, J. K., Improved adsorption energetics within density-functional theory using revised Perdew-Burke-Ernzerhof functionals. *Phys. Rev. B* **1999,** *59* (11), 7413-7421.

49. Monkhorst, H. J.; Pack, J. D., Special Points for Brillouin-Zone Integrations. *Phys. Rev. B* **1976,** *13* (12), 5188-5192.

Chapter 5
Atomically Precise Nanocluster Superlattices through High Temperature Ligand Switching

In the previous Chapter, I discussed anisotropic brookite TiO_2 nanorods that are shape controlled by oleylamine ligands and can be widely doped with various transition metals. In this chapter, the interactions of ligands are again shown to drive anisotropy but this time it is in the context of the self – assembly of nanoclusters. Through transmission electron microscopy and in-situ small angle X-ray scattering, the formation of 1.6 nm ceria nanoclusters that spontaneously self-assemble at high temperature to form micron scale nanorod superlattices can be directly observed, and their lattice parameters were measured at 1.9 nm x 3.3 nm x 3.3 nm. Characterization techniques such as solid state ^{13}C NMR and Raman spectroscopy show that benzoate ligands primarily cap the assembled nanoclusters, while oleate species cap dispersed particles. Computational results suggest that π-π stacking interactions of the benzoate ligands drive this self-assembly. A high temperature ligand switching from oleate to benzoate through breakdown of the benzyl ether solvent, is proposed to drive this switching. Substituting Ce for other rare earth oxides (La, Ho, Eu, Er, etc.) other rare earth oxide superlattices may also be formed. These superlattices may be disassembled by ligand exchange with oleate at room temperature. These particles can then be mixed and matched to form multi-elemental superlattices by reassembly at high temperature. This broadens the scope of materials and opens up the possibility of wide application.

5.1 Background and Motivation

The self-assembly of nanoparticles into superlattices is an important strategy to generate new properties from the collective interactions of the assembling components.[1] Previous works have shown that these structures can be used in applications such as in

electronics, [2-5] in plasmonics, [6-9] and in catalysis.[10-13] To further explore the possibilities offered by these structures, nanoparticle self-assembly is an active area of research. Top-down methods such as lithography or templating have been used to guide nanoparticles into desired structures.[14] Thin layer assemblies can be generated from solvent evaporation in carefully controlled systems at phase interfaces.[3, 15-19] These methods are usually hard to scale up for widespread applications, so bottom-up, solution phase generation of superlattices is desired. This can be achieved by the introduction of interactive surface domains, [20] such as in DNA-guided crystallization,[7, 21, 22] through solvent depletion interactions,[23] or through surfactant templated synthesis.[24] One particularly successful class of superlattice materials has been the lamellar rare earth oxides (REOs) [25, 26] and transition metal oxides.[27, 28] Formed from colloidal chemistry, it is thought that π-π interactions from adsorbed benzoate ligands formed in high temperature organic reactions of the solvent are responsible for their self-assembly. However, depletion force driven assembly for the lamellar structures is not formally excluded.

In this work, we show the importance of benzoate ligands as a self-assembly directing moiety and develop a general colloidal synthesis of atomically precise, non-lamellar, 1.6 nm CeO_2 and other REO nanoparticles that self-assemble into freely dispersible, micron rod superlattices with yields up to the gram scale. Nanoparticle formation and assembly are observed *ex-situ* via transmission electron microscopy and *in-situ* via small angle X-ray scattering (SAXS) as distinct events. Through *ex-situ* nuclear magnetic resonance (NMR) and Raman characterization combined with molecular

dynamics simulations, the replacement of oleate ligands with benzoate ligands at high temperatures is found to be critical to the formation of the assemblies. This synthesis is widely applicable to other REO's that may be mixed and matched to form high-entropy alloy (HEA)[29] analogous superlattices.

5.2 Results and Discussion

5.2.1 Synthesis of Ceria Nanoclusters

Ceria superlattices were generated colloidally from $Ce(CH_3COO)_3$ in degassed benzyl ether solvent and a small amount of oleic acid for 4 hours at 290 °C under a N_2 atmosphere. The finished reaction appears as a cloudy yellow and may be washed with repeated rinses with isopropanol and hexane. The superlattices may be stored in hexane as a grey dispersion that loosely settles to the bottom layer and may be generated on the gram scale. Representative dark field TEM image of the ceria superlattices are presented in **Figures 5.1 A and B** respectively. Rod structures are observed on the order of 1 – 4 microns long and 100 nm across. They are comprised of a superlattice of monodisperse ceria nanoparticles 1.6 nm in size.

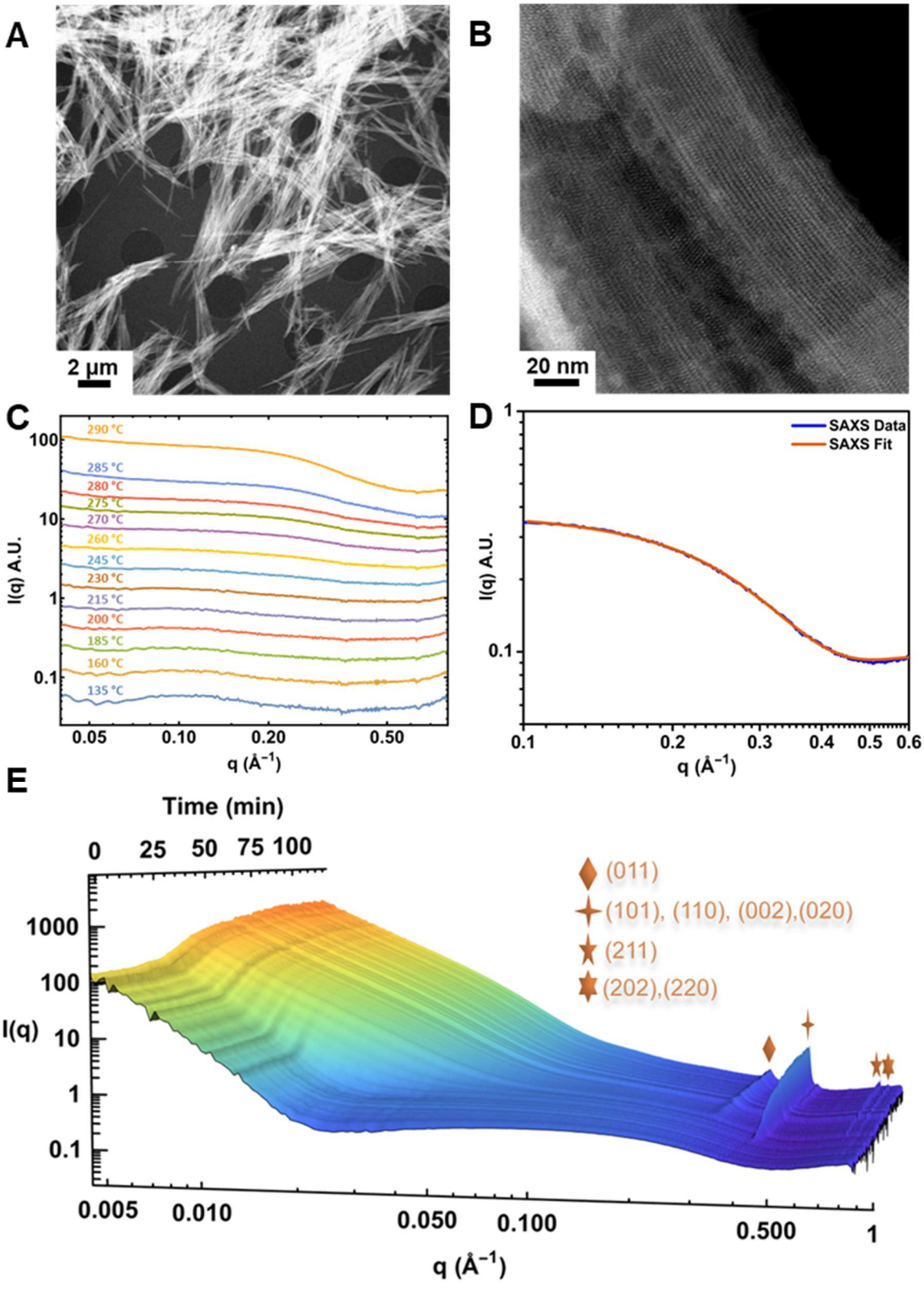
A
2 µm
B
20 nm
C
290 °C
285 °C
280 °C
275 °C
270 °C
260 °C
245 °C
230 °C
215 °C
200 °C
185 °C
160 °C
135 °C
I(q) A.U.
q (Å^{-1})
D
SAXS Data
SAXS Fit
I(q) A.U.
q (Å^{-1})
E
Time (min)
0 25 50 75 100
(011)
(101), (110), (002),(020)
(211)
(202),(220)
I(q)
q (Å^{-1})

Figure 5.1 Dark field TEM image of ceria superlattice shows (**A**) rod-like structures generated from (**B**) the self-assembly of <2 nm nanoclusters. (**C**) SAXS measurements performed at 1-minute intervals shows a small bump at around q = 0.2 $Å^{-1}$ that is a result of the formation of nanoclusters in solution. This change occurs starting after 260 °C. (**D**) A hard sphere model fit of the T = 290 °C SAXS profile indicates particles with a radius around 0.89 nm have been formed. (**E**) Time evolution of the in-situ SAXS profile measured at 290 °C. Time is measured from when the reaction reached 290 °C. Structure peaks associated with the BCT superlattices appear at approximately 25 minutes and are indexed in the inset and in Figure 5.2 D at t = 1 hour.

5.2.2 Small Angle X-ray Scattering

SAXS measurements were performed *in-situ* (**Figure 5.1 C-E**) to learn more about the superlattice formation. *In-situ* experiments were performed in a specialized reactor identical to that used by Tassone *et al.*[30] at beam 12-ID-B in Argonne National Laboratory (**Figure 3.2**). SAXS profiles starting at T = 135 °C and repeating every minute until 290 °C show evolution of a shoulder peak at q = 0.2 $Å^{-1}$ beginning after 260 °C (**Figure 5.1 C**). At 290 °C this feature becomes more pronounced and is fit in a hard sphere model, revealing that particles with a radius on the order of 0.89 nm have formed (**Figure 5.1 D**). Therefore, particles are formed in the initial stages of the reaction. **Figure 5.1 E** is a time profile of the SAXS measurements with t = 0 minutes occurring when the reaction reaches 290 °C. Structure peaks (**Figure 5.1E** and **Figure 5.2A**), accompanied by a large rise in the low q region associated with scattering from the superlattice, form after 25 minutes. The structure peaks may be assigned to a body-centered tetragonal (bct) assembly after considering the following. An asymmetric, short axis aligns well with the long axis of the macrostructure (**Figure 5.2 B,C**). Planes parallel to the long axis of the macrostructure show significant broadening relative to the planes intersecting the long axis due to the high aspect ratio of the superlattices [31]. This renders peaks between the (101)/(110) and (211) peaks (such as the (022) or (112)) unobservable above the noise. With this assignment, we derive lattice parameters (1.9 nm x 3.3 nm x 3.3 nm) for the assembly. The generation of these peaks *in-operando* demonstrates that the superlattices are a product of the synthesis at high temperature and are not an artefact of the washing

procedure or storage. Moreover, particles are formed in a distinct step from the assembly rather than being templated by surfactant molecules like the CdSe structures formed in Robinson *et al.*[24]

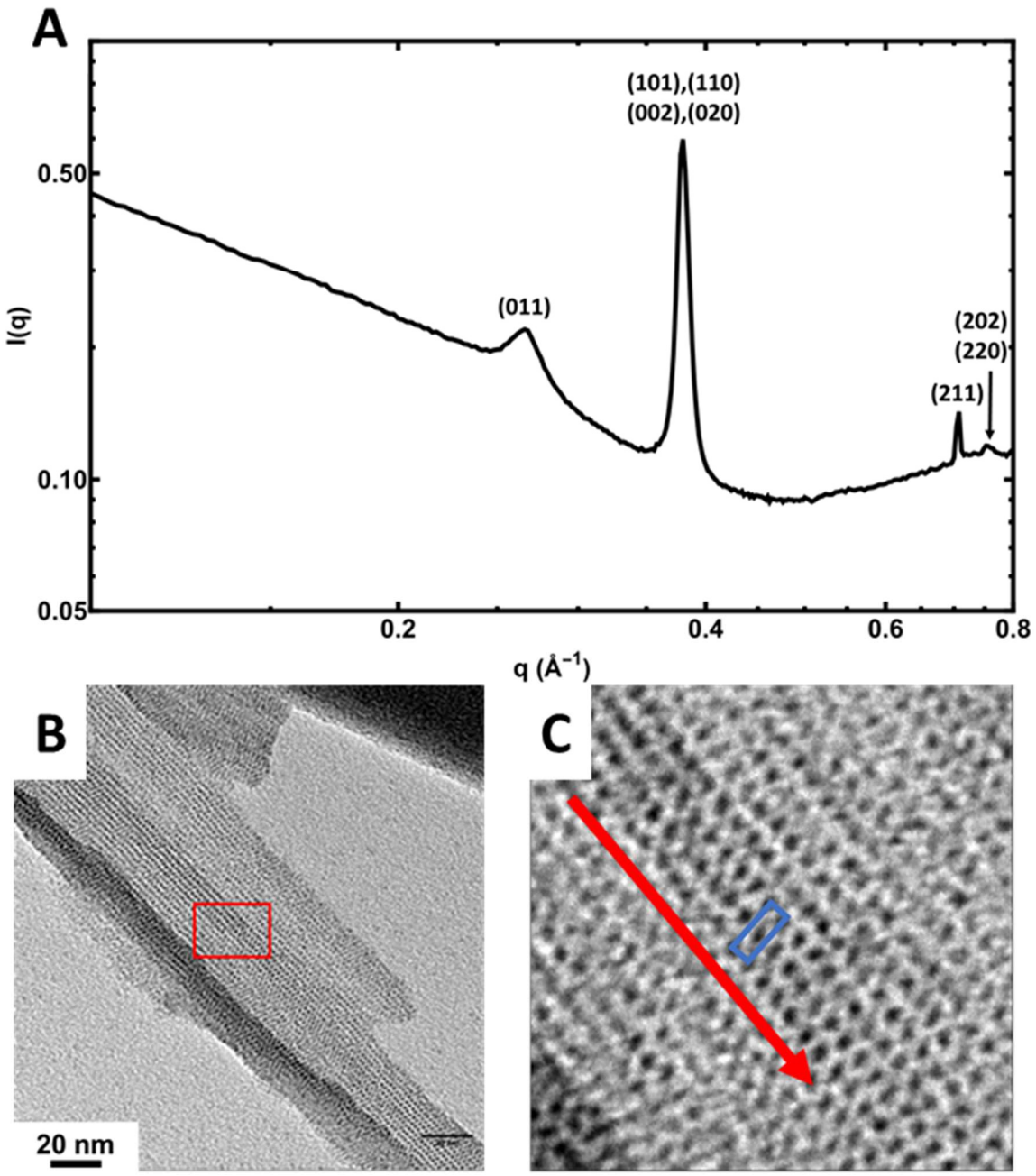

Figure 5.2 (**A**) SAXS profile at t = 60 min showing the superlattice structure peaks. (**B**) Bright field TEM image showing the macrostructure of the ceria nanoclusters and a selected area (**C**) showing the 2D projection of the 1.9 nm x 3.3 nm lattice unit cell boxed in blue. The short axis of the 2D projection aligns with the long axis of the superstructure.

5.2.3 Structural Analysis of Nanoclusters and Ligands

Because the assemblies form only at high temperature, independently from the formation of nanoparticles, we explored the idea that organic reactions of benzyl ether are occurring drive the assembly of the nanoparticles. In fact, decomposition of benzyl ether into products such as benzyl aldehyde and benzyl benzoate has been in implicated in shape variation of magnetite nanocrystals observed in the literature [32]. Attempting this synthesis in alternate solvents such as 1-octadecene (1-ODE), octyl ether, and phenyl ether does not generate superlattices. Therefore, benzyl ether is critical to the formation of these assemblies.

After the reaction, the solution smells strongly of almonds, and ^{1}H NMR experiments of benzyl ether heated to 290 °C shows the steady increase of benzaldehyde (the main component of artificial almond flavoring) over the course of the reaction (**Figure 5.3**). Moreover, injecting neat, excess benzaldehyde to the reaction at 290 °C reduces the reaction time by a factor of 4 without altering the structure. Benzaldehyde has previously been identified as a source of benzoate ligands catalyzed by reaction with benzyl alcohol on Y clusters and oxides, yielding lamellar assemblies. [27] Other metal oxides may catalyze the Cannizzaro reaction to yield benzoate and benzyl alcohol [33].

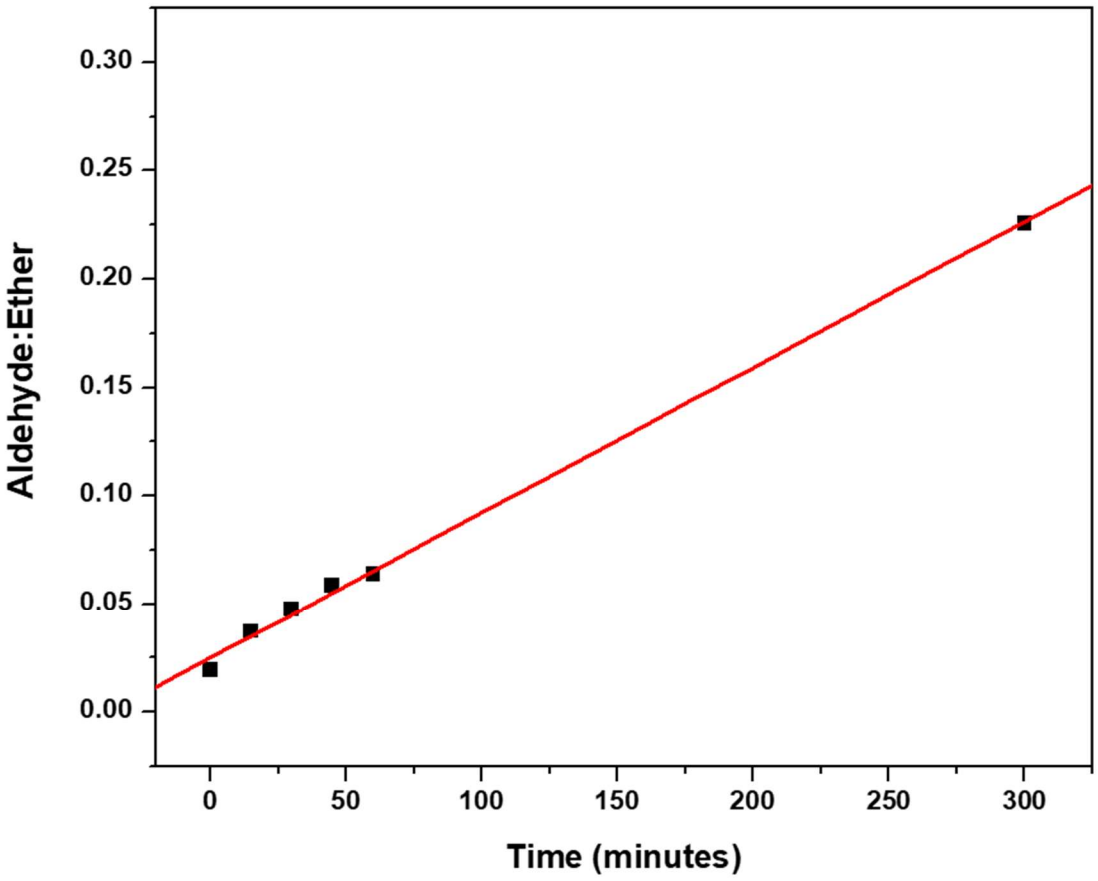

Figure 5.3 The ratio of aldehyde ^{1}H NMR signal to the methylene signal increases in time without the presence of $Ce(CH_3COO)_3$ precursor at 290 °C.

To examine if a similar mechanism is occurring here, solid state ^{1}H cross polarized magic angle spinning ^{13}C NMR (CPMAS) is used to identify the surface ligands after washing and drying particles from different reaction stages in vacuum to remove any hexane and cleaning solvents (**Figure 5.4 A**). Particles isolated before they had the opportunity to form superlattices showed two major resonances around 130 ppm, typical of sp^2 hybridized C, and 40 ppm from sp^3 hybridized C. When measurements were taken from the assembled structures, the peak near 40 ppm was significantly diminished leaving only the broad 130 ppm feature. Raman spectroscopy, performed on the isopropanol washed and dried CeO_2 superlattices, confirms the benzoate assignment in the assembly (**Figure 5.5**)[34]. This suggests that oleate present in the early reaction is replaced by benzoate moieties in the assembled structures. Even when ^{13}C oleate is used as a precursor, oleate is not observed as a major component in the superlattices. Characterization of the superlattice dispersion in solution phase ^{1}H NMR (**Figure 5.6**) reveals evidence of benzoate with resonances at 8.15 ppm, 7.68 ppm, and 7.52 ppm and a 2:1:2 ratio. Benzaldehyde, on the other hand, is not present in the washed assemblies since no peak is observed at 7.88 ppm.

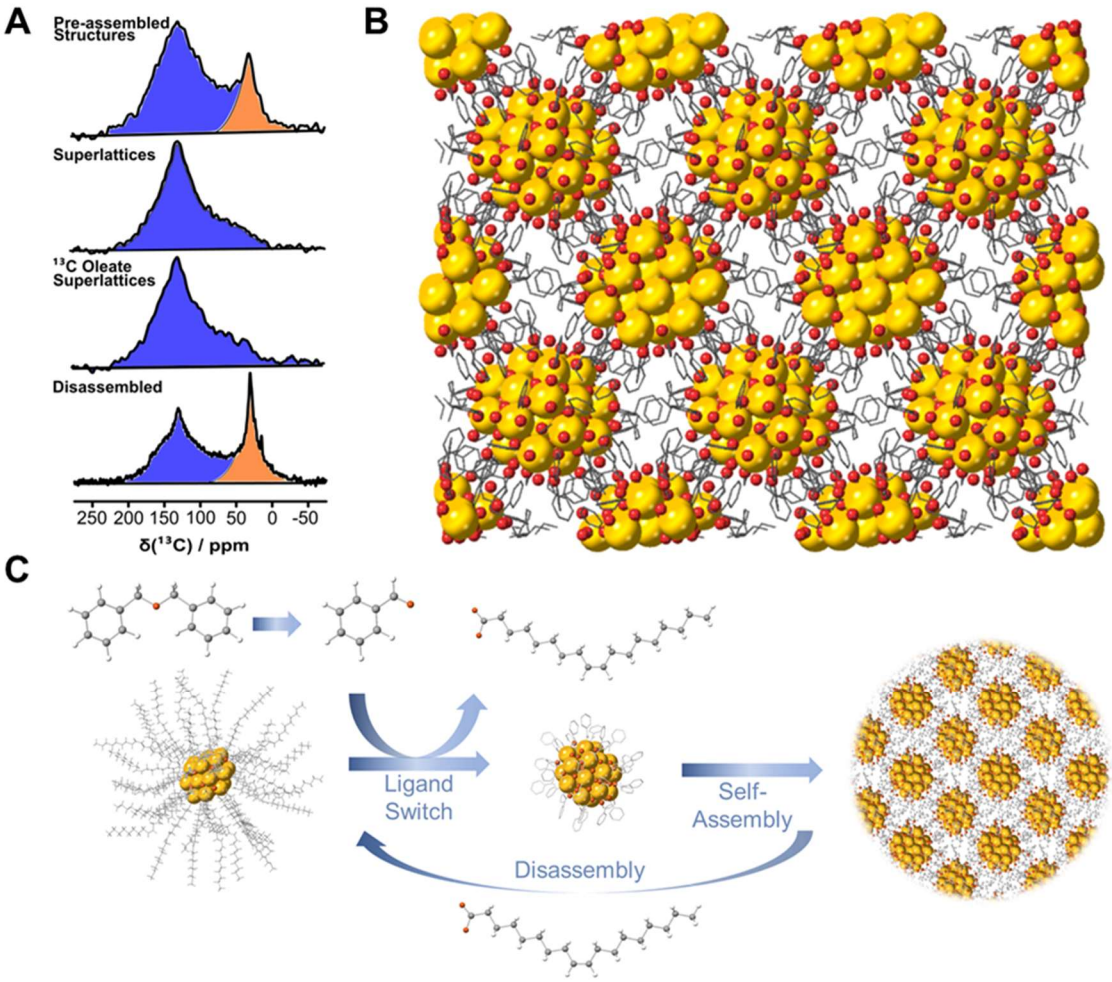

Figure 5.4 A) ^{13}C (^{1}H) CPMAS solid state NMR of the washed and dried CeO_2 nanoparticles in the pre-assembled, assembled, and disassembled forms. Disassembly was driven by introduction of oleic acid. The resonances below 50 ppm are due to sp^3 hybridized C atoms while the resonance at 140 ppm indicates sp^2 hybridized C in aromatic moieties. **B**) Unit cell (BCT 21.32 Å x 25.05 Å x 25.52 Å) generated from single crystal XRD of the disassembled CeO_2 nanoclusters recrystallized in pyridine and acetonitrile. **C**) Proposed mechanism to generate benzoate molecules from benzyl ether. At high temperature, a small amount of benzyl ether decomposes to form benzaldehyde. This may react through a Cannizzaro type mechanism catalyzed by the metal oxide nanoparticles. The benzyl alcohol formed by this mechanism reacts with benzaldehyde to generate more benzoate ligands and toluene, which evaporates off.

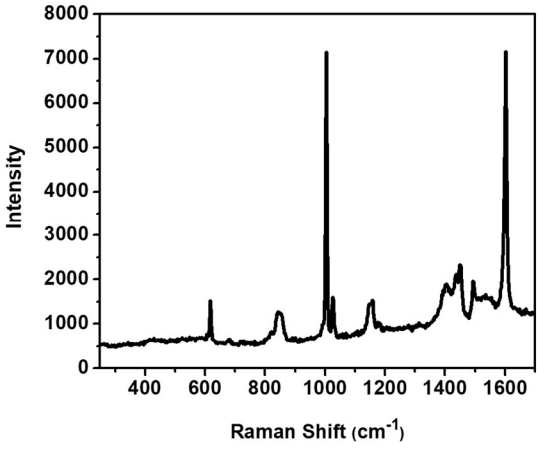

Assignment	CeO_2 Superlattices (cm^{-1})	Published (cm^{-1})
ν(C=O)	1602	1603
ν(C*C)	-	1575
ν(C-C)	1494	1492
ν(C-C)	1435	1438
ν(COO^-)	1403	1400
ν(C-O)	-	1290
β(C-H)	1180	1184
β(C-H)	1157	1159
β(C-H)	1146	1142
β(C-H)	1027.1	1030
Ring Breathing	1004	1004
ν(C-COO^-)	846	843
γ(C-H)	820	820
Ring Breathing	680	679
β(OCO)	619	615
Ring of Out of Plane Skeletal Vibration	414	401

Figure 5.5 Raman spectrum demonstrating chemical signatures of benzoate moieties on the sample. The table contains a peak by peak comparison with sodium benzoate.[34]

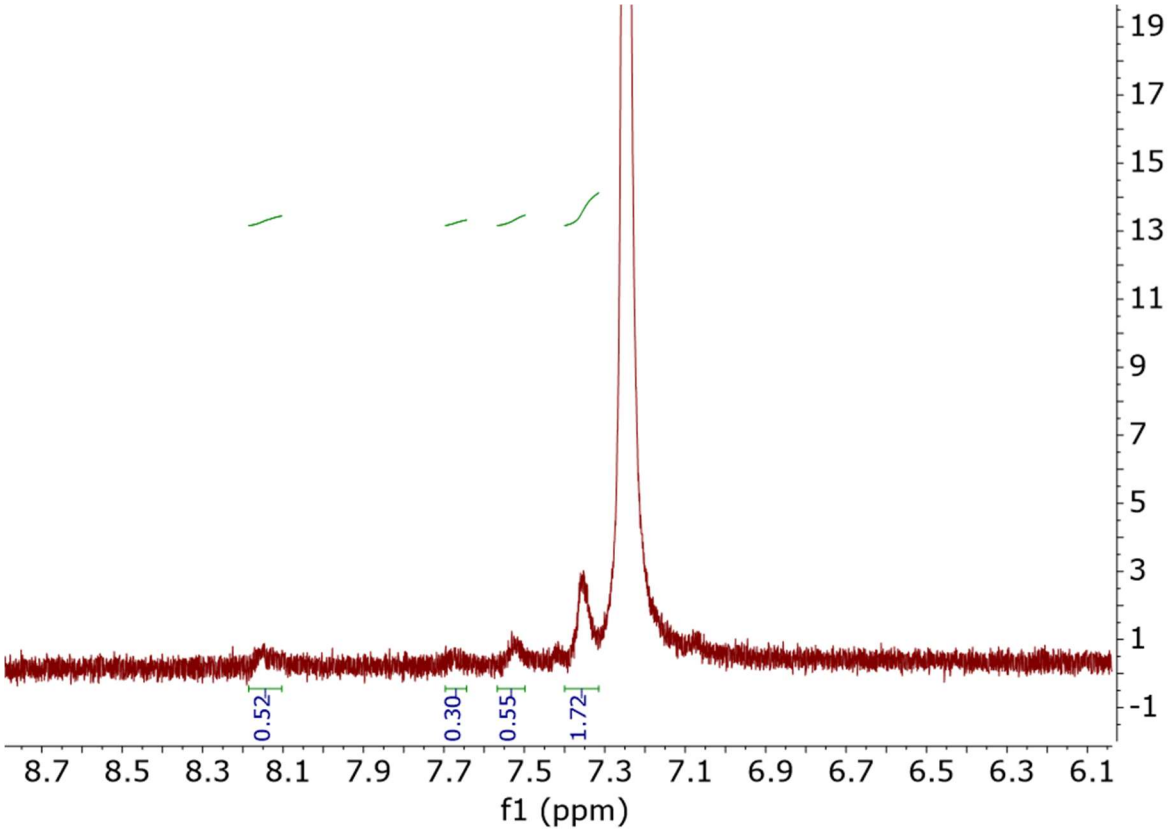

Figure 5.6 ^{1}H NMR Spectrum of solvated assemblies in $CDCl_3$ (7.25 ppm). Resonances at 7.52 ppm, 7.68 ppm, and 8.15 ppm are present in a 2:1:2 ratio and correspond to benzoate. The resonance at 7.36 ppm corresponds with benzyl ether solvent. The absence of a peak at 7.88 ppm indicates that benzaldehyde is not present in a significant amount in this sample.

Furthermore, by adding excess oleic acid to the assemblies at room temperature, the superlattices are broken and a transparent golden-brown dispersion of nanoclusters is generated. CPMAS of these disassembled structures shows that the sp^3 hybridized C peak returns (**Figure 5.4 A**). Oleate introduced in excess may undergo a ligand exchange with the benzoate on the surface. The oleate ligand then breaks up the superlattices by removing the benzoate ligands.

In addition to the disassembly observed in oleic acid, disassembly of the superlattice can be achieved with other solvents such as dichloromethane, pyridine, dimethylformamide, and benzyl alcohol. This is likely due to better solvation of the benzoate capped clusters rather than a ligand exchange as seen in the oleate disassembled structures. After disassembly, the particles may be crashed out of dispersion using an appropriate antisolvent such as acetonitrile. Note that immediately crashing these particles out of dispersion in these instances does not regenerate the superlattices and may suggest that a degree of kinetic control is necessary for superlattice growth. By adding a small amount of acetonitrile to pyridine dispersed CeO_2 nanocrystals and letting it sit for at least 5 weeks, we grew single supercrystals of the component CeO_2 clusters. The single crystals were of sufficient quality to yield X-ray diffraction (XRD) data that shows the nanocrystals are comprised of 24 Ce atoms in a fluorite arrangement (**Figure 5.4 B**) identical to clusters reported by Christou *et al.* [35] The x-ray data clearly show 30 benzoate moieties ligating the nanoclusters. The unit cell is a $P2_1/n$ monoclinic system with lattice parameters of 21.32 Å x 25.05 Å x 25.52 Å.

From the data presented thus far, the assembly procedure is believed to proceed as follows (**Figure 5.4C**). Atomically precise nanoclusters are first formed as the reaction mixture is heated to high temperature. These are capped primarily with oleate ligands. At high temperature, decomposition of the solvent to benzaldehyde occurs. Benzaldehyde reacts to form benzoate ligands, replacing oleate and then self-assembly proceeds.

5.2.4 Molecular Dynamics Simulations

To further test this hypothesis, and to provide a detailed structure, molecular dynamics (MD) simulations were carried out. We constructed two different models, oleate-coated NPs and benzoate-coated NPs, to understand the process from the dispersed oleate-coated NPs to the assembled benzoate coated NPs (**Figure 5.7 A,B**). Each model contains 2 NPs, 68 benzoates, 68 oleates, and 68 benzyl ethers, respectively, where the benzoates in the oleate-coated model and the oleates in the benzoate-coated model were protonated to prevent the binding of both ligand species on the NP surface and to retain neutrality of the system. We find that the benzoate-coated NPs spontaneously aggregate independent of the initial distance between the NPs, with the distance between two nanoclusters becoming close to that of the single-crystal structure, 2.1 nm (**Figure 5.7 C**). In comparison, the NP-NP distance was ~4 nm for the oleate coated NPs, corresponding to the monodispersed structure in the solvent. Moreover, the benzoate-coated nanocluster system was energetically favorable by > 100 kcal/mol than the oleate-coated NPs system (**Figure 5.7 D**), which explains ligand switching at high temperature, with replacement of the oleates coating of the nanocluster surface by benzoates. This energy difference is attributed mainly to the van der Waals interactions, presumably

dominated by π-π interactions between adjacent benzoates. The aromatic ring of the benzoate on the nanocluster surface can form edge-to-face or offset stacked π-π interactions depending on the position, providing the additional energy gain that drives the self-assembly of NPs.

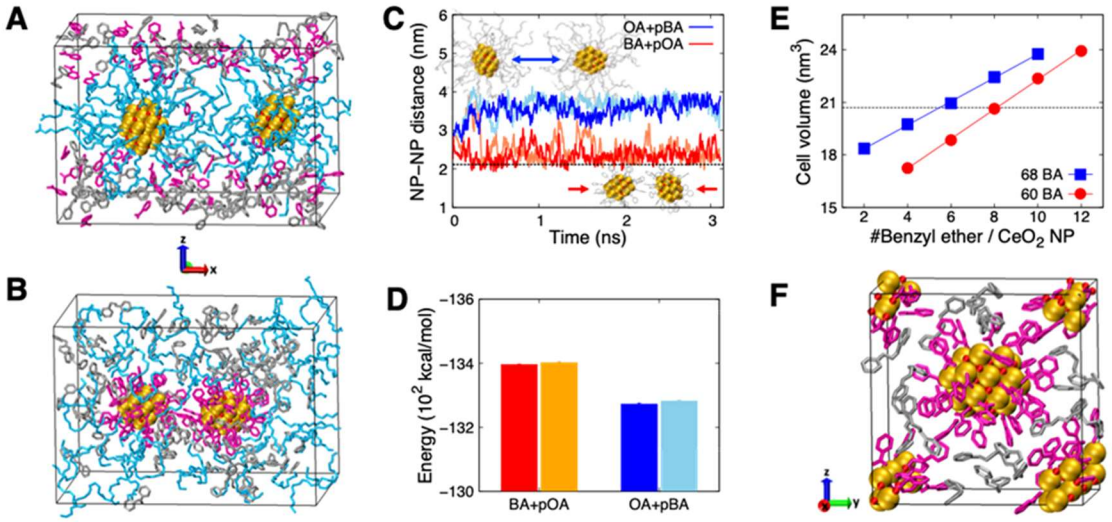

Figure 5.7 Model structures of (**A**) Oleate (OA)-coated NPs and (**B**) Benzoate (BA)-coated NPs. Each model contains 2 NPs (Ce: gold, O: red), 68 OAs (sky blue), 68 BAs (magenta), and 68 Benzyl Ethers (Bes) (grey), where the BAs in the OA-coated model and the OAs in the BA-coated model were protonated. (**C**) The distance between two NPs, where initial NP-NP distances were 2.1 nm (blue and red) and 3 nm (sky blue and orange). (**D**) The average nonbonding energies (Coulomb + van der Waals) for 3 ns MD simulations. (**E**) The cell volume as a function of the number of BEs, where the system contains 68 BAs (blue) or 60 BAs(red). (**F**) Snapshot structure showing the unit cell of the self-assembled structure, which is composed of 2 NPs, 60 BAs, and 16 BEs.

For the self-assembled structure, the SAXS result shows that it has significantly different cell parameters (a = 1.9 nm and b = c = 3.3 nm) compared to that of the single crystal structure (a = 21.3 nm, b = 25 nm, and c = 25.5 nm). Although both structures are bct, the cell volume of the self-assembled structure (20.7 nm^3) is much larger than that of the single-crystal structure (13.6 nm^3). The large volume of the self-assembled structure requires an even much greater number (> 46) of benzoate moieties. It should be noted that only a limited number of benzoates can bind to the NP surface due to the small surface area of the nanocluster. The single crystal data shows that 30 benzoate and 4 pyridine ligands bind per cluster, so this is the number of ligands we can expect to bind with the surface. When an excess of benzoates was included, they were not able to bind or else bound weakly to the nanocluster surface. We find, as predicted, that the optimum number of benzoates that can bind to the NP surface is approximately 34, as observed in the single-crystal structure. This result indicates that the self-assembled structure should contain other components in addition to benzoate. We speculate that some amount of benzyl ether solvent was included during the assembly process, since the isotope-labeled experiment clearly showed no oleates in the structure.

To estimate the number of benzyl ethers in the self-assembled structure, we calculated the cell volume as a function of the number of benzyl ethers (**Figure 5.7 E**), where the system contained either 60 or 68 benzoates (30 or 34 benzoates per NP), since the single-crystal structure showed that each NP is covered by 30 benzoates and 4 pyridines. Our results show that the cell volume matches well to the experimental data, ~20.7 nm^3, when 16 benzyl ethers or 12 benzyl ethers were included for the 30

benzoates/nanocluster system or for the 34 benzoates/nanocluster system, respectively (**Figure 5.7 E**). For the model composed of 68 benzoates and 12 benzyl ethers, however, the position of the nanoclusters changed significantly from the bct starting structure, becoming close to a simple tetragonal structure during the simulation. In contrast the model with 60 BAs and 16 BEs retained its overall structure. These results indicate that the self-assembled structure is composed of 60 benzoates and 16 benzyl ethers in the unit cell (**Figure 5.7 F**).

The $Ce_{24}O_{48}$ nanocluster has two types of facets, [100] and [111]. In the single-crystal structure, pyridine caps the central Ce of the hexagonal [111] facet. However, the carboxyl group of the benzoate does not bind properly to the [111] facet because of repulsion with the O anions bonded to the central Ce. For this reason, the lack of pyridine, and the presence of the benzyl ether leads to a different cell shape and size for the self-assembled structure. The MD simulations show that benzyl ethers surround the benzoate-coated nanocluster across the *yz* plane, filling the space between the nanoclusters. In contrast, the benzoate coated nanoclusters connect periodically along the *x* axis with no incorporation of benzyl ether. For this *x* direction, the [111] facets face one another, allowing compact packing in which one of benzoates bound to the edge of the [111] facet fills the center of the hexagon in the next cell, instead of the pyridine in the single-crystal structure. These results indicate that the size and surface of the NPs, and the ligand species are important factors to determine the asymmetry of the self-assembled structure (**Figure 5.7 F**).

5.2.5 Extension to Other Rare Earth Oxides

The superlattice synthesis was extended to other REOs: La, Sm, Eu, Gd, Tb, Ho, Er, Tm, and Yb with minor modifications (**Figure 5.8 A-D**). Typically, these elements require longer times and/or higher metal acetate concentrations to successfully synthesize the assemblies. Generally, the particles and the superlattices resemble the ceria system with slight variations in macrostructure. Whereas the ceria dispersion takes a distinct grey color, the precipitate of these elements ranges from light brown to bright white. Like ceria, these elements may also be disassembled in different solvents or via ligand exchange with oleic acid. Unlike ceria, XPS results show that these elements exist nearly exclusively in their +3 oxidation state as is typical for these elements.

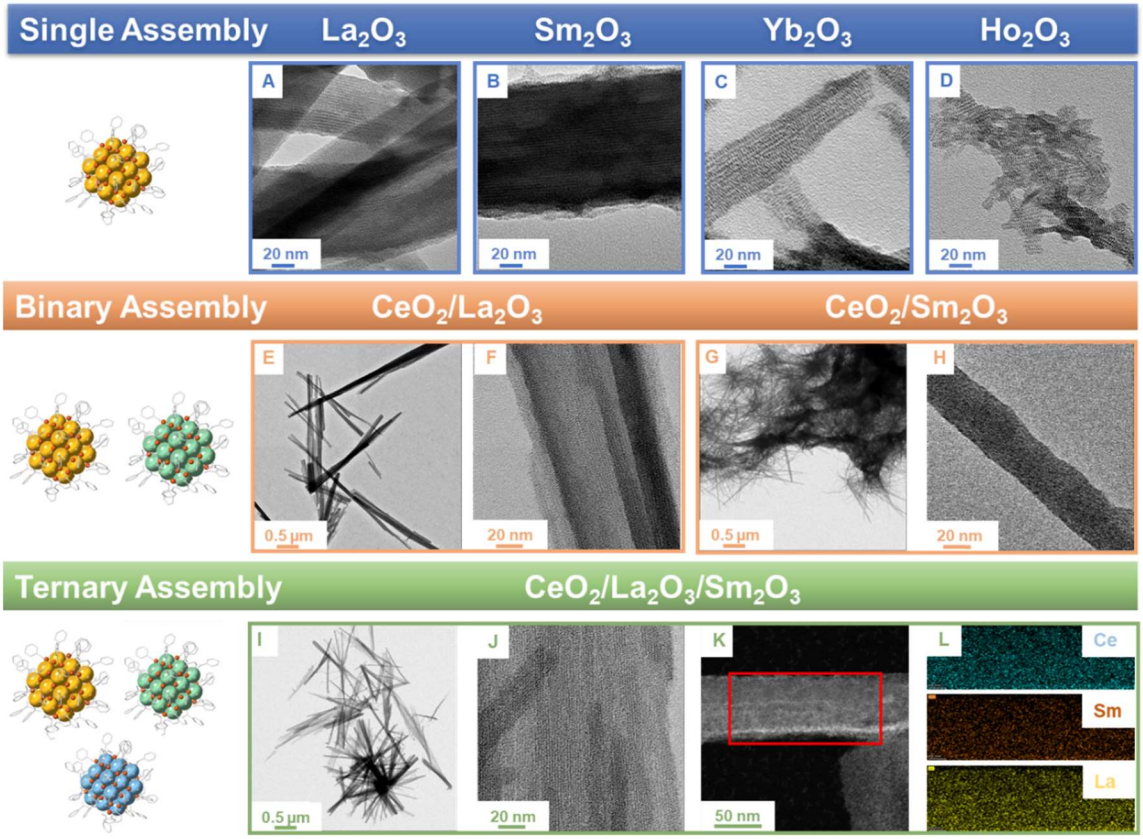

Figure 5.8 Bright field TEM images of La_2O_3 (**A**), Sm_2O_3 (**B**), Yb_2O_3 (**C**), and Ho_2O_3 single component superlattices show similar behavior to CeO_2. Bright field TEM images of binary CeO_2/La_2O_3 demonstrate macrostructure (**E**), and lattice structure (**F**) identical to CeO_2. The bright field TEM images of binary CeO_2/Sm_2O_3 demonstrate macrostructure (**G**) and lattice structure (**H**) that are similar to CeO_2, but narrower. The TEM images of the ternary $CeO_2/La_2O_3/Sm_2O_3$ demonstrate macrostructure (**I**) and lattice structure (**J**) identical to CeO_2. (**K**) HAADF – EELS measurement region of the ternary superlattice. **L**) EELS signals measured are in) Teal (Ce), Orange (Sm), and Yellow (La) and are evenly distributed throughout the measurement area.

An interesting feature of the oleic acid disassembled particles is that they may be purified and reacted in benzyl ether at 290 °C again to form new superlattices. A ceria superlattice was reformed in this way and its macrostructure and microstructure are displayed in **Figure 5.9 A,B**. As seen here, these structures are of similar quality to the superlattices formed from the acetate salts. The ability to reform these superlattices from disassembled nanoparticles is an important consequence of the decoupled steps of nanoparticle formation and superlattice assembly.

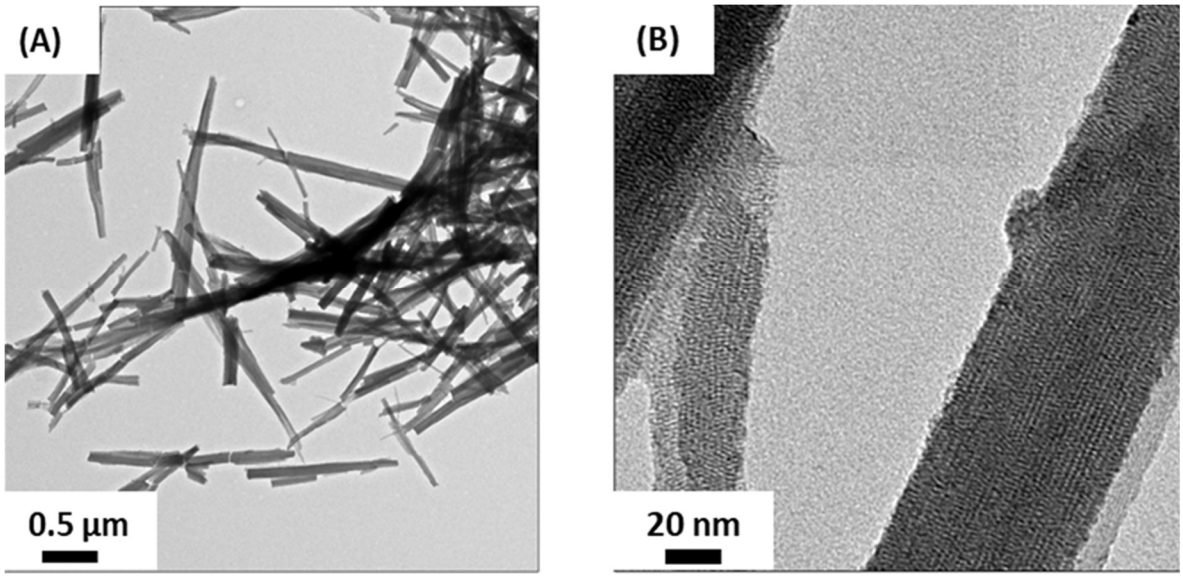

Figure 5.9 TEM images of the macrostructure (**A**) and microstructure (**B**) of CeO2 superlattices formed from oleic acid disassembled superlattices. CeO2 nanocrystals were washed and purified prior to the reassembly procedure.

This ability to be reassembled opens a wide range of possibilities for further superlattice manipulation by mixing dissimilar nanoparticles for an assembly reaction. To demonstrate this, we synthesized CeO_2, La_2O_3, and Sm_2O_3 superlattices and disassembled them with oleic acid. Then, we combined the CeO_2 nanoparticles with dissimilar nanoparticles for reaction in benzyl ether at 290 °C. The results for the binary La + Ce and Sm + Ce and the ternary Sm + La + Ce superlattice assemblies are shown in **Figure 5.8 E,F**, **Figure 5.8 G,H**, and **Figure 5.8 I,J** respectively. Both the superlattice and the nanoparticle structures are retained after the synthesis as was found in the single element case.

The elemental distribution in the ternary superlattice was measured with high angle annular dark field electron energy loss spectroscopy (HAADF – EELS) under cryogenic conditions. **Figure 5.8 K** shows the selected area for measurement and demonstrates, in the bottom right-hand corner, that these structures are prone to beam damage even at liquid N_2 temperatures. This is not surprising for a structure primarily held together by interactions of organic ligands. The EELS signal (**Figure 5.8 L**) for Ce, La, and Sm are displayed in teal, yellow, and orange, respectively. No precursor element was excluded from the assembly, and they appear to be homogeneously distributed throughout the assembly. Therefore, the particles do not show an elemental specific interaction such that they would form, for instance, an individual superlattice of CeO_2 particles and an individual superlattice of Sm_2O_3 nanoparticles. Instead, the same assembly force, the benzoate ligands, is driving superlattice formation for each of these systems. Consequently, a large range of superlattices incorporating REOs can be

generated, leading to systems analogous to HEAs that have unexplored physical and chemical properties.

5.3 Summary

We report a high temperature colloidal synthesis method that generates highly monodisperse, sub-2 nm REO nanoparticles that self-assemble to form micron long superlattices at up to gram scales. We followed the formation of CeO_2 superlattices with *in-situ* SAXS and determined that the particles form independently from the assembly step, but that assembly step is part of the high temperature reaction. Characterization of the surface ligands revealed that organic degradation of the benzyl ether solvent to form benzaldehyde and later benzoate capping ligands is critical for the formation of these superlattices. MD simulations show that to account for the full size of the unit sell observed in SAXS, benzyl ether is also a critical component of the assembly. While the forces keeping the assemblies together are robust in solvents such as hexane, several solvents may also disassemble the superlattices into their component nanoparticles. The nanoparticles are, however, stable to retreatment and may be reassembled with like or dislike nanoparticles, generating a wide range of possible superlattices such as HEA analogous mixes of many elements. This sets some groundwork for exploring the fundamentals of nanoparticle interactions in self-assembled systems.

5.4 Experimental

Chemicals

All chemicals were used without further purification. Cerium acetate hydrate (99.9%) and lanthanum acetate hydrate (99.9%) were purchased from STREM Chemicals Inc. Ytterbium acetate tetrahydrate (99.9 %) was purchased from Accela. Europium acetate hydrate (99.9%), holmium acetate hydrate (99.9%), thulium acetate hydrate (99.9%), samarium acetate hydrate (99.9%) erbium acetate tetrahydrate (99.9%), and gadolinium acetate (99.9%) were purchased from Alfa Aesar. Isopropanol (IPA, Certified ACS Plus), hexanes (Certified ACS), acetonitrile (Certified ACS), and pyridine (Certified ACS) were purchased from Fisher Chemical. Dibenzyl ether (BE, 99%) was purchased from Acros Chemical. Oleic acid (OAc, technical grade 90%) and benzaldehyde (Reagent Plus 99%) were purchased from Sigma Aldrich. ^{13}C labelled oleic acid (1-13C 99%) was purchased from Cambridge Isotope Laboratories, Inc.

Rare Earth Oxide superlattice synthesis

REO superlattices were synthesized colloidally in a one pot synthesis of 0.5 mmol of the corresponding rare earth acetate in 20 mL BE and 0.23 mL OAc. The reaction mixture was heated to 150 °C for 1 hour under flowing N_2 to purge water and other impurities. Then, the reaction was heated to 290 °C, at which point the reaction mixture will reflux. The reaction was held at this temperature for at least 4 hours. The reaction mixture transforms from golden brown to a milky yellow color when complete. After cooling to room temperature, the product was washed with IPA and dispersed in hexane at least twice. Washed samples manifest as a grey dispersion and gently settle to the bottom. This procedure was repeated scaling to 10 mmol without complication. The reaction rate was increased by introducing 0.75 mL of benzaldehyde once the reaction

temperature reached 290 °C. This reaction was finished after 1 hour rather than 4 hours for ceria.

The washed superlattices could be disassembled by introducing 3 mL of OAc to the hexane dispersed sample. Generally, this was carried out over a few minutes. The disassembled particles were washed with acetone and redispersed in hexane. These particles could be reintroduced to 20 mL BE and rerun through the above synthesis procedure to generate new superlattices. By mixing particles that were disassembled and washed, binary and ternary mixes of CeO_2, La_2O_3, and Sm_2O_3 were generated.

Characterization

Transmission electron microscopy (TEM) images were obtained on a FEI Tecnai Spirit operated at 120 kV. Proton NMR spectra were recorded using a Bruker AV800 spectrometer. All Solid-state NMR experiments were performed using an Agilent DD2 400 MHz NMR spectrometer equipped with either a Samoson 1.7 mm fast-MAS probe (^{1}H NMR) or a Chemagnetics 3.2 mm MAS probe (^{13}C NMR). ^{1}H MAS spectra were acquired at an MAS rate of 40 kHz using a Bloch decay pulse sequence. The radiofrequency (RF) power was set to 100 kHz and 4 scans were accumulated with a 1 s recycle delay. ^{13}C MAS spectra were acquired both using cross-polarization (CP) as well as using a Bloch decay sequence. The Bloch decay experiment is expected to be better quantitative while the CP experiment accentuates the solid components of the mixture. All hard pulses used 100 kHz RF power for both the Bloch decay and CP experiments while CP was achieved using

a 2 ms contact time. In all cases a total of 1024 scans were accumulated, with the recycle delay set to 2 s and 4 s for the CP and Bloch decay experiments, respectively.

Single crystals of the ceria nanoparticles were coated with Paratone oil on a MiTeGen Microloop sample holder. The X-ray intensity data were measured on a Bruker Kappa APEXII Duo system. The Incoatec Microfocus IμS (Cu K_α λ = 1.5418 Å) and a multi-layer monochromator was used as the light source. The frames were integrated with the Bruker SAINT software package using a narrow-frame algorithm. The Multi-Scan method (SADABS) was used to correct for absorption effects. Structure solutions were refined in the Bruker SHELXTL Software Package[36] within APEX and OLEX2.[37] Non-hydrogen atoms were refined anisotropically and hydrogen atoms were placed in geometrically calculated positions with U_{iso} = 1.2 U_{equiv} of the parent atom.

Raman measurements were performed on a Renishaw InVia^{TM} confocal Raman microscope with an Ar^+ excitation laser wavelength of 514 nm. X-ray photoelectron spectroscopy was carried out using a PHI VersaProbe III equipped with a monochromatic Al K-alpha (1486.6 eV) x-ray source with spherical capacitor energy analyzer to examine oxidation states of the lanthanide elements. Spectra were measured with a 100 μm spot size and 55 eV pass energy. Charging corrections to the binding energy were made by reference to graphitic C 1s at 284.5 eV. Data were analyzed in PHI Multipak 9.8.0.19 where a Shirley background was subtracted to remove inelastic scattering components.

SAXS

In-situ measurements were executed in a specialized reactor as reported by Tassone *et al*. (32). The reaction was carried out as described earlier but scaled to the 10 mL to accommodate the smaller reactor. Measurements were performed at beam 12-ID-B of the Advanced Photon Source at Argonne National Laboratory. The x-ray wavelength, λ, was set to 0.886 Å. Scattered x-ray intensities were measured with a Pilatus 2M detector (DECTRIS Ltd). The distance from sample to detector is 2 m. 1D SAXS curves were generated by averaging the 2D images azimuthally, performing a solid angle correction, and normalizing to the unimpeded transmitted x-ray beam in the Irena software package developed at beamline 12-ID-B. The 1D SAXS curves were fit in the SasView package (http://www.sasview.org/) to a spherical model.

Computation

The formation and structures of CeO_2 nanocluster were studied using molecular dynamics (MD) simulations. The $Ce_{24}O_{48}$ nanoparticle was constructed based on the experimentally obtained single-crystal structure. In the nanoparticle, O atoms have different bond numbers depending on their positions: O atoms inside of the nanoparticle have 4 bonds, O atoms on the [111] surface have 3 bonds, and O atoms on the [100] surface have 2 bonds, respectively. Since some surface O atoms are replaced by ligands (or nanoparticles are formed together with ligands), we removed 2-fold O atoms from the $Ce_{24}O_{48}$ structure to allow the ligands bind onto the surface. This $Ce_{24}O_{32}$ structure was used as CeO_2 nanoparticle for the MD simulations. For the atomic charge, +4e (≥ 4 bonds; 22 atoms) and +3e (< 4 bonds; 2 atoms) was assigned for Ce atoms, and -2e (4 bonds; 16 atoms) and -1e (3 bonds; 16 atoms) for O atoms, respectively. Thus, one nanoparticle has

+46e charges and was compensated by ligands (-1e for each acid). The charges on Ce atoms were slightly adjusted when the number of ligands was less than 46 to keep the system neutral. These assigned charges on CeO_2 and ligands were reduced by a factor of 0.5 to take account of the screening effect and to prevent too strong Coulombic interaction between CeO_2 and ligands that can lead to unreasonable structure. LAMMPS software[38] was used for MD simulations, and universal force field (UFF)[39] was used to describe the behavior of CeO_2 nanoparticles. For organic ligands, CHARMM force field was used, which was generated by CHARMM-GUI[40] and then converted into LAMMPS format by using InterMol.[41] All MD simulations were carried out by following steps below:

1) Minimization by the steepest descent method was followed by NVT (constant number of molecules, volume, and temperature) simulation at 10 K for 10 ps to generate initial velocities.

2) Heating the system from 10 K to 563 K over 100 ps using NVT, where the cell volume calculation as a function of the number of benzoic acids was performed at 300 K to match the condition of the single-crystal experiment at room temperature.

3) NPT (constant number of molecules, pressure, and temperature) production runs at the target temperature for 3 ns, where Nose-Hoover thermostat and barostat was used with 0.1 ps and 1 ps for temperature and pressure damping times, respectively.

All initial structures were generated by packmol[42], and VMD[43] was used for the visualization and analysis of the MD trajectories.

5.5 References

1. Boles, M. A.; Engel, M.; Talapin, D. V., Self-Assembly of Colloidal Nanocrystals: From Intricate Structures to Functional Materials. *Chem. Rev.* **2016,** *116* (18), 11220-89.

2. Urban, J. J.; Talapin, D. V.; Shevchenko, E. V.; Kagan, C. R.; Murray, C. B., Synergism in binary nanocrystal superlattices leads to enhanced p-type conductivity in self-assembled PbTe/Ag_2Te thin films. *Nat. Mater.* **2007,** *6* (2), 115-21.

3. Dong, A.; Chen, J.; Vora, P. M.; Kikkawa, J. M.; Murray, C. B., Binary nanocrystal superlattice membranes self-assembled at the liquid-air interface. *Nature* **2010,** *466* (7305), 474-477.

4. Koleilat, G. I.; Levina, L.; Shukla, H.; Myrskog, S. H.; Hinds, S.; Pattantyus-Abraham, A. G.; Sargent, E. H., Efficient, stable infrared photovoltaics based on solution-cast colloidal quantum dots. *ACS Nano* **2008,** *2* (5), 833-40.

5. Talapin, D. V.; Lee, J. S.; Kovalenko, M. V.; Shevchenko, E. V., Prospects of colloidal nanocrystals for electronic and optoelectronic applications. *Chem Rev* **2010,** *110* (1), 389-458.

6. Ross, M. B.; Ku, J. C.; Vaccarezza, V. M.; Schatz, G. C.; Mirkin, C. A., Nanoscale form dictates mesoscale function in plasmonic DNA-nanoparticle superlattices. *Nat. Nanotechnol.* **2015,** *10* (5), 453-8.

7. Wang, P.; Huh, J. H.; Park, H.; Yang, D.; Zhang, Y.; Zhang, Y.; Lee, J.; Lee, S.; Ke, Y., DNA Origami Guided Self-Assembly of Plasmonic Polymers with Robust Long-Range Plasmonic Resonance. *Nano Lett.* **2020,** *20* (12), 8926-8932.

8. Lan, X.; Wang, Q., Self-Assembly of Chiral Plasmonic Nanostructures. *Adv. Mater.* **2016,** *28* (47), 10499-10507.

9. Kuzyk, A.; Schreiber, R.; Fan, Z.; Pardatscher, G.; Roller, E. M.; Hogele, A.; Simmel, F. C.; Govorov, A. O.; Liedl, T., DNA-based self-assembly of chiral plasmonic nanostructures with tailored optical response. *Nature* **2012,** *483* (7389), 311-4.

10. Liu, J.; Shi, W.; Ni, B.; Yang, Y.; Li, S.; Zhuang, J.; Wang, X., Incorporation of clusters within inorganic materials through their addition during nucleation steps. *Nat. Chem.* **2019,** *11* (9), 839-845.

11. Akram, B.; Ni, B.; Wang, X., Van der Waals Integrated Hybrid POM-Zirconia Flexible Belt-Like Superstructures. *Adv. Mater.* **2020,** *32* (2), e1906794.

12. Kang, Y.; Ye, X.; Chen, J.; Cai, Y.; Diaz, R. E.; Adzic, R. R.; Stach, E. A.; Murray, C. B., Design of Pt-Pd binary superlattices exploiting shape effects and synergistic effects for oxygen reduction reactions. *J. Am. Chem. Soc.* **2013,** *135* (1), 42-5.

13. Kang, Y.; Ye, X.; Chen, J.; Qi, L.; Diaz, R. E.; Doan-Nguyen, V.; Xing, G.; Kagan, C. R.; Li, J.; Gorte, R. J.; Stach, E. A.; Murray, C. B., Engineering catalytic contacts and thermal stability: gold/iron oxide binary nanocrystal superlattices for CO oxidation. *J. Am. Chem. Soc.* **2013,** *135* (4), 1499-505.

14. Wang, D. Y.; Mohwald, H., Template-directed colloidal self-assembly - the route to 'top-down' nanochemical engineering. *J. Mater. Chem.* **2004,** *14* (4), 459-468.

15. Kutuzov, S.; He, J.; Tangirala, R.; Emrick, T.; Russell, T. P.; Boker, A., On the kinetics of nanoparticle self-assembly at liquid/liquid interfaces. *Phys. Chem. Chem. Phys.* **2007,** *9* (48), 6351-8.

16. Geuchies, J. J.; van Overbeek, C.; Evers, W. H.; Goris, B.; de Backer, A.; Gantapara, A. P.; Rabouw, F. T.; Hilhorst, J.; Peters, J. L.; Konovalov, O.; Petukhov, A. V.; Dijkstra, M.; Siebbeles, L. D. A.; van Aert, S.; Bals, S.; Vanmaekelbergh, D., In situ study of the formation mechanism of two-dimensional superlattices from PbSe nanocrystals. *Nat. Mater.* **2016,** *15* (12), 1248-1254.

17. Weidman, M. C.; Smilgies, D. M.; Tisdale, W. A., Kinetics of the self-assembly of nanocrystal superlattices measured by real-time in situ X-ray scattering. *Nat. Mater.* **2016,** *15* (7), 775-81.

18. Smith, D. K.; Goodfellow, B.; Smilgies, D. M.; Korgel, B. A., Self-assembled simple hexagonal AB(2) binary nanocrystal superlattices: SEM, GISAXS, and defects. *J. Am. Chem. Soc.* **2009,** *131* (9), 3281-90.

19. Winslow, S. W.; Swan, J. W.; Tisdale, W. A., The Importance of Unbound Ligand in Nanocrystal Superlattice Formation. *J. Am. Chem. Soc.* **2020,** *142* (21), 9675-9685.

20. Zhang, Z.; Glotzer, S. C., Self-Assembly of Patchy Particles. *Nano Lett.* **2004,** *4* (8), 1407-1413.

21. Nykypanchuk, D.; Maye, M. M.; van der Lelie, D.; Gang, O., DNA-guided crystallization of colloidal nanoparticles. *Nature* **2008,** *451* (7178), 549-52.

22. Auyeung, E.; Li, T. I.; Senesi, A. J.; Schmucker, A. L.; Pals, B. C.; de la Cruz, M. O.; Mirkin, C. A., DNA-mediated nanoparticle crystallization into Wulff polyhedra. *Nature* **2014,** *505* (7481), 73-7.

23. Young, K. L.; Jones, M. R.; Zhang, J.; Macfarlane, R. J.; Esquivel-Sirvent, R.; Nap, R. J.; Wu, J.; Schatz, G. C.; Lee, B.; Mirkin, C. A., Assembly of reconfigurable one-

dimensional colloidal superlattices due to a synergy of fundamental nanoscale forces. *Proc Natl Acad Sci U S A* **2012,** *109* (7), 2240-5.

24. Nevers, D. R.; Williamson, C. B.; Savitzky, B. H.; Hadar, I.; Banin, U.; Kourkoutis, L. F.; Hanrath, T.; Robinson, R. D., Mesophase Formation Stabilizes High-Purity Magic-Sized Clusters. *J. Am. Chem. Soc.* **2018,** *140* (10), 3652-3662.

25. Karmaoui, M.; Ferreira, R. A. S.; Mane, A. T.; Carlos, L. D.; Pinna, N., Lanthanide-based lamellar nanohybrids: Synthesis, structural characterization, and optical properties. *Chem. Mater.* **2006,** *18* (18), 4493-4499.

26. Karmaoui, M.; Mafra, L.; Ferreira, R. A. S.; Rocha, J.; Carlos, L. D.; Pinna, N., Photoluminescent rare-earth based biphenolate lamellar nanostructures. *J. Phys. Chem. C* **2007,** *111* (6), 2539-2544.

27. Pinna, N.; Garnweitner, G.; Beato, P.; Niederberger, M.; Antonietti, M., Synthesis of yttria-based crystalline and lamellar nanostructures and their formation mechanism. *Small* **2005,** *1* (1), 112-21.

28. Antonietti, M.; Niederberger, M.; Smarsly, B., Self-assembly in inorganic and hybrid systems: beyond the molecular scale. *Dalton Trans.* **2008,** (1), 18-24.

29. Sun, Y.; Dai, S., High-entropy materials for catalysis: A new frontier. *Sci. Adv.* **2021,** *7* (20), eabg1600.

30. Wu, L.; Willis, J. J.; McKay, I. S.; Diroll, B. T.; Qin, J.; Cargnello, M.; Tassone, C. J., High-temperature crystallization of nanocrystals into three-dimensional superlattices. *Nature* **2017,** *548* (7666), 197-201.

31. Burton, A. W.; Ong, K.; Rea, T.; Chan, I. Y., On the estimation of average crystallite size of zeolites from the Scherrer equation: A critical evaluation of its application to zeolites with one-dimensional pore systems. *Microporous Mesoprous Mater.* **2009,** *117* (1-2), 75-90.

32. Qiao, L.; Fu, Z.; Li, J.; Ghosen, J.; Zeng, M.; Stebbins, J.; Prasad, P. N.; Swihart, M. T., Standardizing Size- and Shape-Controlled Synthesis of Monodisperse Magnetite (Fe_3O_4) Nanocrystals by Identifying and Exploiting Effects of Organic Impurities. *ACS Nano* **2017,** *11* (6), 6370-6381.

33. Haffad, D.; Kameswari, U.; Bettahar, M. M.; Chambellan, A.; Lavalley, J. C., Reduction of benzaldehyde on metal oxides. *J. Catal.* **1997,** *172* (1), 85-92.

34. Badr, Y.; Mahmoud, M. A., Size-dependent surface-enhanced Raman scattering of Sodium Benzoate on silver nanoparticles. *Journal of Molecular Structure* **2005,** *749* (1-3), 187-192.

35. Mitchell, K. J.; Abboud, K. A.; Christou, G., Atomically-precise colloidal nanoparticles of cerium dioxide. *Nat Commun* **2017,** *8* (1), 1445.

36. Sheldrick, G. M., SHELXT - integrated space-group and crystal-structure determination. *Acta Crystallogr A Found Adv* **2015,** *71* (Pt 1), 3-8.

37. Dolomanov, O. V.; Bourhis, L. J.; Gildea, R. J.; Howard, J. A. K.; Puschmann, H., OLEX2: a complete structure solution, refinement and analysis program. *Journal of Applied Crystallography* **2009,** *42* (2), 339-341.

38. Plimpton, S., Fast Parallel Algorithms for Short-Range Molecular-Dynamics. *Journal of Computational Physics* **1995,** *117* (1), 1-19.

39. Rappe, A. K.; Casewit, C. J.; Colwell, K. S.; Goddard, W. A.; Skiff, W. M., Uff, a Full Periodic-Table Force-Field for Molecular Mechanics and Molecular-Dynamics Simulations. *J. Am. Chem. Soc.* **1992,** *114* (25), 10024-10035.

40. Jo, S.; Kim, T.; Iyer, V. G.; Im, W., CHARMM-GUI: a web-based graphical user interface for CHARMM. *J Comput Chem* **2008,** *29* (11), 1859-65.

41. Shirts, M. R.; Klein, C.; Swails, J. M.; Yin, J.; Gilson, M. K.; Mobley, D. L.; Case, D. A.; Zhong, E. D., Lessons learned from comparing molecular dynamics engines on the SAMPL5 dataset. *Journal of computer-aided molecular design* **2017,** *31* (1), 147-161.

42. Martinez, L.; Andrade, R.; Birgin, E. G.; Martinez, J. M., PACKMOL: a package for building initial configurations for molecular dynamics simulations. *J Comput Chem* **2009,** *30* (13), 2157-64.

43. Humphrey, W.; Dalke, A.; Schulten, K., VMD: visual molecular dynamics. *J Mol Graph* **1996,** *14* (1), 33-8, 27-8.

Chapter 6
AgPd Nanoparticles for the Electrocatalytic CO_2 Reduction: Bimetallic Composition-Dependent Ligand and Ensemble Effects

Portions published as: Cui, M.; Johnson, G.; Zhang, Z.; Li, S.; Hwang, S.; Zhang, X.; Zhang, S., AgPd nanoparticles for electrocatalytic CO_2 reduction: bimetallic composition-dependent ligand and ensemble effects. *Nanoscale* **2020,** *12* (26), 14068-14075.

In this chapter, I move from thinking about how ligands interact with the surface and their environments to thinking about how small molecules interact with surfaces in the context of catalysis. I discuss CO_2 reduction over monodisperse AgPd nanoparticles with variable Ag:Pd ratios. I perform DFT calculations to show how Ag incorporated into Pd will weaken CO adsorption on all possible Pd sites through the ligand effect. More importantly, however, is that Ag breaks up Pd multimetallic sites that preferentially bind CO so alloying Ag into Pd generates a favorable ensemble effect. Experiment is coupled with these calculations to provide further evidence of the ensemble effect contributions. Diffuse reflectance infrared fourier transform spectroscopy (DRIFTS) shows evidence of linearly bound CO upon addition of Ag into Pd. Maximal activity for CO_2 reduction to CO over the AgPd nanoparticles was found for $Ag_{15}Pd_{85}$ nanoparticles. Greater than 95% faradaic efficiency was observed with a mass activity of 15.2 mA/mg_{metal} at -0.8 V_{RHE}.

6.1 Background and Motivation.

Electrocatalytic CO_2 reduction reaction (CO_2RR) offers the possibility of carbon-neutral production of chemicals and fuels when driven by renewable electricity (solar, wind and hydro etc.).[1-3] CO is one of the CO_2RR products targeted with broad interest, as it is an essential precursor in many industrial processes, including the water-gas shift reaction for hydrogen production as well as the chemical synthesis of methanol, acetic acid, aldehydes, etc.[4] Thermodynamically, the CO_2RR to CO takes place at -0.11 V vs. the reversible hydrogen electrode (V_{RHE}).[5, 6] However, due to the sluggish kinetics of the reaction over most catalysts, the reaction usually requires large overpotentials to yield a desirable production rate of CO.[7,8]

Among the various metal catalysts studied for the CO_2RR, Pd has shown an impressive Faradaic efficiency towards CO (FE_{CO}) at relatively low overpotentials. This is primarily caused by the strong binding energy of C-bound intermediates (including *CO, *COOH etc. which are correlated through a scaling relationship) on the surface of Pd, facilitating CO_2 activation and suppressing the competing hydrogen evolution reaction (HER)[7, 8]. The strong binding energy, however, makes Pd prone to CO-poisoning,[9] which hampers the CO desorption step and decreases the CO production rate.[10] A great deal of effort is devoted to balance the binding energy of C-bound intermediates for improved efficiency by tuning the size and surface structure of Pd nanoparticles (NPs). For example, Gao et. al. investigated the size effect of Pd NPs (from 2.4 to 10.3 nm) and demonstrated that a 91.2% FE_{CO} can be reached on 3.7 nm Pd.[11] Pd concave nanocubes with high index (310) surface facets were found to be more efficient than Pd nano-octahedrons and nanocubes, leading to a FE_{CO} of 90.6%.[12] Despite the encouraging progress, the issue of low CO current density (production rate) associated with over-strong CO adsorption over Pd NPs needs to be further addressed.

Alloying Pd with a second element, M, has been studied as a strategy to lower the CO adsorption strength and enhance the CO production rate. Yin et. al. reported that CuPd alloy NPs can exhibit a significantly improved CO mass current density.[13] Yet the FE_{CO} reduced to 86% because of the promoted HER at the Cu sites. Such a M-induced product selectivity alteration was also observed on other MPd alloy NPs (such as NiPd,[14] SnPd[15] etc.). In this Chapter, AgPd NPs with a uniform size of 2-4 nm and controllable AgPd bimetallic compositions are used to elucidate the composition-dependent catalytic

property for the CO_2RR. Ag is a known metal with weak binding to both *CO and *H.[7] It is anticipated that the incorporation of Ag into Pd can alleviate CO-poisoning without sacrificing the FE_{CO}. A similar concept was employed to construct Pd small clusters in the surface of Au NPs[16], but the use of Ag in the present work benefits from the ease of synthesizing monodisperse AgPd NPs as well as the higher efficiency and relative earth abundance of Ag over Pd. By systematically studying AgPd NPs with a wide range of well-controlled compositions, $Ag_{15}Pd_{85}$ is identified as the most efficient with a FE_{co} greater than 95% and a high CO current density of 15.2 mA mg_{metal}^{-1} at -0.8 V_{RHE}. With the assistance of density functional theory (DFT) calculations and environmental diffuse reflectance infrared Fourier-transform spectroscopy (DRIFTS) analysis, we further demonstrate that the bimetallic enhancement arises from a combination of ligand and ensemble effects that is properly adjusted by the favourable Ag level. The former weakens the CO adsorption on all possible Pd sites, while the latter disrupts the strongest multi-fold CO binding sites.

6.2 Results and Discussion

6.2.1 Synthesis of AgPd, Ag, and Pd Nanoparticles

The AgPd NPs were prepared via a colloidal synthetic approach, reported previously,[17] using oleylamine (OAm) as the reducing agent and the combination of oleic acid (OAc) and OAm as surfactants. In this system, an excessive amount of OAc is crucial to stabilize the Ag precursor from self-nucleation and avoid the formation of polydisperse AgPd NPs. The morphology of AgPd NPs was investigated using TEM, while the chemical composition of NPs was revealed through ICP-OES (**Table 6.1**). As shown in the TEM

images in **Figure 6.1 A-D** , the as-synthesized Ag_5Pd_{95}, $Ag_{15}Pd_{85}$, $Ag_{37}Pd_{63}$, and $Ag_{45}Pd_{55}$ NPs are all uniform, with an average size of 4.5 ± 0.3 nm, 3.3 ± 0.4 nm, 2.8 ± 0.5 nm, and 2.3 ± 0.4 nm, respectively. We further prepared 2.4 ± 0.1 nm Ag NPs **Figure 6.1 E** and 4.8 ± 0.6 nm Pd NPs **Figure 6.1 F**. They are also monodisperse NPs with a similar size as the AgPd particles and can therefore be used in electrocatalysis control experiments. The use of monodisperse particles is a key enabler to unambiguously refine the composition effect in catalysis with minimal influence from other structural parameters.[18, 19] The as-synthesized NPs were deposited on the Vulcan XC 72R carbon black (C-NPs) and treated with the hydrazine/ethanol solution to remove OAc and OAm, bulky hydrophobic surfactants. This process, mediated by hydrazine ligand exchange, has been widely used for activating the surface of NPs produced with bulky organic ligand for various applications.[20-23] TEM analysis indicates that these NPs well preserved their size, shape, and distribution on the carbon support after hydrazine treatment.

Table 6.1 The composition and metal loading of C-AgPd catalysts determined by ICP-OES.

Catalyst	Ag:Pd molar ratio	metal loading wt%	
		Ag	Pd
Ag	100:0	15.6	0
$Ag_{45}Pd_{55}$	45:55	11.2	13.7
$Ag_{37}Pd_{63}$	37:63	8.3	14.7
$Ag_{15}Pd_{85}$	15:85	2.7	15.3
Ag_5Pd_{95}	5:95	1.2	25.1
Pd	0:100	0	26

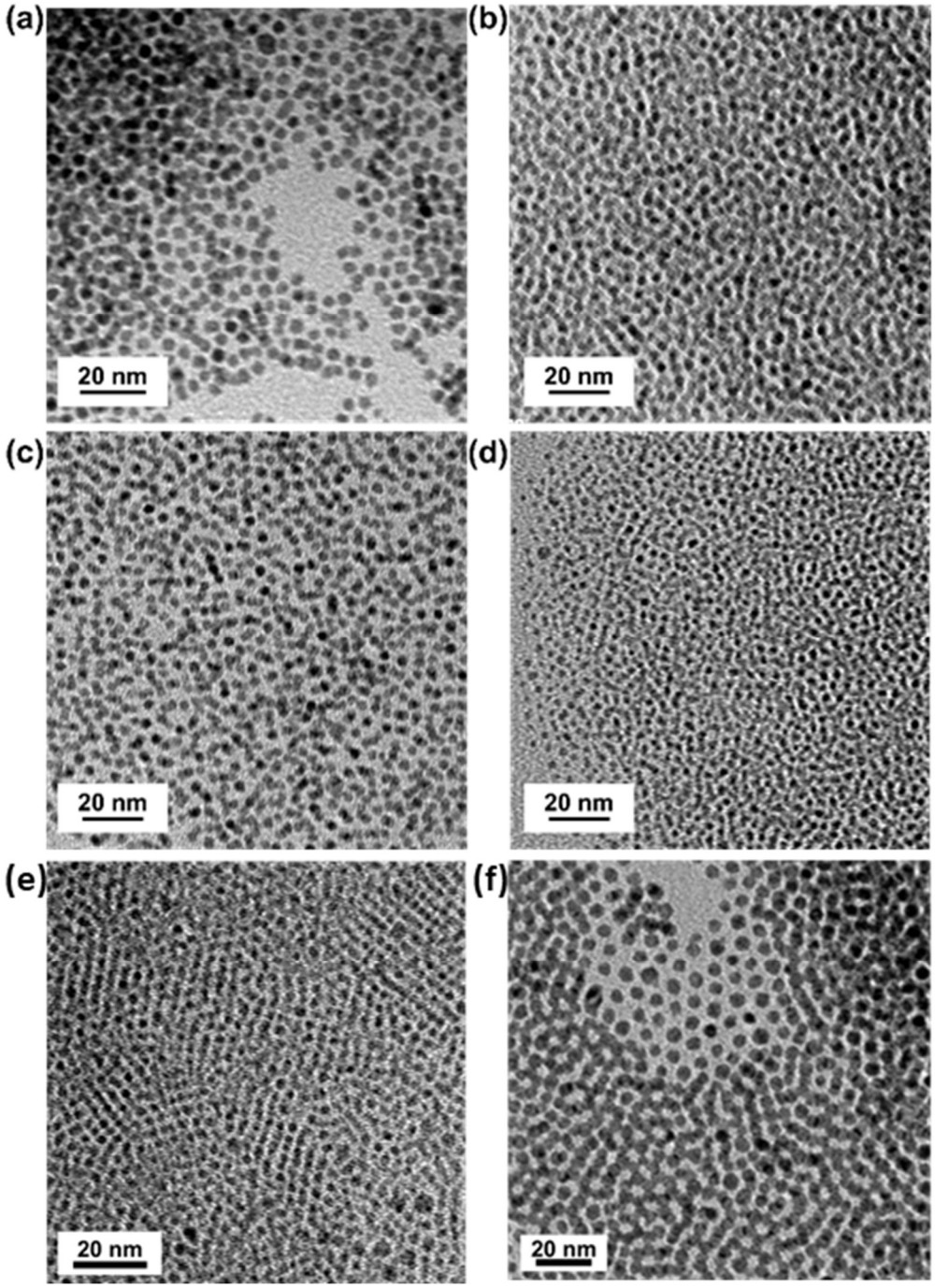

Figure 6.1 TEM Images of (**a**) Ag_5Pd_{95}, (**b**) $Ag_{15}Pd_{15}$, (**c**) $Ag_{37}Pd_{63}$, (**d**) $Ag_{45}Pd_{55}$, (**e**) Ag, and (**f**) Pd

The HRTEM image in **Figure 6.2 A** shows that the AgPd NPs remain crystalline after surfactant removal. Meanwhile, based on STEM high angle angular dark field (HAADF) image and the electron energy loss spectroscopy (EELS) 2D elemental mappings of AgPd displayed in **Figure 6.2 B-D**, we confirmed that Pd and Ag elements are homogenously distributed in the NPs, forming a solid-solution alloy. The X-ray diffraction (XRD) patterns of C-NPs samples were summarized in **Figure 6.3 A.** It is consistent with the NPs presenting typical *fcc* structure (Pd: PDF# 03-065-6174; Ag: PDF# 00-04-0783). The C-Pd displays four diffraction peaks at 40.1^{o}, 45.5^{o}, 68.1^{o}, and 81.3^{o} that are indexed to the (111), (200), (220), and (311) plane diffractions. On C-AgPd and C-Ag samples, only the (111) peak is weakly observed due to the small sizes of these NPs, and the peak slightly shifts to the lower angle with the increase of Ag content, consistent with a previous report.[17] The XPS spectra of AgPd in **Figure 6.3 B** displays a negative binding energy (BE) shift of the Pd 3d peak with the decrease in Pd concentration. Meanwhile, the Ag 3d peak also shifted negatively. These results agree with the previous theoretical and experimental X-ray photoelectron spectroscopy (XPS) studies on AgPd alloy materials, evidencing the alloy structure of the AgPd NPs.[24, 25]

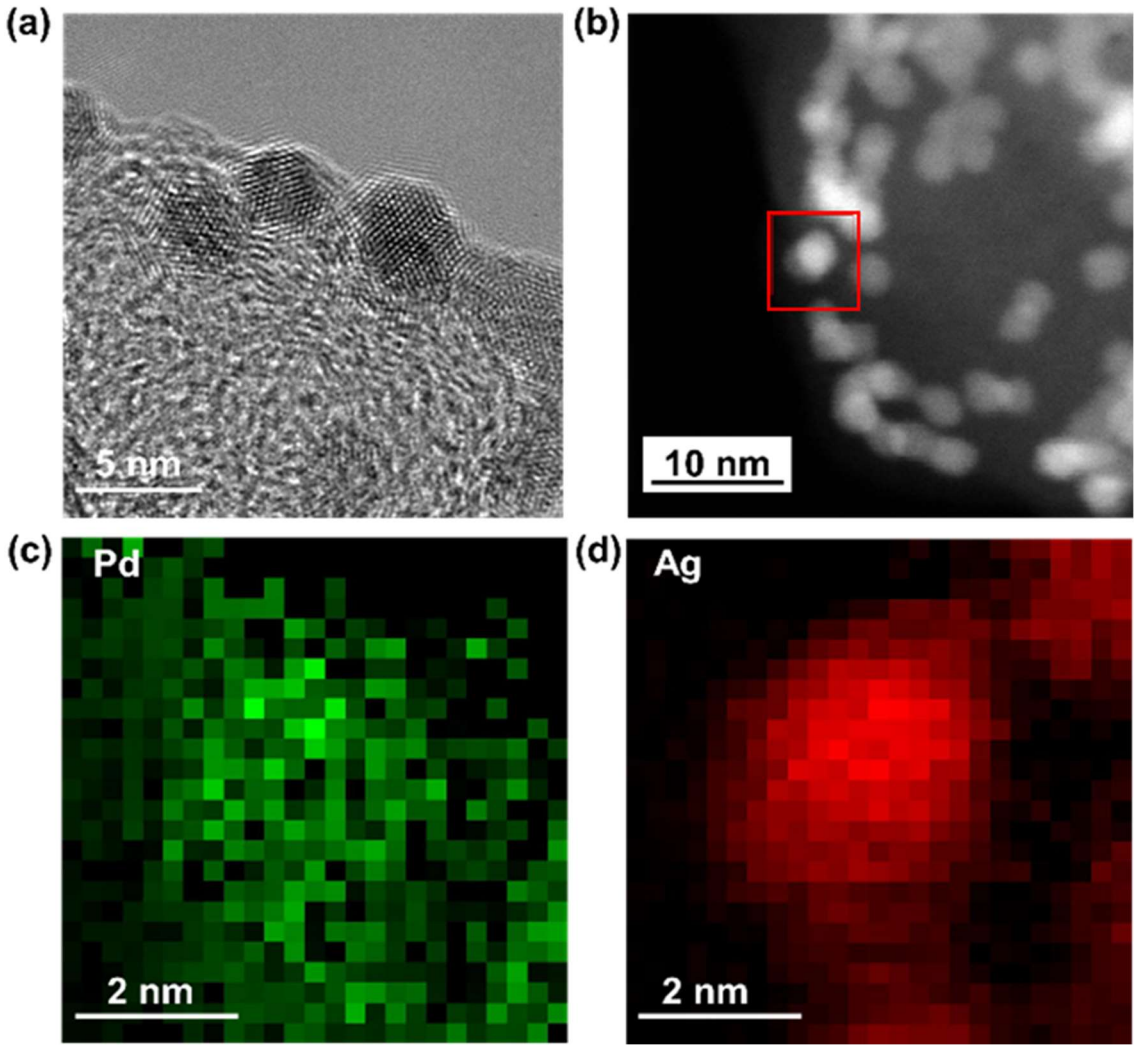

Figure 6.2 (**a**) HRTEM image of C-$Ag_{15}Pd_{85}$. (**b**) HAADF-STEM image and (**c, d**) corresponding 2D EELS elemental mappings of C-$Ag_{15}Pd_{85}$. The red box in b indicates the area of EELS elemental mappings

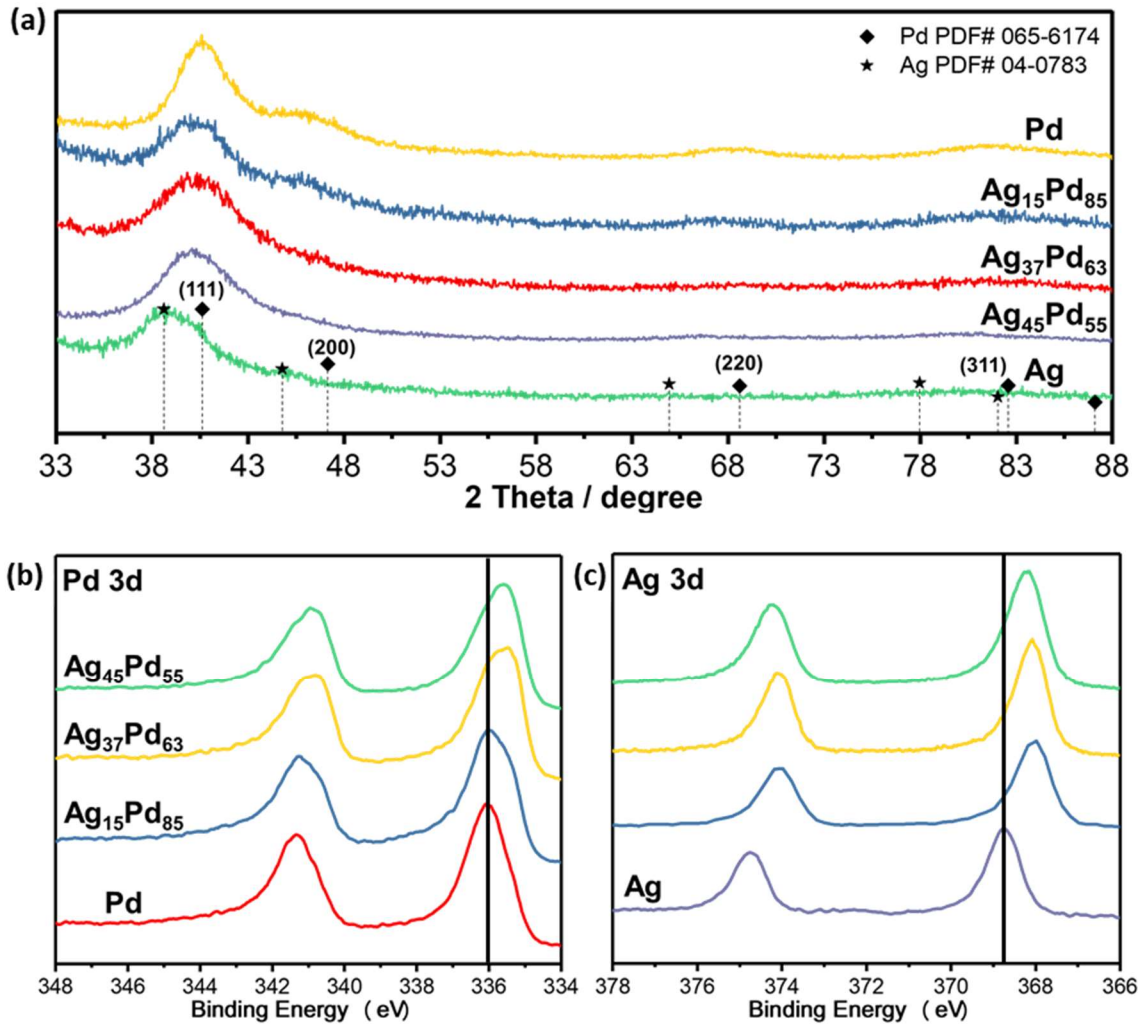

Figure 6.3 (**a**) XRD patterns for Ag, Pd, and AgPd NPs show a gradual shift in the (111) peak from Ag to Pd as expected for random alloys. (**b**) High resolution Pd 3d and (**c**) high resolution Ag 3d XPS spectra both show a shift to lower binding energies as expected of AgPd alloys.

6.2.2 Electrocatalytic CO_2 Reduction Reaction by AgPd Nanoparticles

CO_2RR over the C-AgPd, C-Pd and C-Ag catalysts were systematically investigated using chronoamperometry in the potential range of -0.6 V_{RHE} to -1.0 V_{RHE}. The gas-phase products were simultaneously measured by an on-line GC, while the liquid phase product information was obtained by analysing the catholyte with HPLC after the catalysis. It was found that, after two hours of catalysis, both Pd and AgPd NPs structures were well-maintained on the carbon support. However, the NPs agglomeration and size increase were observed on C-Ag after testing, which may be caused by the surface redox reactivity of ultrasmall Ag NPs. Such a redox-induced small NP coalescence during CO_2RR were also found in the previous studies of Bi[20], Cu[26] and Pb-based nanocatalysts.[27]

The CO_2RR catalytic performances of C-AgPd with different bimetallic compositions, along with that of C-Pd and C-Ag, are summarized in **Figure 6.4**. CO is found as the primary product on all catalysts at these potentials, although the FE_{CO} for each catalyst present a maximum at different potentials (**Figure 6.4 A**). H_2 is the other observed product from the hydrogen evolution reaction and balances the FE to approximately 100%. On C-Pd, the maximum FE_{CO} of 83.9 ± 5.9% is obtained at -0.7 V_{RHE}, which is superior to the Pd electrode (<30%)[28] and is comparable to reported 3.7 nm Pd NPs (91.2%).[29] With lower overpotentials, the FE_{CO} on C-Pd drops to 42.0 ± 3.8%. At more positive potentials (-0.4 to -0.5 V), liquid-phase formic acid is detected as the primary product without the formation of CO; however, these conditions lead to extremely low current densities.[30] CO is not observed until higher overpotentials, but the FE_{CO} due to limited CO_2 solubility, mass transport issues, and the increased HER rate.[31, 32] Opposed to Pd, the C-Ag catalyst

consistently exhibits a low FE_{CO} (<35%), unless potentials as negative as -0.9 V_{RHE} is applied. This behavior is ascribed to the weak CO adsorption energy on Ag that makes CO_2 activation challenging by reducing the thermodynamic drive towards product formation.

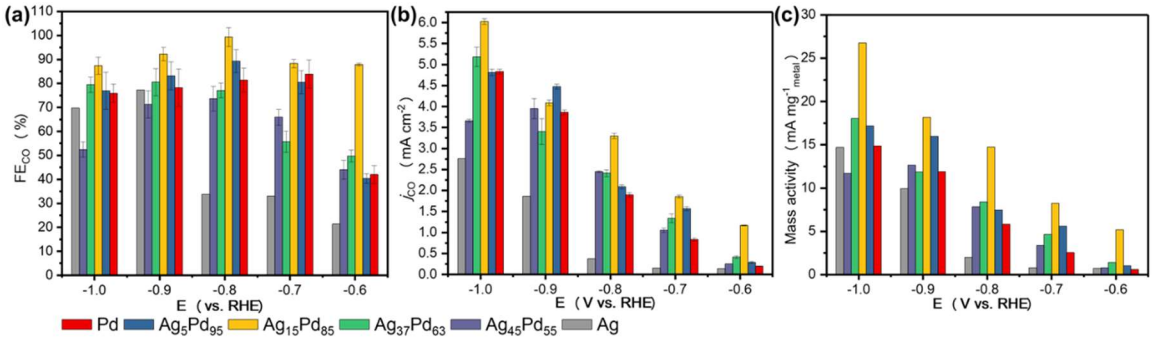

Figure 6.4 The evaluation of eCO2 RR performance of C-AgPd, C-Pd, and C-Ag catalysts: (**a**) Faradic efficiency of CO (FE_{CO}); the remaining balance to 100% is comprised of H_2 from the hydrogen evolution reaction, (**b**) CO partial current density (j_{CO}); and (**c**) mass activity at -0.6 to -1.0 V_{RHE}.

The FE_{CO} is substantially improved on C-AgPd NPs catalysts compared with monometallic counterparts, and more interestingly, it presents a volcano-like behavior associated with its bimetallic composition (**Figure 6.4 A**). The $Ag_{15}Pd_{85}$ exhibits the highest FE_{CO} across all studied potentials. At -0.8 V_{RHE} and -0.9 V_{RHE}, the FE_{CO} on C-$Ag_{15}Pd_{85}$ reaches 100.0 ± 4.0% and 92.3 ± 2.8% respectively. Even at a low overpotential of -0.6 V_{RHE}, the FE_{CO} still maintains at 88.0 ± 0.5%, which is 1.2 and 3.3 times higher than that of C-Pd and C-Ag, respectively.

CO partial current density (j_{CO}) directly reports on the CO production rate. As shown in **Figure 6.4 B**, all catalysts show an increased CO partial current density at higher overpotentials. The C-Pd also shows a low CO production rate at low overpotentials (~ 0.2 mA cm^{-2} at -0.6 V_{RHE}), which increases to ~ 3.9 mA cm^{-2} at -0.9 V_{RHE} and ~ 4.8 mA cm^{-2} at -1.0 V_{RHE}. The j_{CO} is drastically increased on C-AgPd catalysts. For C-$Ag_{15}Pd_{85}$, j_{CO} reaches 3.3 mA cm^{-2} at -0.8 V_{RHE}, leading to an enhancement factor of 1.8 and 8.9 compared with C-Pd and C-Ag.

The current from CO production was further normalized to the total metal mass loading of the catalyst on the electrode to yield mass activity. This is a reasonable metric for catalyst amount due to the similarity in molar masses of Ag and Pd. Again, it was found that the bimetallic catalysts clearly enhance the CO_2RR activity. Especially on C-$Ag_{15}Pd_{85}$, the mass activity reaches 15.2 mA mg^{-1} at -0.8 V_{RHE}, indicating a 2.5- and 3.7-time enhancement over C-Pd and C-Ag, respectively. By all metrics, C-$Ag_{15}Pd_{85}$ is the best performing catalyst for CO_2RR in the present study, exhibiting the highest FE_{CO} and mass activity.

The catalytic stability of C-AgPd NPs were evaluated under chronoamperometry at -0.8 V_{RHE} for up to 12 hours. As illustrated in Figure 6.5 A, the FE_{CO} on the C-$Ag_{15}Pd_{85}$ is highly stable during the stability testing with the minor fluctuations in the range of 95-100%. After the 12-hour test, the morphology of $Ag_{15}Pd_{85}$ NPs was re-examined under TEM. While most of the NP structures are well-preserved, some aggregations are seen in certain areas on the support, and correspondingly, the mass activity decreases by 12.4 % (from 15.2 mA mg^{-1} to 13.3 mA mg^{-1}) after the 12-hour CO_2RR. In comparison, the C-Pd catalyst shows a mass activity decay of 38.1% (from 7.0 mA mg^{-1} to 4.3 mA mg^{-1}) under the same condition (Figure 6.5 B), which is likely resulted from the accumulation of CO over Pd sites,[40] suggesting that bimetallic AgPd NPs catalysts are more durable for long-term CO_2RR.

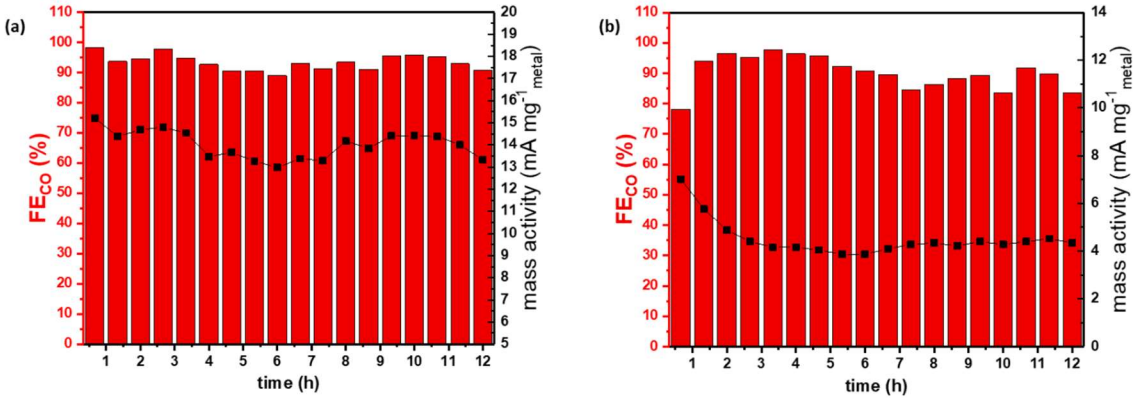

Figure 6.5 FE_{CO} and mass activity evolution of (**a**) C-$Ag_{15}Pd_{85}$ and (**b**) C-Pd over a 12 hour stability test at -0.8 V_{RHE} shows that $Ag_{15}Pd_{85}$ is superior in terms of catalyst stability to Pd alone.

6.2.3 Deconvoluting Ligand and Ensemble Effects: DRIFTS and DFT

Incorporating Ag into the AgPd alloy NPs is expected to alleviate the CO-poisoning issue on Pd by weakening CO adsorption. Two effects that contribute to this weakening are the ensemble and ligand effects.[33, 34] The ligand effect describes the change in chemical properties through means such as electron transfer. It was already observed from XPS measurements for the alloy catalysts that there are some chemical state changes reducing the overall core electron binding energy in both Ag and Pd. The ensemble effect describes changes in adsorption through changes in the geometric configurations of ensembles of atoms on the surface. Using CO as a probe molecule in DRIFTS experiments and DFT calculations, the contribution of ensemble effects is illuminated.

DRIFTS was used to reveal information about the CO binding configuration and strength with Pd surface atoms. To obtain an optimized IR quality, the AgPd NPs and Pd NPs were loaded onto alumina (Al_2O_3) instead of carbon black (1 wt% metal loading), which would reduce the IR signal substantially. The Ag NPs are not included here since CO adsorption was not observed under ambient conditions. The obtained peak positions and their spectroscopic assignments are listed in **Table 6.2**. The stretching frequency of CO on Pd NPs results in several peaks: one broad peak between 1820 and 1950 cm^{-1} is a convolution of multi-center bound *CO on threefold hollow and bridge sites, while the linear *CO on atop site gives rise to a band around 2076 cm^{-1}.[35, 36]

Table 6.2 Peak position of CO_{ads} over Pd and AgPd NPs in DRIFTS spectra at room temperature.

Sample	CO stretch mode cm^{-1}	
	CO_{atop}	CO_{multi}
Pd	2078.6	1945.8
$Ag_{45}Pd_{55}$	2024.9	1917.7
$Ag_{37}Pd_{63}$	2032.2	1914.5
$Ag_{15}Pd_{85}$	2054.8	1908.3

A series of IR spectra on three AgPd samples with different compositions were collected under the same conditions (**Figure 6.6 A**). It is clearly seen that the relative intensities of different *CO species change dramatically with the Ag content. The concentration of multi-center bound *CO shows a clear-cut and significant drop on $Ag_{15}Pd_{85}$. The drop becomes more intense on other two samples with the higher Ag content, while the linear *CO dominates the surface of $Ag_{45}Pd_{55}$ NPs. The multi-center bound *CO intensity decrease is ascribed to the dilution effect of Ag, in which Ag, even at low concentration (15%), can effectively disrupt the Pd ensembles in the surface of NPs. Additionally, the peak positions shift with the Ag concentration. As more Pd atoms diluted by Ag are present in the surface, CO dipole coupling between adjacent sites is extenuated, shifting the atop CO peaks to the lower wavenumber.[37-39,] Such Ag-dilution caused CO peak shifting was also reported in other studies.[38, 40] In the case of the multi-centered bound sites, the removal of the lowest frequency hollow site species with increased Ag combined with the convolution of the bridge and hollow bound sites results in an apparent increase of frequency with Ag content.

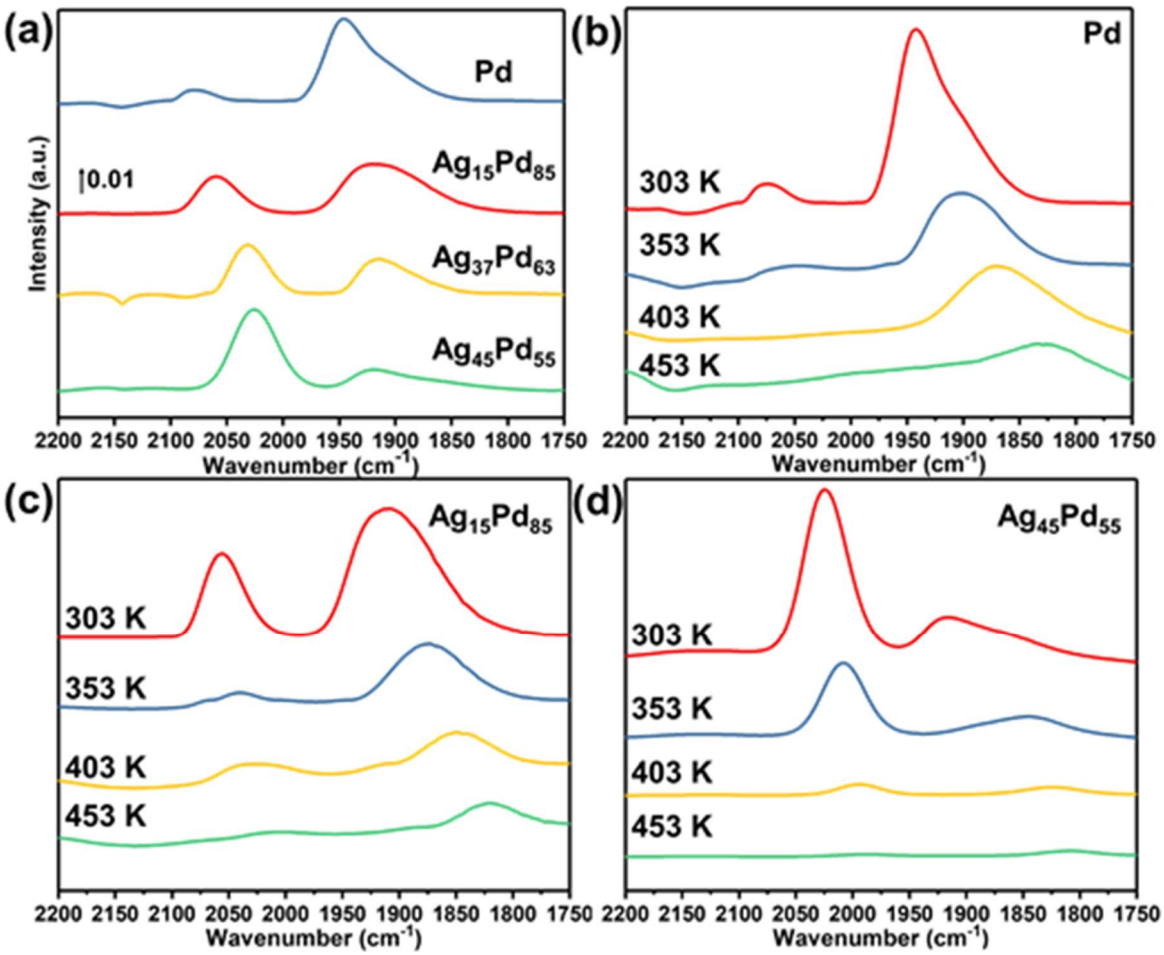

Figure 6.6 (**a**) DRIFTS spectra of alumina supported Pd and Pd Alloy catalysts following saturation with CO at room temperature. (**b-d**) TPD DRIFTS spectra of alumina supported (**b**) Pd, (**c**) $Ag_{15}Pd_{85}$, (**d**) $Ag_{45}Pd_{55}$ at in an Ar atmosphere from 303 K to 453 K at a rate of 5 K/min following the room temperature saturation of CO.

The CO binding strength on these NPs was probed by flushing CO-saturated samples with Ar under a series of temperatures and monitoring the CO-desorption process. The temperature-programmed desorption (TPD) DRIFTS results are shown in **Figure 6.6 B-D**. On both Pd and AgPd NPs, the linear CO_{ad} fully desorbs at a lower temperature than the energetically more stable multi-center bound *CO. Based on these, *CO binds significantly stronger at the multi-centered Pd sites. Furthermore, alloying Pd with Ag disrupts Pd surface ensembles, diminishing the multi-centered *CO adsorption in AgPd NPs surfaces in favor of weakly bound atop CO.

DFT calculations were performed to gain a deeper understanding of the impact that Ag-Pd alloying has on CO adsorption strength, an important parameter dictating the CO_2 reduction activity.[7] Ag_xPd_{100-x} (111) surfaces (x = 0, 12.5, 25, 50, 75, and 100) were used for the CO binding energy ($E_{b,CO}$) calculations, as shown in **Figure 6.7 A-D**. For Ag-rich slab models, surface atoms were rearranged to generate Pd bridge and hollow sites (**Figure 6.7 B-D**). As is shown for Pd (**Figure 6.7 E,** Ag% = 0), CO was found to most favorably bind in the hollow sites ($E_{b,CO}$ = -1.92 eV at *hcp* site and -1.91 eV at *fcc* site) and least favorably bind on atop sites ($E_{b,CO}$ = -1.38 eV). Upon the introduction of Ag, $E_{b,CO}$ decreases for each Pd binding site. Due to the weak CO binding nature of Ag, mixed AgPd sites are less important, as $E_{b,CO}$ at these sites are lower than those of the adjacent Pd only sites.

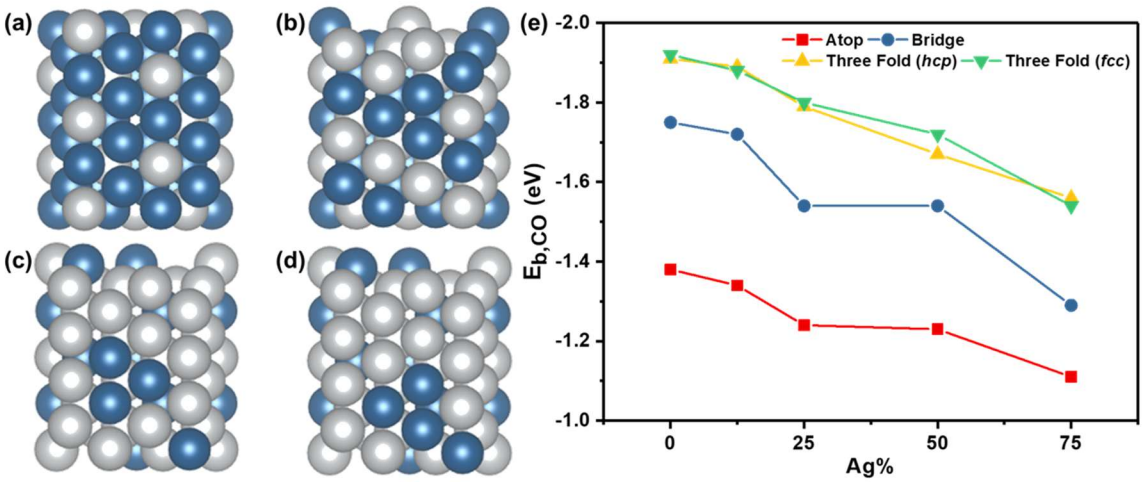

Figure 6.7 Calculated surface slabs of (**a**) $Ag_{25}Pd_{75}$(111), (**b**) $Ag_{50}Pd_{50}$(111) with surface atoms rearranged to generate bridge and three-fold hollow Pd sites, (c,d) $Ag_{75}Pd_{25}$ (111) with (**c**) bridge and hcp Pd three-fold hollow sites, and (**d**) with bridge and fcc Pd three-fold hollow sites. The silver atoms represent Ag and blue atoms represent Pd. (**e**) CO adsorption energies $E_{b.CO}$ at the different Pd sites calculated for AgPd alloys of varying Ag concentrations (Ag%). In general, the binding energy decreases with increasing Ag concentration and with fewer participating Pd atoms.

The initial weakening of $E_{b,CO}$ conflicts with the calculated d-band centers that rise with addition of Ag up to 50% (**Figure 6.8 A**). A contradiction is also seen by comparing $E_{b,CO}$ from the AgPd alloys to that of strained Pd (**Figure 6.8 B**). The tensile strain introduced by Ag and experienced by the Pd would ordinarily strengthen $E_{b,CO}$ over these sites; however, that is clearly not the case observed in any of the AgPd NPs. These inconsistencies have previously been discussed by Abild-Pedersen et al.[41] and are due to an asymmetry in the Pd d-band formed from an energy misalignment with the Ag d orbitals. They adopt an alternative descriptor, ε_u, defined as the highest peak position of the surface atom d-band Hilbert transform. This descriptor better correlates to the antibonding orbital of the absorbate as described in the Newns-Anderson binding model.[42-44] In performing this analysis for our calculations (**Figure 6.8 C**), we find excellent agreement with the trends predicted by this model and resolve the issues (**Figure 6.8 D**). Up to 50% doping, ε_u decreases by 0.4 eV and binding energies average a 0.18 eV reduction. Between 50% and 75% doping, however, there is a much greater decrease in ε_u of 0.75 eV and the binding energies are reduced another 0.17 eV.

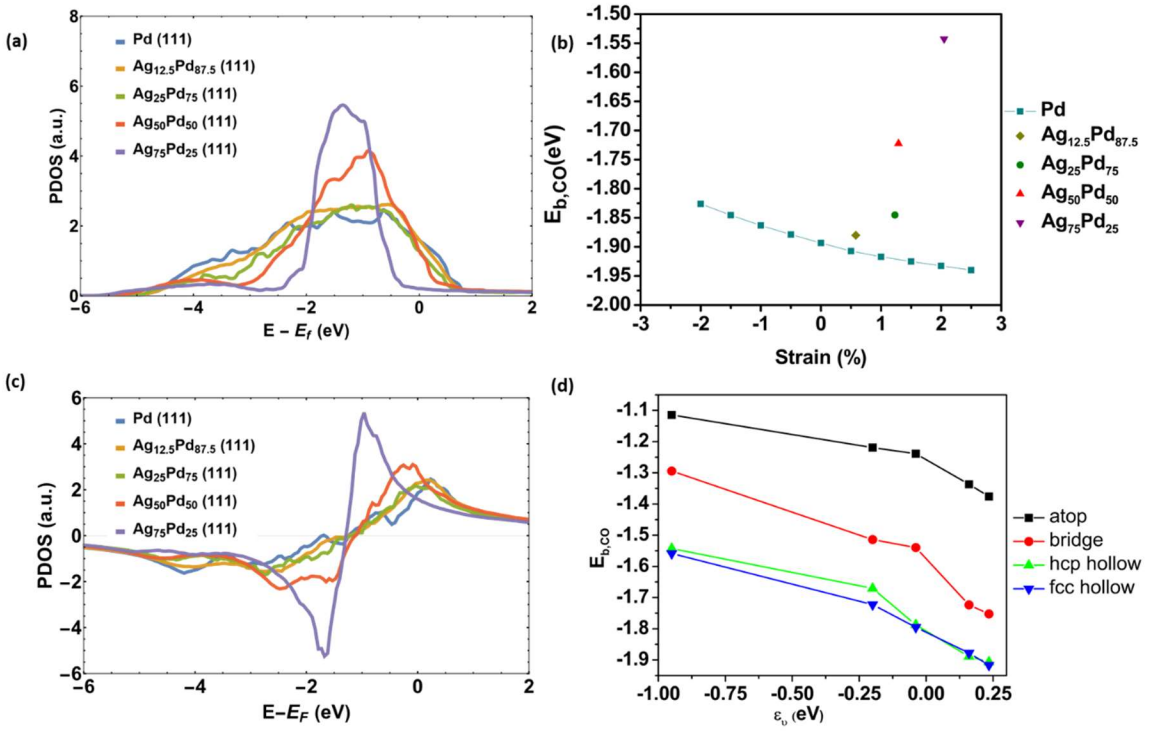

Figure 6.8 (**a**) Calculated d-orbital partial density of states (PDOS) of Pd and AgPd alloy surfaces. The calculated d-band centers are -1.67 eV, -1.57 eV, 1.53 eV, -1.39 eV, and -1.51 eV for Pd, $Ag_{12.5}Pd_{87.5}$, $Ag_{50}Pd_{50}$, and $Ag_{75}Pd_{25}$ respectively. (**b**) Calculated binding energy of CO in the fcc hollow site as a function of strain on the Pd (111) surface was calculated from -2 to 2.5%. The calculated strain of the 3-fold Pd ensembles for the relaxed alloys structures was recorded and the binding energy was compared against that of the pure Pd system. In this type of analysis, points that vary from the artificially strained calculations have contributions from the ligand effect while points falling along the line have contributions solely from the strain. (**c**) Hilbert transform of the Pd d-PDOS. The energy at which the max of this plot occurs correlates with binding energy in that the further below the Fermi energy it is, the lower in energy the antibonding orbital is, and the weaker the binding energy is. (**d**) CO binding energy ($E_{b,CO}$) shown as a function of ε_u. As expected by the Newns-Anderson theory of binding, binding energy is reduced as ε_u falls.

The weakening of $E_{b,CO}$ is important to improving the CO_2 reduction activity since Pd ordinarily binds CO too strongly. We can summarize these calculations by describing two ways in which Ag reduces $E_{b,CO}$. First, there is a strong ligand effect that is introduced by Ag. This results in the large perturbations to the Pd d-band shape that, despite raising the d-band center, lowers the adsorbate anti-bonding orbital to weaken binding. The second means, the ensemble effect, is by reducing the number of multi-center Pd adsorption sites on the surface. Relative to the ligand effect, the ensemble effect generates much greater reductions in $E_{b,CO}$ at lower Ag concentrations. This is critical because Ag is not important for the activation of CO_2 until high overpotentials, and only Pd sites matter for this step. This ensemble effect is the primary source of the observed volcano relationship. Just enough Ag (15%) is needed to break up multi-centered hollow sites, providing balanced surface energetics for CO_2 activation as well as CO desorption. Further addition of Ag reverses this balance and lowers overall activity due to the barrier of CO_2 activation.

6.3 Summary

In summary, monodisperse AgPd alloy NPs with tunable bimetallic compositions and investigated their catalytic property for CO_2 RR were synthesized. It was found that the catalytic performance for the CO production was enhanced and controlled by the bimetallic composition of NPs, with the $Ag_{15}Pd_{85}$ demonstrating the best performance with high activity, selectivity, and durability at low overpotentials. At -0.8 V_{RHE}, the FE_{CO} reached greater than 95% with a mass activity of 15.2 mA mg_{metal}^{-1}. The DFT calculations and DRIFTS measurements elucidated that alloying with Ag alleviated the over-strong

adsorption of CO over Pd, accelerating eCO_2 RR to CO kinetics. This modulation was found to be caused by two effects, i.e., Ag weakens the CO adsorption at all possible Pd sites via the ligand effect and diminishes the population of the strongest CO-binding sites, multi-centered hollow sites in favor of weaker binding atop sites via the ensemble effect.

6.4 Experimental

Chemicals and Materials

Palladium(II) acetylacetonate ($Pd(acac)_2$, >99%), Silver(I) acetate (Ag(ac), 99%), oleic acid (OAc, 90%), olyelamine (OAm, 70%), Nafion (5 wt% in lower aliphatic alcohols and water) were purchased from Sigma-Aldrich. 1-Octadecene (ODE, 90%) was purchased from Acros Organics. Hydrazine monohydrate (>99%) was purchased from Alfa Aesar. Isopropanol (99.5%) and hexanes (98.5%) were purchased from Fisher Scientific. Vulcan-XC 72R carbon black was obtained from Fuel Cell Store. All chemicals and materials were used as received without further purification.

Synthesis of AgPd, Ag, and Pd NPs

All AgPd NPs with different bimetallic compositions were synthesized via an organic-phase colloidal approach, according to a previous report.[17] In a typical synthesis of $Ag_{15}Pd_{85}$ NPs, 244 mg of $Pd(acac)_2$ (0.8 mmol) and 34 mg of Ag(ac) (0.2 mmol) were mixed together with 4.5 ml of OAc, 0.5 ml of OAm, and 10 ml of ODE. The mixture was kept at 60 °C under N_2 atmosphere for 30 minutes to generate a transparent, dark orange solution. It was heated to 180 °C at a ramp rate of 3-5 °C min^{-1} and was then kept at that temperature for 20 minutes. After cooling down to the room temperature, the NPs were

collected by centrifugation at 8000 rpm after the addition of 45 ml of isopropanol. Then, the NPs were purified twice by centrifugation in 5 ml of hexane and 40 ml of isopropanol. The as-synthesized NPs were re-dispersed and stored in hexanes. Following the same procedure, Ag_5Pd_{95}, $Ag_{37}Pd_{63}$ and $Ag_{45}Pd_{55}$ NPs were synthesized by using 274 mg (0.9 mmol) of $Pd(acac)_2$ together with 16.7 mg (0.1mmol) of Ag(ac), 183 mg (0.6 mmol) of $Pd(acac)_2$ together with 67 mg (0.4 mmol) of Ag(ac), and 152 mg (0.5 mmol) of $Pd(acac)_2$ together with 84 mg (0.5 mmol) of Ag(ac), respectively.

For the control experiment, Ag NPs were prepared with 167 mg of Ag(ac) as the sole metal precursor following the same synthetic strategy of AgPd. We also obtained Pd NPs with the similar size according to an established method.[45] 100 mg of $Pd(acac)_2$ was dissolved in 12 ml of OAm under magnetic stirring. After degassing the solution at 60 °C for 30 minutes to remove the moisture and impurities, 200 mg of TBAB that was pre-dissolved in 3 ml of OAm was injected into the reaction system. The solution was reacted for 30 minutes before cooling to room temperature. The Pd NPs were collected and purified following the same procedure of AgPd NPs as detailed above.

Preparation of carbon supported NPs (C-NPs) catalysts

200 mg of carbon black (Vulcan XC 72R) was dispersed in 10 ml of hexanes by sonication for 15 min. 50 mg of the as-prepared NPs (dispersed in hexanes) was then added dropwise into the carbon black suspension and sonicated for 1 hour. The supported NPs were then collected by centrifugation, washed with ethanol, and dried in a vacuum oven overnight. To remove OAc and OAm surfactants attached to the NPs

surface, the catalyst was stirred in 10% v/v hydrazine/ethanol solution overnight, and then washed three times by centrifugation (5000 rpm, 5 minutes) with the addition of 20 ml of ethanol. The catalyst was dried under vacuum before its use.

Characterizations

Transmission electron microscopy (TEM) images were obtained on a FEI Tecnai Spirit (120 kV). High resolution TEM (HRTEM) images were obtained on a FEI Titan 80-300 (300 kV). Scanning TEM (STEM) analyses were carried out using a Hitachi HD2700C (200 kV) equipped with a probe aberration-corrector and an electron energy loss spectroscopy (EELS) detector in the Center for Functional Nanomaterials at Brookhaven National Laboratory. The 2D EELS elemental mappings were collected using a high resolution Gatan-Enfina ER with a probe size of 1.3 Å. A power law function was used for EELS background subtraction. Inductively coupled plasma optical emission spectrometry (ICP-OES) analyses were conducted on a PerkinElmer Avio-200 ICP Optical Emission Spectrometer to determine the compositions of AgPd NPs and the metal loading on the C-NPs catalysts. X-ray diffraction (XRD) characterizations were carried out on an Empyrean Multipurpose X-Ray Diffractometer with Cu Kα radiation (λ = 1.5418 Å). X-ray photoelectron spectroscopy (XPS) was carried out using a PHI VersaProb III to identify the surface composition and electronic structure of the catalysts. Diffuse reflectance infrared Fourier-transform spectroscopy (DRIFTS) was carried out to measure the adsorbed CO profiles using a Nicolet iS 50 FT-IR (Thermo Scientific, USA) equipped with a DiffusIRTM diffuse reflectance cell (Pike Technologies). After the sample was loaded into cell, it was first purged with Ar (50 sccm) at room temperature for 1 hour, and the background was

collected. Then CO (1% balanced in Ar) was introduced into the chamber and purged (25 sccm) for another 1 hour until the sample was completely saturated. The CO desorption behavior was studied by flushing the sample with Ar (25 sccm) again at designed temperature 303 K, 353 K, 403 K and 453 K. The ramping rate is 5 °C min^{-1}.

Electrocatalytic Analysis

The eCO_2RR was investigated in 0.1 M $KHCO_3$ electrolyte solution, using an Autolab Potentiostat (PGSTAT128N, Metrohm AG, Switzerland), a glassy carbon working electrode (5 mm in diameter), a Ag/AgCl electrode reference electrode, and a Pt gauze counter electrode. All potentials were reported vs. reversible hydrogen electrode (RHE) using the following the equation:

$$E(\text{vs. RHE}) = E(\text{vs. Ag/AgCl}) + 0.197 + 0.0591 \times pH \quad \text{Eq. (6. 1)}$$

To prepare the working electrode, 2 mg of the catalyst (~20 wt%) was first sonicated in 200 µl isopropanol and 5.1 µl of Nafion® (5 wt%) for 1 hour to form a uniform ink. An appropriate amount of the ink was then dropcast onto a pre-polished glassy carbon electrode to yield a loading of 250 µg of carbon supported catalysts. The real metal loading on the electrode was subsequently calculated based on this number and the metal concentrations determined by ICP-OES analysis (**Table 6.1**). The electrocatalysis was performed in a gas-tight H-type cell with a Nafion™-212 membrane assembled between the cathode and anode compartments. Each chamber was filled with 12 ml of 0.1 M $KHCO_3$ electrolyte. Cyclic voltammetry (CV) was performed in a CO_2-saturated 0.1 M $KHCO_3$ electrolyte at 20 mV s^{-1} to activate the catalysts. To assess the product

distribution, controlled potential electrolyses (CPE) were performed at selected potentials. During the electrolysis, CO_2 was steadily supplied to the cathode compartment at a rate of 10 sccm, and the gas phase effluent in the headspace of the cathode compartment was continuously introduced to the sampling loop of a Shimadzu gas chromatograph (GC2014). The gaseous product stream was analysed by a thermal conductivity detector (TCD) and a flame ionization detector (FID) equipped with a methanizer, using argon as the carrier gas. The liquid phase products were analysed using a Shimadzu high-performance liquid chromatograph (HPLC) equipped with a Bio-rad Aminex HPX-87H column, a photodiode array detector (PDA), and a reflective index detector (RID), using a 5 mM H_2SO_4 mobile phase.

DFT Calculations

Density functional theory (DFT) calculations were performed using the Vienna ab initio simulation package (VASP)[24] with the projector augmented wave (PAW) pseudopotentials[46] and the revised Perdew-Burke-Ernzerhof (RPBE) exchange correlation functional.[47] An energy cutoff of 450 eV was used for the plane wave basis set. The energy convergence criterion was 10^{-6} eV for geometry optimizations.

All adsorption energy calculations were performed on the (111) surface of the Ag, Pd, and AgPd alloy systems. The surface was modelled by a (1x2) supercell comprised of 4 layers and 15 Å of vacuum. The bottom layer was frozen to the bulk parameter while the top 3 layers were allowed to fully relax. A 3 x 3 x 1 Monkhorst – Pack k – point mesh[48] was the chosen sampling scheme. The binding energy between CO and the surface was

sampled at atop, bridge, *hcp* three-fold hollow, and *fcc* three-fold hollow sites on the pure metals and alloys and is given by the equation.

$$E_{Ads,CO} = E(CO + slab) - E(Slab) - E(CO) \quad \text{Eq. (6. 2)}$$

The CO coverage is held at θ = 1/16. The Ag concentration was varied from 0 to 100% in 12.5% (to 25%) and then 25% intervals. Lattice parameters for each pure metal and the alloys were calculated to be 3.98 Å, 4.04 Å, 4.10 Å, 4.14 Å, and 4.22 Å from Pd to Ag, comparing favorably with previous work after accounting for the slight increase expected with the use of the RPBE functional.[47, 49]. Since the Pd three-fold hollow sites do not exist in the $Ag_{50}Pd_{50}$ and $Ag_{75}Pd_{25}$ (111) slab model surfaces, we generate the three-fold Pd ensembles by rearranging the surface atoms but keeping the chemical composition fixed on the surface (**Figure 6.7 A-D**). These generated structures were fully relaxed and served as the reference for the relevant binding energy calculations.

6.5 References

1. Whipple, D. T.; Kenis, P. J. A., Prospects of CO_2 Utilization via Direct Heterogeneous Electrochemical Reduction. *J. Phys. Chem. Lett.* **2010,** *1* (24), 3451-3458.

2. Centi, G.; Perathoner, S., Opportunities and prospects in the chemical recycling of carbon dioxide to fuels. *Catal. Today* **2009,** *148* (3-4), 191-205.

3. Aresta, M.; Dibenedetto, A.; Angelini, A., Catalysis for the valorization of exhaust carbon: from CO_2 to chemicals, materials, and fuels. technological use of CO_2. *Chem. Rev.* **2014,** *114* (3), 1709-42.

4. Kibria, M. G.; Edwards, J. P.; Gabardo, C. M.; Dinh, C. T.; Seifitokaldani, A.; Sinton, D.; Sargent, E. H., Electrochemical CO_2 Reduction into Chemical Feedstocks: From Mechanistic Electrocatalysis Models to System Design. *Adv. Mater.* **2019,** *31* (31), e1807166.

5. Chaplin, R. P. S.; Wragg, A. A., Effects of process conditions and electrode material on reaction pathways for carbon dioxide electroreduction with particular reference to formate formation. *J. Appl. Electrochem.* **2003,** *33* (12), 1107-1123.

6. Schneider, J.; Jia, H.; Muckerman, J. T.; Fujita, E., Thermodynamics and kinetics of CO_2, CO, and H+ binding to the metal centre of CO_2 reduction catalysts. *Chem. Soc. Rev.* **2012,** *41* (6), 2036-51.

7. Peterson, A. A.; Norskov, J. K., Activity Descriptors for CO_2 Electroreduction to Methane on Transition-Metal Catalysts. *J. Phys. Chem. Lett.* **2012,** *3* (2), 251-258.

8. Peng, Y. Y.; Cui, M. Y.; Zhang, Z. Y.; Shu, S.; Shi, X. L.; Brosnahan, J. T.; Liu, C.; Zhang, Y. L.; Godbold, P.; Zhang, X. M.; Dong, F.; Jiang, G. M.; Zhang, S., Bimetallic Composition-Promoted Electrocatalytic Hydrodechlorination Reaction on Silver-Palladium Alloy Nanoparticles. *ACS Catal.* **2019,** *9* (12), 10803-10811.

9. Burrows, M. G. T.; Stockmayer, W. H.; Chapman, D. L., The Poisoning of a Palladium Catalyst by Carbon Monoxide. *Proc. R. Soc. Lond. A Math Phys. Sci.* **1940,** *176* (967), 474-483.

10. Gao, D. F.; Zhou, H.; Cai, F.; Wang, J. G.; Wang, G. X.; Bao, X. H., Pd-Containing Nanostructures for Electrochemical CO_2 Reduction Reaction. *ACS Catal.* **2018,** *8* (2), 1510-1519.

11. Gao, D.; Zhou, H.; Wang, J.; Miao, S.; Yang, F.; Wang, G.; Wang, J.; Bao, X., Size-dependent electrocatalytic reduction of CO_2 over Pd nanoparticles. *J. Am. Chem. Soc.* **2015,** *137* (13), 4288-91.

12. Dong, H.; Zhang, L.; Yang, P. P.; Chang, X. X.; Zhu, W. J.; Ren, X. H.; Zhao, Z. J.; Gong, J. L., Facet design promotes electroreduction of carbon dioxide to carbon monoxide on palladium nanocrystals. *Chemical Engineering Science* **2019,** *194*, 29-35.

13. Yin, Z.; Gao, D. F.; Yao, S. Y.; Zhao, B.; Cai, F.; Lin, L. L.; Tang, P.; Zhai, P.; Wang, G. X.; Ma, D.; Bao, X. H., Highly selective palladium-copper bimetallic electrocatalysts for the electrochemical reduction of CO_2 to CO. *Nano Energy* **2016,** *27*, 35-43.

14. Lee, J. H.; Kattel, S.; Jiang, Z.; Xie, Z.; Yao, S.; Tackett, B. M.; Xu, W.; Marinkovic, N. S.; Chen, J. G., Tuning the Activity and Selectivity of Electroreduction of CO_2 to Synthesis Gas using Bimetallic Catalysts. *Nat. Commun.* **2019,** *10* (1), 1-8.

15. Bai, X.; Chen, W.; Zhao, C.; Li, S.; Song, Y.; Ge, R.; Wei, W.; Sun, Y., Exclusive Formation of Formic Acid from CO_2 Electroreduction by a Tunable Pd-Sn Alloy. *Angew. Chem., Int. Ed.* **2017,** *56* (40), 12219-12223.

16. Wang, Y.; Cao, L.; Libretto, N. J.; Li, X.; Li, C.; Wan, Y.; He, C.; Lee, J.; Gregg, J.; Zong, H.; Su, D.; Miller, J. T.; Mueller, T.; Wang, C., Ensemble Effect in Bimetallic Electrocatalysts for CO_2 Reduction. *J. Am. Chem. Soc.* **2019,** *141* (42), 16635-16642.

17. Zhang, S.; Metin, O.; Su, D.; Sun, S., Monodisperse AgPd alloy nanoparticles and their superior catalysis for the dehydrogenation of formic acid. *Angew Chem Int Ed Engl* **2013,** *52* (13), 3681-4.

18. Zhang, Z.; Wu, Q.; Johnson, G.; Ye, Y.; Li, X.; Li, N.; Cui, M.; Lee, J. D.; Liu, C.; Zhao, S.; Li, S.; Orlov, A.; Murray, C. B.; Zhang, X.; Gunnoe, T. B.; Su, D.; Zhang, S., Generalized Synthetic Strategy for Transition-Metal-Doped Brookite-Phase TiO_2 Nanorods. *J. Am. Chem. Soc.* **2019,** *141* (42), 16548-16552.

19. Zhang, Y.; Li, N.; Zhang, Z.; Li, S.; Cui, M.; Ma, L.; Zhou, H.; Su, D.; Zhang, S., Programmable Synthesis of Multimetallic Phosphide Nanorods Mediated by Core/Shell Structure Formation and Conversion. *J. Am. Chem. Soc.* **2020,** *142* (18), 8490-8497.

20. Zhang, Z. Y.; Chi, M. F.; Veith, G. M.; Zhang, P. F.; Lutterman, D. A.; Rosenthal, J.; Overbury, S. H.; Dai, S.; Zhu, H. Y., Rational Design of Bi Nanoparticles for Efficient Electrochemical CO_2 Reduction: The Elucidation of Size and Surface Condition Effects. *ACS Catal.* **2016,** *6* (9), 6255-6264.

21. Talapin, D. V.; Murray, C. B., PbSe nanocrystal solids for n- and p-channel thin film field-effect transistors. *Science* **2005,** *310* (5745), 86-9.

22. Zhang, G.; Kirk, B.; Jauregui, L. A.; Yang, H.; Xu, X.; Chen, Y. P.; Wu, Y., Rational Synthesis of Ultrathin n-type Bi_2Te_3 Nanowires with Enhanced Thermoelectric Properties. *Nano Lett.* **2012,** *12* (1), 56-60.

23. Law, M.; Luther, J. M.; Song, Q.; Hughes, B. K.; Perkins, C. L.; Nozik, A. J., Structural, optical, and electrical properties of PbSe nanocrystal solids treated thermally or with simple amines. *J. Am. Chem. Soc.* **2008,** *130* (18), 5974-85.

24. Abrikosov, I. A.; Olovsson, W.; Johansson, B., Valence-band hybridization and core level shifts in random Ag-Pd alloys. *Phys. Rev. Lett.* **2001,** *87* (17), 176403.

25. Olovsson, W.; Abrikosov, I. A.; Johansson, B., Core level shift in random CuPd and AgPd alloys by the complete screening picture. *J. Electron Spectrosc. Relat. Phenom.* **2002,** *127* (1-2), 65-69.

26. Baturina, O.; Lu, Q.; Xu, F.; Purdy, A.; Dyatkin, B.; Sang, X.; Unocic, R.; Brintlinger, T.; Gogotsi, Y., Effect of nanostructured carbon support on copper electrocatalytic activity toward CO_2 electroreduction to hydrocarbon fuels. *Catal. Today* **2017,** *288*, 2-10.

27. Zhang, Z.; Liu, C.; Brosnahan, J. T.; Zhou, H.; Xu, W.; Zhang, S., Revealing structural evolution of PbS nanocrystal catalysts in electrochemical CO_2 reduction using in situ synchrotron radiation X-ray diffraction. *J. Mater. Chem. A* **2019,** *7* (41), 23775-23780.

28. Hori, Y.; Wakebe, H.; Tsukamoto, T.; Koga, O., Electrocatalytic Process of CO Selectivity in Electrochemical Reduction of CO_2 at Metal-Electrodes in Aqueous-Media. *Electrochimica Acta* **1994,** *39* (11-12), 1833-1839.

29. Cai, F.; Gao, D.; Zhou, H.; Wang, G.; He, T.; Gong, H.; Miao, S.; Yang, F.; Wang, J.; Bao, X., Electrochemical promotion of catalysis over Pd nanoparticles for CO_2 reduction. *Chem Sci* **2017,** *8* (4), 2569-2573.

30. Kortlever, R.; Peters, I.; Koper, S.; Koper, M. T. M., Electrochemical CO_2 Reduction to Formic Acid at Low Overpotential and with High Faradaic Efficiency on Carbon-Supported Bimetallic Pd-Pt Nanoparticles. *ACS Catal.* **2015,** *5* (7), 3916-3923.

31. Ooka, H.; Figueiredo, M. C.; Koper, M. T. M., Competition between Hydrogen Evolution and Carbon Dioxide Reduction on Copper Electrodes in Mildly Acidic Media. *Langmuir* **2017,** *33* (37), 9307-9313.

32. Ren, D.; Fong, J.; Yeo, B. S., The effects of currents and potentials on the selectivities of copper toward carbon dioxide electroreduction. *Nat Commun* **2018,** *9* (1), 925.

33. Chen, M.; Kumar, D.; Yi, C. W.; Goodman, D. W., The promotional effect of gold in catalysis by palladium-gold. *Science* **2005,** *310* (5746), 291-3.

34. Liu, P.; Norskov, J. K., Ligand and ensemble effects in adsorption on alloy surfaces. *Phys. Chem. Chem. Phys.* **2001,** *3* (17), 3814-3818.

35. Wolter, K.; Seiferth, O.; Kuhlenbeck, H.; Baumer, M.; Freund, H. J., Infrared spectroscopic investigation of CO adsorbed on Pd aggregates deposited on an alumina model support. *Surf. Sci.* **1998,** *399* (2-3), 190-198.

36. Bertarione, S.; Scarano, D.; Zecchina, A.; Johanek, V.; Hoffmann, J.; Schauermann, S.; Frank, M. M.; Libuda, J.; Rupprechter, G.; Freund, H. J., Surface reactivity of Pd nanoparticles supported on polycrystalline substrates as compared to thin film model catalysts: Infrared study of CO adsorption. *J. Phys. Chem. B* **2004,** *108* (11), 3603-3613.

37. Mink, J.; Keresztury, G.; Szilágyi, T.; Tétényi, P., FT-IR investigation of CO-adsorption on Pd-black and on supported Pd-samples. *Journal of molecular structure* **1993,** *293*, 283-286.

38. Han, Y.; Sun, J.; Fu, H.; Qu, X.; Wan, H.; Xu, Z.; Zheng, S., Highly selective hydrodechlorination of 1,2-dichloroethane to ethylene over Ag-Pd/ZrO_2 catalysts with trace Pd. *Appl. Catal., A* **2016,** *519*, 1-6.

39. Ma, Y.; Diemant, T.; Bansmann, J.; Behm, R. J., The interaction of CO with PdAg/Pd(111) surface alloys--a case study of ensemble effects on a bimetallic surface. *Phys. Chem. Chem. Phys.* **2011,** *13* (22), 10741-54.

40. Ball, M. R.; Rivera-Dones, K. R.; Stangland, E.; Mavrikakis, M.; Dumesic, J. A., Hydrodechlorination of 1,2-dichloroethane on supported AgPd catalysts. *J. Catal.* **2019,** *370*, 241-250.

41. Xin, H. L.; Vojvodic, A.; Voss, J.; Norskov, J. K.; Abild-Pedersen, F., Effects of d-band shape on the surface reactivity of transition-metal alloys. *Phys. Rev. B* **2014,** *89* (11), 115114.

42. Anderson, P. W., Localized Magnetic States in Metals. *Phys. Rev.* **1961,** *124* (1), 41-53.

43. Newns, D. M., Self-Consistent Model of Hydrogen Chemisorption. *Phys. Rev.* **1969,** *178* (3), 1123-1135.

44. Muscat, J. P.; Newns, D. M., Chemisorption on Metals. *Prog. Surf. Sci.* **1978,** *9* (1), 1-43.

45. Mazumder, V.; Sun, S., Oleylamine-mediated synthesis of Pd nanoparticles for catalytic formic acid oxidation. *J. Am. Chem. Soc.* **2009,** *131* (13), 4588-9.

46. Blochl, P. E., Projector augmented-wave method. *Phys. Rev. B.* **1994,** *50* (24), 17953-17979.

47. Hammer, B.; Hansen, L. B.; Norskov, J. K., Improved adsorption energetics within density-functional theory using revised Perdew-Burke-Ernzerhof functionals. *Phys. Rev. B* **1999,** *59* (11), 7413-7421.

48. Monkhorst, H. J.; Pack, J. D., Special Points for Brillouin-Zone Integrations. *Phys. Rev. B* **1976,** *13* (12), 5188-5192.

49. Løvvik, O. M.; Olsen, R. A., Density functional calculations on hydrogen in palladium–silver alloys. *J. Alloys Compd.* **2002,** *330-332*, 332-337.

Chapter 7

Core-Shell Heterostructure Interface in Co_2P/Ir Nanorods and Catalytic Application for the Hydrogen Evolution Reaction

In Chapter 6, alloying Ag into Pd nanoparticles was shown to be an effective way to improve CO_2RR relative to Pd nanoparticles. The combination of DRIFTS and DFT was able to break down the components of the ligand effect and the ensemble effect to explain their contributions to improving this catalytic activity. In this chapter, I turn my attention to interfacial systems with Co_2P/Ir core-shell nanorods (NRs). By tuning the amount of Ir incorporated on Co_2P nanorods, HER in basic conditions is improved relative to commercial IrO and the Co_2P nanorods. The best of these reported catalysts has an overpotential of 48 mV and a current density of 10 mA/cm^2 as well as a mass activity of 179.4 mA/mg$_{Ir}$ at an overpotential of 100 mV. The catalysts were characterized with X-ray absorption spectroscopy (XAS) and XRD demonstrating different Ir species present in the various catalysts, controllable by the amount of Ir introduced to the system. Through DFT, the interaction with H is probed on Ir single atom sites in Co_2P and Co_2P/Ir(111) core/shell interface models. It is shown that Co_2P (100)/Ir(111) interface is particularly important to the improvement of HER in this system and that single atom Ir catalysts are expected to have poor performance for HER.

7.1 Background and Motivation

Ever increasing energy needs along with the environmental impacts of current fossil fuel based sources is rapidly increasing the demand for clean and efficient energy conversion from renewable resources.[1, 2] The electrocatalytic generation of H_2 through water splitting[3, 4] is an excellent technology to achieve this goal for two-fold reasons. First, hydrogen will burn cleanly or can be used directly in fuel cells producing water as a byproduct.[5] Second, at least 2% of the worlds energy is used for extracting H_2 from fossil

fuels for use in processes such as the Haber-Bosch and Fischer-Tropsch processes.[6, 7] To successfully implement water splitting as a technology developments are required to improve the kinetics of HER over materials that minimize dependence on scarce noble metals such as Pt, Ir, or Ru that currently comprise most of the best catalysts for this reaction.[4, 8-10]

A viable strategy to reducing the dependence on noble metals is to improve their atomic utilization efficiencies by increasing the intrinsic activity of the active sites through alloying[11], similar to the previous chapter for CO_2RR,[12] building advanced hollow structures,[13] or through using earth abundant cores with noble metal shells.[14, 15] The structural complexity and varied dimensions of these materials often obscures the fundamentals improving HER impeding their application for further development. For core-shell structures, spherical nanoparticles introduce a myriad of interfaces with varying activities that arise from wide ranges of strain and electronic coupling between layers. Previous work using Co_2P/Pt core/shell NRs reduced the number of interfaces by employing anisotropic NRs consisting of the (001), (010), and (100) facets and coating them in a thin layer of Pt(111).[16] These core/shell NRs improved the cost-effectiveness of the oxygen reduction reaction by reducing the amount of Pt needed and improving the intrinsic activity of the Pt used. The improvement of this activity was directly probed through a series of DFT calculations using the experimentally confirmed interfaces and by using artificially strained Pt models, the individual contributions of the ligand effect, from charge transfer at the interface, and the strain effect, from compressing or stretching the overlayer of Pt were determined.

In this contribution, the synthetic strategy applied for Co_2P/Pt core shell NRs was extended to Co_2P/Ir NRs with controllable dimensions and Ir composition. By tuning the Ir composition, these NRs displayed impressive HER performance. In a series of interface slab models incorporating the Co_2P (001), Co_2P (010), or the Co_2P (001) surface with an Ir(111) overlayer, it was found that the Co_2P(100)/Ir(111) interface was particularly effective with the most favorable hydrogen adsorption free energy. It was also shown that single atom Ir, a proxy for low Ir incorporation to the NRs, are ineffective HER catalysts. Finally, by probing the different possible adsorption sites on Ir(111), (atop, bridge, *hcp* hollow, and *fcc* hollow) it was shown that the strain/ligand effect contributions may differ from site to site even on the same surface.

7.2 Results and Discussion

7.2.1 Synthesis and Characterization of Co_2P/Ir

The core/shell structure of Co_2P/Ir NRs was obtained in a seed-mediated growth method. Monodisperse Co_2P NRs were synthesized according to a previous report.[16] A precursor mixture of cobalt (II) acetate, tributylphosphine (TBP), trioctylphosphine oxide (TOPO) in a solvent of benzyl ether (BE) and oleic acid (OAc) was thermally decomposed under N_2, leading to anisotropic crystal growth of Co_2P NRs. TBP and TOPO function as both phosphorus sources and stabilizers in the reaction. The TEM image in **Figure 7.1 A** shows monodisperse morphology of the as-obtained Co_2P NRs with dimensions of 50 ± 5 nm in length and 2 ± 0.5 nm in width. The resulting Co_2P NRs were used as seeds for controllable Ir shell growth. A low concentration solution of iridium chloride hydrate ($IrCl_3.4H_2O$) in oleylamine (OAm) was degassed and followed by the injection with Co_2P

seeds. OAm is a solvent and reagent for reducing the Ir precursor at high temperature. The TEM images in **Figure 7.1 B** illustrates that the rod shape from the initial synthesis is maintained. Aberration corrected scanning TEM (STEM) high-angle angular dark field (HAADF) in **Figure7.1 C** shows the uniform core/shell structure of the Co_2P/Ir NRs with a thickness of 0.5-1 nm Ir shell which is visualized by the bright contrast due to the higher nucleon number, Z, of Ir compared to Co and P. The elemental mapping images (**Figure 7.1 D-F**) from STEM coupled with electron energy loss spectroscopy (EELS) further confirms the architecture of the core/shell structure, exhibiting Co in the core region encapsulated by an Ir shell. The Ir/Co composition was tuned by feeding different amounts of Ir precursor in the reaction. By using small concentrations of Ir, single atom Ir sites become the predominant feature as seen by the bright spots in **Figure 7.1 G.**

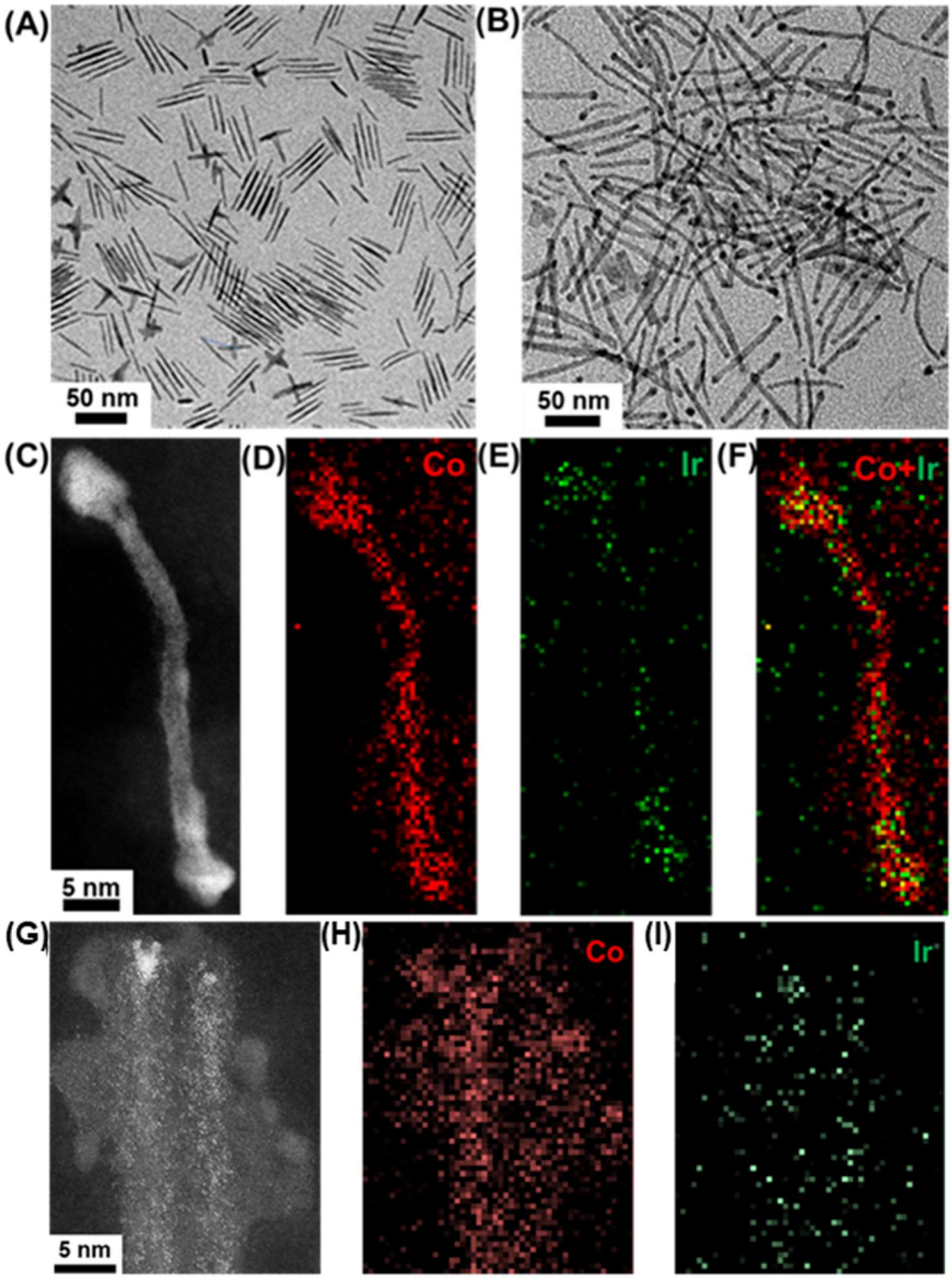

Figure 7.1 A) TEM image of Co_2P NRs. **B**) TEM image of Co_2P/Ir NRs. **C**) STEM – HAADF image of Co_2P/Ir NRs. **D-F**) EELS elemental mapping of (**C**) showing Co (**D**), Ir (**E**), and the combined signals (**F**), **G**) STEM-HAADF Co_2P/Ir NRs when low Ir concentrations are used. H-F) EELS elemental mapping of (**G**) showing Co (**H**) and Ir (**I**).

XRD and XAS were used to perform further structural characterization of the materials. In **Figure 7.2 A**, the prominent peak at 2θ = 16.1° is attributed to the (111) peak of Co_2P (JCPDS No. 54-0413). The (200) peak of Ir at 2θ = 18.6° along with higher order peak grow with increasing Ir composition (JCPDS No. 06-0598). XAS investigation suggests that as more Ir incorporates, the proportion of metallic phase Ir measured is increased. X-ray absorption near edge structure (XANES) spectroscopy shows a negative shift of the Ir absorption edge at higher Ir compositions (**Figure 7.2 B**). This corresponds with a lower energy state of its core electrons and is more similar to metallic Ir foil. Extended X-ray absorption fine structure (EXAFS) spectroscopy (**Figure 7.2 C**) shows the predominant feature as the Ir-P bond at 1.87 Å, for the low Ir concentration. A peak 2.46 Å associated with the Ir-Ir scattering pathway is also present, and this value shifts to 2.48 Å, the value of metallic Ir at high Ir concentration. The Co K-edge (**Figure 7.2 D**), on the other hand, does not show major changes in its spectrum above the noise. This suggests that the Co_2P core is chemically similar to the initial seeds.

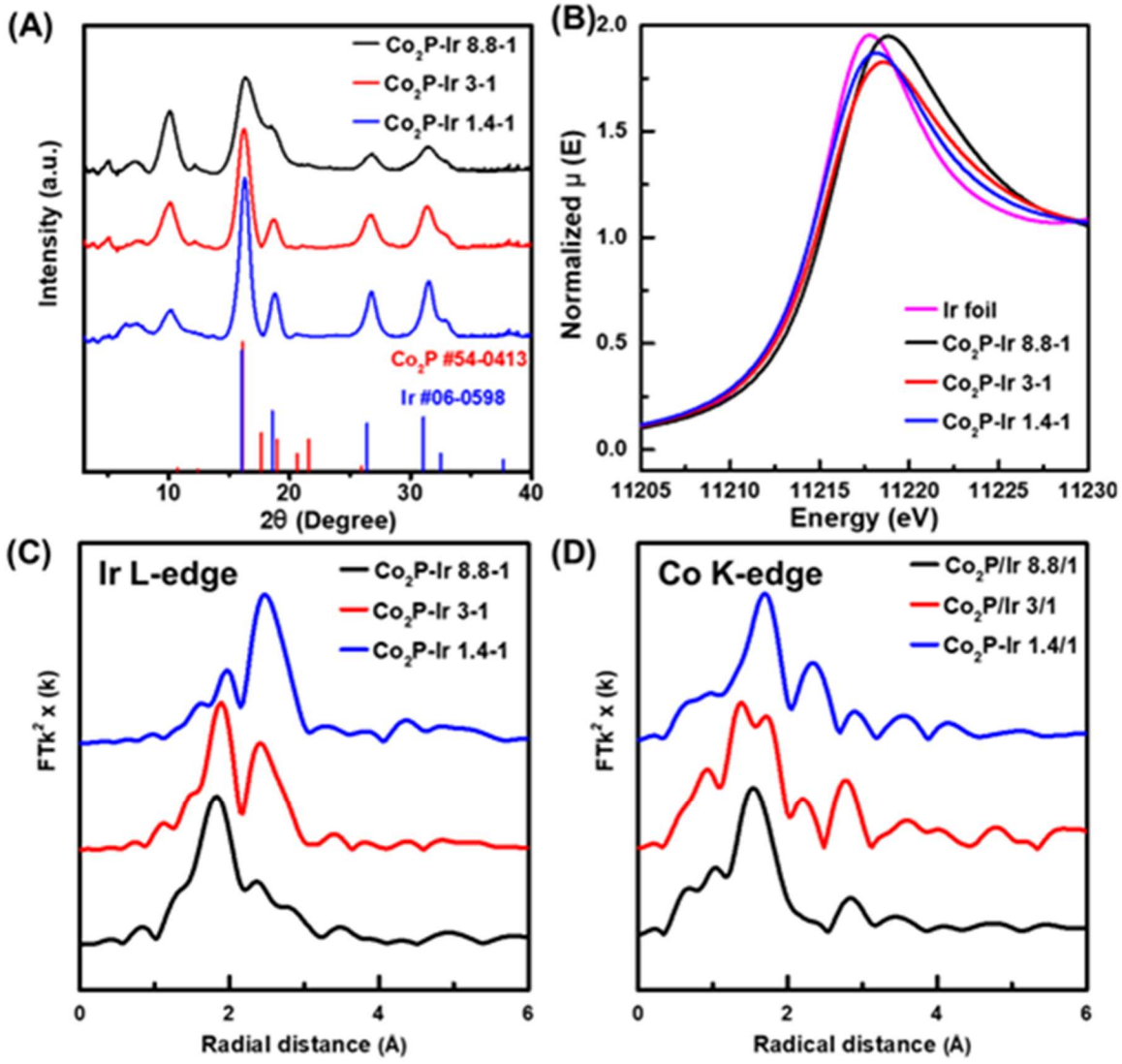

Figure 7.2 A) XRD patterns of Co_2P/Ir with different Ir composition denoted by the ICP measured ratio of Co_2P to Ir; **B**) XANES, **C**) EXAFS of Co_2P/Ir with different Ir composition for Ir L-edge; **D**) EXAFS of Co_2P/Ir with different Ir composition for Co K-edge.

7.2.2 Electrocatalytic Activity of Co_2P/Ir NRs

The Co_2P/Ir NRs were loaded on Vulcan carbon and washed with hydrazine to remove organic ligands. The HER electrocatalysis was studied in a three-electrode system based on a rotating disk electrode (RDE). The electrochemical tests were carried out in H_2-saturated, 1M KOH aqueous electrolyte. A linear sweep voltammetry (LSV) plot from 0.10 – -0.25 V_{RHE} at a scan rate of 10 mV s^{-1} shows the lowest overpotential of Co_2P/Ir 3:1 among all tested catalysts (**Figure 7.3 A**). The overpotentials at current densities of 10 mA cm^{-2} and 100 mA cm^{-2} are 48 mV and 144 mV respectively, superior to commercial IrO_2, Co_2P/Ir 8.8:1 and Co_2P/Ir 1.4:1 at the same active material loadings. Pristine Co_2P NRs show negligible current even at high overpotential, indicating that the electrocatalytic activity of the HER for Co_2P/Ir is exclusively attributed to the presence of Ir species. As shown with Tafel plot in **Figure 7.3 B**, the slopes of Co_2P/Ir 8.8:1, Co_2P/Ir 3/1 and Co_2P/Ir 1.4:1 exhibit a similar range with each other, implying that the HER kinetics are similar. Normalizing for the Ir mass (**Figure 7.3 C**), Co_2P/Ir 3:1 has a current of 179.4 mA/mg_{Ir} at 100 mV overpotential, 6.6 times and 24.7 times the activity observed on Co_2P/Ir 8.8:1 and 1.4:1 respectively. This shows that an intermediate coverage of Ir over the Co_2P NRs imparts a boost to the intrinsic activity of Ir.

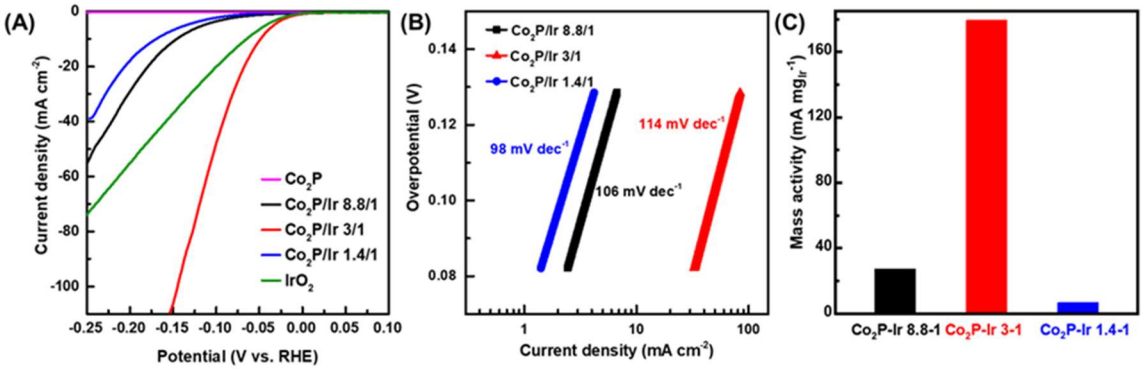

Figure 7.3 A) LSV curves of different catalysts for the HER. **B**) Tafel plot for Co_2P/Ir catalysts. **C**) Mass activity of Co_2P/Ir catalysts at an overpotential of 100 mV

The 12-hour chronopotentiometry (CP) tests at different current densities (**Figure 7.4 A**) were carried out to study the stability of the Co_2P/Ir 3:1 electrocatalyst. There are no obvious potential changes at current densities, lower than 10 mA cm^{-2}. After the electrode is subjected to a current density of 20 mA cm^{-2} for 3 hours, the potential slightly increases from -0.10 V to -0.11 V vs. RHE. Moreover, the morphology of Co_2P/Ir NRs was well-maintained without obvious changes (**Figure 7.4 B**), confirming the excellent stability of the electrocatalyst.

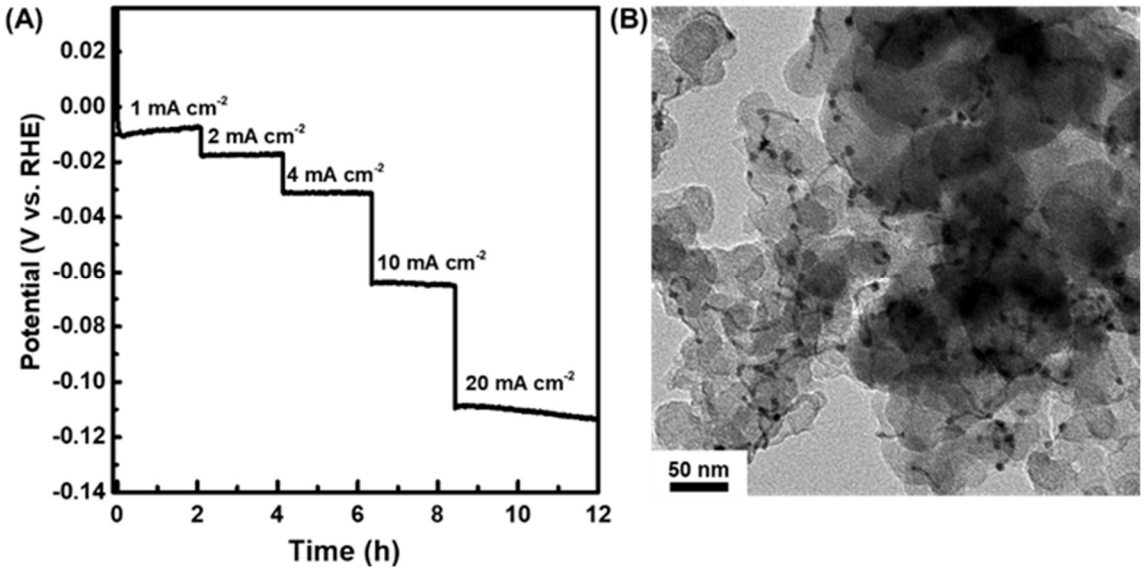

Figure 7.4 A) Stability analyses of the catalytic HER with chronopotentiometry test; **B**) TEM image of Co2P/Ir NRs after the 12 hour stepwise stability measurements.

7.2.3 DFT for Distinguishing Strain and Ligand Effects

DFT calculations were performed to understand the improved catalytic HER activity of the Co_2P/Ir NRs. The Gibbs free energy of the H binding interaction was used to evaluate the thermodynamic limit of the overpotential as a first approximation for HER activity.[17, 18] Neglecting kinetic barriers, the ideal free energy of adsorption is $\Delta G(H^*) = 0$ eV. $Co_2P(100)$/Ir (111), $Co_2P(010)$/Ir (111), and $Co_2P(001)$/Ir (001)/(111) interfaces were constructed as shown in **Figure 7.5** to serve as models for the three sides of the Co_2P/Ir nanorods. Comparisons are drawn between these models, unstrained Ir(111) used to describe the Ir nanoparticles and thick metallic layers over the NRs, and single Ir atom doped Co_2P (001), (010), and (100) surfaces to describe the Co_2P/Ir NRs with low Ir concentration (**Figure 7.1 G**). In the interfacial Co_2P/Ir systems, the underlying Co_2P layer enforces a strain on the Ir(111) overlayer due to the lattice mismatch of the two layers. With this model, we compare strained Ir(111) surfaces without Co_2P to the composite systems to derive the relative importance of strain and ligand effects in affecting catalysis.[16]

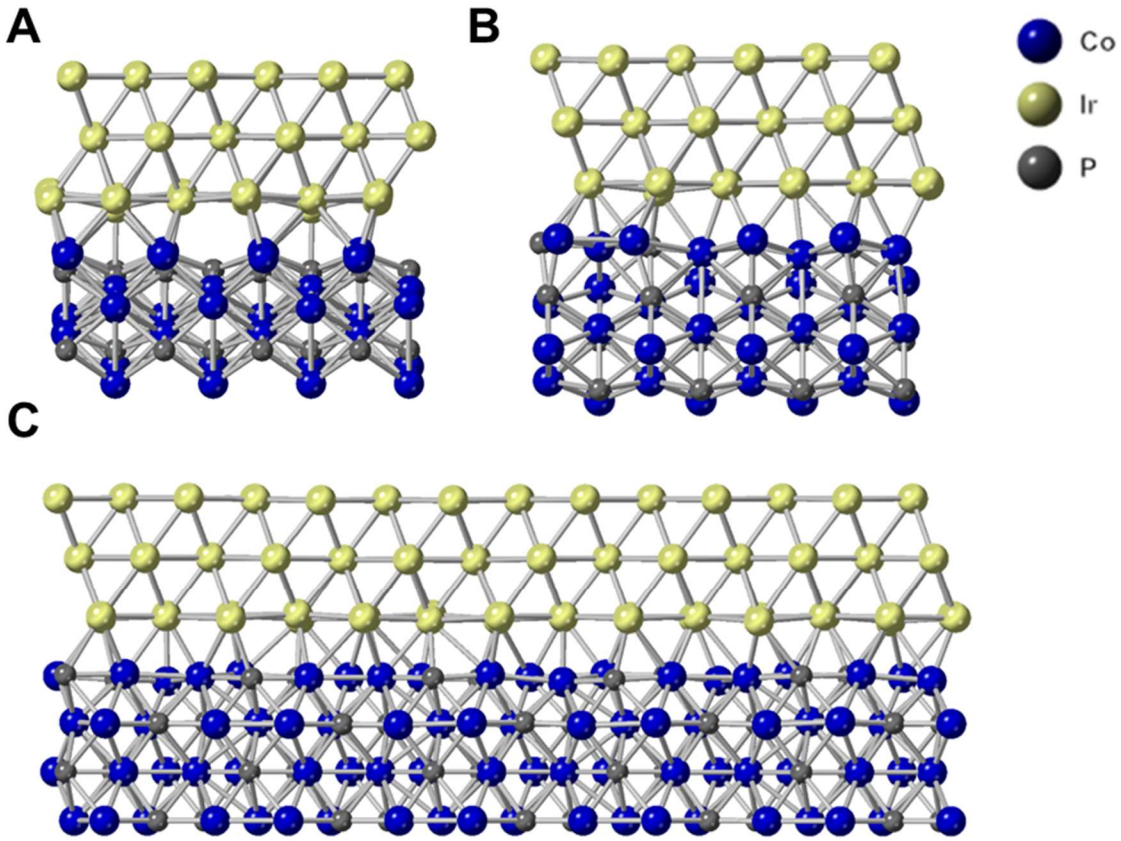

Figure 7.5 DFT model side views for **A**) Co_2P/Ir (100)/(111), **B**) Co_2P/Ir (001)/(111), and **C**) Co_2P/Ir (010)/(111).

H adsorption free energies are calculated on atop sites directly above the surface atom, bridge sites between two surface atoms, and at hollow sites between three surface atoms for the (111) facets. Hollow sites come in two varieties, hollow closed-packed (HCP) with an atom directly below the adsorption site or face-centered cubic (FCC) without the atom below the adsorption site. Beginning with the unstrained Ir(111) system, the $\Delta G(H_{ad})$ was found to be minimum at the FCC hollow site with an energy of -0.33 eV at low coverage (θ = 1/18 Monolayers - ML) **Figure 7.6 A**. However, the adsorption free energy for other sites only differed, at most, by 40 meV. These results are consistent with a previous theoretical study of H adsorption on Ir(111) by Liu *et al,* noting the distinction between the their reported zero-point energy (ZPE) corrected binding energy and the free energy.[19] The small dispersion in free energies is consistent with HREELS data of H on Ir(111) in ultra-high vacuum that shows, at low coverage, H binding is delocalized across the surface.[20] Due to the closeness of these free energies, the atop, bridge, face centered cubic (FCC) hollow, and hexagonal closed packed (HCP) hollow sites were evaluated for each Ir(111) surface in this study.

Considering the low Ir content Co_2P-Ir nanorods modelled by single atom Ir doped Co_2P (001), (010), and (100) surfaces, we calculate reduced performance on every facet relative to Ir(111) in agreement with experiment **(Figure 7.6 A).** Universally this is due to an increased over-binding of H. On doped Co_2P (100), doped Co_2P(010) – 1, and Co_2P(010) – 2 (with 1 and 2 denoting different surface substitution sites), atop sites are preferred with adsorption free energies of -0.55 eV, -0.36 eV, and -0.41 eV respectively. On the

doped $Co_2P(001)$ – 1 and 2 surfaces, bridge sites are preferred with binding free energies of -0.70 eV and -0.65 eV respectively.

The compiled free energy results for binding on the strained Ir(111) surfaces and on the composite Co_2P/Ir(111) surfaces is shown in **Figure 7.6 B**. A notable result is that on the strained Ir(111) surface, the different adsorption binding sites have different sensitivities to strain. Adsorption at atop sites is least sensitive to strain in the range calculated while the adsorption at hollow sites is most sensitive. That such an effect is present isn't surprising since bond geometry is affected more heavily for hollow sites than for atop sites. However, this is an important consideration for systems in which binding sites have similar strengths that is not captured in traditional evaluations of strain involving d-band center shifts.[21] As can be observed near -0.6% strain, there is a site preference switch from FCC hollow sites to atop sites that limits the overall effectiveness of strain as a reactivity modulating factor.

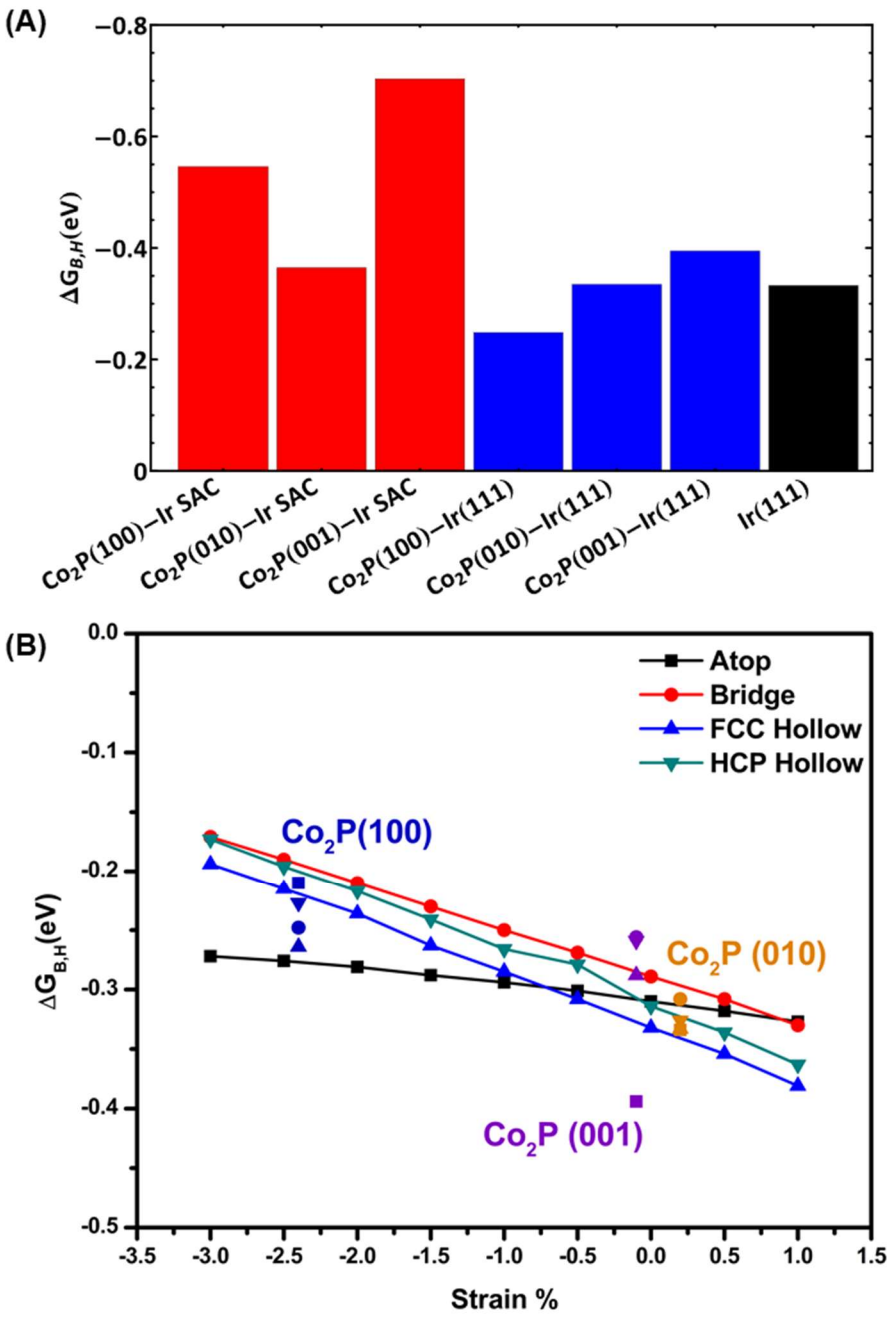

Figure 7.6 A) Summary of the most stable H adsorption free energies for the Co_2P/Ir single atom substituted (red) and interfacial models (blue) compared to the energy on Ir(111) (black) **B)** H adsorption free energy on all adsorption sites of the interfacial models (labeled and color coded by the underlying Co_2P model) are compared to the calculated H adsorption on strained Ir(111)

Comparing the Co_2P/Ir(111) models, it is apparent that only the Co_2P(100)/Ir(111) interface improves $\Delta G(H^*)$ over the Ir(111) value. In the Co_2P(010)/Ir(111) system, strain is fairly well balanced to minimize this effect (+0.2% tensile strain), and there is not a significant electronic shift of the adsorption energies to generate any improvement. Co_2P(001)/Ir(111) on the other hand, also balances strain (-0.1 % compressive strain). However, there appears to be a strong electronic effect that strengthens atop binding of H to -0.39 eV. The only interface that is calculated to improve HER activity is Co_2P(100)/Ir(111), which generates a more compressively strained surface than the other interfaces. The atop site binding is further weakened by a small ligand effect but the FCC hollow site is strengthened by the ligand effect to become the most stable adsorption site with $\Delta G(H^*)$ = -0.25 eV. This shows that the ligand effect is not globally applied to surface adsorption sites but is instead a local effect driven by inhomogeneous charge modification to the surface for intermediate number of layers. The exceptionally weak binding of the atop site relative to the other sites also suggests that alloying an unlike, poor H binding metal, such as Ag, to break up hollow sites could generate further improvement of the HER activity by introducing an ensemble effect.

7.3 Conclusion

In this chapter, 1D core/shell Co_2P/Ir NRs were synthesized by a seed mediated approach. By increasing the Ir composition, the Ir species can be varied from single atom like to metallic like as observed in STEM, EELS, and EXAFS. Moderate coverages of Ir coverages on the Co_2P NRs optimize HER activity over that of commercial IrO_2. DFT shows that Ir incorporated into Co_2P is binds H too strongly, but that a moderate overlayer on

the (100) Co_2P surface improves binding over that on pure Ir. It is also calculated that the strain effect modifies adsorbate binding differently for different adsorption sites on the surface. Moreover, electronic effects may not always be uniformly applied around adsorption sites probably due to symmetry breaking of the material. Finally, on the best calculated surface for hydrogen binding, the multicentered binding sites all bind H stronger than atop sites. Therefore, this material may be improved by incorporating a weak H binding metal to break up those ensembles and improve H binding even further.

7.4 Experimental

Materials.

Cobalt acetate tetrahydrate ($Co(Ac)_2.4H_2O$, >98%), oleylamine (OAm, 90%), oleic acid (OAc, 90%), tributylphosphine (TBP, 97%), trioctylphosphine oxide (TOPO, 90%) and Nafion (5% in ethanol) were all bought from Sigma-Aldrich and used without any further purification. 1-octadecene (ODE, 90%) was purchased from Acros Organics and used without any further purification. All syntheses were performed using standard Schlenk techniques.

Synthesis of Co_2P NRs.

Co_2P NRs were synthesized according to the modified published method.[16] The precursor solution was prepared by mixing $Co(Ac)_2.4H_2O$ (2g), TOPO (3.2g), ODE (80 ml) and OAc (8 ml) at the room temperature. The mixture was first degassed at 140 °C under N_2 and further at 100 °C under vacuum. The solution was then heated to 220 °C with a N_2 blanket by maintaining a controlled heating ramp of 5 °C min^{-1}, further injecting 12 mL of

TBP. Subsequently, the mixture was heated up to 280 °C and aged for 2 hours. The obtained NRs were precipitated by isopropanol (IPA) and then separated by centrifugation (at a speed of 8000 rpm for 8 min). The purification process of the NRs was repeated for two times.

Synthesis of core/shell Co_2P/Ir NRs

$IrCl_3.4H_2O$ was dissolved in a solvent mixture of ODE (10 ml) and OAm (10 ml). The solution was degassed at 110 °C under vacuum for 1 h. 40 mg of Co_2P NRs in hexane was then injected into the reaction flask under N_2. The system was maintained at 110 °C under N_2 blanket to remove the introduced hexane, and then slowly heated to 270 °C with a heating ramp of 2 °C min^{-1}. After maintaining at 270 °C for 2 h and removing from the heating mantle, the reaction system was cooled down to room temperature. The resulting products were further purified with an IPA wash twice. The amount of $IrCl_3 \cdot 4H_2O$ is controlled to 10 mg, 20 mg, and 40 mg, leading to the sample Co_2P/Ir 8.8/1, Co_2P/Ir 3/1, and Co_2P/Ir 1.4/1 respectively as measured by ICP.

Structural Characterization

XRD patterns were taken with synchrotron X-ray radiation source with a wavelength of 0.6199 Å at Brookhaven National Laboratory. The distance from detector to the sample was 307.8 mm, and the exposure interval was 3 seconds. The XAS results of XANES and EXAFS were collected from synchrotron X-ray source at the Brookhaven National Laboratory. The raw data process of EXAFS for Co K-edge and Ir L-edge was conducted with ATHENA program according to standard procedure.[22] The least-squares

curve fitting analysis of the EXAFS χ(k) data was carried out by the ARTEMIS program. The fitting model was built based on structural information from Co_2P and Ir. TEM images were taken on FEI Spirit (120 kV). HAADF-STEM images were collected on a Hitachi HD2700C with a probe Cs corrector (200kV) at the Center for Functional Nanomaterials at Brookhaven National Lab. Elemental composition of Ir and Co were characterized by ICP-OES on a PerkinElmer Avio-200 ICP spectrometer.

The preparation of catalysts

Mixtures of NRs and Vulcan carbon (mass ratio 1/1) were dispersed in hexane (20 ml) and sonicated for 1 hour. The NRs-loaded Vulcan carbon (NRs-C) was collected by centrifugation (8000 rpm for 8 min) and dried in vacuum. For removal of organic surfactants on the NRs, the NRs-C were stirred in a solution of ethanol/hydrazine (10 ml/100 μl) for 2 h. The NRs-C was then washed with ethanol two more times and collected by centrifugation, in order to remove excess hydrazine.

Electrocatalytic HER measurements

The HER electrocatalytic performance was characterized at room temperature with a three-electrode system in H_2-saturated 1M KOH aqueous electrolyte, which is conducted on Biologic (Model VMP3) potential station. The working electrode was glassy carbon electrode with a geometric area of 0.196 cm^{-2}; the counter electrode was Pt foil; and the reference electrode was Hg/HgO (1M KOH). The electrocatalyst ink was prepared by dispersing and sonicating NRs-C catalysts (concentration 5 mg ml^{-1}) in IPA and Nafion™ solution (volumetric ratio IPA/Nafion™ 100/1). The glassy carbon electrode was cleaned

by polishing with alumina slurry. The working electrode was prepared by spin-coating the electrocatalyst ink (20 µl). All reported potentials were converted to reversible hydrogen electrode (RHE) according to the following E(vs. RHE) = E(vs. HgO) + 0.926 V, where 0.926 V was obtained from an open circuit voltage test, describing the potential deviation from the Hg/HgO (1.0 M KOH) reference electrode to RHE in 1.0 M KOH. The HER catalytic activity was evaluated with linear sweep voltammetry (LSV) at a scan rate of 10 mV s^{-1} from 0.1V to -0.25V vs. RHE. The overpotential (η) for the HER is calculated with the following equation η=E (vs. RHE) - 0 V. The stability of the catalyst was evaluated by chronopotentiometry (CP) test at different current densities.

DFT Calculation Method

Hydrogen binding free energies were calculated with spin polarized DFT calculations performed in the VASP (5.2.11) package[23, 24] with projector augmented wave pseudopotentials[25] and the Perdew-Burke-Ernzerhof (PBE) generalized gradient approximation.[26] The energy cutoff for the plane-wave basis set was 400 eV. The van der Waals interactions were explicitly considered with the D2 method of Grimme.[27] The C_6 and R_0 parameters for Co, P, and H are as reported by Grimme. The parameters for Ir were not defined in the initial formulation, so we used C_6 = 81.242 J/nm^6 and R_0 = 1.672 Å.[28] The energy convergence criteria were set to 10^{-5} eV and structure optimization ceased when forces on the component atoms was less than 0.02 eV/Å.

Three model classes were considered to complement the experimental results. A 4-layer, 2x2 supercell Ir(111) slab with the bottom layer frozen to the bulk lattice positions

was used to model the Ir nanoparticles. The Ir bulk lattice constant was calculated to be 3.863 Å, in good agreement with the experimental value of 3.834 Å.[29] To model low Ir composite systems, 4-layer Co_2P(001), Co_2P(010), and Co_2P(001) surfaces with a single Ir substituted at each unique surface Co site and with the bottom layer frozen to the bulk Co_2P lattice positions were used. In total there are two 2 x 3 Co_2P(001) supercells, two 2 x 2 Co_2P(010) supercells, and one 3x2 Co_2P(100) supercell for the low Ir cases. The Co_2P lattice constants, a = 5.515 Å, b = 3.503 Å, and c = 6.585 Å, are also near experimental values, a = 5.646 Å, b = 3.513 Å, and c = 6.608 Å.[30] Finally, the high Ir concentration Co_2P/Ir composite models are comprised of 3 atomic layers of Ir cut to the (111) plane and 4 atomic layers of Co_2P cut to the (100), (010), or (001) plane. The bottom layer of the Co_2P slab is frozen to the calculated bulk lattice parameters while all other layers are permitted to relax in the calculation. A vacuum layer of at least 15 Å is added to each model to prevent interactions between the periodic slabs. The unit supercells are carefully chosen to balance computational time while achieving minimal lattice mismatch between the layers. Total strain is calculated by averaging the bond distance between surface Ir nearest neighbors and comparing to an unstrained model. The Co_2P/Ir(111) interface models along with the Monkhorst-Pack[31] k-point Brillouin zone sampling schemes are detailed in **Table 6-1.** The k-point meshes for the Ir(111) slab and the single atom doped Co_2P slabs are 5 x 5 x 1.

Table 7-1 Co_2P/Ir(111) interface models along with their Monkhorst-Pack k-point meshes.

Model	Supercell	Lattice Mismatch	K-Point Mesh
Co_2P(100)/Ir(111)	Co_2P(100): 4 x 2 Ir(111): 5 x 3	Co_2P[001]/Ir[1-10]: -3.6% Co_2P[010]/Ir[11-2]: -1.2%	3 x 3 x 1
Co_2P(010)/Ir(111)	Co_2P(010): 1 x 5 Ir(111): 2 x 7	Co_2P[100]/Ir[1-10]: +1.0% Co_2P[001]/Ir[11-2]: -0.5%	5 x 3 x 1
Co_2P(001)/Ir(111)	Co_2P(001): 1 x 4 Ir(111): 2 x 3	Co_2P[100]/Ir[1-10]: +1.0% Co_2P[010]/Ir[11-2]: -1.2%	7 x 3 x 1

The hydrogen adsorption energy, E_{ads}, is defined from

$$E_{Ads}(H^*) = E(H^* + Slab) - E(Slab) - \frac{1}{2}E(H_2) \quad \text{Eq. (7. 1)}$$

where E(H + slab) is the total energy of the model slab with the adsorbed hydrogen atom, E(Slab) is the total energy of the bare slab, and $E(H_2)$ is the total energy of free, gas phase H_2. The adsorption Gibbs free energy is calculated from

$$\Delta G(H^*) = E_{Ads}(H^*) + \Delta ZPE - T\Delta S(H^*) \quad \text{Eq. (7. 2)}$$

ΔZPE is the zero point energy difference between the adsorbed and the gas phase. The ZPE was calculated from the vibrational frequencies obtained from the Hessian matrices in the finite differences method in VASP. The ZPE of gas phase hydrogen was calculated at 0.267 eV while the adsorbed ZPE is system dependent. The entropy of adsorption change, $\Delta S(H^*)$ is taken to be ~ -½ $S^0(H_2(g))$ from gas phase standard conditions and $T\Delta S(H^*)$ = 0.2 eV.[17]

7.5 References

1. Xu, P. T.; Huang, T.; Huang, J. B.; Yan, Y.; Mallouk, T. E., Dye-sensitized photoelectrochemical water oxidation through a buried junction. *Proc. Natl. Acad. Sci. USA* **2018,** *115* (27), 6946-6951.

2. Meyer, T. J., Chemical Approaches to Artificial Photosynthesis. *Acc. Chem. Res.* **1989,** *22* (5), 163-170.

3. Sultan, S.; Tiwari, J. N.; Singh, A. N.; Zhumagali, S.; Ha, M.; Myung, C. W.; Thangavel, P.; Kim, K. S., Single Atoms and Clusters Based Nanomaterials for Hydrogen

Evolution, Oxygen Evolution Reactions, and Full Water Splitting. *Adv. Energy Mater.* **2019,** *9* (22), 1900624.

4. Subbaraman, R.; Tripkovic, D.; Strmcnik, D.; Chang, K. C.; Uchimura, M.; Paulikas, A. P.; Stamenkovic, V.; Markovic, N. M., Enhancing Hydrogen Evolution Activity in Water Splitting by Tailoring Li+-Ni($OH)_2$-Pt Interfaces. *Science* **2011,** *334* (6060), 1256-1260.

5. Jacobson, M. Z.; Colella, W. G.; Golden, D. M., Cleaning the air and improving health with hydrogen fuel-cell vehicles. *Science* **2005,** *308* (5730), 1901-5.

6. Pivovar, B.; Rustagi, N.; Satyapal, S., Hydrogen at Scale (H_2@Scale) Key to a Clean, Economic, and Sustainable Energy System. *Electrochem. Soc. Interface* **2018,** *27* (1), 47-52.

7. Foerder, C. A.; Klebanoff, S. J.; Shapiro, B. M., Hydrogen peroxide production, chemiluminescence, and the respiratory burst of fertilization: interrelated events in early sea urchin development. *Proc Natl Acad Sci U S A* **1978,** *75* (7), 3183-7.

8. Nørskov, J. K.; Bligaard, T.; Logadottir, A.; Kitchin, J.; Chen, J. G.; Pandelov, S.; Stimming, U., Trends in the exchange current for hydrogen evolution. *J. Electrochem. Soc.* **2005,** *152* (3), J23.

9. Cherevko, S.; Geiger, S.; Kasian, O.; Kulyk, N.; Grote, J. P.; Savan, A.; Shrestha, B. R.; Merzlikin, S.; Breitbach, B.; Ludwig, A.; Mayrhofer, K. J. J., Oxygen and hydrogen evolution reactions on Ru, RuO_2, Ir, and IrO_2 thin film electrodes in acidic and alkaline electrolytes: A comparative study on activity and stability. *Catal. Today* **2016,** *262*, 170-180.

10. Li, C.; Baek, J. B., Recent Advances in Noble Metal (Pt, Ru, and Ir)-Based Electrocatalysts for Efficient Hydrogen Evolution Reaction. *ACS Omega* **2020,** *5* (1), 31-40.

11. Gong, S. P.; Wang, C. L.; Jiang, P.; Yang, K.; Lu, J.; Huang, M. X.; Chen, S.; Wang, J. Z.; Chen, Q. W., O species-decorated graphene shell encapsulating iridium-nickel alloy as an efficient electrocatalyst towards hydrogen evolution reaction. *J. Mater. Chem. A* **2019,** *7* (25), 15079-15088.

12. Cui, M.; Johnson, G.; Zhang, Z.; Li, S.; Hwang, S.; Zhang, X.; Zhang, S., AgPd nanoparticles for electrocatalytic CO_2 reduction: bimetallic composition-dependent ligand and ensemble effects. *Nanoscale* **2020,** *12* (26), 14068-14075.

13. Park, J.; Sa, Y. J.; Baik, H.; Kwon, T.; Joo, S. H.; Lee, K., Iridium-Based Multimetallic Nanoframe@Nanoframe Structure: An Efficient and Robust Electrocatalyst toward Oxygen Evolution Reaction. *Acs Nano* **2017,** *11* (6), 5500-5509.

14. Zhang, J.; Chen, Z. L.; Liu, C.; Zhao, J.; Liu, S. L.; Rao, D. W.; Nie, A. M.; Chen, Y. N.; Deng, Y. D.; Hu, W. B., Hierarchical iridium-based multimetallic alloy with double-core-shell architecture for efficient overall water splitting. *Sci. China Mater.* **2020,** *63* (2), 249-257.

15. Kuttiyiel, K. A.; Sasaki, K.; Chen, W. F.; Su, D.; Adzic, R. R., Core-shell, hollow-structured iridium-nickel nitride nanoparticles for the hydrogen evolution reaction. *J. Mater. Chem. A* **2014,** *2* (3), 591-594.

16. Liu, C.; Ma, Z.; Cui, M.; Zhang, Z.; Zhang, X.; Su, D.; Murray, C. B.; Wang, J. X.; Zhang, S., Favorable core/shell interface within Co2P/Pt nanorods for oxygen reduction electrocatalysis. *Nano letters* **2018,** *18* (12), 7870-7875.

17. Nørskov, J. K.; Bligaard, T.; Logadottir, A.; Kitchin, J. R.; Chen, J. G.; Pandelov, S.; Stimming, U., Trends in the Exchange Current for Hydrogen Evolution. *J. Electrochem. Soc.* **2005,** *152* (3), J23-J26.

18. Tang, M. T.; Liu, X. Y.; Ji, Y. F.; Norskov, J. K.; Chan, K. R., Modeling Hydrogen Evolution Reaction Kinetics through Explicit Water-Metal Interfaces. *J. Phys. Chem. C* **2020,** *124* (51), 28083-28092.

19. Liu, C. L.; Zhu, L.; Wen, X. D.; Yang, Y.; Li, Y. W.; Jiao, H. J., Hydrogen Adsorption on Ir(111), Ir(100) and Ir(110)-Surface and Coverage Dependence. *Surf. Sci.* **2020,** *692*, 121514.

20. Hagedorn, C. J.; Weiss, M. J.; Weinberg, W. H., Dissociative chemisorption of hydrogen on Ir(111): Evidence for terminal site adsorption. *Phys. Rev. B* **1999,** *60* (20), 14016-14018.

21. Mavrikakis, M.; Hammer, B.; Norskov, J. K., Effect of strain on the reactivity of metal surfaces. *Phys. Rev. Lett.* **1998,** *81* (13), 2819-2822.

22. Ravel, B.; Newville, M., ATHENA, ARTEMIS, HEPHAESTUS: data analysis for X-ray absorption spectroscopy using IFEFFIT. *Journal of Synchrotron Radiation* **2005,** *12* (4), 537-541.

23. Kresse, G.; Hafner, J., Ab initio molecular dynamics for liquid metals. *Phys. Rev. B.* **1993,** *47* (1), 558-561.

24. Kresse, G.; Furthmuller, J., Efficient iterative schemes for ab initio total-energy calculations using a plane-wave basis set. *Phys. Rev. B.* **1996,** *54* (16), 11169-11186.

25. Blochl, P. E., Projector augmented-wave method. *Phys. Rev. B.* **1994,** *50* (24), 17953-17979.

26. Perdew, J. P.; Burke, K.; Ernzerhof, M., Generalized Gradient Approximation Made Simple. *Phys. Rev. Lett.* **1996,** *77* (18), 3865-3868.

27. Grimme, S., Semiempirical GGA-type density functional constructed with a long-range dispersion correction. *J. Comput. Chem.* **2006,** *27* (15), 1787-99.

28. Bokareva, O. S.; Kühn, O., DFT-D investigation of the interaction between Ir (III) based photosensitizers and small silver clusters Ag_n (n=2–20,92). *Chemical Physics* **2014,** *435*, 40-48.

29. Kittel, C.; McEuen, P.; McEuen, P., *Introduction to Solid State Physics*. Wiley New York: 1996; Vol. 8.

30. Rundqvist, S., The Structures of Co_2P, Ru_2P and Related Phases. *Acta Chemica Scandinavica* **1960,** *14* (9), 1961-1979.

31. Monkhorst, H. J.; Pack, J. D., Special Points for Brillouin-Zone Integrations. *Phys. Rev. B* **1976,** *13* (12), 5188-5192.

Chapter 8

DFT Study of Adsorbate Driven Anisotropy in Cu and Cu_3M (M = Pd, Pt) Nanocrystal

In this Chapter, I return to thinking about how ligands and their interactions with metals surfaces influence nanocrystal anisotropy. Cu and Cu_3Pd can be shaped into nanocubes comprised of (100) facets when synthesized from CuBr in the presence of trioctylphosphine oxide and oleylamine. Here, I perform DFT calculations to calculate the interactions of each of these molecules with each of these moieties to explain the excessive stabilization of the (100) facet over other low index facets, (111) and (110). All three species show significant binding to the three surfaces at low coverages. The stabilization of the (100) surface however, can be explained by the (111) facet quickly experiences repulsive effects between adsorbates that weaken binding energies. The (100) surface, with fewer adsorption sites per area than the (111), can accommodate more adsorbate. When combined with the increased strength of Br adsorption on the (100) surface, ends up sufficiently stabilized so that it is the dominant facet.

8.1 Background and Motivation

The merits of CO_2RR were discussed briefly in Chapter 6 and a AgPd system was introduced as an alloy to improve generation of CO.[1] Another class of catalysts, which constitute a significant portion of the CO_2RR literature, are Cu and Cu alloy materials due to the unique nature of Cu converting CO_2 into multicarbon products such as ethylene.[2-15] An interesting property of Cu nanocrystals for CO_2RR is that shape plays a considerable role in tuning the products. The Cu(100) facet, typically dominant on nanocubes, is usually

cited as an ethylene producer,[10, 11, 16, 17] whereas Cu(111) octahedra demonstrate improved methane production.[13]

Critical to the studies that describe the facet dependence of CO_2RR is the ability to synthesize monodisperse Cu nanoparticles that selectively express a single kind of facet. Cu (111) nano-octahedra for instance may be synthesized from $CuCl_2$ in a mix of trioctylphosphine and oleylamine (OAm).[13] The (100) nanocubes, on the other hand, (**Figure 8.1**), may be synthesized with a reaction mix of OAm, trioctylphosphine oxide (TOPO), and CuBr.[11] Moreover, it is found that by performing a galvanic exchange reaction with of the Cu nanocubes with $Pd(acac)_2$ in the same conditions, the morphology may be retained, but when performing a galvanic exchange with $Pt(acac)_2$, (101) facets develop at the expense of the (100) facets (**Figure 8.1**).

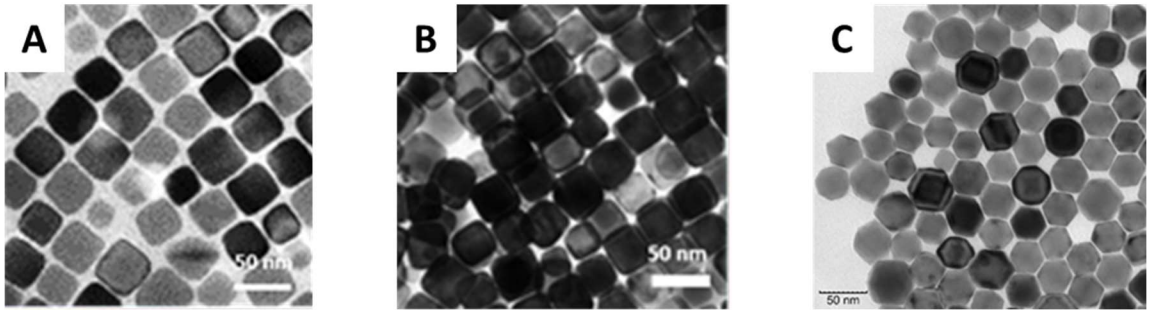

Figure 0.1 TEM images of **A**) Cu (100) nanocubes, **B**) Cu_3Pd nanocubes, and **C**) Cu_3Pt (101) rhombic dodecahedra.

Clearly, there is rich chemistry that drives anisotropy in CuM nanoparticles, and the benefits of using this chemistry has major impacts on catalysis research. Yet, the exact interactions are not clearly understood. Understanding this chemistry will help to improve the efficiency of nanomaterial synthesis and increase research capabilities in forming anisotropic nanoparticles. Previous research has looked at how chemical adsorbates, such as CO, or O, will stabilize high energy surface facets to influence nanoparticle shapes using DFT.[18-20] Adopting a similar strategy, this chapter examines the chemical interactions between the synthetic ingredients (OAm, TOPO, and Br) and the surfaces of Cu (100) nanocubes, Cu_3Pd (100) nanocubes, and Cu_3Pt (101) nanocrystals to see what is responsible for the differential stability of the various facets.

8.2 Results and Discussion

8.2.1 Surface Energies of (100), (101), and (111) Facets

To begin thinking about how these nanoparticle shapes are formed, the surface energies of the various facets (**Figure 8.2)** are calculated. As expected for FCC metals, the bare (111) surface is the most stable with surface energies of 1.31 J/m^2, 1.27 J/m^2, and

1.31 J/m^2 for Cu, Cu_3Pd, and Cu_3Pt respectively. The (100) is the second most stable and the (101) is the least stable of the 3 surfaces calculated. The Cu values, 1.31 J/m^2 (111), 1.45 J/m^2 (100), and 1.53 J/m^2 (101) agree well with other calculated values.[21, 22] For the (100) and the (101) facets, two terminations are possible: a Cu termination (T1) and a CuM (T2) termination. The two terminations of Cu_3Pd (100) are equal in energy. T2 of Cu_3Pt (101) is more stable than T1. For Cu_3Pt on both facets, T1 is most stable.

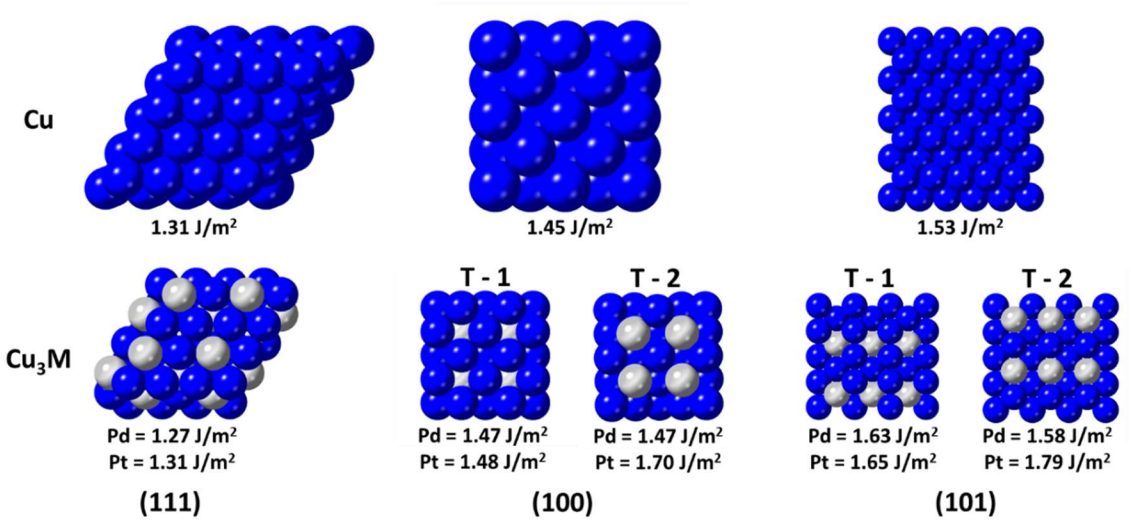

Figure 0.2 Top view of DFT surface models used for surface energy calculations. Blue atoms are Cu and grey atoms are Pt/Pd. T-1 and T-2 are used to denote the 2 terminations observed for both the (100) and (101) facets. T-1 denotes the Cu termination while T-2 denotes the CuM termination. The surface energy for each model is listed.

In the following sections, the interactions of Br, OAm, and TOPO are calculated to understand their effects on different surface facets. Van der Waals interactions are included as described by the D2 method of Grimme.[23] Their contributions can be understood by

$$\gamma(covered) = \gamma(clean) + \frac{\theta \Delta H(\theta)}{A^*} \quad \text{Eq (8. 1)}$$

where θ is the surface coverage of the adsorbate, ΔH(θ) is the adsorption enthalpy of the adsorbate as a function of coverage, A* is the area per surface atom, and γ is the surface energy.[18, 19] The values of A^* are denoted in **Table 8-1**. As can be seen, the (111) and (100) surfaces have small A^* values, while the open (101) has a large A^* value. Consequently, larger adsorption values are necessary to stabilize more open surfaces to the same extent as close-packed surfaces. On the other hand, open surfaces may be able to accommodate higher fractional coverages have fewer repulsion effects at high coverages.

Table 8.1. Area per surface atom (A*) for each examined surface**.**

	(100)	**(101)**	**(111)**
Cu	6.59 Å	9.32 Å	5.71 Å
Cu_3Pd	6.95 Å	9.74 Å	6.01 Å
Cu_3Pt	6.97 Å	9.86 Å	6.04 Å

On this calculation, two points should be addressed to ensure careful interpretation of the results. First, the PBE-DFT calculated surface energies tend to underestimate the experimental values by significant margins. For Cu(111) the calculated value referenced, and produced here, 1.31 J/m^2 is 27% below the experimental value of 1.79 J/m^2.[24] In previous work using this method of calculating surface energies for CO on Pt, calculated surface energies were converted to more realistic values by a scaling factor that was derived from the ratio of the experimental Pt(111) result to the calculated Pt(111) result.[18] It was assumed that this scaling factor, 1.82, would be constant for the higher index facets examined. In this work, it is unclear if the scaling factor derived for Cu, 1.37, correctly applies to the Cu_3M alloys, however since the alloys are Cu rich, that is the assumption under which the calculations will be performed. This is an important point for ordering the surface energies, however, since this method scales only the separation of the surface energies and not their adsorbate corrections.

The second point requiring attention is that the formula, as presented, will very easily lead to negative surface energy values. While in one component systems this would be unphysical, two component systems after accounting for the interactions in those systems, may have negative surface energies.[25]

8.2.2 Br Adsorption

The interaction of Br with each of the surfaces was calculated at low coverage (0.125 monolayer - ML or below, **Figure 8.3**) and medium coverage (0.5 ML, **Figure 8.4**). On the (111) and the (100) surfaces, Br adsorbs in the 3-fold and 4-fold hollow sites, respectively, at low coverage. Br binds particularly strongly on the Cu_3Pt (100) T1 surface

with a binding energy of -3.13 eV and on the Cu_3Pt (111) with a binding energy of -2.69 eV. On the (110) facets, short bridge sites are preferred on the Cu_3Pd – T1 and Cu_3Pt – T1. On Cu and the T2 surfaces, Br adsorbs in the long bridge site between rows. On the Cu surface, the (101) adsorption site binds Br the strongest, whereas on the Cu_3Pd and Cu_3Pt, the (100)-T1 surface had the highest binding energy. Plugging these values into eq. 8.1 with an assumed coverage of 0.25 ML, the (111) surface is still most stable in all instances with surface energies of 1.11 J/m^2, 0.95 J/m^2, and 0.90 J/m^2 for Cu, Cu_3Pd, and Cu_3Pt respectively.

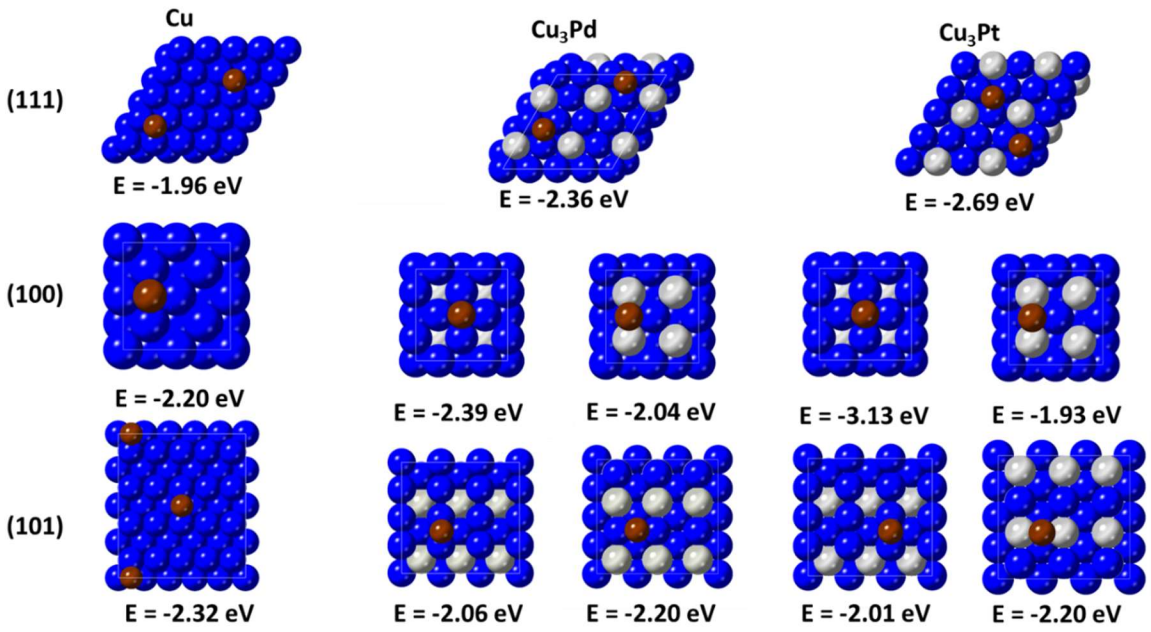

Figure 0.3 DFT models of Br adsorption on Cu and Cu_3M surfaces. Cu is Blue, Br is brown, and Pd/Pt is grey.

In the case of moderate coverage (0.5 ML) there is a notable change that occurs with the (111) facet of the Cu surface. The Br atoms move towards a row configuration of atop adsorption. This is significantly different from the (111) facets of the Cu_3Pd and Cu_3Pt systems where the Br remain in the hollow sites. On all (111) surfaces the adsorption energy drops dramatically by approximately 50%. The (101) and (100) surfaces decrease by 10% and 7% respectively. At this coverage the (100) facet becomes the strongest binding facet for all three alloys. That the (111) has a drastically reduced binding at the same moderate fractional coverage as the (101) or (100) is not surprising since the number of atoms per unit area will be drastically higher in the (111) case. Consequently, the surface energy for the (100) surface drops to -0.54 J/m^2 on Cu and the T1 Cu_3M surfaces. This is significantly more stable than the (111) surface, the next most stable facet of the half Br coverage, with surface energies of 0.38, 0.19, and 0.42 J/m^2 respectively. Therefore, calculations show that Br, for these Cu systems, has a significant driving force towards the (100) facet.

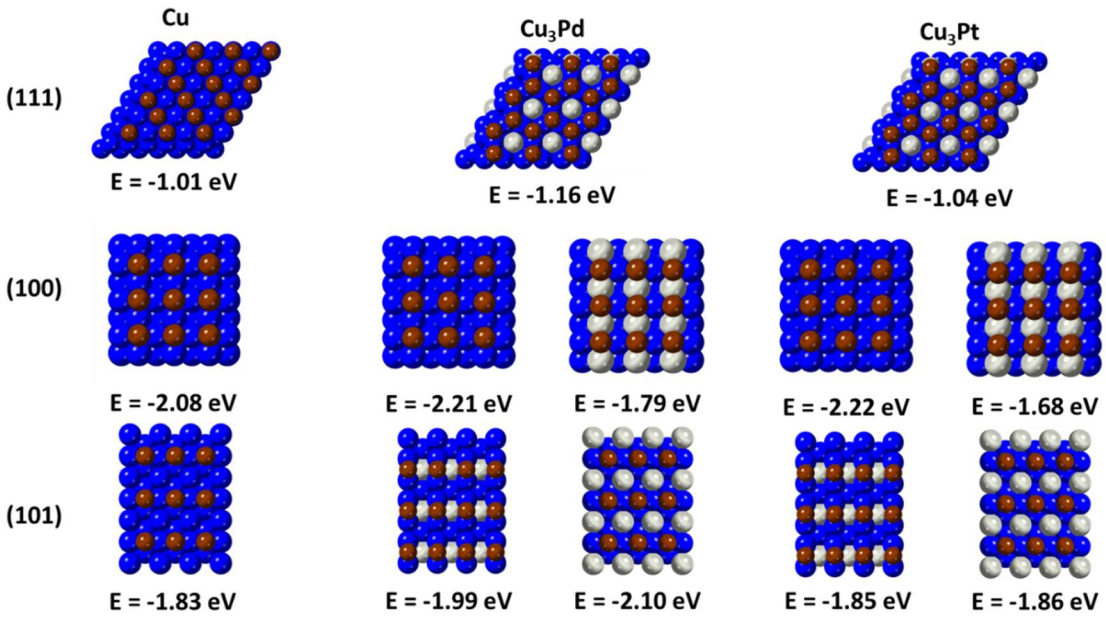

Figure 0.4 DFT models for Br adsorption at 0.5 ML on Cu and Cu_3M surfaces Cu is Blue, Br is brown, and Pd/Pt is grey.

8.2.3 Trioctylphosphine Oxide Adsorption

TOPO is a bulky organic molecule consisting of three, 8 carbon chains bound to a central P atom with an O atom attached. Due to the long flexible C chains, calculations involving this molecule are slow to converge and have many local minima. In the low coverage limit ($\theta \leq 0.063$ ML) binding was calculated to be quite strong in an absolute sense (**Table 8-2**). The strongest binding energies are on the (101) surfaces of Cu_3Pd and Cu_3Pt. However, these configurations have TOPO with the C chains laying flat to the surface (**Figure 8.5**). Furthermore, at least 90% of this interaction is calculated from the vdW correction, suggesting that the chemical interaction of the surface with these compounds is minimal. Therefore, when these interfaces are put in solvent, the difference in energy between the solvated state and the bound state is unlikely to be significant. Therefore, coverage of this molecules is likely to be low in experimental conditions.

Table 8.2 Adsorption Energies of TOPO under 0.063 ML coverage

	Cu	**Cu_3Pd**	**Cu_3Pt**
(100) – T1	-2.23 eV	-2.546 eV	-2.494 eV
(100) – T2	-	-2.833 eV	-2.486 eV
(101) – T1	-1.99 eV	-2.602 eV	-2.786 eV
(101) – T2	-	-3.960 eV	-4.071 eV
(111)	-2.18 eV	-2.299 eV	-2.724 eV

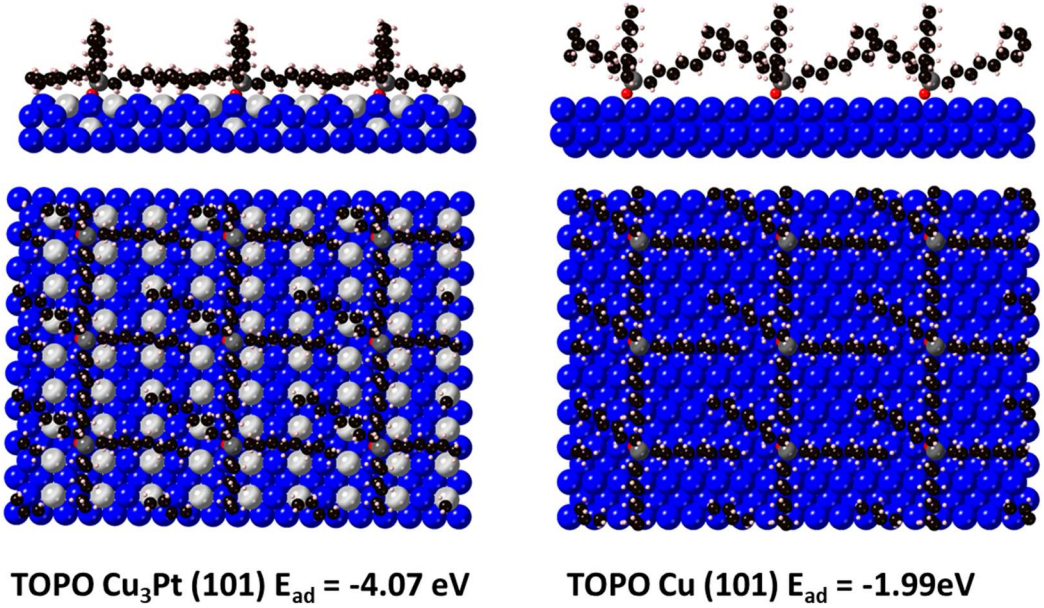

Figure 0.5 DFT models of TOPO on Cu_3Pt and Cu at ultra low coverage. Cu is blue, Pt is light grey, P is dark grey, C is black, O is red, and H is pink. The stronger adsorbing TOPO lays flatter to the surface.

Additionally, because these molecules are so bulky, they are unable to saturate many of the bonds at the interface to lower the surface energy. Even in the case of TOPO on Cu_3Pt, the stabilization is not enough to drive the surface energy (scaled from the DFT results) below 2.08 J/m^2. Increasing the coverage amount to 0.125 just about halves all of the adsorption energies ensuring their stabilization of surface energy decreases further. Consequently, TOPO is not likely to be a significant molecule to shape direction through surface stabilization through direct bonding.

8.2.4 Oleylamine Adsorption

OAm, having only one long C chain rather than three, can pack a little more densely than TOPO and has already been reported to have surface directing capabilities.[26] Here, calculations were performed for coverages of 0.5 ML on (100) and (101) as well as 0.25 on (111) (**Figure 8.6**). No stable adsorption was found for coverages of OAm at 0.5 ML on the (111) surface. The preferred adsorption sites are atop sites on all surfaces. The Cu_3Pt (100) and (101) surfaces generally show stronger adsorption than either Cu or Cu_3Pd. On each of the three surfaces, the (101) surface adsorbs OAm strongest with adsorption energies of -1.97 eV, -2.33 eV, and -2.52 eV for the Cu, Cu_3Pd T – 2, and Cu_3Pt T – 2 respectively.

In none of the three cases does the surface energy decrease below that observed for Br adsorption at 0.5 ML. For Cu, the (101) interface has a surface energy of 0.4 J/m^2. Cu_3Pd, likewise, has a (101) T – 2 surface energy of 0.25 J/m^2. Cu_3Pt (101) T - 2 has a surface energy of 0.4 J/m^2, but also has a (100) T – 1 surface energy of 0.32 J/m^2. Though,

the (101) T – 2 surface energy decreases below the (100) T – 1 for coverages higher than 0.63 ML using the current scale factor to bring calculations closer to experiment. If a lower scale factor, like 1.1 was required for the alloy, the surface energies would be equal 0.5 ML to be equal. Higher scale factors such as 1.82, the value previously used for Pt,[18] that value would be as high as 0.85 ML assuming constant binding.

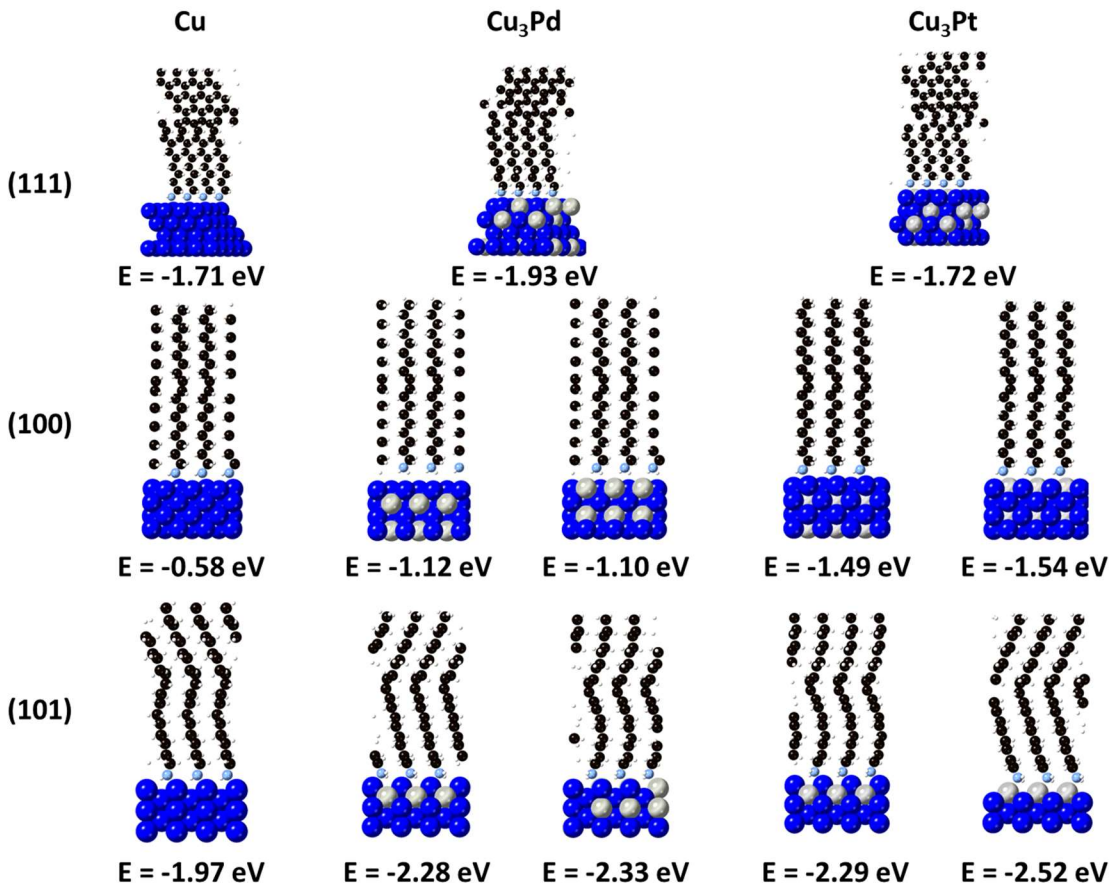

Figure 0.6 DFT Models for OAm adsorption on Cu and Cu_3M systems. The (111) model systems are calculated at a coverage of 0.25 ML while all other systems are calculated at a coverage of 0.5 ML. Cu is dark blue, Pd/Pt is light grey, C is black, H is white, and N is light blue.

The propensity for oleylamine to bind more strongly to the (101) surface facet may be directing agent for the Cu_3Pt nanocrystals. OAm binds more strongly to Cu_3Pt than it does the Cu_3Pd, so this may explain the difference between these two systems. In the galvanic exchange reactions, Br is not reintroduced to the system through the metal precursor, so it is unclear how much would continue to stick around from the initial Cu seed synthesis. The interaction of OAm is 0.4 eV weaker on the Cu_3Pd (100) surface so Br may not be driven off quickly, even when flooded with excess OAm. This exchange may be more facile on the Cu_3Pt nanocrystal due to the enhanced binding with OAm.

8.3 Summary

The binding interactions of TOPO, OAm, and Br with Cu and Cu_3M (100), (101), and (111) surfaces were calculated to identify shape directing additive candidates. These species were chosen based off experiments that show that this mix of reactants can form Cu (100) nanocubes. The nanocubes can be used as seeds with $Pd(acac)_2$ or $Pt(acac)_2$ to generate Cu_3Pd (100) nanocubes or Cu_3Pt (101) nanocrystals respectively. TOPO is not found to interact through a strong chemical means but does have a strong vdW interaction. Br is found to be strongly selecting for the (100) facet and likely explain the formation of Cu nanocubes from CuBr. OAm appears to interact strongly with the (101) surface and may be responsible for directing to this facet. The interaction strength of OAm with Cu_3Pt is stronger than with Cu_3Pd or Cu and may be able to drive the crystal more easily to the (101) facet by flooding out Br more easily.

8.4 Calculation Details

DFT calculations were performed within the VASP (5.2.11) package[27, 28] with projector augmented wave pseudopotentials[29] and the Perdew-Burke-Ernzerhof (PBE) generalized gradient approximation (GGA).[30] The energy cutoff for the plane-wave basis set was 400 eV. The van der Waals interactions were explicitly considered with Grimme's D2 method.[23] The Pt parameters were not defined in the original paper, so parameters reported elsewhere: C_6 = 40.62 J nm^6 mol^{-1} and R_0 = 1.772 Å were used.[31]

Cu, Cu_3Pd, and Cu_3Pt were geometrically optimized with electronic step energy criteria of 10^{-6} eV and for criteria of 0.001 eV/Å. Partial occupancies were set by the 1st order method of Methfessel and Paxton with a width of 0.2 eV. The Brillouin zone was sampled in each case by a 12 x 12 x 12 Monkhorst Pack k-point mesh.[32] Lattice parameters derived from these calculations are 3.63 Å , 3.73 Å, and 3.73Å for Cu, Cu_3Pd, and Cu_3Pt respectively.

These bulk cells were used to generate 9 layer surface slabs of the (100), (101), and (111) surfaces. 15 Å of vacuum was set between slabs to avoid spurious interactions within the models. The middle 3 layers were frozen to the reported bulk parameters while the outside layers relaxed. Convergence criteria were the same as the lattice parameter determination, except the k-point mesh was set to 9 x 9 x 1. Surface energies were calculated without vdW corrections by

$$\gamma(clean) = \frac{E_{slab} - N * E_{Bulk}}{2A} \qquad \text{Eq (8. 2)}$$

where E_{slab} is the energy of the 9-layer slab, E_{bulk} is the energy of the bulk, A is the surface area of 1 face of the slab, and N is the number of bulk unit cells needed to construct the slab.

Adsorption energy calculations were performed and calculated according to

$$E_{Ads} = E(Ads + Slab) - E(Slab) - E(Ads) \quad \text{Eq (8. 3)}$$

with E(Ads + Slab) is the energy of the adsorption model, E slab is the energy of the slab alone, and E(Ads) is the energy of the adsorbate alone. OAm and TOPO were taken directly as their molecular form and E(Ads) was calculated in an asymmetric box with a gamma point only calculation. Br was calculated in a similar way as ½ Br_2. Slabs were at least 4 layers with the bottom layer frozen to the bulk values. Both (1x1) and (2x2) supercells were used for all three surfaces. The convergence criteria of the adsorbate calculations were 10^{-5} eV and 0.02 eV/Å for the energy and force respectively. K-point meshes were 7 x 7 x 1 for the 1 x 1 cells and 5 x 5 x 1 for the 2 x 2 (100) and (111) cells. For the 2 x 2 (101) unit cell, 5 x 3 x 1 k-point meshes were used and for the (1 x 1) cell a 7 x 5 x 1 k -point mesh was used.

8.5 References

1. Cui, M.; Johnson, G.; Zhang, Z.; Li, S.; Hwang, S.; Zhang, X.; Zhang, S., AgPd nanoparticles for electrocatalytic CO_2 reduction: bimetallic composition-dependent ligand and ensemble effects. *Nanoscale* **2020,** *12* (26), 14068-14075.

2. Kyriacou, G.; Anagnostopoulos, A., Electroreduction of CO_2 on Differently Prepared Copper Electrodes - the Influence of Electrode Treatment on the Current Efficiencies. *J. Electroanal. Chem.* **1992,** *322* (1-2), 233-246.

3. Kas, R.; Kortlever, R.; Milbrat, A.; Koper, M. T.; Mul, G.; Baltrusaitis, J., Electrochemical CO_2 reduction on Cu_2O-derived copper nanoparticles: controlling the catalytic selectivity of hydrocarbons. *Phys. Chem. Chem. Phys.* **2014,** *16* (24), 12194-201.

4. Kim, Y. G.; Baricuatro, J. H.; Javier, A.; Gregoire, J. M.; Soriaga, M. P., The evolution of the polycrystalline copper surface, first to Cu(111) and then to Cu(100), at a fixed CO_2RR potential: a study by operando EC-STM. *Langmuir* **2014,** *30* (50), 15053-6.

5. Hahn, C.; Hatsukade, T.; Kim, Y. G.; Vailionis, A.; Baricuatro, J. H.; Higgins, D. C.; Nitopi, S. A.; Soriaga, M. P.; Jaramillo, T. F., Engineering Cu surfaces for the electrocatalytic conversion of CO_2: Controlling selectivity toward oxygenates and hydrocarbons. *Proc Natl Acad Sci U S A* **2017,** *114* (23), 5918-5923.

6. Clark, E. L.; Singh, M. R.; Kwon, Y.; Bell, A. T., Differential Electrochemical Mass Spectrometer Cell Design for Online Quantification of Products Produced during Electrochemical Reduction of CO_2. *Anal. Chem.* **2015,** *87* (15), 8013-20.

7. Kwon, Y.; Lum, Y.; Clark, E. L.; Ager, J. W.; Bell, A. T., CO_2 Electroreduction with Enhanced Ethylene and Ethanol Selectivity by Nanostructuring Polycrystalline Copper. *ChemElectroChem* **2016,** *3* (6), 1012-1019.

8. Clark, E. L.; Hahn, C.; Jaramillo, T. F.; Bell, A. T., Electrochemical CO_2 Reduction over Compressively Strained CuAg Surface Alloys with Enhanced Multi-Carbon Oxygenate Selectivity. *J. Am. Chem. Soc.* **2017,** *139* (44), 15848-15857.

9. Eilert, A.; Cavalca, F.; Roberts, F. S.; Osterwalder, J.; Liu, C.; Favaro, M.; Crumlin, E. J.; Ogasawara, H.; Friebel, D.; Pettersson, L. G.; Nilsson, A., Subsurface Oxygen in Oxide-Derived Copper Electrocatalysts for Carbon Dioxide Reduction. *J Phys Chem Lett* **2017,** *8* (1), 285-290.

10. Roberts, F. S.; Kuhl, K. P.; Nilsson, A., High selectivity for ethylene from carbon dioxide reduction over copper nanocube electrocatalysts. *Angew. Chem., Int. Ed.* **2015,** *54* (17), 5179-82.

11. Loiudice, A.; Lobaccaro, P.; Kamali, E. A.; Thao, T.; Huang, B. H.; Ager, J. W.; Buonsanti, R., Tailoring Copper Nanocrystals towards C_2 Products in Electrochemical CO_2 Reduction. *Angew. Chem., Int. Ed.* **2016,** *55* (19), 5789-5792.

12. Huang, J.; Mensi, M.; Oveisi, E.; Mantella, V.; Buonsanti, R., Structural Sensitivities in Bimetallic Catalysts for Electrochemical CO_2 Reduction Revealed by Ag-Cu Nanodimers. *J. Am. Chem. Soc.* **2019,** *141* (6), 2490-2499.

13. Iyengar, P.; Huang, J.; De Gregorio, G. L.; Gadiyar, C.; Buonsanti, R., Size dependent selectivity of Cu nano-octahedra catalysts for the electrochemical reduction of CO_2 to CH_4. *Chem. Commun.* **2019,** *55* (60), 8796-8799.

14. Popovic, S.; Smiljanic, M.; Jovanovic, P.; Vavra, J.; Buonsanti, R.; Hodnik, N., Stability and Degradation Mechanisms of Copper-Based Catalysts for Electrochemical CO_2 Reduction. *Angew. Chem., Int. Ed.* **2020,** *59* (35), 14736-14746.

15. De Gregorio, G. L.; Burdyny, T.; Loiudice, A.; Iyengar, P.; Smith, W. A.; Buonsanti, R., Facet-Dependent Selectivity of Cu Catalysts in Electrochemical CO_2 Reduction at Commercially Viable Current Densities. *ACS Catal.* **2020,** *10* (9), 4854-4862.

16. Perez-Gallent, E.; Figueiredo, M. C.; Calle-Vallejo, F.; Koper, M. T., Spectroscopic Observation of a Hydrogenated CO Dimer Intermediate During CO Reduction on Cu(100) Electrodes. *Angew. Chem., Int. Ed.* **2017,** *56* (13), 3621-3624.

17. Hori, Y.; Takahashi, I.; Koga, O.; Hoshi, N., Selective formation of C2 compounds from electrochemical reduction of CO_2 at a series of copper single crystal electrodes. *J. Phys. Chem. B* **2002,** *106* (1), 15-17.

18. Avanesian, T.; Dai, S.; Kale, M. J.; Graham, G. W.; Pan, X.; Christopher, P., Quantitative and Atomic-Scale View of CO-Induced Pt Nanoparticle Surface Reconstruction at Saturation Coverage via DFT Calculations Coupled with in Situ TEM and IR. *J. Am. Chem. Soc.* **2017,** *139* (12), 4551-4558.

19. Barmparis, G. D.; Remediakis, I. N., Dependence on CO adsorption of the shapes of multifaceted gold nanoparticles: A density functional theory. *Phys. Rev. B* **2012,** *86* (8).

20. Duan, X.; Warschkow, O.; Soon, A.; Delley, B.; Stampfl, C., Density functional study of oxygen on Cu(100) and Cu(110) surfaces. *Phys. Rev. B* **2010,** *81* (7).

21. Da Silva, J. L. F.; Barreteau, C.; Schroeder, K.; Blügel, S., All-electron first-principles investigations of the energetics of vicinal Cu surfaces. *Phys. Rev. B* **2006,** *73* (12).

22. Peljhan, S.; Kokalj, A., DFT study of gas-phase adsorption of benzotriazole on Cu(111), Cu(100), Cu(110), and low coordinated defects thereon. *Phys. Chem. Chem. Phys.* **2011,** *13* (45), 20408-17.

23. Grimme, S., Semiempirical GGA-type density functional constructed with a long-range dispersion correction. *J. Comput. Chem.* **2006,** *27* (15), 1787-99.

24. Tyson, W. R.; Miller, W. A., Surface Free-Energies of Solid Metals - Estimation from Liquid Surface-Tension Measurements. *Surf. Sci.* **1977,** *62* (1), 267-276.

25. Mathur, A.; Sharma, P.; Cammarata, R. C., Negative surface energy - Clearing up confusion. *Nat. Mater.* **2005,** *4* (3), 186-186.

26. Zhang, Z.; Wu, Q.; Johnson, G.; Ye, Y.; Li, X.; Li, N.; Cui, M.; Lee, J. D.; Liu, C.; Zhao, S.; Li, S.; Orlov, A.; Murray, C. B.; Zhang, X.; Gunnoe, T. B.; Su, D.; Zhang, S., Generalized Synthetic Strategy for Transition-Metal-Doped Brookite-Phase TiO_2 Nanorods. *J. Am. Chem. Soc.* **2019,** *141* (42), 16548-16552.

27. Kresse, G.; Hafner, J., Ab initio molecular dynamics for liquid metals. *Phys. Rev. B.* **1993,** *47* (1), 558-561.

28. Kresse, G.; Furthmuller, J., Efficient iterative schemes for ab initio total-energy calculations using a plane-wave basis set. *Phys. Rev. B.* **1996,** *54* (16), 11169-11186.

29. Blochl, P. E., Projector augmented-wave method. *Phys. Rev. B.* **1994,** *50* (24), 17953-17979.

30. Perdew, J. P.; Burke, K.; Ernzerhof, M., Generalized Gradient Approximation Made Simple. *Phys. Rev. Lett.* **1996,** *77* (18), 3865-3868.

31. Ramos-Sanchez, G.; Balbuena, P. B., Interactions of platinum clusters with a graphite substrate. *Phys. Chem. Chem. Phys.* **2013,** *15* (28), 11950-9.

32. Monkhorst, H. J.; Pack, J. D., Special Points for Brillouin-Zone Integrations. *Phys. Rev. B* **1976,** *13* (12), 5188-5192.

Chapter 9
Interactions of N-Heterocyclic Carbenes (NHC's) with Pt Surfaces

In this Chapter, I continue thinking about the interactions of ligands with metal surfaces and how they influence structure by considering a molecule that only recently been explored in the realm of nanomaterial and has a chemical diversity that could open wide applications. N-heterocyclic carbenes (NHCs) have shown promise as a phosphine ligand removal agent with a high binding strength through the carbene carbon, but an instability to acid that allows it to be easily removed. Furthermore, NHCs are a class of molecules that can have their chemistry tuned in many ways at the 1 and 3 N positions and at the 4 and 5 C positions. I investigate the possibility of tuning steric interactions between the NHC at the 1 and 3 positions and the surface. It is found that significant atom extraction can be driven with sufficient steric interactions, but adsorption of the ligand is still strong. Therefore, NHC's may have possible application as a ligand that can drive the formation of high Miller index facets.

9.1 Background and Motivation

There has been a recent interest in how NHCs (**Figure 9.1**) interact with different nanomaterials.[1-6] Since they are strong σ – donors and strong π – acceptors,[6-9] NHC ligands can be easily added to nanomaterials, acting as a strong ligand exchange agent with a wide, tunable range of chemistry. Their unique chemistry has showed applications in the self-assembly of nanoparticles[10] or as catalytic enhancers on surfaces.[6, 11, 12] One property, their instability to acid,[7] ensures that it is easy to clean them from nanocrystalline surfaces to open active sites for catalysis and makes ligand exchange with NHCs a useful technique in removing even notoriously hard to remove phosphine ligands.[13] This multistep cleaning procedure is simplified in the case that NHCs are used

directly as ligands in nanomaterial synthesis.[3, 14] For application in colloidal synthesis, this might mean using M-bound NHCs with nonpolar moieties such as hexadecyl or benzyl groups at the 4- and 5- positions.

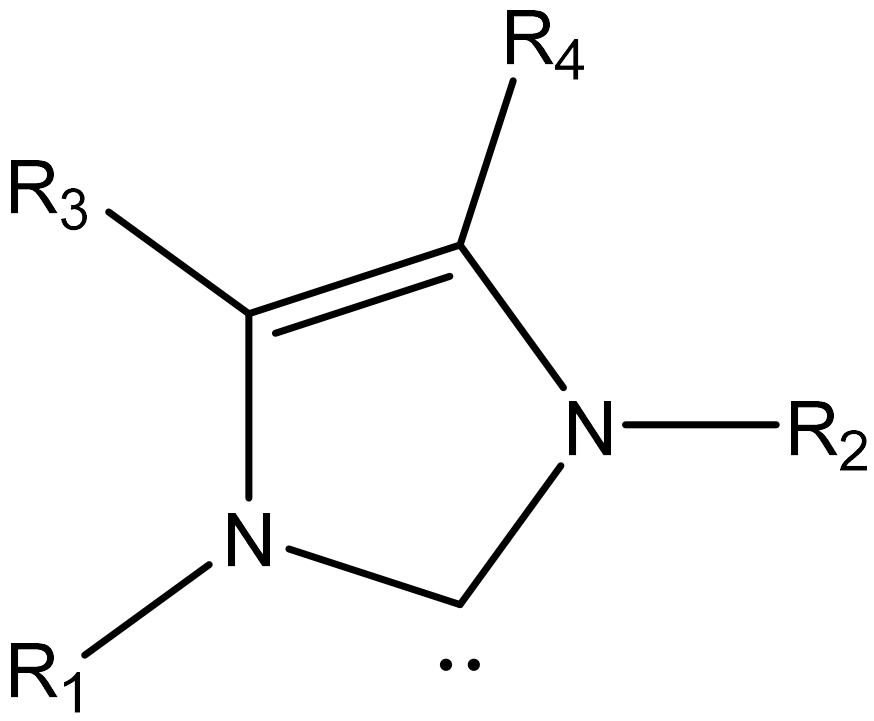

Figure 9.1 N-heterocyclic carbene. Chemical tunability comes from the ability to change the R groups at the 1, 3, 4, and 5 positions of the molecule. In this chapter, $R_3 = R_4 = CH_3$. Two groups are considered at the $R_1 = R_2$ position: R = CH_3 and R = $CH(CH_3)_2$

However, there is the question of how these ligands may influence nanomaterial syntheses broadly. For instance, can tuning the 1- and 3- positions of the carbene be used to stabilize the surface in predictable ways to generate novel nanomaterials? It has been previously shown through a combination of theory and scanning tunneling microscopy that NHCs bound to Au surfaces can result in Au atom abstraction and/or surface reconstruction.[15-18] Therefore, if tunable NHCs can be used to synthesize nanoparticles directly, and they have predilection for forming adatom heavy, reconstructed, or otherwise high Miller index surfaces, then they may be able to generate some particularly reactive nanomaterials with easily cleaned ligands.

With this motivation, the interaction of NHCs on several Pt surfaces was investigated. Both high index ((221) and (211)) and low index ((111) and (100)) facets were probed and it was found that the high index facets bound NHCs more tightly than low index facets. Including isopropyl groups as $R_1 = R_2$ increased the significance of the effect over including methyl groups at the same position. The increase in steric repulsion for the isopropyl group appears to range from 0.7 to 1.6 eV depending on the surface facet.

9.2 Results and Discussion

9.2.1: 1,3,4,5-Tetramethylimidazole-2-ylidene

The adsorption of 1,3,4,5 tetramethylimidazole-2-ylidine (^{Me}IMe) was calculated on the Pt (111), Pt(100), Pt(221), and Pt(211) surfaces. The binding interaction is through the carbene carbon and occurs at atop sties on all surfaces. For the (221) and (211) surfaces, binding occurs at the step edge rather than at the terrace sites. The binding of

^{Me}IMe is strong, ranging from -2.44 eV on the flat (111) surface to -3.01 eV on the stepped (211) surface (**Figure 9.2**). On the flat surfaces, there is a displacement of the Pt in the z direction, normal to the surface, of approximately 0.5 Å. This is in line with a particularly strong C-Pt bond that is expected of NHCs[9] despite deforming the surface as seen with calculations of NHCs on Au (111).[15] On stepped surfaces because the methyl groups have more room, and the NHC can adopt a slanted configuration relative to the surface, the displacement is only about 0.2 Å. This contributes to the increased stability of these configurations.

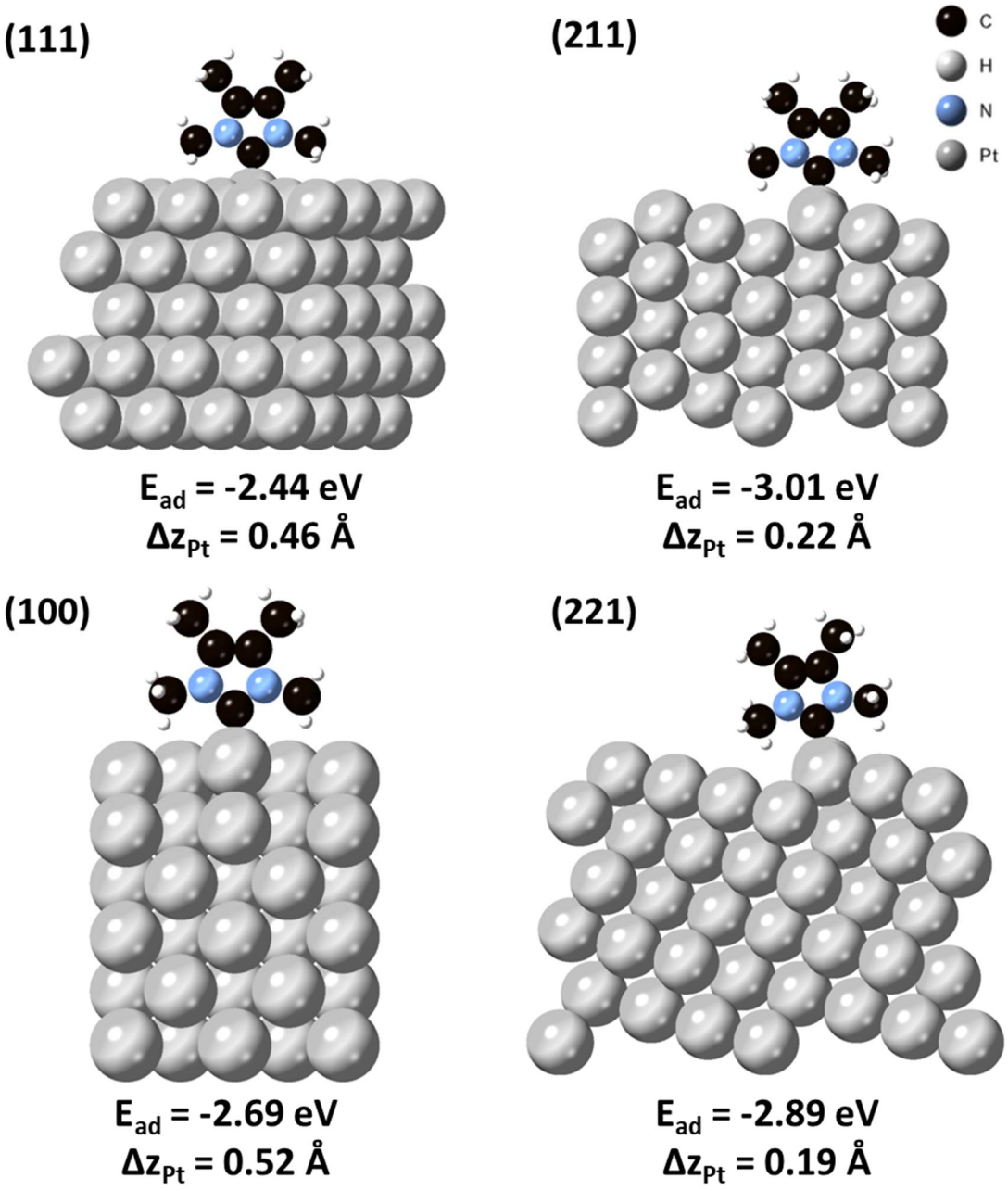

Figure 9.2 DFT optimized models and energies of ^{Me}IMe on Pt (111), Pt(100), Pt(211), and Pt(221) surfaces.

9.2.2: 1,3-Diisopropyl-4,5-dimethylimidazole-2-ylidene

Changing the 1- and 3- positions to isopropyl groups to generate 1,3-diisopropyl-4,5-dimethylimidazole-2-ylidene (^{IPr}IMe) increases the bulkiness adjacent to the surface and greatly increases the steric repulsion. Yet, experimentally it has been shown that they are capable of exchanging with phosphine ligands on nanocrystal surfaces.[13] Therefore, this was the species chosen for studying the steric repulsion with the underlying Pt surface. On the (111) surface steric repulsion decreases the binding energy to -0.88 eV, a reduction of 64%, from the methyl-substituted species. This corresponds with a 1.01 Å displacement of Pt from the top layer. The stepped surfaces, while they accommodate the bulky isopropyl groups more readily than the flat surfaces, there is still a significant decrease in binding energy to -2.09 and -2.01 eV for the (211) and (221) surfaces respectively. The abstraction of the Pt atoms doubles from the ^{Me}IMe system.

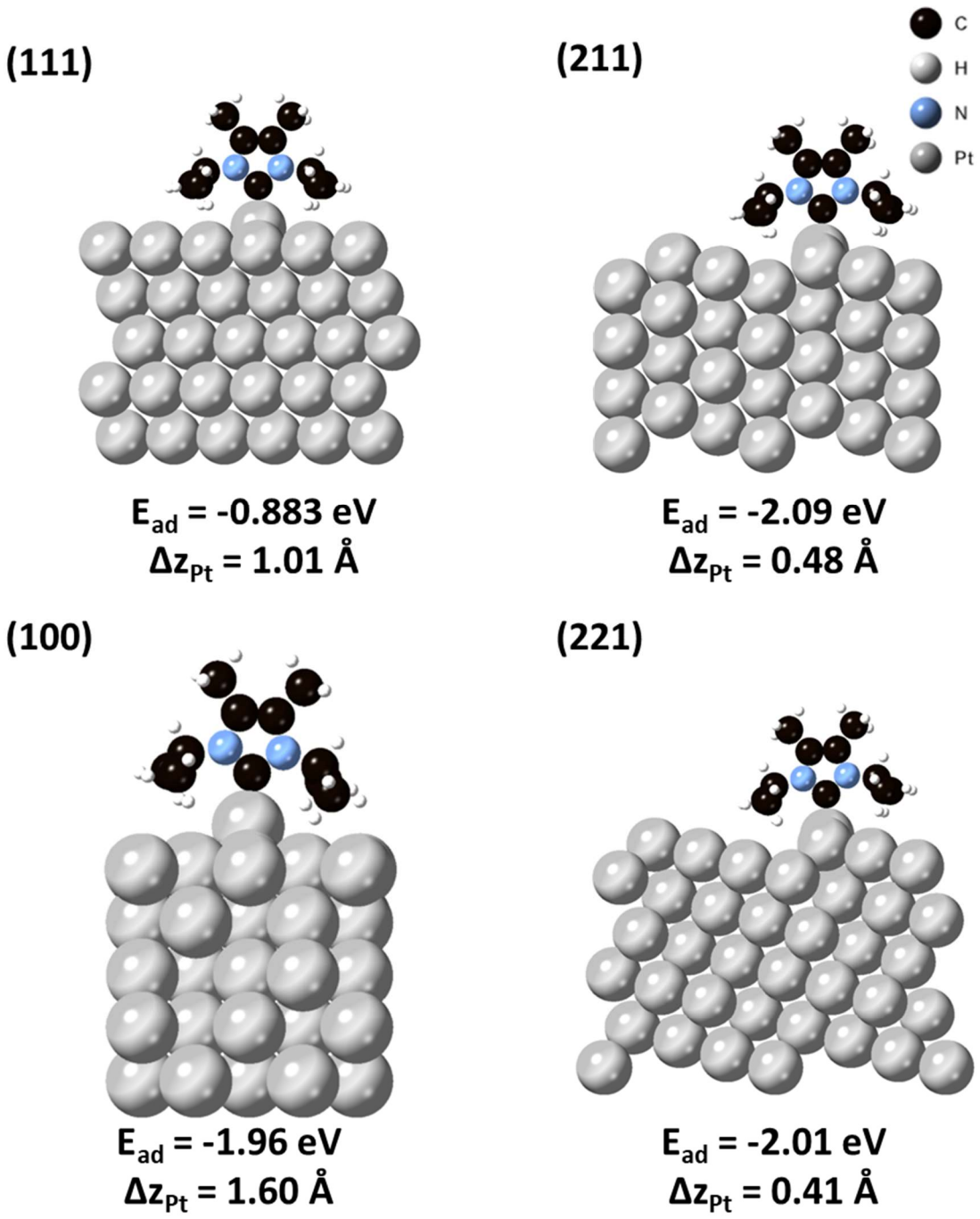

Figure 9.3 DFT optimized models and energies of ^{IPr}IMe on Pt (111), Pt(100), Pt(211), and Pt(221) surfaces.

The (100) surface shows an even more dramatic effect than the (111) surface. The adsorption energy decreases by a less substantial margin on the (100) surface. This is despite a 1.6 Å change in the Pt z position. The Pt atom is essentially abstracted from the top layer and is adsorbed into the adjacent hollow site to form a pyramidal structure (Figure 9.4). This reconstruction apparently relieves a portion of the steric repulsion and there is still significant binding between the ^{IPr}IMe and the (100) surface.

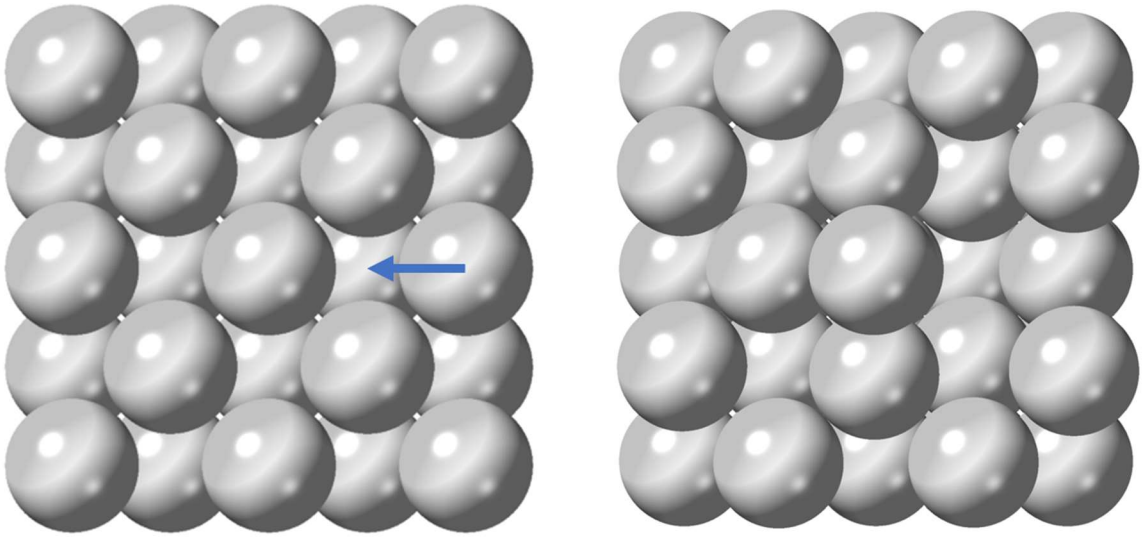

Figure 9.4 DFT model of the Pt (100) surface showing the adsorbate driven abstraction of the surface Pt atom to a pseudo-hollow site.

9.3 Summary

The above calculations point to a sizable difference in the adsorption behavior between ^{Me}IMe and ^{IPr}IMe on the different Pt surfaces. The difference in adsorption energy between high index surfaces and the (111) surface is accentuated with the increase of steric repulsion. The (100) surface also binds ^{IPr}IMe strongly, but only after abstraction of the Pt atom into pyramidal type structures. This suggests that manipulating ligand sterics by introducing bulky groups on at the 1- and 3- positions of the imidazole could be a useful tool synthetically to generate higher energy, coordinatively unsaturated, stepped surfaces or adatom rich surfaces for enhanced catalytic reactivity.

9.4 Calculation Details

Density functional theory (DFT) calculations were performed in the Vienna ab initio simulation package (VASP version 5.2.11)[19] with the projector augmented wave (PAW) pseudopotentials[20] and the Perdew-Burke-Ernzerhof (PBE)[21] exchange correlation functional. An energy cutoff of 400 eV was used for the plane wave basis set. The energy convergence criterion was 10^{-6} eV for each ionic step. The force convergence criterion for geometric optimization was 10^{-2} eV/Å.

Adsorption energy calculations were performed on 5 layer Pt(100) (4x4), 5 layer Pt(111) (3x3), 6 layer Pt(211) (3x2), and 9 layer Pt(221) (3x2) consisting of 160, 180, 144, and 144 atoms each. The unit cells were constructed from the bulk relaxed unit cell with lattice parameter 3.977 Å For the low index surfaces, the bottom 2 layers are frozen to bulk values. The (211) surface has its bottom 3 layers frozen to core values and the (221)

surface has its bottom 4 layers frozen to the bulk values. 15 Å of vacuum in the z direction was added to each cell to avoid interactions between slabs. All supercells were sampled with a 5x5x1 Monkhorst-Pack k-point mesh.[22] The binding energy was calculated by the equation

$$E_B(NHC) = E(NHC + Slab) - E(Slab) - E(NHC) \quad \text{Eq (9.4)}$$

Where E_B is the binding energy, E(NHC + Slab) is the energy of the relaxed NHC adsorbed on the Pt slab, E(Slab) is the energy of the relaxed slab, and E(NHC) is the energy of the relaxed NHC molecule.

9.5 References

1. Ernst, J. B.; Schwermann, C.; Yokota, G. I.; Tada, M.; Muratsugu, S.; Doltsinis, N. L.; Glorius, F., Molecular Adsorbates Switch on Heterogeneous Catalysis: Induction of Reactivity by N-Heterocyclic Carbenes. *J. Am. Chem. Soc.* **2017,** *139* (27), 9144-9147.

2. Smith, C. A.; Narouz, M. R.; Lummis, P. A.; Singh, I.; Nazemi, A.; Li, C. H.; Crudden, C. M., N-Heterocyclic Carbenes in Materials Chemistry. *Chem Rev* **2019,** *119* (8), 4986-5056.

3. Ling, X.; Schaeffer, N.; Roland, S.; Pileni, M. P., Nanocrystals: why do silver and gold N-heterocyclic carbene precursors behave differently? *Langmuir* **2013,** *29* (41), 12647-56.

4. Lu, H.; Zhou, Z.; Prezhdo, O. V.; Brutchey, R. L., Exposing the Dynamics and Energetics of the N-Heterocyclic Carbene-Nanocrystal Interface. *J. Am. Chem. Soc.* **2016,** *138* (45), 14844-14847.

5. Man, R. W. Y.; Li, C. H.; MacLean, M. W. A.; Zenkina, O. V.; Zamora, M. T.; Saunders, L. N.; Rousina-Webb, A.; Nambo, M.; Crudden, C. M., Ultrastable Gold Nanoparticles Modified by Bidentate N-Heterocyclic Carbene Ligands. *J. Am. Chem. Soc.* **2018,** *140* (5), 1576-1579.

6. Cao, Z.; Kim, D.; Hong, D.; Yu, Y.; Xu, J.; Lin, S.; Wen, X.; Nichols, E. M.; Jeong, K.; Reimer, J. A.; Yang, P.; Chang, C. J., A Molecular Surface Functionalization Approach to Tuning Nanoparticle Electrocatalysts for Carbon Dioxide Reduction. *J. Am. Chem. Soc.* **2016,** *138* (26), 8120-5.

7. Munz, D., Pushing Electrons—Which Carbene Ligand for Which Application? *Organometallics* **2018,** *37* (3), 275-289.

8. Narouz, M. R.; Osten, K. M.; Unsworth, P. J.; Man, R. W. Y.; Salorinne, K.; Takano, S.; Tomihara, R.; Kaappa, S.; Malola, S.; Dinh, C. T.; Padmos, J. D.; Ayoo, K.; Garrett, P. J.; Nambo, M.; Horton, J. H.; Sargent, E. H.; Hakkinen, H.; Tsukuda, T.; Crudden, C. M., N-heterocyclic carbene-functionalized magic-number gold nanoclusters. *Nat. Chem.* **2019,** *11* (5), 419-425.

9. Hopkinson, M. N.; Richter, C.; Schedler, M.; Glorius, F., An overview of N-heterocyclic carbenes. *Nature* **2014,** *510* (7506), 485-96.

10. Vignolle, J.; Tilley, T. D., N-heterocyclic carbene-stabilized gold nanoparticles and their assembly into 3D superlattices. *Chem. Commun.* **2009,** (46), 7230-7232.

11. Ye, R.; Zhukhovitskiy, A. V.; Kazantsev, R. V.; Fakra, S. C.; Wickemeyer, B. B.; Toste, F. D.; Somorjai, G. A., Supported Au Nanoparticles with N-Heterocyclic Carbene

Ligands as Active and Stable Heterogeneous Catalysts for Lactonization. *J. Am. Chem. Soc.* **2018,** *140* (11), 4144-4149.

12. Shen, H.; Xu, Z.; Hazer, M. S. A.; Wu, Q.; Peng, J.; Qin, R.; Malola, S.; Teo, B. K.; Hakkinen, H.; Zheng, N., Surface Coordination of Multiple Ligands Endows N-Heterocyclic Carbene-Stabilized Gold Nanoclusters with High Robustness and Surface Reactivity. *Angew. Chem., Int. Ed.* **2021,** *60* (7), 3752-3758.

13. Godbold, P.; Johnson, G.; Obi, A. D.; Brown, R.; Hwang, S.; Gilliard, R. J., Jr.; Zhang, S., Surfactant Removal for Colloidal Nanocrystal Catalysts Mediated by N-Heterocyclic Carbenes. *J. Am. Chem. Soc.* **2021,** *143* (7), 2644-2648.

14. Tappan, B. A.; Chen, K.; Lu, H.; Sharada, S. M.; Brutchey, R. L., Synthesis and Electrocatalytic HER Studies of Carbene-Ligated $Cu_{3-x}P$ Nanocrystals. *ACS Appl. Mater. Interfaces.* **2020,** *12* (14), 16394-16401.

15. Bakker, A.; Timmer, A.; Kolodzeiski, E.; Freitag, M.; Gao, H. Y.; Monig, H.; Amirjalayer, S.; Glorius, F.; Fuchs, H., Elucidating the Binding Modes of N-Heterocyclic Carbenes on a Gold Surface. *J. Am. Chem. Soc.* **2018,** *140* (38), 11889-11892.

16. Amirjalayer, S.; Bakker, A.; Freitag, M.; Glorius, F.; Fuchs, H., Cooperation of N-Heterocyclic Carbenes on a Gold Surface. *Angew. Chem., Int. Ed.* **2020,** *59* (47), 21230-21235.

17. MacLeod, M. J.; Goodman, A. J.; Ye, H. Z.; Nguyen, H. V.; Van Voorhis, T.; Johnson, J. A., Robust gold nanorods stabilized by bidentate N-heterocyclic-carbene-thiolate ligands. *Nat. Chem.* **2019,** *11* (1), 57-63.

18. Jiang, L.; Zhang, B.; Medard, G.; Seitsonen, A. P.; Haag, F.; Allegretti, F.; Reichert, J.; Kuster, B.; Barth, J. V.; Papageorgiou, A. C., N-Heterocyclic carbenes on close-packed coinage metal surfaces: bis-carbene metal adatom bonding scheme of monolayer films on Au, Ag and Cu. *Chem Sci* **2017,** *8* (12), 8301-8308.

19. Kresse, G.; Joubert, D., From ultrasoft pseudopotentials to the projector augmented-wave method. *Phys. Rev. B* **1999,** *59* (3), 1758-1775.

20. Blochl, P. E., Projector augmented-wave method. *Phys. Rev. B.* **1994,** *50* (24), 17953-17979.

21. Perdew, J. P.; Burke, K.; Ernzerhof, M., Generalized Gradient Approximation Made Simple. *Phys. Rev. Lett.* **1996,** *77* (18), 3865-3868.

22. Monkhorst, H. J.; Pack, J. D., Special Points for Brillouin-Zone Integrations. *Phys. Rev. B* **1976,** *13* (12), 5188-5192.

Chapter 10
Surface Enhanced Infrared Absorption Spectroscopy for Reactive Intermediate Observation in Electrochemistry

Portions published as: Gao, Q.; Mou, T. Y.; Liu, S. K.; Johnson, G.; Han, X.; Yan, Z. H.; Ji, M. X.; He, Q.; Zhang, S.; Xin, H. L.; Zhu, H. Y., Monodisperse PdSn/SnOx core/shell nanoparticles with superior electrocatalytic ethanol oxidation performance. *J. Mater. Chem. A* **2020,** *8* (40), 20931-20938.

In this last Chapter, I return to experiment to focus on reactive intermediates that are formed in electrocatalysis. Surface enhanced infrared absorption spectroscopy (SEIRAS) is a technique that takes advantage of the plasmon resonances of nanoparticles to enhance near surface electric field interactions with adsorbed species and improve infrared absorption. In a completed electrochemical cell, the SEIRAS measurements can be taken while electrochemistry is occurring at the working electrode so that electrochemical intermediates may be measured *in-situ* as a function of applied potential. This provides real time information to correlate adsorbed species with different reaction outcomes, providing evidence to develop mechanism level understanding of reactions. In this chapter, I extend the SEIRAS technique, usually performed on nanostructured metal films, to other synthesized PdSn/SnO_x nanomaterials deposited on C for observation of reaction intermediates in the ethanol oxidation.

10.1 Background and Motivation

The identification of reaction intermediates in catalytic pathways is critical to the development of theoretical models necessary for developing improved catalysts. From this information and how it changes with material properties such as shape and composition, computational models can be tuned to work our way towards more predictive tools for catalyst design.[1] This is a challenging task due to the need to perform measurements under reaction conditions to ensure the observation of transient intermediates. Plus, the measurement must be non-destructive to ensure that the reactive surface is equivalent to the real catalyst. For this application, infrared

spectroscopies have been incredible useful as it probes the vibrational modes of adsorbed species with low energy photons that are non-destructive. These modes describe the connectivity of intermediates and can provide information on the sites at which they are adsorbed.[2]

Several *in-situ* methods of infrared spectroscopy have been developed. Reflection absorption infrared spectroscopy (RAIRS) has been used for gas phase surface chemistry in highly tunable ultra-high vacuum (UHV) conditions.[3-5] This technique can provide extremely accurate information for single crystal metal surfaces, but the UHV requirements weaken the relevance to real, high pressure systems.[6] A solution to this issue has come in the form of diffuse reflectance infrared Fourier transform spectroscopy (DRIFTS).[7-11] *In-situ* cells for this technique allow for treatments with various gases at elevated temperatures, and draws measurements closer to realistic conditions. The challenge with this technique, however, is that it requires a powdered catalyst to diffusely scatter the IR light, and for high quality understanding of the catalyst, it must be well synthesized with precise size, shape, and composition. Plus, liquid phase interfaces are impractical for this measurement.

For liquid phase measurements, particularly for electrochemical measurements, SEIRAS – attenuated total reflection (ATR) can be used to achieve *in-situ* measurements.[12-15] In this configuration (**Figure 3.4**), the infrared beam penetrates an ATR crystal (usually Si, Ge, or ZnSe depending on compatibility with other species) from below in a purged gas line, and undergoes total internal reflection at the interface. The evanescent wave interacts with the surface species to generate the spectroscopy. On the ATR crystal, the

catalyst material is deposited and is typically metal such as Pt, Cu, Ag, or Au.[14-17] These metals are given nanostructure to generate surface plasmon effects that increase the interaction of the electric field with the adsorbates. The metal catalyst can be connected in an electrochemical cell to apply different potentials and observe how species change on the surface. Introducing different species at constant potentials may also be a valid means of perturbing the system and identifying intermediates.[18]

In this Chapter, *in-situ* SEIRAS is used to study the ethanol oxidation reaction (EOR). EOR can proceed to CO_2 through a C-C cleavage route or acetate if C-C cleavage is inhibited and is a key component of direct ethanol fuel cells to generate electricity from biomass.[19, 20] Complications for this reaction, such as poor reaction kinetics and catalyst poisoning from CO and acetyl (*CH_3CO), need to be resolved before it is used in the green energy economy.[21] Pd based catalysts in particular are prone to poisoning but do show significant activation of ethanol.[22, 23] Adding a poor CO binding metal, Sn, is adopted as a strategy to improve EORl by reducing the effects of catalyst poisoning.[24, 25] PdSn/SnO_x core shell nanoparticles are generated that demonstrate 3.2 times higher EOR than commercial Pd.[26] Comparing the core-shell and Pd nanocatalysts in SEIRAS, direct confirmation that CO poisoning is reduced is achieved.

10.2 Results and Discussion

10.2.1 PdSn/SnO_x Nanoparticles Synthesis and Characterization

The PdSn/SnO_x nanoparticles are shown in **Figure 10.1**. The nanoparticles are uniform in size with dimensions of 4.5 +/- 0.5 nm. They appear to contain a crystalline

core and an amorphous shell that is 0.5 nm thick (**Figure 10.1 B**). The lattice fringes are attributable to the (111) planes of PdSn. XRD of these particles shows the (111) peak of PdSn but does not show any peaks associated with crystalline SnO_x as expected for amorphous materials. EDS mapping (**Figure 10.1 C, F**) show that the amorphous shell is comprised of Sn and is relatively Pd poor. Overall, EDS and ICP-OES show a 1:1 ratio of Pd:Sn as expected from the feeding ratio for the synthesis. Other Pd:Sn ratios were also synthesized but were not used in the SEIRAS component of this research.

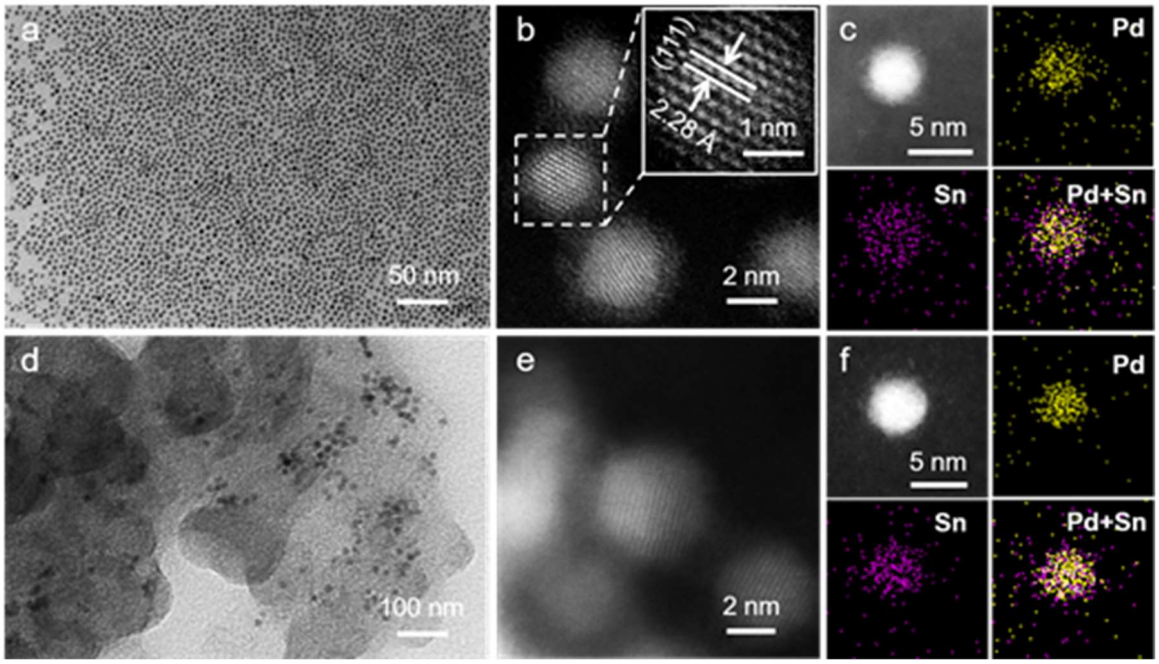

Figure 10.1 A) TEM image of $PdSn/SnO_x$ nanoparticles **B**) High magnification STEM – HAADF image of the $PdSn/SnO_x$ nanoparticles. A crystalline core is clearly visible within a 0.5 nm amorphous shell. **C**) STEM-HAADF image with EDS mapping of $PdSn/SnO_x$ nanoparticle. **D**) TEM image of $PdSn/SnO_x$ nanoparticles deposited on C. **E**) High magnification STEM-HAADF image of C-$PdSn/SnO_x$ catalyst. **F**) STEM-HAADF image with EDS mapping of C-$PdSn/SnO_x$ nanoparticles.

The nanoparticles were supported on C (**Figure 10.1 D**) to prepare for EOR. The particles were washed with acetic acid to remove ligands from the surface. The core-shell morphology of the nanoparticles is retained after acetic acid washing, but the shell is reduced slightly in thickness (**Figure 10.1 E**).

XPS measurements were performed for C-PdSn/SnO_x nanoparticles before and after the acetic acid treatment (**Figure 10.2**) The Pd $3d_{5/2}$ peak (**Figure 10.2 A,B**) is upshifted 0.5 eV relative to Pd^0 to 335.4 eV in both cases, without significant change between treatments. This suggests an electronic modulation of the Pd electronic state by the Sn and SnO_x interface of the nanoparticles. The Sn $3d_{5/2}$ peak (**Figure 10.2 C,D**) shows two major components consisting of the core component (Sn^0) and the amorphous shell component (Sn^{4+}). The ratio of Sn^0 to Sn^{4+} increases upon acetic acid treatment, further supporting the loss of Sn from the amorphous shell in the acetic acid treatment. The O 1s spectrum (**Figure 10.2 E,F**) is deconvoluted into 3 peaks at 530.2 eV, 531.7 eV, and 532.8 eV that correspond to lattice O in SnO_x, adsorbed O species, and H_2O species respectively. The lattice O component, like the Sn^{4+} component, decreases after the acetic acid treatment.

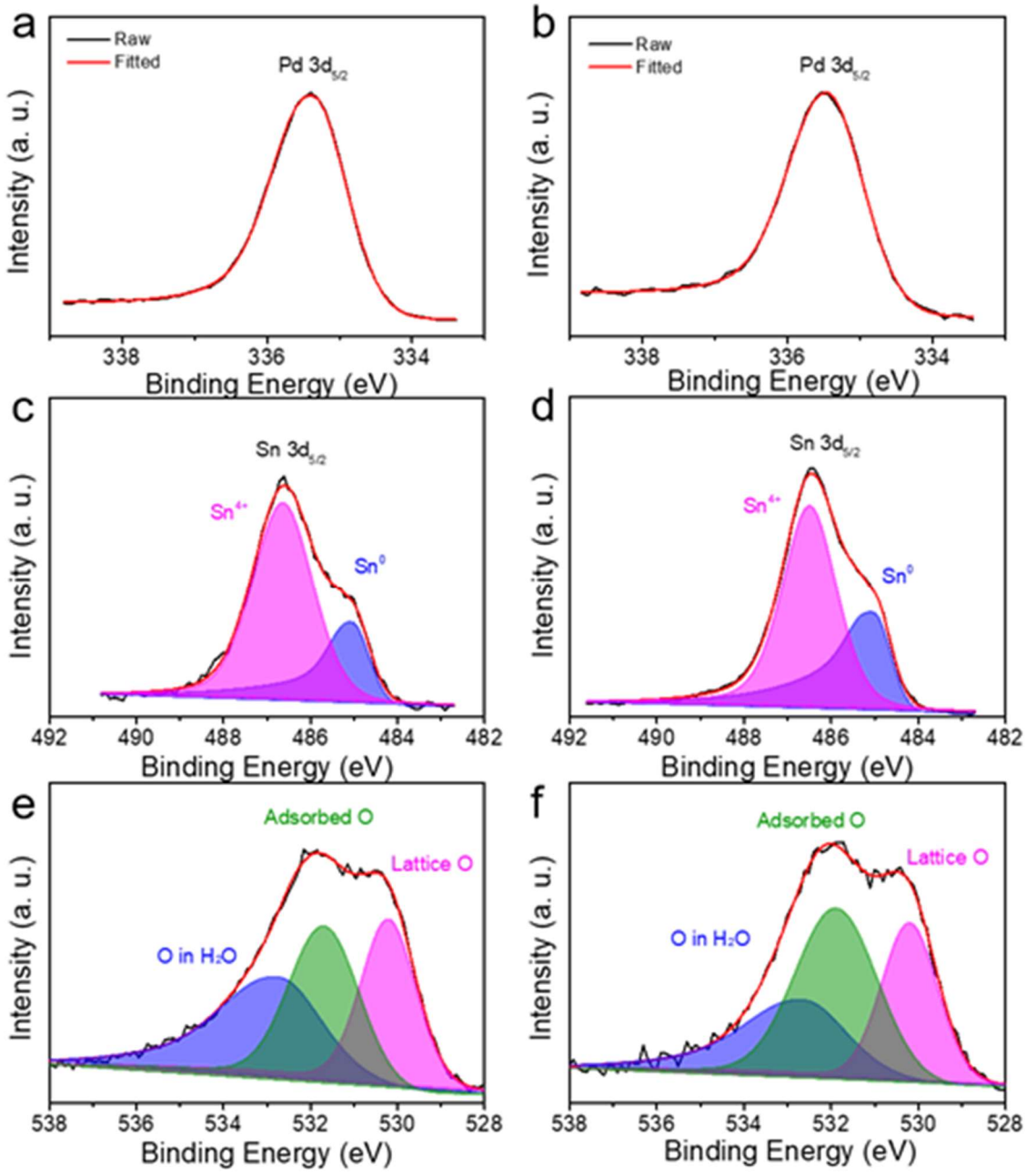

Figure 10.2 High-resolution XPS spectra of (**a, b**) Pd $3d_{5/2}$, (**c, d**) Sn $3d_{5/2}$ and (**e, f**) O 1s of the C-PdSn/SnO_x nanoparticles before (**a, c, e**) and after acetic acid treatment (**b, d, f**).

10.2.2 EOR Measurements

Catalysts (C-PdSn/SnO_x, C-Pd, commercial C-Pd, and C-SnO) were cleaned and activated with cyclic voltammetry (CV) scanning in N_2 saturated 1M KOH and 1 M Ethanol over 50 cycles at room temperature with a scan rate of 250 mV/s. Measurements were performed in the same conditions at 50 mV/s (**Figure 10.3**). The C-PdSn/SnO_x catalyst demonstrated superior activity (3.2 A/mg_{Pd} at 0.85 V_{RHE}) to the C-Pd and the C-SnO reference catalysts with the SnO catalyst demonstrating no activity whatsoever and the C-Pd catalysts maxing at 1 A/mg_{Pd} at 0.83 V_{RHE}. The onset potential of C-PdSn/SnO_x was 80 mV lower than that of the commercial C-Pd, demonstrating that EOR is more favorable on the core-shell structure. The ratio of the forward to reverse peaks yields information about the resistance to poisoning with high ratios suggesting a more tolerant surface. This ratio is higher for the C-PdSn/SnO_x catalyst (0.84) than the commercial C-Pd (0.634) showing that the new catalyst is not as easily poisoned. The electrochemically active surface area can be estimated from the integrated peak area of PdO reduction in N_2 saturated 1 M KOH (**Figure 10.3 C**). The C-PdSn/SnO_x catalyst demonstrates a significantly enhanced surface area relative to the commercial Pd catalyst. Even normalizing to this surface area, however, the C-PdSn/SnO_x catalyst retains an edge in EOR activity (**Figure 10.3 D**). The primary liquid product from this catalysis is acetate as determined by ^1H NMR spectroscopy while the primary gaseous product is CO_2.

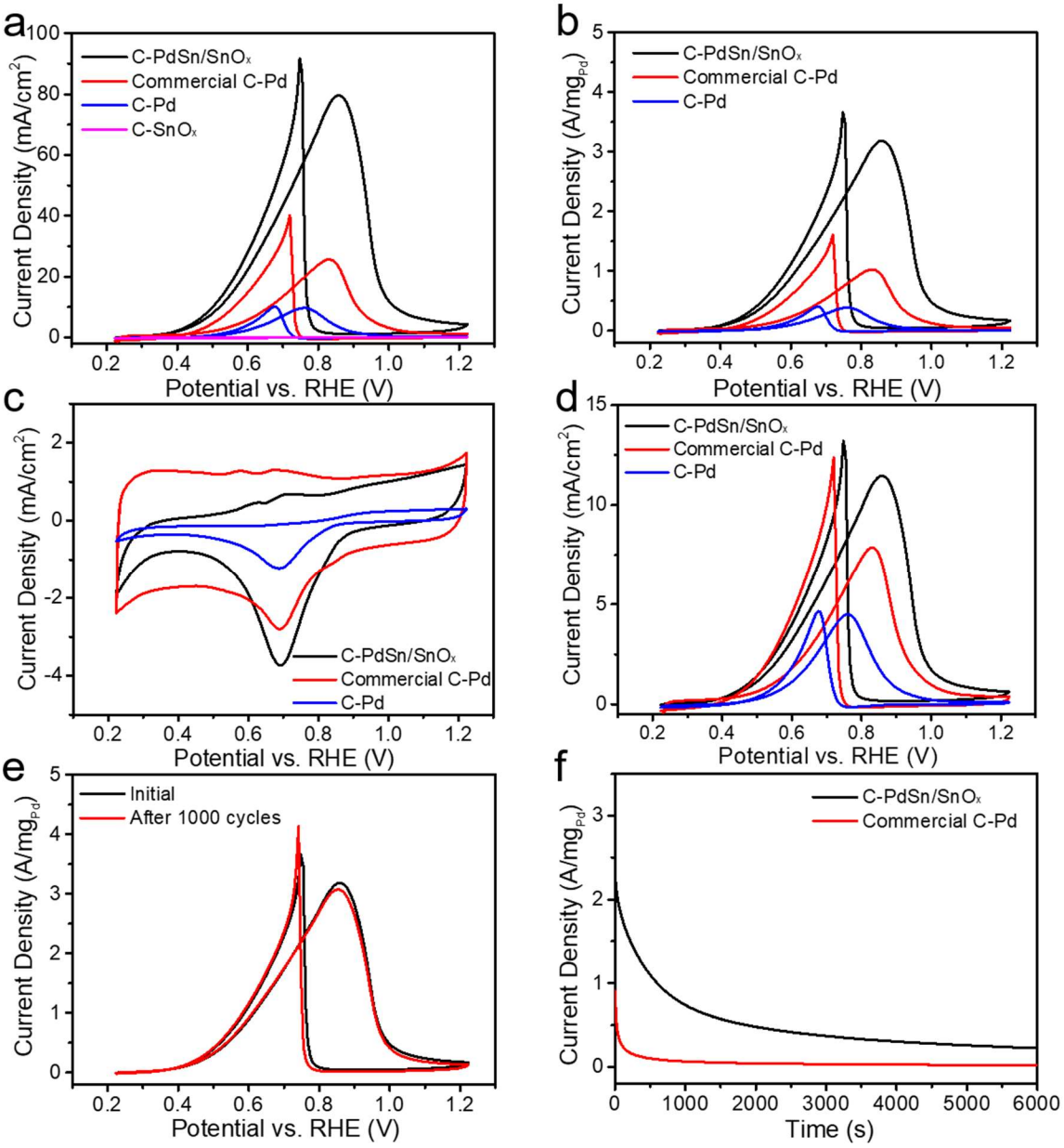

Figure 10.3 (**A**) CV curves of ethanol oxidation for C-PdSn/SnOx, C-Pd, C-SnO and commercial C-Pd catalysts in 1 M KOH + 1 M ethanol (normalized to the electrode geometric area). (**B**) The mass current density (normalized to the mass of Pd) of C-PdSn/SnOx C-Pd, and commercial C-Pd catalysts. (**C**) CV curves for C-PdSn/SnOx, C-Pd, and commercial C-Pd catalysts in 1 M KOH. (**D**) The ECSA-normalized EOR activity for C-PdSn/SnOx, C-Pd, and commercial C-Pd catalysts. (**E**) EOR CV curves of C-PdSn/SnOx before and after 1000 cycles of accelerated stability tests. (**F**) Chronoamperometric curves of C-PdSn/SnOx and commercial C-Pd catalyst at 0.824 V vs. RHE electrode in 1 M KOH+1 M ethanol

The activity of the C-PdSn/SnOx was submitted to a stress test of 1000 cycles of CV measurements and retained the majority of its activity (Figure 10.3 E). In long term chronoamperometry experiments, commercial Pd quickly deactivates while the C-PdSn/SnO_x catalyst retains some activity throughout. Structural characterization post stress test shows that morphological changes in commercial Pd occur but the core shell C-PdSn/SnO_x catalysts are retained. Thus, it is thought that the SnO_x shell provides some protection against agglomeration.

10.2.3 ATR-SEIRAS

In-situ ATR-SEIRAS measurements were carried out to identify the intermediates of the EOR process. **Figure 10.4** shows the ATR-SEIRAS spectra results collected from C-PdSn@SnOx and commercial Pd/C during a CV cycle between 0.565 V_{RHE} and 1.165 V_{RHE} at 5 mV/s in 0.1 M KOH and 1 M ethanol solution and referenced to 1.60 V_{RHE}. The Au film, activated through at least 30 cycles between -0.3 V_{RHE} and 1.2 V_{RHE} to generate a nanostructured surface, is fragile to high pH values and therefore, the 1 M KOH electrolyte used in the electrochemical characterization could not be used. The reference spectrum was selected at a highly oxidative potential to minimize adsorbed intermediates on the surface. Rather, the catalyst is in an oxidized, inactive form. Spectra measured against this reference will contain positive peaks for species building on the surface and negative peaks for species that disappear from the reference state.

As shown in a previous report, the absorptions observed at 1415 and 1553 cm^{-1} can be attributed to the symmetric and asymmetric stretching band of ν(OCO) in the acetate product, respectively, and the absorption between 1665-1830 cm^{-1} is due

primarily to CO_{ad} species [$\nu(CO_{ad})$].[27, 28] It should be noted, however, that there is a water peak near 1656 cm^{-1} that is convoluted with this broad peak. This is primarily due to replacement of adsorbed oxide species at the reference (1.60 V_{RHE}) by water and is ubiquitous in SEIRAS measurements.[29] This water need not be at the Pd or PdSn interface, and it is the only peak present in measurements containing only the underlying Au film.

The vibrational peak at 1830 cm^{-1} of C-PdSn@SnOx is commonly assigned to bridge-bonded CO on Pd.[30] The presence of this peak suggests that despite being a predominantly amorphous SnO_x shell as synthesized, some Pd is present at the surface, agreeing with ECSA measurements. Likely the acetic acid wash opened up holes in the SnO_x shell, which was only around 2 or 3 ML thick to begin with. The form of the Pd is such that ensembles are present to generate multifold binding sites rather than single atom like sites. As the potential increases, the peak gradually disappears due to the oxidative removal of CO (**Figure 10.4 A**), while the CO signal grew in the ATR-SEIRAS spectra of commercial Pd/C over the entire potential range (**Figure 10.4 B**). Notably, this peak shifts to higher wavenumber with increasing coverage as is expected from the dipole-dipole coupling of CO on surfaces.[14, 31] The CO peak on PdSn/SnO_x disappears around the peak voltage of indicated in **Figure 10.3 A,B,D.** This is where oxides begin to take up surface space and block reactivity. On Pd, CO persists even through part of the oxide region, not disappearing until at least 1.2 V_{RHE}.

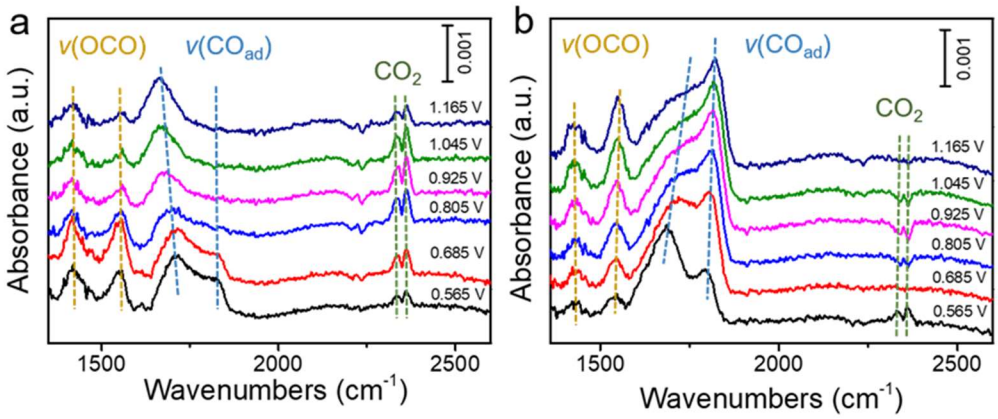

Figure 10.4 ATR-SEIRAS Spectra of **A**) C-PdSn/SnO_x and **B**) commercial Pd/C during CV cycling between 0.565 V_{RHE} and 1.165 V_{RHE} at 5 mV/s in 0.1 M KOH and 1 M ethanol solution. Measurements were taken in the positive direction (from top to bottom). CO_2 signal is a direct result of CO_2 generation and fluctuations of CO_2 that occur in the IR beamline.

The v(OCO) peaks follows a similar trend as CO, although with much smaller dipole dependencies shifting their peaks. Above the peak potential, some acetate is still being produced on PdSn/SnO_x but at a reduced rate. On Pd, however, both acetate and CO are strongly bound throughout the oxidative potentials. This means that both intermediates, rather than just CO, can contribute to poisoning at these potentials.

The stability of the adsorbed species in the negative going scan after the positive sweep may also be observed. The CO region of the spectrum is blank after being cleared at the highest potential in both cases, and shows a step jump at the onset of the return peak observed in the CV. On the negative scan, CO is observed to persist to the lowest voltages measured (-0.115 V_{RHE}) on both catalysts. The acetate species (OCO) peaks, however, disappear below 0.475 V_{RHE} on PdSn/SnOx (**Figure 10.5 A**). On the Pd catalyst, acetate disappears below 0.005 V_{RHE} (**Figure 10.5 B**). This suggests that, while we observe better performance from PdSn/SnO_x, its ability to activate ethanol is actually lower than that of pure Pd.

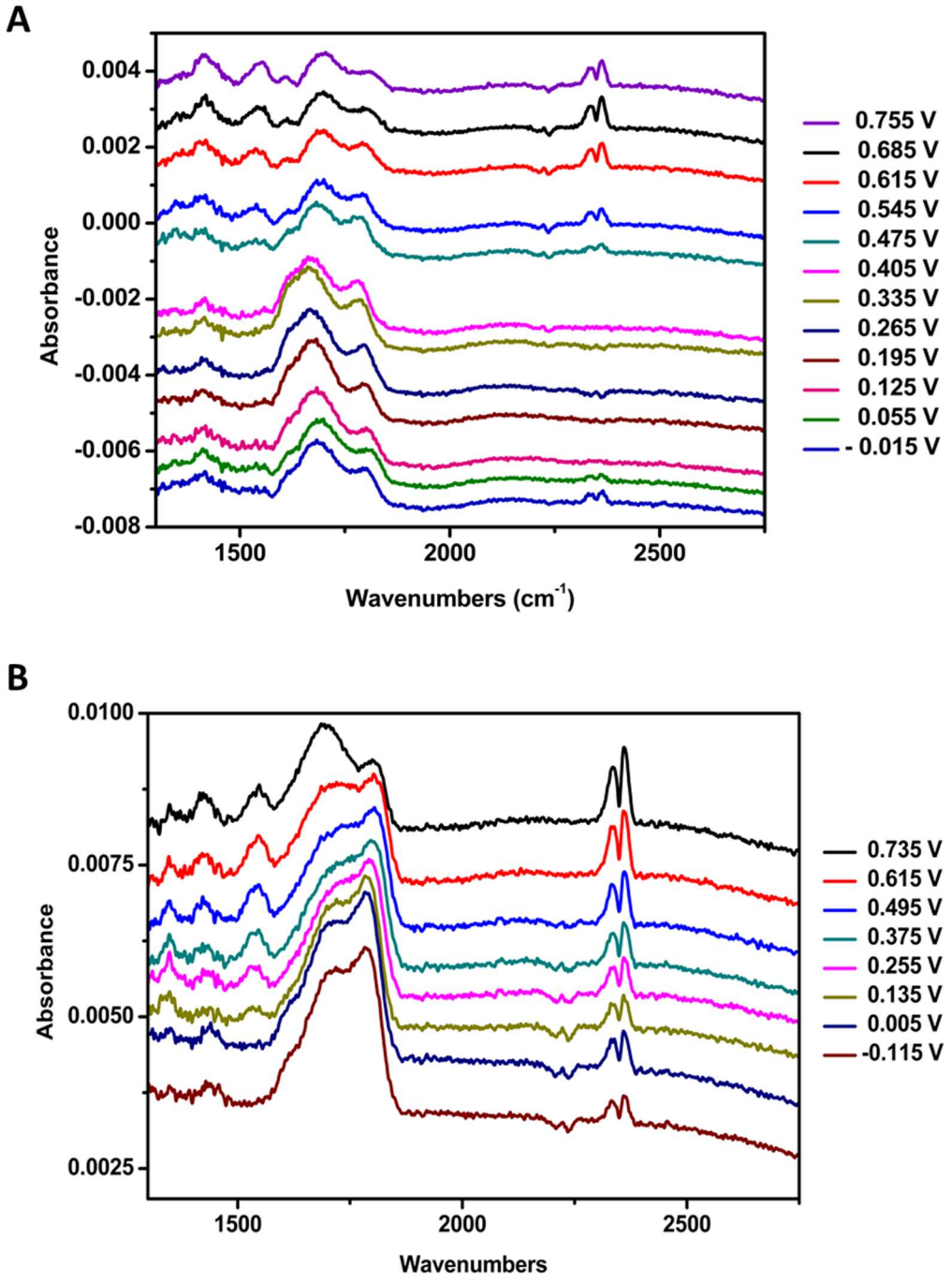

Figure 10.5 ATR-SEIRAS Spectra of **A**) C-PdSn/SnO_x and **B**) commercial Pd/C during CV cycling between 0.755 V_{RHE} and -0.115 V_{RHE} at 5 mV/s in 0.1 M KOH and 1 M ethanol solution. Measurements were taken in from top to bottom. CO_2 is gas phase intruding into the IR beamline.

10.3 Summary

In this chapter, a PdSn/SnO_x core shell nanocatalyst was discussed for EOR. The catalyst as synthesized has a 0.5 nm amorphous SnO_x shell that is weakened upon acetic acid washing. This catalyst shows enhanced performance on a per surface area basis relative to Pd and SnO separately. SEIRAS is used to show that poisoning is significantly reduced on the Sn containing catalyst, in agreement with the electrochemical measurements. Multifold Pd sites on shown to be accessible by the reactant due to the presence of CO in multifold binding sites. Combined with the evidence of losses from the amorphous shell, it is possible that the shell has holes after the acetic acid wash that permits reactant penetration. Finally, the ability of each catalyst to activate ethanol is examined with SEIRAS. Acetate from the early stages of EOR is observed until 0.005 V_{RHE} on Pd but production halts at 0.475 V_{RHE} on PdSn/SnO_x, showing that Pd despite being the worse overall catalyst, is superior at activating ethanol.

10.4 Experimental

Chemicals

Palladium(II) chloride ($PdCl_2$, 99%), tin acetate ($Sn(OAc)_2$, 99%), oleylamine (OAm, 70%), trioctylphosphine (TOP, 90%), potassium hydroxide (KOH), acetic acid, hydrazine, and Nafion (5 wt %) were all purchased from Sigma-Aldrich. Hexane and ethanol were technical grade and used without further purification.

Synthesis of monodisperse PdSn/SnO_x nanoparticles

In a typical procedure, 0.1 mmol of $PdCl_2$, 0.1 mmol of $Sn(OAc)_2$, 10 mL OAm and 0.5 mL TOP were added into a 50 mL three-necked flask under stirring. The mixture was heated under nitrogen (N_2) atmosphere to 100 °C and kept at this temperature for 30 mins. Then the mixture was heated to 200 °C at a heating rate of 10 °C/min and incubated at this temperature for 30 min, generating a black solution. After cooling down to room temperature, the black precipitate was centrifuged and washed three times with excessive ethanol and redispersed in hexane. $PdSn/SnO_x$ nanoparticles with different Pd/Sn ratios were synthesized using a similar approach by varying the amounts of metal precursors. SnO aggregates were obtained using a similar approach without adding Pd precursor, while 25 nm Pd nanoparticles were obtained at a higher temperature of 300 °C without adding Sn precursor.

Preparation of C-$PdSn/SnO_x$ catalysts (10% loading)

To prepare our C-$PdSn/SnO_x$ catalysts, we mixed a hexane dispersion of 5 mg of $PdSn/SnO_x$ nanoparticles with 45 mg activated carbon (Vulcan XC-72R) and sonicated for 2 h. The product was then collected by centrifugation. In order to remove organic ligands on the surface of these $PdSn/SnO_x$ nanoparticles, the catalysts were immersed in a mixture of 10 mL ethanol and 10 mL acetic acid for 10 h at 70 °C according to our previous work[32, 33]. The catalysts were washed three times with excessive ethanol and dried for 8 h in a vacuum oven at 60 °C.

Characterization

The morphology was characterized by the transmission electron microscopy (TEM, EM-420). High-resolution TEM (HRTEM), high-angle annular dark-field scanning TEM (HAADF-STEM), X-ray energy dispersive spectroscopy (X-EDS) and EDS mapping were conducted on a JEOL ARM 200CF equipped with an Oxford Instrument X-ray Energy Dispersive Spectrometer. The crystal structure was determined by the X-ray diffraction (XRD) on a Philips X' Pert PRO SUPER with Cu Kα (λ = 1.54056 Å). X-ray photoelectron spectroscopy (XPS) was performed on a PHI Versa Probe III scanning XPS microscope using a monochromatic Al K-alpha X-ray source (1486.6 eV). The element contents of the products were determined by inductively coupled plasma optical emission spectrometry (ICP-OES) on a SPECTRO GENESIS ICP spectrometer. Fourier transform infrared spectroscopy (FTIR) was performed on an Agilent Cary 630. Liquid products were analyzed by ^{1}H NMR using dimethyl sulfoxide (DMSO) as an internal standard.

Electrochemical Measurements

Electrochemical measurements were conducted on a BioLogic electrochemical workstation using a three-neck-type cell at room temperature. Pt foil was used as the counter electrode and Ag/AgCl (3.5 M KCl) was used as the reference electrode. The potential was converted to RHE according to E (vs. RHE) = E (vs. Ag/AgCl) + 0.198 V + 0.059 × pH. A glassy carbon rotating disk electrode (RDE) (PINE, 5 mm diameter, 0.19625 cm^2) was used as the substrate for catalysts. The preparation method of the working electrode can be found as follows: 5 mg of carbon-supported catalyst powder was dispersed in 1mL isopropanol with 20 μL of Nafion solution (5 wt%, Sigma-Aldrich), then the mixture was ultrasonicated for at least 30 min to generate a homogeneous ink. Next, 20 μL of the

dispersion was drop-casted onto the RDE, leading to a Pd loading ~25 μg/cm^2. For comparison, the Pd loadings for C-Pd, and commercial C-Pd were ~25 μg/cm^2 as well. Finally, the as-prepared catalyst on RDE was dried at room temperature. Before the electrochemical tests, surface cleaning and activating was executed by cyclic voltammetry (CV) scanning to reach a steady-state in N_2-saturated 1 M KOH + 1 M ethanol solution for 50 cycles at room temperature with a sweep rate of 250 mV/s. CV curves were then recorded at a scan rate of 50 mV/s in N_2-saturated 1 M KOH + 1 M ethanol solution. Chronoamperometry (CA) measurements were conducted at -0.2 V vs. Ag/AgCl for 6000 s in the 1 M KOH + 1 M ethanol solution for stability evaluation. For CO stripping tests, electro-oxidation of adsorbed CO molecules was carried out in the solution of 1 M KOH. Before the test, the solution was purged with N_2 for 30min and then bubbled with CO gas (99.99%) for 15 min. The residual CO in the solution was purged by N_2 for 30 min.

***In-situ* attenuated total reflectance surface enhanced infrared absorption spectroscopy (ATR-SEIRAS) experiments.**

Experiments were conducted in a one compartment PEEK spectroelectrochemical cell with the VeeMAXIII ATR accessory. A graphite rod counter electrode and a saturated Ag/AgCl reference electrode controlled by a Metrohm Autolab potentiostat were used. IR measurements were performed in a Thermo Nicolet iS50 FTIR equipped with a liquid nitrogen cooled MCT detector. All spectra were collected with a 4 cm^{-1} resolution and 32 coadded scans. Each set of 32 spectra takes approximately 12 s to complete, so at the potential sweep rate of 5 mV/s, each spectrum averages ~60 mV. A modified chemical

deposition method was used to generate Au film electrodes on the reflecting plane of Si ATR crystal prisms cut to 60° incidence.[34] The Au film working electrode was cycled from -0.3 V_{RHE} to 1.2 V_{RHE} in N_2 purged 0.1 M $KHCO_3$ (Sigma Aldrich 99.7%) until the CO absorption frequency at ~2100 cm^{-1} was observed, indicating infrared surface enhancement. The activated film was rinsed with DI water and dried to remove the $KHCO_3$ electrolyte and residues from the crystal. A catalyst ink was prepared by sonicating in an ice bath a mix 1 mg of the carbon supported catalyst in 1 mL of isopropanol and 10 µL Nafion solution (5 wt%). Next, 250 µL of the desired catalyst ink was drop cast onto the film and dried. The reassembled cell was filled with 5 mL of 0.1 M KOH and N_2 purged for at least 30 minutes. All SEIRAS experiments were performed in 1 M ethanol/ 0.1 M KOH solution.

10.5 References

1. Somorjai, G. A.; Kliewer, C. J., Reaction selectivity in heterogeneous catalysis. *Reaction Kinetics and Catalysis Letters* **2009,** *96* (2), 191-208.

2. Meunier, F. C., Relevance of IR Spectroscopy of Adsorbed CO for the Characterization of Heterogeneous Catalysts Containing Isolated Atoms. *J. Phys. Chem. C* **2021,** *125* (40), 21810-21823.

3. Zaera, F.; Chrysostomou, D., Propylene on Pt(111) I. Characterization of surface species by infra-red spectroscopy. *Surf. Sci.* **2000,** *457* (1-2), 71-88.

4. Chrysostomou, D.; French, C.; Zaera, F., The thermal activation of propyl groups on Pt(111). *Catal. Lett.* **2000,** *69* (3-4), 117-128.

5. Krooswyk, J. D. K., Christopher M.; Trenary, Michael, In-Situ Spectroscopic Monitoring of the Ambient Pressure Hydrogenation of C_2 to Ethane on Pt(111). *Surf. Sci.* **2016**.

6. Woodruff, D. P., Bridging the pressure gap: Can we get local quantitative structural information at 'near-ambient' pressures? *Surf. Sci.* **2016,** *652*, 4-6.

7. Wang, Q.; Tichit, D.; Meunier, F.; Guesmi, H., Combined DRIFTS and DFT Study of CO Adsorption and Segregation Modes in Pt-Sn Nanoalloys. *J. Phys. Chem. C* **2020,** *124* (18), 9979-9989.

8. Cui, M.; Johnson, G.; Zhang, Z.; Li, S.; Hwang, S.; Zhang, X.; Zhang, S., AgPd nanoparticles for electrocatalytic CO_2 reduction: bimetallic composition-dependent ligand and ensemble effects. *Nanoscale* **2020,** *12* (26), 14068-14075.

9. Kale, M. J.; Christopher, P., Utilizing Quantitative in Situ FTIR Spectroscopy To Identify Well-Coordinated Pt Atoms as the Active Site for CO Oxidation on Al_2O_3-Supported Pt Catalysts. *ACS Catal.* **2016,** *6* (8), 5599-5609.

10. Sápi, A.; Halasi, G.; Kiss, J.; Dobó, D. G.; Juhász, K. L.; Kolcsár, V. J.; Ferencz, Z.; Vári, G.; Matolin, V.; Erdőhelyi, A.; Kukovecz, Á.; Kónya, Z., In Situ DRIFTS and NAP-XPS Exploration of the Complexity of CO_2 Hydrogenation over Size-Controlled Pt Nanoparticles Supported on Mesoporous NiO. *J. Phys. Chem. C* **2018,** *122* (10), 5553-5565.

11. Zhou, Y.; Doronkin, D. E.; Chen, M. L.; Wei, S. Q.; Grunwaldt, J. D., Interplay of Pt and Crystal Facets of TiO_2: CO Oxidation Activity and Operando XAS/DRIFTS Studies. *ACS Catal.* **2016,** *6* (11), 7799-7809.

12. Xue, X. K.; Wang, J. Y.; Li, Q. X.; Yan, Y. G.; Liu, J. H.; Cai, W. B., Practically modified attenuated total reflection surface-enhanced IR absorption spectroscopy for high-quality frequency-extended detection of surface species at electrodes. *Anal. Chem.* **2008,** *80* (1), 166-71.

13. Morhart, T. A.; Unni, B.; Lardner, M. J.; Burgess, I. J., Electrochemical ATR-SEIRAS Using Low-Cost, Micromachined Si Wafers. *Anal. Chem.* **2017,** *89* (21), 11818-11824.

14. Papasizza, M.; Cuesta, A., In Situ Monitoring Using ATR-SEIRAS of the Electrocatalytic Reduction of CO_2 on Au in an Ionic Liquid/Water Mixture. *ACS Catal.* **2018,** *8* (7), 6345-6352.

15. Corson, E. R.; Kas, R.; Kostecki, R.; Urban, J. J.; Smith, W. A.; McCloskey, B. D.; Kortlever, R., In Situ ATR-SEIRAS of Carbon Dioxide Reduction at a Plasmonic Silver Cathode. *J. Am. Chem. Soc.* **2020**.

16. Katayama, Y.; Giordano, L.; Rao, R. R.; Hwang, J.; Muroyama, H.; Matsui, T.; Eguchi, K.; Shao-Horn, Y., Surface (Electro)chemistry of CO_2 on Pt Surface: An in Situ Surface-Enhanced Infrared Absorption Spectroscopy Study. *J. Phys. Chem. C* **2018,** *122* (23), 12341-12349.

17. Malkani, A. S.; Dunwell, M.; Xu, B., Operando Spectroscopic Investigations of Copper and Oxide-Derived Copper Catalysts for Electrochemical CO Reduction. *ACS Catal.* **2018,** *9* (1), 474-478.

18. Yang, Y. Y.; Cai, W. B., Self assembly of iron protoporphyrin and its binding with carbon monoxide on dithiol modified gold electrode as probed by in situ ATR-SEIRAS. *J. Electroanal. Chem.* **2013,** *688*, 379-383.

19. Antolini, E., Catalysts for direct ethanol fuel cells. *J. Power Sources* **2007,** *170* (1), 1-12.

20. An, L.; Zhao, T. S., Transport phenomena in alkaline direct ethanol fuel cells for sustainable energy production. *J. Power Sources* **2017,** *341*, 199-211.

21. Wang, P.; Yin, S.; Wen, Y.; Tian, Z.; Wang, N.; Key, J.; Wang, S.; Shen, P. K., Ternary Pt_9RhFe_x Nanoscale Alloys as Highly Efficient Catalysts with Enhanced Activity and Excellent CO-Poisoning Tolerance for Ethanol Oxidation. *ACS Appl. Mater. Interfaces.* **2017,** *9* (11), 9584-9591.

22. Iqbal, M.; Kaneti, Y. V.; Kim, J.; Yuliarto, B.; Kang, Y. M.; Bando, Y.; Sugahara, Y.; Yamauchi, Y., Chemical Design of Palladium-Based Nanoarchitectures for Catalytic Applications. *Small* **2019,** *15* (6), e1804378.

23. Bianchini, C.; Shen, P. K., Palladium-based electrocatalysts for alcohol oxidation in half cells and in direct alcohol fuel cells. *Chem Rev* **2009,** *109* (9), 4183-206.

24. Ding, L. X.; Wang, A. L.; Ou, Y. N.; Li, Q.; Guo, R.; Zhao, W. X.; Tong, Y. X.; Li, G. R., Hierarchical Pd-Sn Alloy Nanosheet Dendrites: An Economical and Highly Active Catalyst for Ethanol Electrooxidation. *Sci. Rep.* **2013,** *3* (1), 1181.

25. Du, W. X.; Mackenzie, K. E.; Milano, D. F.; Deskins, N. A.; Su, D.; Teng, X. W., Palladium-Tin Alloyed Catalysts for the Ethanol Oxidation Reaction in an Alkaline Medium. *ACS Catal.* **2012,** *2* (2), 287-297.

26. Gao, Q.; Mou, T. Y.; Liu, S. K.; Johnson, G.; Han, X.; Yan, Z. H.; Ji, M. X.; He, Q.; Zhang, S.; Xin, H. L.; Zhu, H. Y., Monodisperse PdSn/SnOx core/shell nanoparticles with

superior electrocatalytic ethanol oxidation performance. *J. Mater. Chem. A* **2020,** *8* (40), 20931-20938.

27. Yu, N. F.; Tian, N.; Zhou, Z. Y.; Sheng, T.; Lin, W. F.; Ye, J. Y.; Liu, S.; Ma, H. B.; Sun, S. G., Pd Nanocrystals with Continuously Tunable High-Index Facets as a Model Nanocatalyst. *ACS Catal.* **2019,** *9* (4), 3144-3152.

28. Yang, Y. Y.; Ren, J.; Li, Q. X.; Zhou, Z. Y.; Sun, S. G.; Cai, W. B., Electrocatalysis of Ethanol on a Pd Electrode in Alkaline Media: An in Situ Attenuated Total Reflection Surface-Enhanced Infrared Absorption Spectroscopy Study. *ACS Catal.* **2014,** *4* (3), 798-803.

29. Dunwell, M.; Yan, Y. S.; Xu, B. J., A surface-enhanced infrared absorption spectroscopic study of pH dependent water adsorption on Au. *Surf. Sci.* **2016,** *650*, 51-56.

30. Huang, W.; Ma, X. Y.; Wang, H.; Feng, R.; Zhou, J.; Duchesne, P. N.; Zhang, P.; Chen, F.; Han, N.; Zhao, F.; Zhou, J.; Cai, W. B.; Li, Y., Promoting Effect of $Ni(OH)_2$ on Palladium Nanocrystals Leads to Greatly Improved Operation Durability for Electrocatalytic Ethanol Oxidation in Alkaline Solution. *Adv. Mater.* **2017,** *29* (37), 1703057.

31. Martin, N. M.; Van den Bossche, M.; Gronbeck, H.; Hakanoglu, C.; Zhang, F.; Li, T.; Gustafson, J.; Weaver, J. F.; Lundgren, E., CO Adsorption on Clean and Oxidized Pd(111). *J. Phys. Chem. C* **2014,** *118* (2), 1118-1128.

32. Zhang, Z. Y.; Chi, M. F.; Veith, G. M.; Zhang, P. F.; Lutterman, D. A.; Rosenthal, J.; Overbury, S. H.; Dai, S.; Zhu, H. Y., Rational Design of Bi Nanoparticles for Efficient

Electrochemical CO_2 Reduction: The Elucidation of Size and Surface Condition Effects. *ACS Catal.* **2016,** *6* (9), 6255-6264.

33. Zhu, H.; Zhang, S.; Guo, S.; Su, D.; Sun, S., Synthetic control of FePtM nanorods (M = Cu, Ni) to enhance the oxygen reduction reaction. *J. Am. Chem. Soc.* **2013,** *135* (19), 7130-3.

34. Dunwell, M.; Lu, Q.; Heyes, J. M.; Rosen, J.; Chen, J. G.; Yan, Y.; Jiao, F.; Xu, B., The Central Role of Bicarbonate in the Electrochemical Reduction of Carbon Dioxide on Gold. *J. Am. Chem. Soc.* **2017,** *139* (10), 3774-3783.